Benthic irradiance in the Great Barrier Reef:

model, spatiotemporal patterns, and index of water quality

Thesis submitted by:

Marites Magno Canto

MSc. Marine Science (Physical Oceanography) – University of the Philippines Diliman

in March 2022

for the degree of Doctor of Philosophy (Natural and Physical Sciences)

in the College of Science and Engineering

James Cook University

Dedicated to my husband, Robert,
our son, Gabriel Adrie,
and
my entire family back home in the Philippines.

In loving memories of
Ulpiano de Belen Magno (1939 – 2012),
Isabella Louise Canto (2013 – 2013),
and
Matthew Canto (2015 – 2015)

Statement of Contribution of Others

Financial Support

AIMS@JCU Scholarship (stipend 4.5 years)	$135000
AIMS@JCU Quantitative Marine Science Funding	$ 5000
AIMS@JCU Travel Award (Domestic)	$ 750
AIMS@JCU Travel Award (International)	$ 1500
AIMS@JCU Incentivised Writing Fund	$ 3000
National Environmental Science Program	$ 10000
Australian Institute of Marine Science in-kind support	(NA)
Integrated Marine Observing System in-kind support	(NA)
National Aeronautics and Space Administration (NASA) in-kind support (Ocean Optics 2017 Summer Course, Darling Marine Centre, University of Maine, USA)	(NA)

Thesis Committee

Dr Barbara Robson, Australian Institute of Marine Science (AIMS)

Dr Lachlan McKinna, Go2Q Pty Ltd

Dr Katharina Fabricius, Australian Institute of Marine Science (AIMS)

Prof Yvette Everingham, School of Science and Engineering, James Cook University (JCU)

Analytical and Programming Assistance

Dr Lachlan McKinna

Dr Barbara Robson

Editorial Assistance

Dr Katharina Fabricius

Dr Barbara Robson

Dr Lachlan McKinna

Acknowledgements

I would like to thank my supervisors, Dr Katharina Fabricius, Dr Lachlan McKinna, Prof Yvette Everingham and Dr Barbara Robson, for their unwavering support, kindness and understanding throughout this PhD journey. Katharina, I am very grateful for the opportunity to do a PhD as part of your project. Your genuine belief, patience, and intellect have set me afoot early on and onwards. To Barbara, who eventually took on the role as my primary supervisor midway through my second year, I sincerely thank you for your assistance during this undertaking. I appreciate you for understanding the personal difficulties I was going through and allowing me to navigate towards the end at my own pace with reassuring and kind motivation to ensure the completion of my research. To Yvette, thank you for your guidance and logistical advice, which proved beneficial to me as a student and researcher. To my secondary supervisor Lachlan, I sincerely appreciate all the countless hours you have invested in me from the very beginning as I was learning the fundamentals of ocean optics. Your constant guidance helped me traverse the deep sea of optical literature and have profoundly contributed to developing, implementing, and publishing my benthic irradiance model. Your passion for and knowledge in optical oceanography and remote sensing, patience, kindness, and humility were inspirations throughout this undertaking.

My sincere gratitude also goes to Geoff Millar, the System Administrator at AIMS. Geoff went above and beyond in helping me set up an environment on the AIMS-HPC where I can implement my model development, testing and subsequent satellite data processing and analysis, which form the baseline work of my PhD. I also would like to acknowledge other AIMS staff including the AIMS-IMOS Oceanography group, especially Chris Bartlett, for deploying the PAR loggers and retrieving *in situ* PAR data I used for model validation and my co-commuters for their camaraderie and those witty and dreary conversations alike. Sincere thanks also go to the AIMS@JCU staff for their support and encouragement through the years.

In addition, I would like to acknowledge the lecturers, support staff, and fellow students of the NASA-sponsored Ocean Optics 2017 Summer course. I have learned so much from you, and I appreciate the incredible network of optical and remote sensing scientists I am privileged to be acquainted.

To my fellow PhD students and friends with whom I shared either a physical or ‘virtual’ AIMS office space (during these unusual pandemic times) and cups of coffee over the past few years, Marina Santana, Felicity Kuek, Stephanie DiPerna, Michaela Miller, and Chinenye Ani, thank you all for your companionship. Marina and Felicity, thank you for the dinners and pleasant distractions. I am grateful for your friendship.

Sincere thanks also go to a good friend Kristina ('Tch') Pahang-Horowitz for spoiling my family and me through great foods, emergency Uber-ing, and just genuine friendly chats. Tch, your sunny personality is always an amiable pause from my PhD frenzies. Thank you for sticking around.

There are other people not directly involved in this work but who also warrant my heartfelt gratitude. To Dr Cesar Villanoy and Dr Laura David, former work supervisors (but also close friends) from The University of the Philippines (UP) Marine Science Institute (MSI), who helped build the foundation and hone my research skills in oceanography (physical and satellite) and remote sensing before coming to Australia. Your passion for research, ingenuity, great work ethics and humility despite the success have ingrained upon me. To Dr Scarla Weeks, a former work supervisor from The University of Queensland (UQ), who paved the network which presented this PhD opportunity, thank you. To friends near (Brisbane and Townsville) and across the seas with whom I have shared the same passion for research, especially my closest friends Pach, JD, Aubrey, Olive, Zinnia, and our late dear friend, Mimoy, thank you for the encouragement, but especially for the lasting friendship here on Earth or the other side. Thank you all for believing that I will earn a PhD title next to my name one day.

Across the globe, I would like to thank my beloved family for the motivation, support, and encouragement. To my sister Josie, thank you for sacrificing your own dreams and investing in my education. You and our entire family have inspired me to dare and achieve a daunting aspiration. To my dear *Inay* (mother) Rufina Magno, who is my biggest fan at almost 82 years of age. *Inay*, you are the epitome of resilience and unconditional love. Thank you for raising me to be the determined and caring individual that I am. To my mother-in-law, Elizabeth Chiongson, thank you for always being there for us, for spoiling your only grandson Gabriel when his parents are unable to, and for always making us laugh with your funny mishaps and misadventures. I love you all unconditionally.

Finally, I would like to thank my husband Robert and our son Gabriel for the unconditional love and support throughout. They say it is not much the destination but the journey itself that counts more. I am grateful that we have sailed through this far as a family against the many challenges and a few successes that peppered our course. Dada, you are my rock, and I am beyond blessed to have spent half my life with you. I pray for more years together so we can keep doing the things we love and dream of. Gabe, you are the centre of my universe. You gave me the best title and occupation a woman could ask for; being a mum to a great son is nothing short of amazing. I hope I have made you proud. I love you to bits.

I am thankful and grateful, God, for so many things.

"Success is the sum of small efforts, repeated day in and day out." – Robert Collier (1885 – 1950)

Abstract

Benthic irradiance is the total amount of visible light (specifically the photosynthetically active radiation, PAR) reaching the seafloor or bottom of the water column, determined by depth, water quality and incident PAR at the surface. The impact of light on the health of benthic organisms such as corals and seagrasses is a strong motivation to understand the spatial and temporal variability in benthic light. However, despite its importance in the marine environment, there has been insufficient information about benthic PAR, including in the largest coral reef ecosystem on Earth, the Great Barrier Reef (GBR). To address this gap, I used a remote sensing approach to develop a model to generate the much-needed benthic irradiance dataset. The model was developed using MODerate Resolution Imaging Spectroradiometer (MODIS)-Aqua satellite data but has the potential to be extended to any available multispectral remote sensing imagery.

The primary goal of this PhD research project is to characterise, quantify the variability of, and monitor benthic irradiance in the Great Barrier shelf region. To achieve this, this work has the following specific objectives:

1. To develop a physics-based model for estimating benthic irradiance using satellite imagery.
2. To characterise the baseline spatial and temporal patterns and quantify the variability of benthic PAR in the GBR.
3. To investigate the drivers of light variability.
4. To develop an ecologically-relevant benthic light-based index of water quality that complements existing GBR water quality metrics.

Chapter 2 describes the benthic irradiance model, the input parameters, and the steps necessary to derive benthic irradiance values at each location coincident with the selected model validation or test sites. The benthic irradiance model is a simple implementation of Lambert-Beer's Law. It requires three fundamental input parameters: (i) spectral solar irradiance reaching the sea surface, (ii) spectral inherent optical properties (IOPs), specifically the total absorption coefficient ($a(\lambda)$) and the total backscattering coefficient ($b_b(\lambda)$), that can be used to calculate spectral light attenuation coefficients, $K_d(\lambda)$, and (iii) high-resolution bathymetry data with spatial resolution matching the satellite datasets. The satellite-derived benthic irradiance values allowed estimation of two benthic PAR (bPAR) parameters: (i) instantaneous bPAR, which is coincident with the satellite overpass and (ii) daily-integrated bPAR, which is the total amount of light at depth in a day from sunrise to sunset, which was then used in model

validation. These two bPAR variables were compared with *in situ* measurements from four optically diverse test sites during matchups and model validation exercises. Type II linear regression analysis and performance metrics, bias and mean absolute error (MAE), indicated a strong correlation between the satellite-derived and the *in situ* bPARs with small bias and MAE, suggesting that the model was able to produce realistic estimates of benthic irradiance in the optically representative sites and has the potential to be implemented to a more extensive study region.

The benthic irradiance model was then applied to the whole GBR shelf study region within latitudes 10 to 26°S and longitudes 142 to 156°E using all available daily Level 1A satellite imagery from the MODIS-Aqua sensor between July 2002 and December 2018. In this instance, only the daily-integrated bPAR was generated for use in the remaining chapters of this PhD thesis. The satellite data processing and benthic irradiance model implementation culminated in 210 monthly aggregated daily-integrated bPAR maps representing 16.5-years' worth of information about benthic irradiance in the GBR. **Chapter 3** focuses on analysing this dataset aiming to characterise the baseline spatial and temporal patterns of bPAR in the GBR, using different temporal aggregations and quantitative analysis techniques. This chapter highlighted that bPAR varies strongly both spatially and temporally within the GBR and the different zones (defined by the NRM regions and cross-shelf waterbodies) with variations that align with drivers along the coast and overall local shelf dynamics.

The spatial and temporal variability of bPAR in the GBR is determined by a complex interplay of many factors, potentially including various in-water constituents and physical environmental influences. To investigate what controls the spectral light attenuation and hence light availability and variability in the different zones in the GBR, **Chapter 4** analyses the spectral light attenuation coefficients, $K_d(\lambda)$. Here, Random Forest models were created to understand how these constituents and other environmental predictors affect spectral light attenuation. Results for the inshore (enclosed and open) coastal and offshore waterbodies suggest that variability in K_d align with optical properties expected in these waterbodies. On the other hand, K_d variability in the mid-shelf reflects the potential combined influence of variations in chlorophyll *a* concentration (Chl *a*) driven by land-derived nutrient inputs and local oceanography within the shelf. In optically complex coastal waters like the GBR shelf region, information about drivers of light variability may provide additional crucial insights that could help better manage and address the pressures affecting vital benthic marine ecosystems, including coral and seagrass habitats. This is the first time an analysis using a spatially and temporally relevant benthic light dataset has been applied in the whole GBR region.

Light penetration and the amount of light reaching benthic organisms is strongly affected by water quality. Benthic light can thus be used as a water quality indicator. A method for developing a benthic light-based water quality metric (here referred to as the 'bPAR index') is presented within **Chapter 5**. The bPAR index indicates the cumulative stress due to benthic light levels falling below the defined combined benthic light threshold. The cumulative stress calculated from daily bPAR data spanning

from July 2002 to December 2019 (containing one year more data than presented in Chapter 3) is summarised over the different GBR management zones (NRM and water body), temporally aggregated, and mapped to five-letter grade scores aligned with the current GBR Water Quality Report Card. Zones and water years with 'no light stress' is equivalent to a 'very good water quality' score (or Grade A), while those with 'very high light stress' indicate a 'very poor water quality' score (or Grade E). Results showed that the bPAR index in the GBR has an overall gradient indicating decreasing water quality from offshore to inshore and from north to south. Historically, the poorest water quality obtained coincided during years or seasons with extreme events often associated with intense rainfall and flood events. The sensitivity of the bPAR index to changes in light availability makes it an ecologically relevant and complementary, if not a more suitable, water quality metric in the GBR.

The potential to operationalise the production of the benthic irradiance (hence, bPAR) dataset from remote sensing imagery and the successful demonstration of the bPAR index in mapping the water quality in the GBR highlights the additional important contributions of this PhD research.

Publications Produced During the PhD Candidature

Publications

Magno-Canto, M.M., McKinna, L.I.W., Robson, B.J. and Fabricius, K.E. (2019). *Model for deriving benthic irradiance in the Great Barrier Reef from MODIS satellite imagery*. Opt. Express 27, A1350-A1371. (DOI: 10.1364/OE.27.0A1350).

Magno-Canto, M.M., McKinna, L.I.W., Robson, B.J., Fabricius, K.E. and Garcia, R. (2020). *Model for deriving benthic irradiance in the Great Barrier Reef from MODIS satellite imagery: erratum*. Opt. Express 28, 27473-27475. (DOI: 10.1364/OE.405306).

Castro-Sanguino, C., Ortiz, J.C., Thompson, A., Wolff, N.H., Ferrari, R., Robson, B., **Magno-Canto, M.M.**, Puotinen, M., Fabricius, K.E., and Uthicke, S. (2021). *Reef state and performance as indicators of cumulative impacts on coral reefs*. Ecological Indicators, Volume 123, 107335, (DOI: 10.1016/j.ecolind.2020.107335).

Canto, M.M., Fabricius, K.E., Logan, M., Lewis, S., McKinna, L.I.W., and Robson, B.J. (2021). *A benthic light index of water quality in the Great Barrier Reef, Australia*. Marine Pollution Bulletin, 169, 112539. (DOI: 10.1016/j.marpolbul.2021.112539).

Reports and Technical Documents

Robson, B., **Canto, M.**, Collier, C., di Perna, S., Logan, M., Menendez, P., McKinna, L., Noonan, S., and Fabricius, K. (2019) *Benthic light as ecologically-validated GBR-wide indicator for water quality.* Report to the National Environmental Science Program. Reef and Rainforest Research Centre Limited, Cairns (40pp.).

Robson, B., **Canto, M**., McKinna, L., Logan, M., Lewis, S., and Fabricius, K. (2020) *Benthic light as ecologically-validated GBR-wide indicator for water quality: Drivers, thresholds and cumulative risks.* Report to the National Environmental Science Program. Reef and Rainforest Research Centre Limited, Cairns (116pp.).

Robson, B.J., **Canto, M.M.**, McKinna, L.I., Logan, M., Lewis, S., Fabricius, K.E. (2021) *Benthic light as ecologically-validated GBR-wide indicator for water quality: Drivers,*

thresholds and cumulative risks, Report to the National Environmental Science Program, Reef and Rainforest Research Centre Limited, Cairns (110pp.).

Presentations

Canto, M.M., Fabricius, K.E., McKinna, L.I.W., and Everingham, Y. *Developing benthic irradiance algorithm for the Great Barrier Reef shelf waters using MODIS satellite imagery*, AIMS@JCU Student Seminar Day, Townsville Yacht Club, 01 September 2017.

Canto, M.M., McKinna, L.I.W., Fabricius, K.E., Robson, B. and Everingham, Y. *A model for deriving benthic irradiance in the Great Barrier Reef lagoon using MODIS satellite imagery*, AIMS@JCU Student Seminar Day, Townsville Yacht Club, 14 September 2018.

Canto, M.M., McKinna, L.I.W., Fabricius, K.E., Robson, B. and Everingham, Y. *A model for deriving benthic irradiance in the Great Barrier Reef lagoon using MODIS satellite imagery*, Ocean Optics XXIV, Dubrovnik, Croatia, 07 - 12 October 2018.

Canto, M.M. *Benthic light from space*, AIMS@JCU Student Seminar Day, Townsville Yacht Club, 08 November 2019 (Speed talk).

Magno-Canto, M.M., McKinna, L.I.W., Fabricius, K.E., Robson, B. *Measuring benthic light from space: model results and first applications*, AIMS@JCU Student Seminar Day, Townsville Yacht Club, 08 November 2019 (Poster).

Magno-Canto, M.M. *Understanding the underwater light field in the Great Barrier Reef using MODIS satellite imagery*, Digital Earth Australia, Geoscience Australia, Canberra, 19 September 2019.

Magno-Canto, M.M. *Understanding the underwater light field in the Great Barrier Reef using MODIS satellite imagery*, School of Earth and Environmental Sciences, Remote Sensing Research Centre, University of Queensland, Brisbane, Australia, 23 September 2019.

McWhorter, J., Halloran, P., Mumby, P., Skirving, W., Steinberg, C., and **Canto, M**. *Under pressure: Climate change at depth across the Great Barrier Reef*, 14th International Coral Reef Symposium.

Robson, B., **Canto, M.M.**, McKinna, L.I.W., and Fabricius, K. *Monitoring water quality from space: benthic light as a new indicator of water quality for corals and seagrasses of the Great Barrier Reef*, The NESP TWQ Hub Impacts and Achievements Conference, Pullman Reef Hotel Casino, Cairns, Queensland, Australia, 28-29 April 2021.

Codes

Implementation of benthic irradiance model on NASA's SeaDAS software package
https://seadas.gsfc.nasa.gov/

Code for generating benthic PAR
https://github.com/eatlas/NESP-TWQ-5.3_Benthic-Light_WQIcode

Code for generating benthic light index of water quality
https://github.com/eatlas/NESP-TWQ-5.3_Benthic-Light_WQIcode

Datasets

GBR benthic PAR dataset (Jul 2002 to Dec 2019)
http://maps.eatlas.org.au/thredds/catalog_NESP5-3_xr_parb.html

GBR spectral light attenuation coefficient, Kd(λ) - (Jul 2002 to Dec 2019)
http://maps.eatlas.org.au/thredds/catalog_NESP5-3_kd-data.html

Processed *in situ* PAR dataset for selected IMOS mooring stations (Mar 2015 to Nov 2017)
https://eatlas.org.au/pydio/public/gbr-nesp-twq-2-3-1-aims-benthic-light-bpar-dataset1-20190218

Table of Contents

List of Figures

Chapter 1

Chapter 2

Chapter 3

Chapter 4

Chapter 5

Thesis Appendix

List of Tables

Chapter 2

Chapter 3

Chapter 4

Chapter 5

Thesis Appendix

List of Common Symbols

Symbol	Units	Description
$E_d(\lambda)$	W m^{-2}	Spectral downwelling plane irradiance
$E_d(\lambda,0^+)$	W m^{-2}	Spectral downwelling plane irradiance just above the sea surface
$E_d(\lambda,0^-)$	W m^{-2}	Spectral downwelling plane irradiance just below the sea surface
$K_d(\lambda)$	m^{-1}	Spectral diffuse light attenuation coefficient
K_d(PAR)	m^{-1}	Diffuse light attenuation coefficient of photosynthetically active radiation
λ	nm	Wavelength
$a(\lambda)$	m^{-1}	Total spectral absorption coefficient
$b_b(\lambda)$	m^{-1}	Total spectral backscattering coefficient
$R_{rs}(\lambda)$	sr^{-1}	Above-water remote sensing reflectance
$E_b(\lambda)$	µmol photons m^{-2} s^{-1}	Spectral benthic irradiance
$bPAR_i$	µmol photons m^{-2} s^{-1}	Instantaneous benthic photosynthetically active radiation
$bPAR_n$	µmol photons m^{-2} s^{-1}	Benthic photosynthetically active radiation at noon
$bPAR_d$	mol photons m^{-2} d^{-1}	Daily-integrated benthic photosynthetically active radiation
θ_{solz}	degrees	Solar zenith angle in air during satellite overpass
θ_t	degrees	Solar zenith angle of light transmitted downward in the water
n_w	dimensionless	Refractive index of seawater
t_g	dimensionless	Global transmittance of the air-water interface
ρ_{sky}		Sea surface reflectance of the diffuse irradiance
ρ_{sun}		Sea surface reflectance of the direct irradiance
ϕ	radians	Solar hour angle
δ	radians	Declination angle
γ	radians	Date angle
ϕ_{rise}	radians	Solar hour angle at sunrise
ϕ_{noon}	radians	Solar hour angle at noon

lat	radians	Latitude coordinate
π	dimensionless	Pi
Chl *a*	mg m^{-3}	Chlorophyll *a* concentration
Z_{sd}	m	Satellite-derived photic depth

List of Abbreviations

Abbreviation	Meaning
PAR	Photosynthetically active radiation
bPAR	benthic photosynthetically active radiation
NRM	Natural Resource Management
GBR	Great Barrier Reef
GBRMP	Great Barrier Reef Marine Park
AIMS	Australian Institute of Marine Science
IMOS	Integrated Marine Observing System
Q-IMOS	Queensland – Integrated Marine Observing System
MODIS	Moderate Resolution Imaging Spectroradiometer
MODISA	Moderate Resolution Imaging Spectroradiometer Aqua
IOPs	Inherent Optical Properties
CDOM	Coloured Dissolved Organic Matter
NAP	Non-algal Particulate Matter
SWIM	Shallow Water Inversion Model
DLI	Daily Light Integral
P-E	Photosynthesis-Irradiance
WQI	Water Quality Index
APD	Absolute Percent Difference
UPD	Unbiased Percent Difference
MAE	Mean Absolute Error
USR	Usable Solar Radiation
DEM	Digital Elevation Model
MSL	Mean Sea Level

"If I have seen further, it is by standing on the shoulders of Giants." – Isaac Newton (1642 – 1727)

1 General Introduction

1.1 Overview and significance of solar radiation

Solar radiation is essential for life in aquatic ecosystems. Specifically, the solar radiation within the visible spectral range (400-700 nm) or the photosynthetically active radiation (PAR) is most important for marine organisms (Lalli and Parsons, 1997; Gattuso et al., 2006; Kirk, 2011). The portion of the visible light that reaches the seafloor, referred to as benthic irradiance or benthic PAR, provides the energy needed by benthic organisms like corals (with the help of their symbionts) and seagrasses to convert inorganic nutrients into organic compounds via photosynthesis. Light is a critical limiting resource for oceanic photosynthesis because only a fraction of light reaching the ocean's surface can penetrate at depth (Kirk, 2011).

The need to understand and estimate benthic irradiance pertaining to primary production in the coastal zone is well appreciated, and the associated limitations have been highlighted (Ackleson, 2003; Gattuso et al., 2006; Gattuso et al., 2020). Recently, global-scale estimates of the distribution of benthic PAR and the percentage of the area of the coastal zone receiving specific average irradiance at depth have been published (Gattuso et al., 2006; Gattuso et al., 2020), providing a global perspective on the distribution of light limitation experienced by benthic photosynthetic organisms. However, a range of effects of variable and reduced light conditions on coastal ecosystems also underscore specific motivations to further our understanding of benthic light availability at a regional scale. Previous studies have highlighted that sub-optimal light conditions can lead to limited photosynthesis (Fabricius, 2005; Ralph et al., 2007), declining seagrass abundance, growth and distribution (Ralph et al., 2007; Collier et al., 2012a; Bertelli and Unsworth, 2018) or drive seagrass loss (Collier et al., 2016a), reduced coral recruitment and biodiversity (Fabricius, 2005), and can result in shallower depth limit for coral reef development (Kleypas et al., 1999; Grigg, 2006; Cooper et al., 2007; Dubinsky and Falkowski, 2011; Fabricius, 2011; Muir et al., 2015). Low irradiance may also amplify the negative effects of ocean acidification on the recruitment of coralline algal communities (Kluibenschedl et al., 2021) where the interaction between ocean acidification and light alters the photosynthetic responses of coralline algae (i.e., likely shifting light tolerance and limiting coral distribution to a narrower range of light environments) (Briggs and Carpenter, 2019). In conjunction with elevated suspended sediment concentrations, light reduction also poses a greater risk to corals than increased turbidity alone (e.g.,

corals exposed to low light in turbid conditions showed increased mortality), which suggests that understanding of the interactive effects of light is needed to understand how turbidity pressure influence corals (Bessell-Browne et al., 2017a) and potentially seagrasses (Adams et al., 2016).

Not only low but also high solar irradiance can play an important role for benthos. During coral bleaching, cellular damage in both the coral host and zooxanthellae during thermal stress (Lesser and Farrell, 2004) is exacerbated by high irradiance conditions (Lesser and Farrell, 2004; Lesser, 2011). Thus, while irradiance is essential for photosynthesis, high irradiance similarly presents a complicating factor that can increase coral bleaching during thermal stress (Mumby et al., 2001; Lesser, 2011; Leahy et al., 2013). These contradictions emphasise the critical role of light, the complex interactions and ecological responses influenced by light, and the need to understand these interactions better. Information about benthic irradiance at relevant spatial and temporal scales is critical to achieving such understanding.

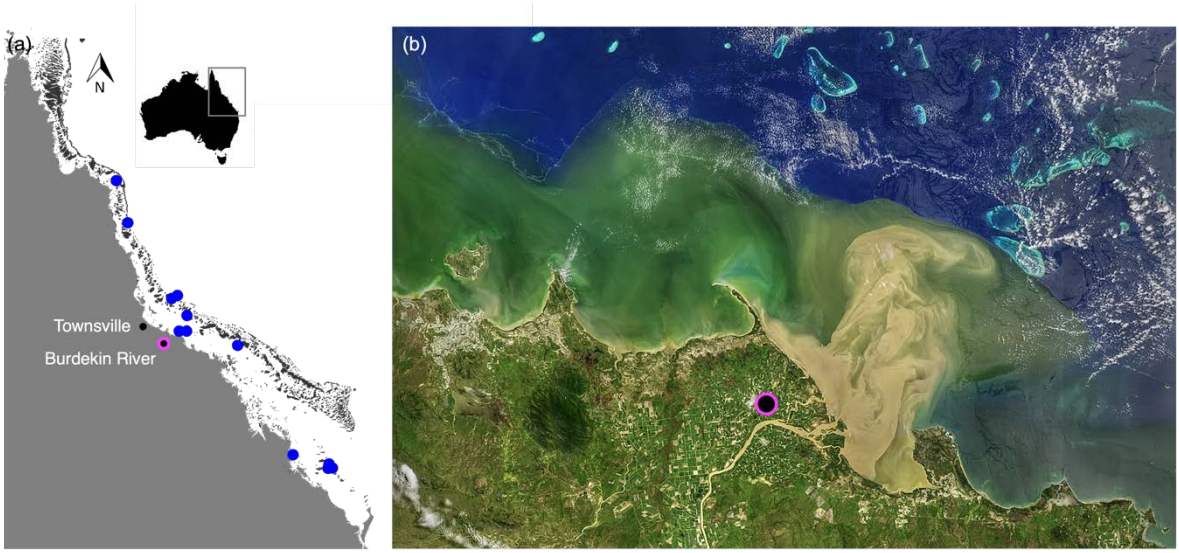

Figure 1.1. (a) Map showing current and historical mooring stations (blue filled circles) equipped with PAR sensors in the GBR, maintained by the Australian Institute of Marine Science, highlighting the spatial limitation of in situ data against the vast spatial scale of the GBR; (b) Landsat 8 image of the Burdekin River flood plume taken on the 11th of February 2019, highlighting the transition from suspended sediments (brown) to phytoplankton (green) dominated waters. Image courtesy of NASA – Ocean Biology Processing Group (OBPG).

Despite the significance of benthic irradiance in the marine environment, there has been insufficient information about the nature of the underwater light field reaching the benthic ocean (Gattuso et al., 2006) because the problem and solution to the lack of relevant datasets are not straightforward nor economical. Benthic PAR can be measured *in situ* with high accuracy using light (PAR) sensors to retrieve instantaneous or continuous measurements (e.g., moored). However, this option also has some limitations related to the type (e.g., shape and design) of sensors being used, which will influence how these sensors intercept the incoming radiation (Long et al., 2012). Planar PAR sensors have a flat

surface light collector which detects photons headed downward (Mobley, 1994) impinging the horizontal plane surface (2π steradians). Scalar PAR sensors have either a hemispherical or spherical light collector, which allows incoming light along 180° (2π steradians) or in most directions (4π steradians), respectively (Mobley, 1994; Long et al., 2012). The data obtained from the latter is considered more accurate as it represents radiation from most directions that can potentially reach a photosynthetic cell (e.g., phytoplankton) (Mobley, 1994). Scalar PAR sensors (e.g., LICOR spherical quantum sensor) offer more accurate *in situ* PAR measurements but are more expensive than planar PAR sensors (e.g., Onset's HOBO pendant temperature/light data logger) which are cheaper and logistically simpler to operate (Long et al., 2012). The quality of data from these sensors further depends on whether appropriate protocols are in place during sensor deployment that guide PAR measurement *in situ*. For example, for extended deployment periods, the logger must be equipped with a wiper system to help avoid biofouling of the optical sensor, which is a primary issue for submerged sensors and cause of data quality degradation (Manov et al., 2004) or be regularly checked for biofouling and replaced if needed. *In situ* data collection campaigns using these PAR sensors thus tend to be resource-intensive not to mention spatially limited, with the resulting dataset only representing discrete points. In the Great Barrier Reef (GBR), there are currently only a few ocean-observing systems across the eastern coast of Australia equipped with PAR sensors that collect either surface or in-water light measurements (Figure 1.1a). These observing platforms are part of the Australian Integrated Marine Observing System (IMOS) national array facility funded by the Australian Government and maintained and operated in collaboration with other research institutions, in particular the Australian Institute of Marine Science (AIMS) (Rigby et al., 2014).

These current platforms offer an opportunity for near-real-time observations and open access to *in situ* data, including PAR. However, this benefit is perhaps immediately superseded because of the insufficient spatial data generated from these platforms for studying a vast, spatially and geographically complex region such as the GBR. In addition, water masses in the GBR have strong spatial heterogeneity. A logger within the plume (Figure 1.1b), for instance, will capture the benthic light variability directly above it but would fail to capture other spatial features within and beyond the boundaries of the plume, highlighting the spatial limitations of *in situ* point measurements. Also, the light sensors available in these moorings are limited to obtaining a single broad-band quantity, PAR.

While PAR is often the most convenient parameter to measure *in situ,* estimates of spectral light intensities may be more useful, given that the optical properties of oceanic waters that determine the remaining optical signal are wavelength-dependent (IOCCG, 2000). As light varies spectrally depending on the waterbody and the materials present in the water (Mobley, 1994; IOCCG, 2000; Ackleson, 2003; Kirk, 2011), it is more desirable to obtain measurements at different wavelengths (or spectrally). This would permit the derivation of PAR quantity and the opportunity to inspect the individual contribution of optically active components to light variability.

Fortunately, the limitations of *in situ* data collection methods can be resolved by using a remote sensing approach. Ocean colour remote sensing collects information on the amount of light penetrating the water. It offers a way to derive quantitative data on the types and concentrations of constituents present in the water (IOCCG, 2000) that are critical to estimating benthic irradiance.

Before this PhD project, there was no direct method for accurately estimating benthic irradiance from satellite observations. However, there have been other advances in remote sensing applications in the GBR (discussed later), and insights obtained from these efforts have been instrumental in developing a remote sensing, physics-based model through this PhD project for accurately estimating benthic irradiance for each location within the GBR where satellite observations are available.

Developing the benthic irradiance model requires understanding the various processes that determine the propagation and diminution of light in the water. The subsequent sections give brief information regarding the optical pathways and significant interactions between light and the materials found within the water medium, which provides the rationale for choosing an approach that considers these optically-active constituents for calculating the light attenuation coefficient (detailed in **Chapter 2**). I also discuss the role of water quality for the iconic GBR, as an additional motivation for this research, based on the immediate need for a more ecologically relevant metric for water quality monitoring. The last section of this chapter lists the identified knowledge gaps, the main goals, and the specific aims of this PhD project, as Introduction to the succeeding Thesis Chapters.

1.2 The Great Barrier Reef

The GBR is the largest continuous coral reef ecosystem on Earth (Hutchings et al., 2008). It was inscribed on the World Heritage List in 1981. The GBR Marine Park covers an area of approximately 345,500 km^2 along the northeastern Australian coast spanning > 13 degrees in length between latitudes 10.5°S to 24°S (Haynes and Michalek-Wagner, 2000; De'ath et al., 2012; Hutchings et al., 2019). The GBR encompasses extensive coral reef areas providing vast stretches of coastal protection with over 3,000 individual reefs, and its nearshore and deep water seagrass meadows cover approximately 5700 km^2 and 40000 km^2, respectively (Great Barrier Marine Park Authority, 2014). Tropical and subtropical coral reefs are the most biodiverse ecosystem in the ocean, which support around 25% of all marine fish species and other marine animals despite only covering 0.1% surface area globally, the GBR being an iconic example (Heron et al., 2017). The GBR is also enlisted as a natural and cultural World Heritage (Lucas et al., 1997) and has been valued at $56 billion (Deloitte Access Economics, 2017). The combined tourism, commercial fishing, and recreational activities from the Reef contribute $6.4 billion to the Australian economy annually (Deloitte Access Economics, 2017).

Like many other coral reef systems worldwide that are in a state of decline (Richmond and Wolanski, 2011; Brodie and Waterhouse, 2012; De'ath et al., 2012), the GBR is not impervious to pressures from climate change and increased human activities near the coasts (Haynes and Michalek-Wagner, 2000).

Coral reefs are under immense threat from increased ocean temperature, which has already caused successive mass coral bleaching events (Hughes et al., 2017; Hughes et al., 2018a; Hughes et al., 2018b) and enormous pressure from local anthropogenic stressors (Heron et al., 2017). The declining water quality conditions associated with increased loads of contaminants (i.e., sediments, nutrients, and pesticides from agricultural activities) (Brodie et al., 2003; Brodie et al., 2011; Brodie et al., 2012) leading to turbidity-induced light reduction are considered as a significant threat to the health of the GBR (De'ath and Fabricius, 2010; Devlin et al., 2015). Developing efficient and cost-effective methods or tools (e.g., employing remote sensing techniques) to understand the dynamics of benthic light availability within the vast GBR region will help protect and manage the Reef in the face of changing coastal water quality conditions.

1.3 Considerations for developing a benthic irradiance model

1.3.1 Light in the water: optical pathways and significant interactions

The amount of sunlight reaching the ocean's surface is of interest to oceanographers because of its application in many ocean studies, including ocean colour remote sensing. Photons from the sun follow different pathways in the atmosphere and water mediums, subject to various attenuation (absorption and scattering) processes (Mobley, 1994; IOCCG, 2000; Kirk, 2011). Figure 1.2 summarises the pathways of light in the air and water reaching the satellite sensor. The signal measured by the satellite remote sensor comes from three main contributions, namely (i) the photons scattered by the atmosphere, (ii) the direct sunlight reflected off the sea surface, and (iii) the upwelling light backscattered out of the water (IOCCG, 2000). Of these three, the latter is the remote signal with direct importance in studying the colour of the ocean. The backscattered light contains valuable information about the water body, including the various materials (or constituents) that contribute to the colour of the water (Werdell et al., 2018) and comprise the critical information needed to quantify how much light penetrates at depth and understand the different optical processes within the water column.

Light penetrating at depth is a function of the wavelength and the clarity of the water. The clarity of water is, in turn, influenced by the presence and the concentration of substances within the water column. The portion of the sunlight able to penetrate the sea surface is thus further subject to different interactions in the water. In shallow, clear coastal waters where the absorption and scattering processes are primarily due to water molecules, a large proportion of the sunlight may reach the bottom (IOCCG, 2000; Ackleson, 2003). In contrast, in shallow, turbid, and optically complex water types, various optically active constituents are present in significant concentrations that determine the diminution of light and penetration depth is typically less for all wavelengths (IOCCG, 2000).

The absorption and scattering of sunlight within the water define the remaining upwelling light leaving the sea surface measured by the remote satellite sensor. Overall, three primary components influence

the optical properties of the water, including (i) phytoplankton, (ii) suspended sediment (inorganic) material, and (iii) coloured dissolved organic matter. In addition, ocean optics are influenced by water molecules and reflectance from the sea bed or benthic habitat (Figure 1.2).

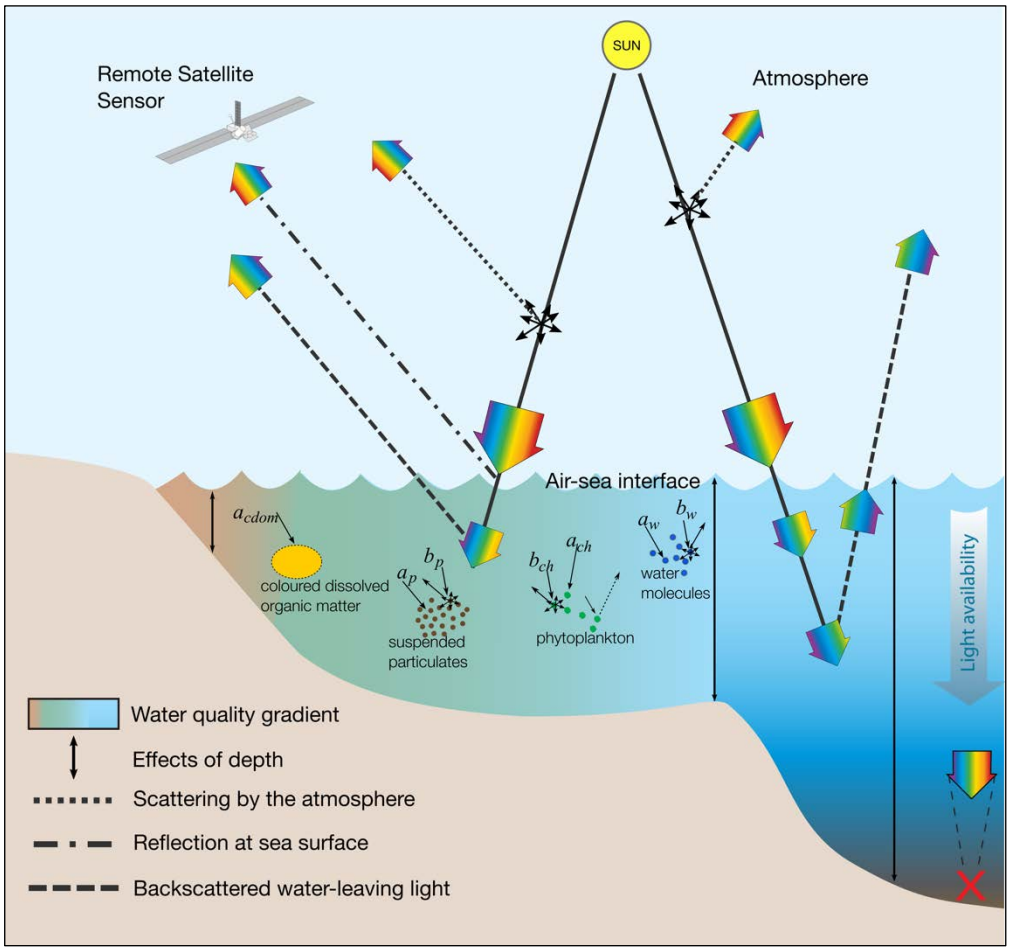

Figure 1.2. Schematic diagram of the optical pathways of sunlight, including the different interactions between light and the atmosphere, sea surface, and various constituents in the water that determines the remotely-sensed signal detected by the satellite remote sensor. The in-water interactions depicted are for optically complex water where several substances influence the optical properties of the waterbody. The water-leaving signal measured by the satellite, which contains information about the waterbody, can then be used to estimate benthic irradiance, the portion of light reaching the seafloor (modified from Reichstetter (2016) and referenced from IOCCG (2000)).

The phytoplankton is the most important component responsible for variations in the optical properties of the water (IOCCG, 2000) and mapping its distribution has been the most fundamental application of the ocean colour remote sensing. Chlorophyll-*a* (Chl *a*), the primary phytoplankton pigment, absorbs sunlight strongly in specific wavelengths of the spectrum, with a strong peak at 440 nm and a weaker peak at 675 nm, but with an overall absorption curve that decreases with wavelength (Robinson, 1985; IOCCG, 2000; Kirk, 2011). Phytoplankton is composed of free-floating, microscopic, single-celled multicellular autotrophic and mixotrophic organisms forming the base of the aquatic food web. The size and shape of the cells (aside from the concentration and refractive indices) also determine light

attenuation via scattering (Stramski and Kiefer, 1991). Although light scattering does not readily remove light, it modifies the direction of light propagation (increasing the optical pathlength), increasing the likelihood of the photons being captured by an absorbing component present in the water (Kirk, 2011). The phytoplankton component, thus, attenuates light by absorbing and scattering light in the water.

Inorganic suspended particulate material is also an important component that modifies benthic light. These materials may include small particles (<10 um in size) delivered to marine environments by terrestrial (land-based) runoff, coastal erosion, and river outflows (and floods) (IOCCG, 2000; Stramski et al., 2007) as well as resuspended bottom sediment materials reintroduced in the water column via wave action, tidal currents, and wind mixing (Kirk, 2011). Coastal and inland waters tend to have higher concentrations of the inorganic suspended particulate component than offshore clear waters, which distinguish the optical properties of these water bodies. The contribution of the particulate component to the attenuation of light (both by absorption and scattering) also depends on the particle size distribution (Stramski et al., 2007) and the composition (or what constitute the particle assemblage).

Coloured dissolved organic matter (CDOM) constitute a fraction of the DOM pool (Kirk, 2011; Lønborg et al., 2021) and is comprised of materials smaller than 2 microns (average filter pore size) (Mitchell et al., 2000). It naturally occurs in the ocean as a degradation component of phytoplankton cells and other organic particles, especially in productive water bodies (IOCCG, 2000) but may also contain leached soluble humic substances from soils and leaf litter (Kirk, 2011). A large fraction of CDOM in the coastal marine environment comes from land delivered by river discharge. Hence, CDOM concentrations are higher in inland coastal waters near river systems. CDOM strongly absorbs photons in the UV and blue wavelengths, with the absorption spectrum decreasing exponentially with wavelength. Scattering by CDOM is considered negligible. Thus, CDOM contributes to light attenuation primarily via light absorption.

These optically active constituents contribute differently to the optical signal measured by the satellite depending on the wavelength and the dominant optical constituent in the waterbody. The relative contributions of these three optically active components are typically used to distinguish between water bodies. For example, clear oceanic water bodies with optical properties primarily determined by phytoplankton and its detritus (Morel and Gentili, 2009) are classified as Case 1, whereas other water bodies with a substantial concentration of constituents other than Chl *a* are classified as Case 2. These constituents and their optical properties should be accounted for to understand and accurately characterise the underwater light field.

1.3.2 Inherent Optical Properties (IOPs)

Inherent optical properties (IOPs) are essential for characterising the marine optical environment (Loisel et al., 2001), including deriving the remaining irradiance at depth. IOPs are determined by the nature and concentration of various in-water constituents and include the scattering and absorption properties of the seawater and its components (Werdell et al., 2018). IOPs are not directly affected by the changes in radiance distribution – in other words, they are independent of the light field (Jerlov, 1976; Zaneveld, 2013). IOPs can be described as the additive contribution of the individual components (Morel and Prieur, 1977). The total spectral absorption coefficients, $a(\lambda)$ (units: m^{-1}), and the total spectral backscattering coefficients, $b_b(\lambda)$ (units: m^{-1}), are two of the most common IOPs retrieved from spectral remote sensing reflectance, $R_{rs}(\lambda)$ (units: sr^{-1}), to describe the spectral composition and transmission of light through the water column. The total absorption coefficient, for example, can be estimated as the additive contribution of absorption due to (optically absorbing components) phytoplankton, CDOM and NAP.

Inversion of the remote sensing signal to retrieve IOPs and information about the individual (absorbing and scattering) components has long been a challenge, but a few algorithms have been refined and are generally considered robust with fewer assumptions (McKinna et al., 2015). The Generalised IOP (GIOP) model (Franz and Werdell, 2010; Werdell et al., 2013), Garver-Siegel-Maritorena (GSM) algorithm (Maritorena et al., 2002), and the Quasi-Analytical Algorithm (QAA) (Lee et al., 2002) are some of the widely (and operationally) used algorithms for deriving spectral marine absorption and backscattering coefficients of the water column constituents. A common advantage of these algorithms over many IOP models is that the retrieval of the IOPs and the magnitude of each constituent that contributes to the full spectral distribution of the $R_{rs}(\lambda)$ does not rely wholly on empirical relationships that define the spectral shape function of each optically active components (Franz and Werdell, 2010). Although these algorithms have been successfully used for global and coastal water applications, there are still some limitations to their applicability in optically shallow (e.g., where signal off the bottom influences the water-leaving radiance) and optically complex (e.g., where constituents other than phytoplankton influences the optical properties of the water column) environments.

Bio-optical parameters and concentrations describing the absorption and scattering properties of the inshore (estuarine and lagoonal) and reef waters within the GBR shelf have been shown to vary significantly in space and time, with these variations driven by environmental conditions (e.g., proximity to the river system and other sources) and physical forcings (e.g., wind, tide) that result in processes (e.g., water column mixing, sediment resuspension) that modify the optical signal (Blondeau-Patissier et al., 2009).

Light absorption coefficients in the GBR indicate a broad range of values delineating apparent differences between coastal and estuarine to offshore reef waters. For example, in six spatial regions in

the GBR, Blondeau-Patissier et al. (2009) reported total absorption coefficients at 440 nm wavelength (a_{tot} (440), units: m^{-1}) ranging from 0.002 m^{-1} (in deep offshore, oligotrophic reef waters) to 3.257 m^{-1} (estuarine waters in Mossman-Daintree site, wet season). The contribution of the individual optically absorbing components to the total absorption budget also varied regionally (e.g., absorption due to NAP was lowest in reef waters and highest in estuarine waters, especially in the Fitzroy region; absorption due to CDOM was proportionally high in reef waters; and absorption due to phytoplankton was most important in the offshore stations in the Fitzroy region). In waters directly affected by river discharge, the total light absorption may be dominated by CDOM, which can further impact phytoplankton absorption efficiency (Cherukuru et al., 2017). Similarly, light scattering and backscattering coefficients obtained from the differing water types also indicate large variability with total scattering coefficient at 555 nm wavelength, b_p (555), varying between 0.032 m^{-1} (reef waters) and 28.044 m^{-1} (Mossman-Daintree estuary during the wet season) (Blondeau-Patissier et al., 2009). These IOP coefficients suggest that in a complex region like the GBR, where biogeochemical parameters and concentrations vary significantly, spatially and temporally, accurate retrieval of optical water quality parameters from the ocean colour remote sensing will be strongly affected by this variability. Optical characterisation that considers spatial and temporal variations (Oubelkheir et al., 2006; Blondeau-Patissier et al., 2009) is thus essential for developing regional remote sensing IOP algorithms (e.g., (Brando et al., 2012)).

In addition to optical complexity, the signal reflected off the bottom (i.e., bottom albedo) that often contaminates the water-leaving radiance signal presents another challenge in IOP retrievals from ocean colour remote sensing. While another inversion model for IOP retrievals exists (e.g., (Brando et al., 2012)), a model that explicitly corrects for the bottom albedo and incorporates information on the bottom topography for the GBR offers a notable improvement. The Shallow Water Inversion Model (SWIM) is an inversion algorithm based on the Hyperspectral Optimization Process Exemplar (HOPE) model (Lee et al., 1998) that improves retrievals of spectral IOPs by incorporating pre-existing information on the bathymetry and benthic substrate brightness (McKinna et al., 2015) where the latter includes bottom reflectance parameterisation optimised using two distinct classes: “light” and “dark” pixels (Reichstetter et al., 2015; Reichstetter, 2016). Comparisons with the GIOP and the QAA methods revealed that SWIM-derived IOP estimates of the non-water absorption coefficient (the bulk or total absorption coefficient except due to the water medium itself) and the particulate backscattering coefficient (the bulk or total backscattering coefficient) were more realistic and in agreement with radiative transfer modelling (McKinna et al., 2015). This PhD research exploits the information on $a(\lambda)$ and $b_b(\lambda)$ that can be obtained from SWIM to determine the light attenuation at each satellite-observed pixel within the GBR to characterise the underwater light field and derive benthic irradiance from remote sensing satellite imagery.

1.3.3 Diffuse light attenuation coefficient for the downwelling irradiance

The spectral diffuse attenuation coefficient for the downwelling irradiance, $K_d(\lambda)$ (units: m^{-1}), describes the exponential rate of light attenuation with depth in the water (Mobley, 1994; Kirk, 2011). Simply, $K_d(\lambda)$ governs the vertical propagation of the downwelling irradiance through the water column (Lee et al., 2005a; Lee et al., 2005b) and determines the amount of light energy transmitted vertically and whether light reaches the seafloor. $K_d(\lambda)$ depends strongly on the IOPs that characterise the water than on external environmental influences (e.g., solar zenith angle, cloud cover, or surface waves) (Mobley, 1994). This dependence makes $K_d(\lambda)$ useful in deriving relationships between light measurements and water properties (Mobley, 1994), hence has practical applications in monitoring water clarity or turbidity, water type classification (Jerlov, 1976), deriving pigment concentration of phytoplankton (or chlorophyll concentration), mapping algal blooms, and assessing photosynthesis and other biogeochemical fluxes.

Remote sensing determination of $K_d(\lambda)$ has received considerable attention with algorithms manipulating the retrieved radiometric spectral signals in various manners (Morel et al., 2007). These algorithms range from the simplest empirical method (Austin and Petzold, 1981; Morel, 1988; Mueller, 2000; Morel et al., 2007) typically suited for deep oceanic conditions to a more complex estimation (Lee et al., 2005b) based on the radiative transfer theory (Mobley, 2001). For optically complex coastal waters like the GBR, $K_d(\lambda)$ derivation formulated around the radiative transfer, which considers both the IOPs and the change in solar zenith angle, presents a more robust estimate of light attenuation coefficient for the downwelling irradiance. A semi-analytical algorithm for $K_d(\lambda)$ (Lee et al., 2005b) from remotely sensed data based on parameters evaluated from Hydrolight (Mobley and Sundman, 2008) numerical simulations is considered in developing the benthic irradiance model through this PhD research. The advantage of Lee et al. (2005b)'s model is that it permits the estimation of $K_d(\lambda)$ with high accuracy provided the IOPs, i.e., $a(\lambda)$ and $b_b(\lambda)$, for the region of interest is known or can be obtained with a certain degree of accuracy. For the GBR shelf region, these IOPs could be derived accurately from SWIM outputs as mentioned in Section 1.3.2. Since the IOPs are derived or modelled separately, and by using Lee et al. (2005b)'s model that does not rely on the empirical relationships with pigment concentrations (e.g., chlorophyll-*a* concentration), large uncertainties on resulting $K_d(\lambda)$ are expected to be minimised and estimates for GBR waters from remote sensing will be improved. The spectral $K_d(\lambda)$ values estimated for PAR spectral range can then be used to propagate the incident irradiance through the water column and derive benthic irradiance values based on the Beer-Lambert Law with accuracy.

1.4 Linking light and water quality in the GBR

Water quality is vital for the integrity of coral reefs and the overall health of the coastal ecosystem (Schaffelke et al., 2012; Devlin et al., 2015). Land-based runoff delivering pollutants, including

nutrients and fine sediments that affect water quality conditions and light availability, is a major cause of the poor state of coastal and marine ecosystems of the GBR (2017 Scientific Consensus Statement for the Great Barrier Reef). Suspended sediments increase water column turbidity (or decrease water clarity), reducing light penetration. Increased nutrients from runoff can also drive phytoplankton biomass production, increasing turbidity and light attenuation. Since water quality determines light availability at depth, declining marine water quality condition in the GBR has been of primary concern (Fabricius et al., 2016) and the focus of recent efforts and government investments in the last decade (State of Queensland, 2018).

The consensus of declining water quality in the GBR and the importance and urgency in addressing the issue has led to the establishment of the Reef Water Quality Protection Plan (Reef Plan) in 2003 (The State of Queensland and Commonwealth of Australia, 2003). The Reef Plan is an initiative aimed at halting and reversing the decline in water quality entering the GBR. Previous efforts have focused on monitoring and further understanding changes in water quality (Devlin and Brodie, 2005; McKergow et al., 2005; Fabricius et al., 2014; Fabricius et al., 2016), its ecological effects (Fabricius, 2005; De'ath and Fabricius, 2008; McKenzie et al., 2012), and management implications (Brodie and Waterhouse, 2012; Schaffelke et al., 2012). Others highlighted that turbidity over reefs near river mouths could be significantly higher (e.g., up to 10 times higher) (Fabricius et al., 2013; Fabricius et al., 2014; Fabricius et al., 2016), that water clarity (e.g., photic depth) can remain poor for an extended period (~six months) following the onset of river floods (Fabricius et al., 2016), and that the Reef could be exposed to runoffs contaminated with pesticides and herbicides from agriculturally used chemicals (Lewis et al., 2009; Shaw et al., 2010). These studies underscore and justify efforts to address the declining water quality in the GBR.

GBR Report Cards are currently being used to monitor the condition and trend of GBR ecosystems and drivers and facilitate management based on a consistent national strategy for managing water quality. These report cards are produced annually under the Australian and Queensland Governments' joint initiative, the Reef 2050 Water Quality Improvement Plan 2017-2022 (Reef 2050 WQIP) (State of Queensland, 2018). Reef 2050 WQIP builds on the preceding Reef Water Quality Protection Plan 2013 (State of Queensland, 2013) under the broader Reef 2050 Long-term Sustainability Plan (Reef 2050 Plan) (Commonwealth of Australia, 2015) with the overarching aim to reduce the pressures on the Reef and improve the Reef's resilience by enhancing the quality of water flowing from the adjacent catchments to the coast. Under this plan, GBR Report Cards amalgamate information from a range of programs that monitor and model the conditions of the GBR (Robillot et al., 2018), including inshore marine conditions (with a focus on the status of corals, seagrasses and water quality), management practices, catchment indicators and catchment loads.

The current framework for generating annual GBR Report Cards for water quality (Robillot et al., 2018) was implemented in 2016. It provides an easy-to-interpret grade score to indicate conditions (e.g., from

"very poor" to "very good") for each region in each year. This approach uses results from the data-assimilating version of the eReefs marine models (Jones et al., 2016a; Skerratt et al., 2019; Baird et al., 2020), which were validated against *in situ* measurements. The GBR reporting framework uses consistent, well-defined spatial and temporal boundaries for aggregation based on a combination of Natural Resource Management (NRM) regions and cross-shelf waterbody boundaries (see Figure 1 for spatial boundaries). Reporting is conducted annually, using a "water year" defined as 01 October to 30 September of the following calendar year, to ensure that wet seasons are not split across reporting years (Waterhouse et al., 2017). Clear threshold values are defined for quantitative water quality parameters. The current report card framework (Robillot et al., 2018) improves upon previous versions by using thresholds that are ecologically relevant and regionally specific and water quality metrics that can be monitored not only in the *in situ* sampled inshore coastal region but also in the mid-shelf and outer-shelf regions of the GBR, for which few *in situ* measurements are available. These report cards provide a science-based outlook on the health of the GBR and measure the progress towards the goal and targets of the Reef 2050 WQIP.

Contemporary water quality studies have focused mainly on the effects of nutrients and their relation to eutrophication, suspended sediment loads, and water column clarity measured with a Secchi disk (Browne et al., 2012; Waterhouse et al., 2012; Jones et al., 2016b). Consequently, guidelines on water quality are based on annual mean Secchi disk depth and Chl *a* pigment concentration. GBR Report Cards currently use two marine water quality indicators to provide information about GBR inshore marine conditions: Chl *a* and Secchi depth. Chl *a* is a proxy for nutrient enrichment, whereas Secchi depth indicates water clarity (measured as the depth at which the Secchi disk disappears when lowered vertically into the water (Preisendorfer, 1986)). Secchi depth thus also informs on turbidity.

Both Secchi depth and Chl *a* are considered useful individual indicators for describing water quality status and its associated changes. However, these parameters do not directly indicate what environmental conditions are experienced by seagrasses and corals since the relationship varies with depth and with the colour of the water. Whilst these factors directly impact the amount of light received by underwater ecosystems, light availability has received very little attention as a component of existing water quality guidelines (De'ath and Fabricius, 2010).

Benthic irradiance is a parameter that incorporates the effects of environmental conditions including depth and offers a more ecologically relevant measure of water quality to light-dependent benthic organisms. Estimates of benthic irradiance at spatial and temporal scales that capture GBR-wide conditions could be used to assess potential light stress (e.g., light levels falling below light requirements of benthic organisms) experienced by important benthic habitats and would provide a complementary if not a more suitable indicator of water quality in the GBR. As discussed in **Chapter 5** of this PhD Thesis, a benthic light-based index of water quality can effectively and efficiently inform on water quality conditions in the GBR.

1.5 Thesis Objectives and Outline

This Thesis aims to characterise and understand the spatiotemporal patterns and variability of benthic irradiance within the GBR shelf region at spatial and temporal scales relevant to this vast iconic region. The specific objectives of this Thesis were to:

1. Develop a model for deriving benthic irradiance from satellite remote sensing datasets.
2. Characterise the baseline (spatial and temporal) patterns and distribution of benthic PAR in the GBR, emphasising the long-term patterns of benthic light variability.
3. Investigate what controls the light attenuation and thus light availability and variability in the GBR.
4. Develop an ecologically-relevant marine index of water quality based on benthic light availability.

Each chapter of this Thesis is an independent, self-contained chapter. The manuscripts presented were either published (Chapters 2 and 5) or in preparation (Chapters 3 and 4) for submission to scientific journals for peer review and publication, each addressing the specific objectives mentioned. This Thesis has the following structure:

Chapter 1 (this chapter) presents the theoretical background, relevant literature preceding this work, the gap of knowledge and motivation, and the aims of this thesis. In this chapter, I highlighted the significance of solar radiation in the marine environment, including the application in water quality of the GBR. The information on relevant input parameters used in the model development was also compiled.

In **Chapter 2**, an algorithm for estimating benthic irradiance from MODIS (Aqua) satellite imagery is presented. This chapter describes the input datasets used and the development and validation of the model. First, the model was used to calculate the instantaneous benthic irradiance values coincident with each satellite overpass encompassing the period of the *in situ* datasets used for validation. The instantaneous estimates were then integrated into the PAR wavelength region (i.e., benthic PAR) and used to estimate the daily integrated values, representing the total amount of photons available for use in photosynthesis by benthic organisms. The validation of the model was conducted on both the instantaneous and daily-integrated benthic PAR, underlining high accuracy and low bias model results.

The model validation results provided the confidence to implement the model to the whole GBR shelf region using the available MODIS (Aqua) imagery to generate daily benthic PAR from July 2002 to December 2019. **Chapter 3** explores the baseline spatial and temporal patterns of benthic PAR in the

GBR using the monthly aggregated benthic PAR dataset. This chapter highlights the first-ever picture of benthic irradiance in the GBR in nearly two decades of remote sensing imagery.

Chapter 4 investigates the drivers of variability in the spectral light attenuation in the different Natural Resource Management (NRM) regions and cross-shelf water bodies in the GBR, using a suite of environmental predictors, which were analysed using random forest models. This chapter thus explores the potential causal relationship between light availability and the effects of water quality (as influenced by inputs from land) or physical oceanographic processes and their potential temporal variability.

The dependence of benthic organisms on optimal light levels in a variable and sometimes light-limited shelf zone underscores the need to better characterise and understand the benthic light climate in shallow coastal waters. Central to this is the need to maintain good water quality that is essential to the health of marine ecosystems. **Chapter 5** presents a metric that can be used to track water quality in the GBR that is ecologically relevant. The benthic light index of water quality tracks the chronic effects of light limitation in the GBR. This chapter describes the index development that can be easily adapted for routine GBR water quality reporting through GBR Report Cards.

A summary of this PhD research is presented in **Chapter 6**. This chapter includes a discussion of the outcomes, limitations, applications, and future directions of this PhD research.

"All models are wrong; some are useful" – George Edward Pelham Box (1919 – 2013)

2 Model for deriving benthic irradiance in the Great Barrier Reef from MODIS satellite imagery

This chapter[**] was published as:

Magno-Canto, M., McKinna, L., Robson, B., and Fabricius, K., *Model for deriving benthic irradiance in the Great Barrier Reef from MODIS satellite imagery*, Opt. Express 27, A1350-A1371 (2019). https://doi.org/10.1364/OE.27.0A1350

Abstract

We demonstrate a simple, spectrally-resolved ocean colour remote sensing model to estimate benthic photosynthetically active radiation (*bPAR*) for waters of the Great Barrier Reef (GBR), Australia. For coastal marine environments and coral reefs, the underwater light field is critical to ecosystem health, but data on *bPAR* rarely exist at ecologically relevant spatio-temporal scales. The *bPAR* model presented here is based on Lambert-Beer's Law and uses: (i) sea surface values of the downwelling solar irradiance, $E_s(\lambda)$, (ii) high-resolution seafloor bathymetry data, and (iii) spectral estimates of the diffuse attenuation coefficient, $K_d(\lambda)$, calculated from GBR-specific spectral inherent optical properties (IOPs). We first derive estimates of instantaneous *bPAR*. Assuming clear skies, these instantaneous values were then used to obtain daily-integrated benthic PAR values. Matchup comparisons between concurrent satellite-derived *bPAR* and *in situ* values recorded at four optically varying test sites indicated strong agreement, small bias, and low mean absolute error. Overall, the matchup results suggest that our benthic irradiance model was robust to spatial variation in optical properties, typical of complex shallow coastal waters such as the GBR. We demonstrated the *bPAR* model for a small test region in the central GBR, with the results revealing strong patterns of temporal variability. The model will provide baseline datasets to assess changes in *bPAR* and its external drivers and may form the basis for a future GBR water quality index. This model may also be applicable to other coastal waters for which spectral IOP and high-resolution bathymetry data exist.

[**] Erratum: Magno-Canto et al., 2020 in Appendix 1

2.1 Introduction

Benthic irradiance is defined as photosynthetically active radiation (PAR, or benthic PAR) at 400 – 700 nm wavelengths that reach the seafloor. Benthic PAR provides the primary energy resource that drives benthic photosynthesis, thus essentially defines primary production in the benthic coastal ocean (Gattuso et al., 2006). Previous studies have emphasised the importance of light availability for benthic habitats. For example, light limitation determines photosynthesis, growth, and distribution of seagrasses (Dennison, 1987; Ralph et al., 2007; Collier et al., 2012a; Collier et al., 2016a), depth limits for coral reef development (Kleypas, 1997; Cooper et al., 2007; Fabricius, 2011; Muir et al., 2015), and vulnerability of coral reefs to ocean acidification as a result of reduced calcification (Suggett et al., 2013; Vogel et al., 2015). On the other hand, high light levels in combination with heat stress from elevated seawater temperature can also lead to coral bleaching (Mumby et al., 2001; Leahy et al., 2013). Such juxtaposition thus highlights the need for an improved understanding of the underwater light field and benthic light availability, to better assess and manage marine ecosystem health (Fabricius, 2011; Collier et al., 2012a). Efficient management of these benthic ecosystems would greatly benefit from a synoptic-scale understanding of spatial and temporal patterns of benthic light availability. Unfortunately, benthic light availability remains poorly understood (Ackleson, 2003; Gattuso et al., 2006), because datasets that could provide the much-needed information are either insufficient or lacking, including in one of the largest coral reef ecosystems on Earth, the Great Barrier Reef (GBR). As such, our main objective is to demonstrate the feasibility of estimating benthic light values within the GBR region using a remote sensing model to bridge this knowledge gap.

The GBR Marine Park (GBRMP) is a world heritage listed site adjacent to the northeastern Australian coast spanning from 10°S to 24°S latitude. It is located on a continental shelf with an area of ~344,000 km^2. While direct observations of the underwater light field have historically been measured by ships of opportunity and *in situ* moorings in the GBR, these existing data are spatially and temporally sparse. Although PAR in surface waters is frequently reported for marine ecosystems (Frouin and McPherson, 2012; Frouin et al., 2012), benthic PAR is usually available only at a few point locations over relatively short periods (Anthony et al., 2004; Ralph et al., 2007; Whinney et al., 2017). To understand the responses of whole ecosystems at regional scales, we need to estimate environmental conditions, including benthic PAR, at relevant scales (in this case, the scale of the whole GBR). Ocean colour remote sensing presents an option for observing benthic PAR in the GBR at ecologically relevant spatio-temporal scales, which can provide near-daily images of the entire GBR at a nominal pixel resolution of 1 km^2. While a number of ocean colour satellite processing algorithms have been developed for monitoring optically complex waters of the GBR (Brando et al., 2012; Weeks et al., 2012; Slivkoff, 2014; McKinna et al., 2015), we note that none have focused on deriving benthic light availability.

Benthic irradiance, here denoted as $E_b(\lambda)$, is essentially regulated by three factors. First, the downwelling irradiance incident on the ocean surface, $E_s(\lambda,0^+)$ (W m^{-2}), which is subject to atmospheric processes (e.g., gaseous absorption and molecular scattering) that diminishes light as it makes its way to the sea surface. Second, the absorption and scattering processes within the water column (Ackleson, 2003; Kirk, 2011; Werdell et al., 2018) that depends on the wavelength and have magnitudes and shapes that are proportional to the relative concentration of optically-active constituent matter (Robinson, 2004) including: phytoplankton, non-algal particles (NAP) and coloured dissolved organic matter (CDOM). It is important to note that IOPs are impartial to the direction and magnitude of the ambient light field (Mobley, 1994). In coastal regions, IOPs can be regulated by a number of drivers including, but not limited to: run-off and resuspension of fine sediments, nutrients and organic matter due to wave-induced vertical mixing, human activity such as dredging and dredge-spoil placement on the seafloor, and biological processes related to phytoplankton growth. Collectively, these drivers make the inversion of sensor-observed remote sensing reflectance, $R_{rs}(\lambda)$ (sr^{-1}), to derive IOP values, a non-trivial problem. Third, and also important is the water column depth which defines the distance of light penetration.

In optically shallow waters like those of the GBR, light reflected off the seafloor is another factor that limits the application of contemporary ocean colour algorithms developed for deep, open-ocean waters (McKinna et al., 2015; McKinna and Werdell, 2018). Fortunately, a GBR-specific IOP inversion model (Shallow Water Inversion Model, SWIM) has recently been developed (McKinna et al., 2015) that improves the derivation of spectral estimates of IOPs, specifically, total absorption coefficients, $a(\lambda)$ (m^{-1}), and total backscattering coefficients, $b_b(\lambda)$ (m^{-1}), for any pixel within the GBR where $R_{rs}(\lambda)$ are available. We note that $R_{rs}(\lambda)$ is a fundamental sensor-observed radiometric variable used in ocean colour algorithms. SWIM is described in detail elsewhere (see (McKinna et al., 2015)). In brief, SWIM takes advantage of two mapped GBR-specific ancillary datasets, namely: (i) a high-resolution shelf bathymetry map (Beaman, 2010b) matching the resolution of the remote sensing datasets, and (ii) a bottom substrate brightness (albedo) map (Reichstetter et al., 2015). Using these ancillary datasets, SWIM can generally correct for optically shallow effects. Note, however, that for more optically complex waters, the skill of the SWIM model may still be challenged in deriving IOP values. Nonetheless, the IOP estimates that can be obtained via SWIM are very valuable and sufficient for our current purpose. By using SWIM-derived IOPs, it is thus possible to spectrally characterise near-daily GBR-wide light attenuation and, in turn, estimate benthic light availability (i.e., PAR) using ocean colour remote sensing.

A contemporary approach for estimating PAR at depth is to use the broadband, water-column averaged diffuse attenuation coefficient of PAR, K_d(PAR) (m^{-1}), and Lambert-Beer's Law which assumes K_d(PAR) is constant over the optical pathlength (depth). However, in practice, K_d(PAR) exhibits strong depth dependence, particularly in the upper water column, even in well-mixed waters (Lee, 2009; Lee et al., 2014). Thus, using a K_d(PAR)-based method may lead to inaccurate estimates of PAR at depth.

We note that usable solar radiation (USR), a spectrally integrated broadband term (integrated over the 400 – 560 nm range), has recently been proposed as a promising alternative to PAR (Lee et al., 2014) as its diffuse attenuation coefficient, K_d(USR) (m^{-1}), exhibits less depth dependence. However, most ecological studies report their findings (e.g., benthic light stress thresholds) in terms of PAR. Here, we described a remote sensing approach to estimate benthic PAR that does not utilize K_d(PAR).

In this study, we demonstrate a simple physics-based ocean colour remote sensing model to estimate two spectrally integrated benthic light variables, namely: (i) instantaneous PAR at the seafloor (hereby denoted as $bPAR_i$) (μmol photons m^{-2} s^{-1}), and (ii) daily integrated PAR at the seafloor (hereby denoted as $bPAR_d$) (mol photons m^{-2} d^{-1}). Estimates are derived from (i) $E_s(\lambda,0^+)$, (ii) high-resolution shelf bathymetry, and (iii) spectral estimates of IOPs obtained using SWIM McKinna et al. (2015). Here, $E_s(\lambda)$ and IOPs are derived from data collected by NASA's Moderate Resolution Imaging Spectroradiometer aboard the Aqua spacecraft (MODISA). We then validate the model by comparing concurrent satellite-derived and observed *in situ* benthic PAR values from four test sites within the GBR. Finally, results, as well as limitations and future applications of the model within the GBR region are discussed.

2.2 Benthic irradiance model

2.2.1 Benthic irradiance model description

To derive $E_b(\lambda)$, the total amount of subsurface downwelling planar irradiance, $E_d(\lambda,0^-)$ (W m^{-2}), transmitted to a depth z (m) under a clear sky, we used the Lambert-Beer's Law:

$$E_b(\lambda) = E_d(\lambda,0^-)\exp(-K_d(\lambda)z) \tag{2.1}$$

where $K_d(\lambda)$ (m^{-1}) is the spectral diffuse attenuation coefficient. We emphasise that in our approach, spectral dependence was kept throughout all calculations.

Satellite-derived $E_s(\lambda,0^+)$ (W m^{-2}) represents the downwelling planar irradiance when the Sun is at zenith and just above the air-sea surface. Here, $E_s(\lambda,0^+)$ was obtained by employing the standard NASA atmospheric transmittance model as described in Mobley et al. (2016) which assumes that the cloud/surface system is non-reflecting and non-absorbing. Because $E_s(\lambda,0^+)$ is estimated just above the sea surface, it is necessary to propagate this parameter across the air-sea interface to derive $E_d(\lambda,0^-)$ (Kirk, 1992, 2011). Here, we followed Baker and Smith (1990) and used:

$$E_d(\lambda,0^-) = t_g E_s(\lambda,0^+) \tag{2.2}$$

where t_g is the global transmittance of the air-water interface (Smith and Baker, 1986). Essentially, the total downwelling global irradiance just above the interface can be decomposed into direct ("sun") and diffuse ("sky") components, both of which are functions of wavelength and the corresponding solar

zenith angle in air (Baker and Smith, 1990) and t_g is equal to $t_g = (1 - \rho_{sun})(1- y) + (1 - \rho_{sky})(y)$, where ρ_{sky} and ρ_{sun} are the sea surface reflectance of the diffuse and the direct irradiances, respectively. The value of ρ_{sky} is roughly equivalent to 0.066 for cloud-free conditions (Baker and Smith, 1990) while the ρ_{sun} can be approximated by employing the Fresnel reflectance equation for unpolarized light (Mobley, 1994) written as:

$$\rho_{sun} = \left(\left[\frac{\sin(\theta_{solz} - \theta_t)}{\sin(\theta_{solz} + \theta_t)} \right]^2 + \left[\frac{\tan(\theta_{solz} - \theta_t)}{\tan(\theta_{solz} + \theta_t)} \right]^2 \right) * 0.5 \quad (2.3)$$

where θ_{solz} (degrees) is the solar zenith angle in air at the time of satellite overpass and θ_t (degrees) is the solar zenith angle of light transmitted downward in the water calculated as:

$$\theta_t = \sin^{-1}(\sin\theta_{solz} / n_w) \quad (2.4)$$

where n_w is the real refractive index of seawater approximately equal to 1.34 (Mobley, 1994). For cases where $\theta_{solz} \neq 0.0$ (e.g., sun not overhead), Equation (2.3) was used. Otherwise, for normally incident light, the reflectance of the direct irradiance was calculated as:

$$\rho_{sun} = \left(\frac{n_w - 1}{n_w + 1} \right)^2 . \quad (2.5)$$

We note that in this study we have assumed cloud-free, clear sky conditions for all calculations and neither considered the effect of a wind-roughened surface in our air-sea transmittance calculations. Further details on deriving the transmitted irradiance across the interface are described elsewhere [35,36].

An IOP-based method for deriving of $K_d(\lambda)$ (Lee et al., 2005b) was employed as this approach is more robust in optically complex coastal waters relative to simple empirical methods (Austin and Petzold, 1981; Morel, 1988; Mueller, 2000; Morel et al., 2007). The IOP-based $K_d(\lambda)$ model we have used in this study is described and evaluated in detail elsewhere (Lee et al., 2005a; Lee et al., 2005b) and has a general form:

$$K_d(\lambda) = (1 + 0.005\theta_{solz})a(\lambda) + 4.18(1 - 0.52e^{-10.18a(\lambda)})b_b(\lambda) \quad (2.6)$$

where $a(\lambda)$ and $b_b(\lambda)$ are the coefficients of spectral total absorption and spectral total backscattering, respectively. An interesting feature of this model (Lee et al., 2005b) is that it allows estimation of the attenuation coefficient for any wavelength with high accuracy, given the coefficients for $a(\lambda)$ and $b_b(\lambda)$ for any region-of-interest can be obtained with suitable accuracy. For our purpose, we obtained location- and time-specific estimates of $a(\lambda)$ and $b_b(\lambda)$ from the SWIM algorithm and implemented Equation (2.6) for each pixel location within our test sites to obtain $K_d(\lambda)$. We note, however, that the $K_d(\lambda)$ model above can utilise IOPs derived from other IOP algorithms and is hence not tied to the SWIM algorithm.

2.3 Integrating benthic irradiance within the PAR range

2.3.1 Instantaneous benthic PAR

Values of $bPAR_i$ were calculated by spectrally integrating the values of $E_b(\lambda)$ as:

$$bPAR_i = \int_{400}^{700} E_b(\lambda) d\lambda. \tag{2.7}$$

Note that the spectral range (as further detailed later) is not continuous and corresponds to the MODISA ocean colour band centres. The integration was performed in Python 3.6.3 using the numerical python (NumPy) library's "trapz" function that implements the trapezoidal method to numerically approximate the area under the curve using definite integral over discrete intervals (i.e., here defined by the band centres of MODISA).

2.3.2 Daily integrated benthic PAR

To obtain $bPAR_d$ from sunrise to sunset for any given day and pixel location, we first estimated the instantaneous benthic PAR at noon, $bPAR_n$ (μmol photons m^{-2} s^{-1}), which gives the maximum potential PAR irradiance at the seafloor, using:

$$bPAR_n = \int_{400}^{700} \left[t_g E_s(\lambda, 0^+) \cos\theta_{solz} \right] e^{K_d(\lambda) z} d\lambda \tag{2.8}$$

where the subsurface downwelling planar irradiance is multiplied by the cosine of θ_{solz} (the term enclosed in square brackets). Assuming clear skies (i.e., no clouds) and that the cloud/sky system is non-reflecting and non-absorbing, the magnitude of $E_s(\lambda,0^+)$ can be estimated as a function of θ_{solz} and is approximately sinusoidal in relation to the daylight hours and symmetric about noon (Kirk, 2011). Further, we can compute the solar zenith angle for a given solar hour angle, ϕ, as:

$$\theta'_{solz}(\phi) = \cos^{-1}\left(\sin(lat)\sin(\delta) + \cos(lat)\cos(\delta)\cos(\phi)\right) \tag{2.9}$$

where, for a given pixel on a single day latitude, *lat* (radians), the solar declination angle, δ (radians) is computed as:

$$\begin{aligned} \delta = {} & 0.006918 - 0.399912\cos(\gamma) + \\ & 0.070257\sin(\gamma) - 0.006758\cos(2\gamma) + \\ & 0.000907\sin(2\gamma) - 0.002697\cos(3\gamma) + 0.00148\sin(3\gamma) \end{aligned} \tag{2.10}$$

The term γ (radians) is the date expressed as an angle:

$$\gamma = \frac{2\pi}{365} * (jday - 1) \tag{2.11}$$

where *jday* is the Julian day (0-365 in a regular year, or 0-366 in a leap year).

Thus, $bPAR_d$ can be expressed as the double integral:

$$bPAR_d = 2 * \left(\int_{\phi_{rise}}^{\phi_{noon}} d\phi \int_{400}^{700} d\lambda \left[t_g E_s(\lambda, 0^+) \cos\theta_{solz} \cos\left\{\theta'_{solz}(\phi)\right\}\right] e^{K_d(\lambda)z} \right) \quad (2.12)$$

where ϕ_{rise} and ϕ_{noon}=0 denote hour angles at sunrise and noon, respectively. The integral with respect to solar hour angle in Equation (2.12) is computed numerically using a trapezoidal rule by discretising the solution into fifty ϕ steps ranging from ϕ_{rise} to ϕ_{noon} = 0, where ϕ_{rise} is computed as:

$$\phi_{rise} = \cos^{-1}\left(\tan(\delta)\tan(lat)\right). \quad (2.13)$$

2.4 Data and model evaluation

2.4.1 Satellite data processing

MODISA raw Level-1A (L1A) data files spanning 2002 – 2018 were downloaded from NASA (https://oceancolor.gsfc.nasa.gov/) and spatially subsetted to encompass four tests sites within the GBR (black filled circles in Figure 1). These data files were then processed to geophysical Level-2 (L2) data products using NASA's Ocean Color Software Suite (OCSSW) processing code that is distributed as part of the SeaDAS display and analysis software package (Baith et al., 2001). L2 data products were produced for ten visible MODISA bands centred on: 412, 443, 469, 488, 531, 547, 555, 645, 667, and 678 nm and stored in NetCDF4 files. These L2 data products included: $E_s(\lambda,0^+)$, θ_{solz}, and SWIM-derived IOPs, $a(\lambda)$ and $b_b(\lambda)$. NASA's standard ocean colour atmospheric correction was used to produce all L2 data products (Siegel et al., 2000; Bailey et al., 2010; Ahmad et al., 2011). The data processing yielded nearly 5500 daily MODISA L2 files for each of the four test sites.

2.4.2 GBR bathymetry data

Bathymetric data used to define the water column depth (datum: mean sea level (MSL)) was extracted from a gridded high-resolution bathymetry and digital elevation model (DEM) of the GBR, 3D-GBR (Beaman, 2010b). This DEM dataset has a grid pixel resolution of ~100 m x 100 m that can resolve fine-scale details of the bottom topography of the GBR reefs and inter-reefal systems (see Figure 2.1). The full GBR bathymetric dataset is available from Australia's eAtlas website and environmental research data mapping and management system https://eatlas.org.au/data/uuid/200aba6b-6fb6-443e-b84b-86b0bbdb53ac.

2.4.3 *In situ* data collection and processing

The Australian Integrated Marine Observing System (IMOS) maintains an array of observing sub-facilities (Rigby et al., 2014). One of the regional Shelf Mooring Array sub-facilities is located on the coast of Queensland, which is part of the Queensland IMOS (Q-IMOS) node established in 2007 and currently operated by the Australian Institute of Marine Science (AIMS). To conduct validation for this

study, four existing mooring stations: Yongala, Palm Passage, Myrmidon, and Heron Island South (referred to as Heron throughout the manuscript) were expanded in 2015/2016 to also include PAR sensors, all located >1 km away from reefs and other geometrically shallow features (Table 1). These four mooring stations were therefore selected as *in situ* benthic PAR validation sites.

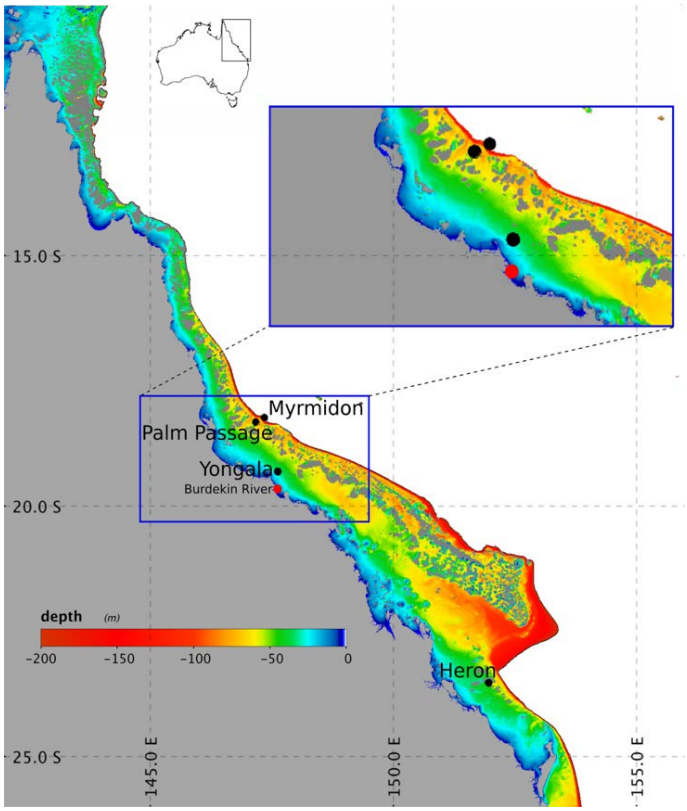

Figure 2.1. Location map of the four validation test sites (black filled circles) within the GBR region along the northeastern coast of Australia (inset map). The colour gradient indicates depth contours within the 200 m bathymetric shelf. The blue rectangle indicates the boundary of the small regional box, Burdekin region, used for temporal evaluation of the model (as detailed in section 2.4.6) with the corresponding subset bathymetry showing the complex topographic features in the model region. The red filled circle indicates the location of the Burdekin River mouth, while grey masked regions indicate land and coral reefs.

It is worth noting that the sites used for validation represent spatially and optically diverse water bodies. The Yongala mooring site is located mid-shelf and closest inshore with shallow lagoon waters often subject to wind-driven resuspension of bottom sediments and terrestrial influence. Hence, it encompasses both turbid and moderately clear seawater conditions and strong variation in optical properties (>20-fold range in PAR values). It is also exposed to seasonal runoff from the nearby Burdekin River. The Palm Passage and Myrmidon test sites are both located on the edge of the continental shelf, and although they are seasonally exposed to the influence of the East Australian Current (EAC), the southwest Pacific poleward western boundary current, these two stations most typically represent clear oceanic optical conditions (four- to six-fold range in PAR values), typical of oligotrophic waters. Meanwhile, the Heron station represents relatively stable intermediate in-water

optical conditions (clarity and variability) although it may also be influenced by other important local oceanographic features (e.g., eddy-driven intrusion and productivity, tidally-driven flows, seasonal *Trichodesmium* blooms), yet not much more than the effects of the EAC oceanic intrusions experienced by the two deep oceanic test sites. Overall, the selected test regions comprise a range of optical water types within the GBR lagoon, and hence, suitable to test the capability of the newly developed benthic irradiance model over an optical dynamic range found in this region.

Table 2.1. IMOS mooring stations for in situ PAR data collection in the Great Barrier Reef.

IMOS Mooring station	Latitude (°S)	Longitude (°E)	Characteristics	Station depth (m)	Mean PAR logger depth (m)	Dates of deployment (inclusive)	No. of *in situ* data collected
Yongala	19.302	147.621	shallow mid-shelf, closest inshore, periodically turbid	30	29	22 Mar 2015 to 26 Sep 2017	77,486
Heron	23.513	151.955	shallow mid-shelf, clear	46	24.5	03 Apr 2016 to 04 Oct 2017	248,849
Palm Passage	18.308	147.167	deep, outer shelf, clear oceanic	70	25	28 May 2016 to 22 Nov 2016	84,920
Myrmidon	18.220	147.344	deep, shelf edge, clear oceanic	192	19	25 May 2016 to 15 Nov 2017	145,859

To measure *in situ* benthic PAR at Yongala, a Seabird Scientific SBE16PLUS v2 SEACAT profiler with upward-facing WETLabs Environmental Characterisation Optics (ECO) PARSB sensor was deployed 0.5 m above the bottom substrate at ~30 m water depth. At the other three mooring sites, WETLabs ECO PARSB sensors were clamp-mounted to a permanent mooring wire at a fixed distance from the seafloor at each deployment period.

PAR sensors collected 5-second data bursts every 15 minutes (480 benthic PAR records per day) at all stations except Yongala where single measurements were collected every 15 minutes (96 benthic PAR records per day). Deployments and servicing of sensors occurred approximately every six months. After each deployment period, data were downloaded and the instrument's optical component was checked, characterized, and tested to ensure the quality and validity of the data between deployments. For each recovery period, the data was analysed and quality controlled such that: (i) data records from the beginning and end of each deployment were excluded to ensure that only stable PAR measurements were included in the subsequent analysis or within a complete day cycle in the case of $bPAR_d$ validation, (ii) data points when instrument failure was experienced (e.g., battery problems) were also excluded (e.g., Palm Passage deployments 2 and 3), and (iii) night-time values were forced to zero by applying an offset based on the dark count readings of the sensor for each deployment period. Table 2.1 lists the deployment details and the total number of *in situ* PAR data remaining after quality controls were applied.

2.4.4 Algorithm validation approach

The model performance was evaluated via matchups between: (i) concurrent instantaneous parameters, $bPAR_i$ and *in situ* measured instantaneous PAR near the seafloor (Yongala) or in the water column (Myrmidon, Palm Passage and Heron), (ii) concurrent daily-integrated parameters, $bPAR_d$ and the daily-integrated *in situ* measurements, and (iii) all four test sites combined against overall satellite retrieval performance for both instantaneous and daily integrated cases.

For clarity, because the PAR loggers, except in Yongala, were mounted in mid-water rather than on the bottom, the model was also run for the depths that complemented the *in situ* data for each site and deployment period. Consequently, for brevity, we use the term 'benthic PAR' hereto for both PAR near the benthos (i.e., Yongala) or at specific water column depth (i.e., clamp-mounted logger depths at Palm Passage, Myrmidon and Heron).

2.4.4.1 Matchups of satellite-derived to in situ data pairs

For each L2 file containing results of the benthic irradiance model (either the instantaneous $bPAR_i$ and daily integrated $bPAR_d$) corresponding to an *in situ* measurement, satellite-derived values were extracted for a 3 x 3-pixel box centred at the mooring station locations (see Table 2.1 for coordinates). Next, image pixels were discarded if any of the pixels were associated with the following NASA L2 quality flags: LAND, CLDICE, HILT, HIGLINT and STRAYLIGHT (Robinson et al., 2003) for quality assurance. Extracted pixels were also discarded using two additional quality control procedures: (i) if any of the 9 pixels within the test box had been masked (Barnes et al., 2013), and (ii) if the coefficient of variation (CV, standard deviation/mean) between the nine pixels of the satellite-derived $bPAR_i$ or $bPAR_d$ was greater than 15%, indicating low intra-pixel stability of the modelled parameter over relevant time-scale (Seegers et al., 2018). Finally, common statistical parameters including minimum, maximum, mean, standard deviation, and median values were calculated for each nine-pixel box as a final check, but we only reported and used median values in further analysis. Matchups between concurrent data pairs of satellite-derived and *in situ* measured *bPAR* were then performed using quality-controlled median $bPAR_i$ (and $bPAR_d$) time series compared against the *in situ bPAR* time series. To qualify as 'concurrent', we included *in situ* data from ±3 hours around the MODISA satellite overpass time similar to previous studies (Bailey and Werdell, 2006). Matchups were conducted using R Studio (version 1.1.456) running R version 3.5.2 (R Core Team, 2017) (codes available upon request).

2.4.4.2 Regression analysis and other performance metrics

Type-II linear regression analysis was used to compare the concurrent satellite-derived and *in situ* measured *bPAR* values per test site and on the combined dataset to assess how well the model performed over the dynamic range of benthic PAR in the GBR. The regression slope, intercept, and coefficient of determination (r^2) were calculated on $\log_{10}$-transformed data. Reduced major axis regression analysis

was completed using lmodel2 package (Legendre, 2018) in R version 3.5.2. Model type II linear regression was chosen due to assumed inherent error in both the satellite and *in situ* datasets (e.g., because pixels from satellite imagery are not in exactly the same location and time as the *in situ* data, etc.). Lastly, additional metrics, including bias and mean absolute error (MAE), were calculated on $\log_{10}$-transformed data as measures of overall algorithm bias (i.e., systematic error) and accuracy (i.e., average model prediction error) that were back-transformed out of logarithmic scale before interpreting the results. Following Seegers et al. (2018), bias and MAE were calculated as:

$$bias = 10 \wedge \left(\frac{\sum_{i=1}^{n} \log_{10}(bPAR_{sat}) - \log_{10}(bPAR_{insitu})}{n} \right) \tag{14}$$

$$MAE = 10 \wedge \left(\frac{\sum_{i=1}^{n} |\log_{10}(bPAR_{sat}) - \log_{10}(bPAR_{insitu})|}{n} \right) \tag{15}$$

where $bPAR_{sat}$ is either $bPAR_i$ or $bPAR_d$, $bPAR_{insitu}$ is the corresponding *in situ* measured benthic PAR, and n is the number of observations. The resulting error metrics are in multiplicative space and dimensionless. As such, multiplicative bias values of 1.0 indicates no bias, and bias < 1.0 denotes negative bias (e.g., underestimation of the observed values). Whilst for a multiplicative MAE, lower values (or closer to 1.0) would indicate better model performance.

2.4.5 Evaluation of model components: the diffuse attenuation model coefficients and spectral IOP-based approach ($K_d(\lambda)$ vs. $K_d(PAR)$)

It is worth noting that the $K_d(\lambda)$ model coefficients (0.005, 4.18, 0.52, and -10.18) in Equation (2.6) were derived empirically from a dataset simulated with radiative transfer code (Lee et al., 2005b). These coefficients best estimate layer-averaged $K_d(\lambda)$ for the photic zone depth (i.e. the layer of water over which irradiance is diminished to 10% of surface incident values). Because we wish to estimate irradiance at the seafloor, the Lee et al. (2005b) $K_d(\lambda)$ model may be limited when the geometric depth is not equivalent to the photic depth. Hence, to evaluate the limitations of the $K_d(\lambda)$ model, we conducted a cursory comparison study for two optical scenarios: (i) 'oligotrophic' (chlorophyll-*a* concentration of 0.05 mg m^{-3}) and (ii) 'mesotrophic' (chlorophyll-a concentration of 0.5 mg m^{-3}); where the IOPs were known. We then compared layer-averaged $K_d(\lambda)$ values computed using the Lee et al. (2005b) against the $K_d(\lambda)$ values more accurately simulated with Hydrolight-Ecolight 5.1 (HE5) radiative transfer code (Mobley and Sundman, 2008). We used absolute percent difference (APD) as a metric for this comparison. The radiative transfer modelling exercise we used followed the methodology described in McKinna et al. (2015) and considered four geometric depths (5, 10, 20, and 30 m), four θ_{solz} (10, 30, 50, and 80°) and used sand seafloor albedo for all simulations.

We next evaluated the skill of our spectrally-resolved $bPAR_i$ model and two other approaches based on the method of Morel et al. (2007). These alternative methods use K_d(PAR). In one model, K_d(PAR) is modelled as a function of known/derived chlorophyll-*a* pigment concentration. We refer to this as the "Chlorophyll-based" approach. In the other approach, K_d(PAR) is modelled as a function of known/derived K_d(490). We refer to this as the "K_d(490)-based" approach. Our spectrally-resolved $bPAR_i$ model is referred to as the "IOP-based" approach. In this case study, we also used radiative transfer modelling to accurately simulate $bPAR_i$ values to which we could compare our satellite-derived $bPAR_i$. For this radiative transfer modelling exercise, a large set of synthesized IOPs were used as HE5 inputs that were generated using 14 depths (spanning 3 – 30 m), fixed $\theta_{solz} = 30^{\circ}$, and a sand seafloor albedo. These simulated data were generated by McKinna and Werdell (2018) and further details can be found therein. Also, note that we used a consistent value of t_g for transmitting surface irradiance values, either $E_s(\lambda,0^+)$ or PAR, across the air-water interface. We note that for this radiative study, model inputs for each of the three approaches (Chlorophyll-based, K_d(490)-based, and IOP-based) were taken directly from the radiative transfer simulation outputs (i.e., no satellite algorithms were employed in this brief case study).

2.4.6 Temporal evaluation

Performance metrics described above (see section 2.4.4.3) are robust indicators of the absolute accuracy of the model but do not provide additional information on the temporal structure or variability of the parameter being considered against the validation dataset used. To assess whether the benthic irradiance model produces temporally stable estimates of benthic PAR (e.g., no unreasonable extreme values or unrealistic trends in the time series), we examined a regional box, the Burdekin region, within the central GBR that encompasses three of the four test sites considered in the study (inset map on Figure 2-1) by implementing the model to MODISA data from July 2002 to December 2018.

2.4.7 Simple depth sensitivity analysis

So far, we have used the MSL Beaman 3D-GBR bathymetry (Beaman, 2010b) as a proxy for water-column depth. However, one of the possible sources of error of our benthic irradiance model could be driven by changes in water-column depth due to tidal fluctuations. The tides in the GBR are predominantly semidiurnal (tidal cycle with two high and two low tides of approximately equal size each lunar day) and with regional differences in maximum amplitudes ranging between 2.5 to 7 m (Hutchings et al., 2008). To assess the importance of correcting the water depth for tidal effects, we also conducted a *bPAR* model run using *in situ* depth (i.e., pressure data measured using seafloor-mounted SEABIRD SBE16+ V2 SEACAT CTD with a pressure sensor at the Yongala site) as z in Equation (2.1). The depth sensitivity analysis (DSA) thus compared two *bPAR* model parameterisations: (i) the original model using MSL Beaman 3D-GBR bathymetry referred to as "3D-

GBR" model, and (ii) a model using *in situ* CTD depth measurements referred to as "*pressure"* model, to assess and evaluate differences, if any. As neither of these two model parameterizations was assumed initially superior, the difference was quantified using unbiased percent difference (UPD) calculated as per (Barnes et al., 2013).

2.5 Results and discussion

2.5.1 Spectral IOP-based K_d model structure

Figure 2.2 and Figure 2.3 show the various layer-averaged $K_d(\lambda)$ spectra calculated for four different layer depths and two optical water scenarios. The solid lines in the upper panels of Figure 2.2 and Figure 2.3 respectively show the RT-modelled layer-averaged $K_d(\lambda)$ values for oligotrophic and mesotrophic optical scenarios, while the black dotted lines (also in upper panels of Figure 2.2 and Figure 2.3) show the model layer-averaged $K_d(\lambda)$ calculated via Equation (2.6). For both examples, layer-averaged $K_d(\lambda)$ values for a given θ_{solz} are generally consistent with each other over the spectral range 400 – 600 nm, except for the 30m layer in the mesotrophic scenario. It can also be seen that as θ_{solz} increases, the magnitude of $K_d(\lambda)$ also increases slightly whilst the shapes stay much the same. Plots of APD show that the analytical $K_d(\lambda)$ model typically agrees to within 10% of radiative transfer values over 400 – 600 nm. We note that for the 30 m depth mesotrophic scenario, radiative transfer-simulated $K_d(\lambda)$ consistently deviates from the model of Lee et al. (2005b) in both the blue (400 – 450 nm) and red regions (600 – 700 nm) for all solar zenith values.

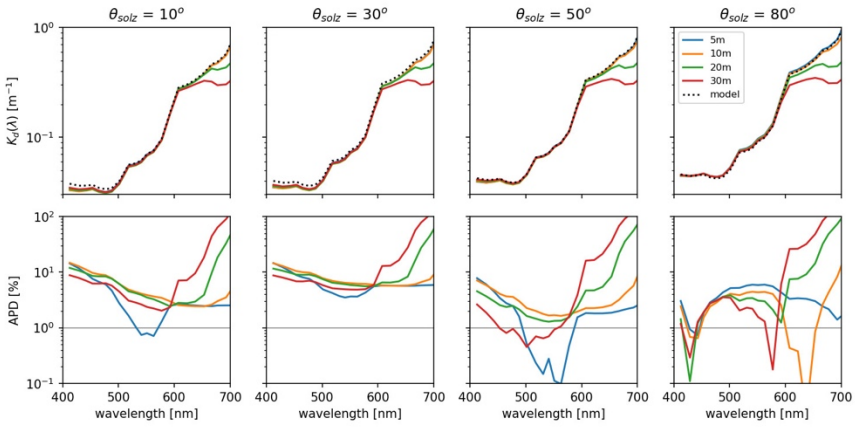

Figure 2.2. Top row: solid lines represent layer-averaged spectral diffuse attenuation coefficients for four different layer depths for an oligotrophic scenario. Blue, orange, green, and red lines correspond to layer depths of 5, 10, 20, and 30 m, respectively. The dashed line represents layer averaged spectral diffuse attenuation coefficient derived by the Lee et al. (2005b) model. Each panel (left-to-right) corresponds to four solar zenith angles (10, 30, 50, and 80°). Bottom row: absolute percent difference (APD) between radiative transfer modelled layer-averaged spectral diffuse attenuation coefficients and values estimated using the Lee et al. (2005b) model. The horizontal grey line represents 1% APD.

This brief analysis, whilst not exhaustive, nonetheless provides some confidence that the Lee et al. (2005b) model, although tuned for the photic depth layer, can estimate $K_d(\lambda)$ to within 10% of true values over a range of geometric depths. Indeed, Lee et al. (2005b) model for $K_d(\lambda)$ has been previously tested in optically shallow coral reef waters of the West Florida Shelf by Barnes et al. (Barnes et al., 2013). Using *in situ* validation data, Barnes et al. (Barnes et al., 2013) showed the Lee et al. (2005b) model had good skill at estimating $K_d(\lambda)$ at wavelengths shorter than 500 nm, which is consistent with this cursory case study.

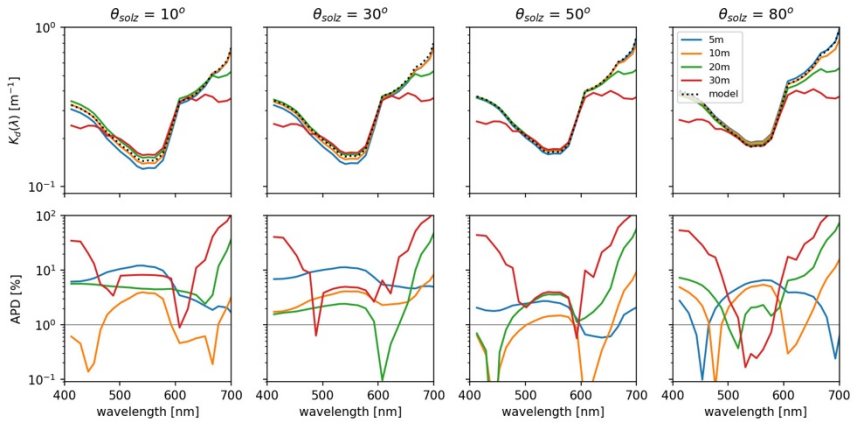

Figure 2.3. Top row: solid lines represent layer-averaged spectral diffuse attenuation coefficients for four different layer depths for a mesotrophic scenario. Blue, orange, green, and red lines correspond to layer depths of 5, 10, 20, and 30 m, respectively. The dashed line represents layer averaged spectral diffuse attenuation coefficient derived by the Lee et al. (2005b) model. Each panel (left-to-right) corresponds to four solar zenith angles (10, 30, 50, and 80°). Bottom row: absolute percent difference (APD) between radiative transfer modelled layer-averaged spectral diffuse attenuation coefficients and values estimated using the Lee et al. (2005b) model. The horizontal grey line represents 1% APD.

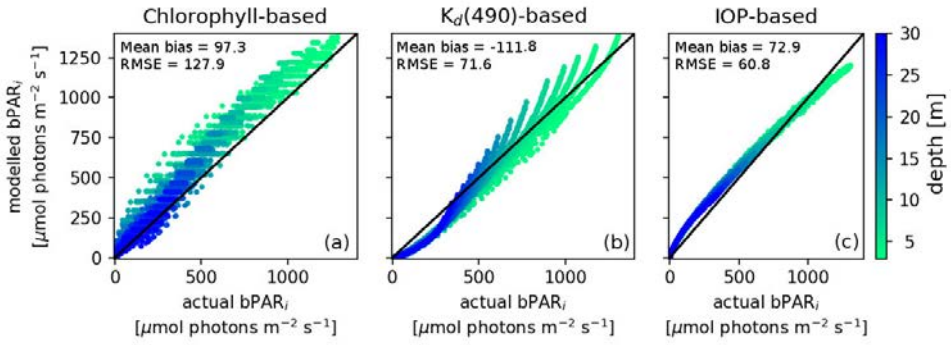

Figure 2.4. Scatter plots that compare known $bPAR_i$ (i.e., derived from radiative transfer simulations) with modelled values. Each panel (left-to-right) corresponds to a different model approach: (a) Chlorophyll-based, (b) $K_d(490)$-based, and (c) the IOP-based. The one-to-one line is plotted in a solid black line. Data points are colour coded by geometric depth. The highest values of $bPAR_i$ typically occur in shallow waters less than 5 m in depth. For our radiative transfer simulations, incident surface PAR values were 1679 μmol photons m^{-2} s^{-1}.

Figure 2.4 shows scatter plots comparing modelled $bPAR_i$ with values computed from radiative transfer simulations. The results show that the IOP-based model derives $bPAR_i$ with root mean square error (RMSE) and mean bias statistics that are better than the Chlorophyll-based and K_d(490)-based methods. Thus, this brief analysis demonstrates the benefit of using our spectrally resolved $K_d(\lambda)$-based model as opposed to a K_d(PAR)-based methods when estimating $bPAR_i$.

2.5.2 Instantaneous benthic PAR matchup analysis

We acquired 1134 matchup pairs (i.e., days of observations) between satellite-derived $bPAR_i$ and *in situ* measured data across the test sites when only the L2 quality flags were used as exclusion criteria (Table 2.2). After the application of the two additional exclusion criteria (i.e., adjacent to a masked pixel in the 3x3 pixel box and CV > 0.15), 696 data pairs remained. These quality-controlled data pairs comprised the dataset that was subsequently used in the regression analysis. The highest number of valid concurrent data pairs were found for Yongala and Heron, with 348 and 210 days of observations considered for the matchups, respectively. Palm Passage had the lowest number of valid concurrent data pairs at 45 days, as this test site had only one deployment period with good data because of *in situ* instrument failures experienced during the other deployment periods. Consequently, the number of concurrent matchups between the test sites varied by almost a factor of eight between sites with the most and the least data pairs. Nevertheless, across all test sites, only high-quality concurrent data pairs were included in the validation analyses, hence, the veracity of the model performance evaluation should not be diminished despite the above discrepancy.

In situ measurements of instantaneous benthic PAR varied by almost two orders of magnitude ranging from 13 to 906 μmol m^{-2} s^{-1}, indicating that the validation dataset spanned a wide range of environmental conditions (Table 2.2). The satellite-derived $bPAR_i$ values showed comparable magnitudes spanning 22 to 672 μmol m^{-2} s^{-1}. Despite the wide range of inherent optical diversity across the test regions, regression analyses showed strong agreement between concurrent satellite-derived and *in situ bPAR* data pairs (Figure 2.5, Table 2.2), indicating that our approach was able to produce a realistic estimate of *bPAR* values across a range of complex and optically shallow coastal waters. The model performed strongest at Heron and was only slightly weaker at Yongala and the two deep oceanic test sites, Palm Passage and Myrmidon. Yongala and Heron had smaller dynamic ranges of benthic PAR over the period of observation compared to Palm Passage and Myrmidon and may somewhat explain the better agreement found in the two former test sites.

Note that the capability of our newly developed benthic irradiance model may be limited under certain environmental conditions. For example, tropical cyclones can lead to extreme optical conditions via mixing and re-suspension of near bottom sediments which might not be fully captured by remotely sensed datasets. Excessive rainfall events during the wet season can also cause major flooding of river catchments (Devlin et al., 2012). During such events, freshwater plumes discharge from rivers and

disperse outward across the GBR lagoon, leading to distinct stratification in near-shore regions. Buoyant freshwater flood plumes are typically NAP- and CDOM-laden, thus the water column becomes optically inhomogeneous and the *bPAR* model's assumption of vertically homogenous IOPs is violated.

Table 2.2. Matchup statistics for instantaneous satellite-derived ($bPAR_i$) and concurrent in situ bPAR observations for the four test sites and all sites combined (denoted as ALL). The number of concurrent valid data pairs (days of observation) after all quality criteria were applied and used in regression analyses is indicated as n. The number of valid data points when only the L2 flags were used as the exclusion criterion is given by (n_0), shown to emphasise the importance of additional exclusion criteria as described in section (2.4.4.1). The highlighted row for Yongala indicates matchup statistics when extremely low bPAR values (coinciding with a severe tropical cyclone that passed across the Queensland coast in late March 2017) were included in the regression analysis. Note that model performance metrics are in multiplicative space, while the range of concurrent satellite-derived and in situ PAR values are given in the observed (non-transformed) scale to facilitate interpretation.

Site	n (n_0)	PAR range (μmol photons m^{-2} s^{-1})		Model II regression			bias	MAE
		in situ	$bPAR_i$	r^2	slope	intercept		
Yongala	348 (523)	13.1, 247.3	21.9, 274.0	0.71	0.90	0.25	1.15	1.26
Heron	210 (320)	25.4, 288.8	26.5, 283.6	0.73	1.10	-0.23	0.95	1.22
Palm Passage	45 (81)	80.2, 353.6	54.6, 332.4	0.68	1.18	-0.49	0.82	1.31
Myrmidon	93 (210)	146.7, 906.1	102.2, 672.1	0.66	1.08	-0.26	0.88	1.26
ALL	696 (1134)	13.1, 906.1	21.9, 672.1	0.80	0.91	0.19	1.03	1.25
Yongala	353	1.1, 247.3	8.0, 274.0	0.73	0.83	0.41	1.18	1.28

The *bPAR* model's limitation under optically extreme conditions can be seen at the Yongala test site during early April 2017 when several extremely low *in situ bPAR* values (filled triangles in Figure 2.5 (a, c, and f) resulted in a weaker overall agreement between the derived and actual measurements (i.e., lower slope = 0.83 and higher intercept = 0.41, hence less unity, but high $r^2 = 0.73$) (see the last row of Table 2.2). The *in situ bPAR* values, the minimum of which was an order of magnitude smaller than satellite-derived values during this extreme event period, coincided with Tropical Cyclone Debbie that affected the Queensland coast in late March 2017 (Bureau of Meteorology, 2018) and led to low water clarity (due to high terrestrial river runoff) in the vicinity of the Yongala site long after the event (Fabricius et al., 2016). In Figure 2.5 (a), wet season (colour-coded red) validation data for the Yongala site, which is seasonally dominated by the Burdekin River plume, were biased slightly high; again suggesting that the *bPAR* model is underperforming during optically challenging events. Although the scope of the current study did not allow to further explore this limitation, an additional investigation is warranted.

Further analysis conducted on the combined dataset also echoed the overall strong agreement between derived and *in situ* measured *bPAR* values (Figure 2.5 (c and f), Table 2.2). Across all test sites, the calculated bias was small and ranged between 0.82 (–18%) at Palm Passage to 1.15 (+15%) at Yongala which respectively suggest an underestimation and overestimation of the observed PAR values by an average of ±16.5%. MAE values were very similar for all four test sites. Again, Heron had the smallest MAE of 1.22 while Palm Passage had the highest MAE of 1.31 indicating an average error of satellite-derived $bPAR_i$ ranging between 22% to 31%, respectively. The overall model error of the combined satellite-derived $bPAR_i$ values was about 25% (ALL dataset MAE = 1.25). This average model prediction error is much smaller and well within the 35% uncertainty and accuracy goal set for the retrievals of chlorophyll-a concentration which is a widely-used ocean colour variable ((Hooker and Esaias, 1993) as mentioned in (McClain et al., 2004; Barnes et al., 2014)).

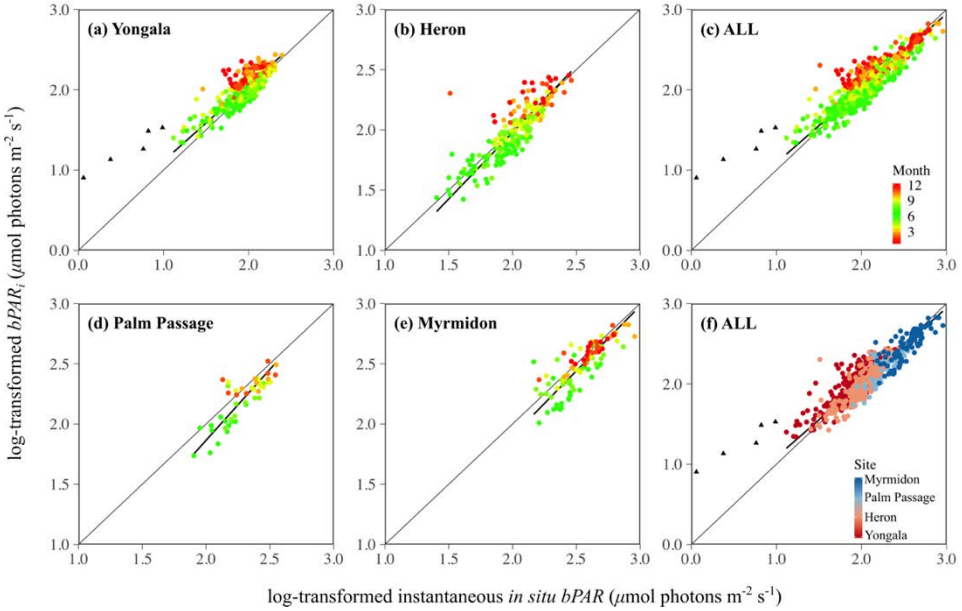

Figure 2.5. Scatterplots of concurrent log-transformed instantaneous satellite-derived ($bPAR_i$) and in situ bPAR for the four test regions of varying optical properties (a-b, d-e) plotted according to the month of observation, and ALL sites combined plotted (c) by month of observation and (f) according to site. Colour scale gradients for the months of observations are defined to delineate seasonal contrast between austral wet (November to April of following calendar year, yellow-red) and austral dry (May to October, green) seasons. The thin and thick solid black lines indicate the 1:1 line and the reduced major axis regression slope, respectively. Filled triangles in (a, c, and f) indicate the extremely low bPAR values coinciding with a severe tropical cyclone but were excluded in the regression analysis.

Collective consideration of the bias and MAE suggest agreement between satellite-derived $bPAR_i$ and *in situ* was best at the optically clear-water site Heron where many validation points existed, and lowest at the optically clear-water sites Palm Passage and Myrmidon, where relatively fewer data points were available. Given the overall strong agreement and small error of the derived values, we suggest that the larger error noted in Palm Passage and Myrmidon was more related to the quality of the *in situ* validation

datasets and/or possibly related to fewer data points resulting in higher variability in the regression statistics rather than to a diminished ability of the model in these water bodies.

Table 2.3. Matchup statistics for daily integrated satellite-derived ($bPAR_d$) and concurrent in situ bPAR observations. The number of concurrent valid data points (days of observation) after all quality criteria were applied and which were used in regression analyses is indicated as n. Note that model performance and error metrics are in multiplicative space, while the range of bPAR values is given in the observed scale to facilitate interpretation.

Site	n	PAR range (mol photons m^{-2} d^{-1})		Model II regression			bias	MAE
		in situ	$bPAR_d$	r^2	slope	intercept		
Yongala	347	0.4, 6.6	0.6, 6.9	0.65	0.98	0.06	1.13	1.26
Heron	208	0.9, 7.7	0.8, 7.2	0.80	1.16	-0.09	0.96	1.21
Palm Passage	21	2.5, 6.7	1.9, 5.3	0.73	1.08	-0.18	0.75	1.35
Myrmidon	90	4.8, 22.7	3.1, 17.1	0.75	1.21	-0.29	0.83	1.28
ALL	666	0.4, 22.7	0.6, 17.1	0.80	0.94	0.04	1.01	1.25

2.5.3 Daily integrated benthic PAR matchup analysis

The same *in situ* validation datasets used for the instantaneous matchup analysis were integrated to obtain daily *in situ* benthic PAR values and compared with concurrent satellite-derived $bPAR_d$. The dynamic range of the *in situ* and satellite-derived daily values were comparable at 0.4 to 23 mol photons m^{-2} d^{-1} and 0.6 to 17 mol photons m^{-2} d^{-1}, respectively. Results of the Type II linear regression analysis on the daily integrated datasets also showed an overall strong positive relationship (Figure 2.6, Table 2.3). Again, agreement between derived and *in situ* values is most notable at the Heron test site with small negative bias (– 4%) and highest accuracy (smallest MAE of 21%). Although Yongala showed a relatively lower coefficient of determination (r^2 = 0.65) amongst the test sites, the other regression statistics as well as bias and accuracy metrics indicate better model performance compared to the two deep test sites.

As previously discussed, the relatively weaker agreement between the satellite-derived and the *in situ* data at Yongala may be attributed to our *bPAR* model underperforming under more complex and/or stratified in-water optical conditions in this shallow inshore test site. More specifically, this effect may be compounded when estimating daily-integrated PAR due to intra-daily temporal variability in physical factors that drive nearshore IOPs. For example, clear water, offshore pixels will have optical variability that occurs at longer time-scales, being distant from terrestrial sources of particles and other pollutants, such that temporally extrapolating the IOPs derived at the time of the MODISA satellite overpass for the whole day, is a reasonable assumption and one that indeed showed strong agreement with observed values. However, for more dynamic inshore waters that may have IOPs with variability occurring at shorter time scales or higher frequency (e.g., hours), it becomes more challenging to temporally extrapolate the IOPs over the whole day. On the other hand, while the agreement between

satellite-derived and *in situ* values was strong for the deep oceanic test sites, the bias and MAE at Yongala showed better results than at Palm Passage or Myrmidon. Again, we suggest that these results may be related to the quality of the validation data obtained for these test sites. As for the combined dataset, satellite retrievals showed strong positive agreement with an almost negligible systematic error (bias of +1%) and high accuracy (low MAE of 25%) (see Figure 2.6 (c and f) and Table 2-3).

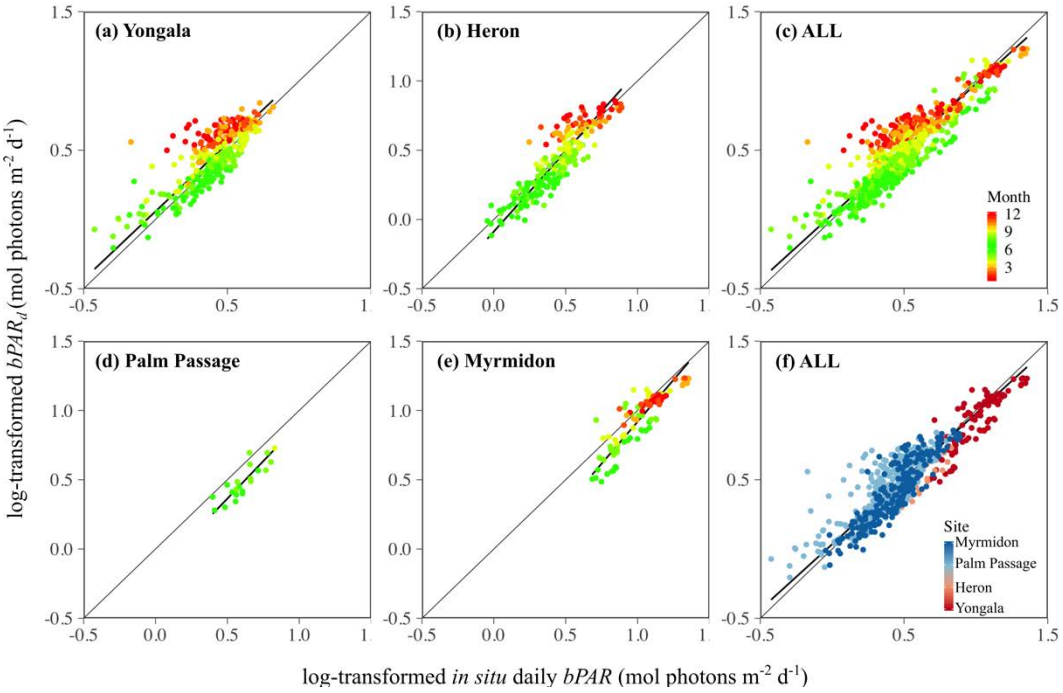

Figure 2.6. Scatterplots of concurrent log-transformed daily integrated satellite-derived ($bPAR_d$) and in situ bPAR for the four test regions of varying optical properties (a-b, d-e) plotted according to the month of observation, and ALL sites combined plotted (c) by month of observation and (f) according to site. Colour scale gradients for the months of observations are defined to delineate seasonal contrast between austral wet (November to April of following calendar year, yellow-red) and austral dry (May to October, green) seasons. The thin and thick solid black lines indicate the 1:1 line and the reduced major axis regression slope, respectively.

Although we consider $bPAR_d$ to be an ecologically important parameter due to its role as an autotrophic requirement (e.g., the energy source for photosynthesis), we also acknowledge that perhaps a more complete measure of light relevant for marine photosynthetic organisms is a PAR value estimated from the scalar irradiance (Mobley, 1994; Kirk, 2011) wherein light in every direction is considered (e.g., PAR measured by a spherical collector). However, as discussed earlier, the available validation dataset for this study is only collected for visible light measured on a plane (i.e., plane irradiance) which allowed us to only consider the downwelling plane irradiance in our model development. Indeed, if *in situ* scalar irradiance data becomes available in the future, this potential improvement could be considered.

While we acknowledge that our approach has several limitations and has room for further improvement, the baseline results obtained via this newly developed approach have demonstrated that our simple model can realistically estimate daily benthic PAR values within the GBR with good skill. Our new GBR-specific ocean colour benthic irradiance algorithm can thus be utilized for ecological studies within this important and world-heritage listed region by providing estimates of benthic light values.

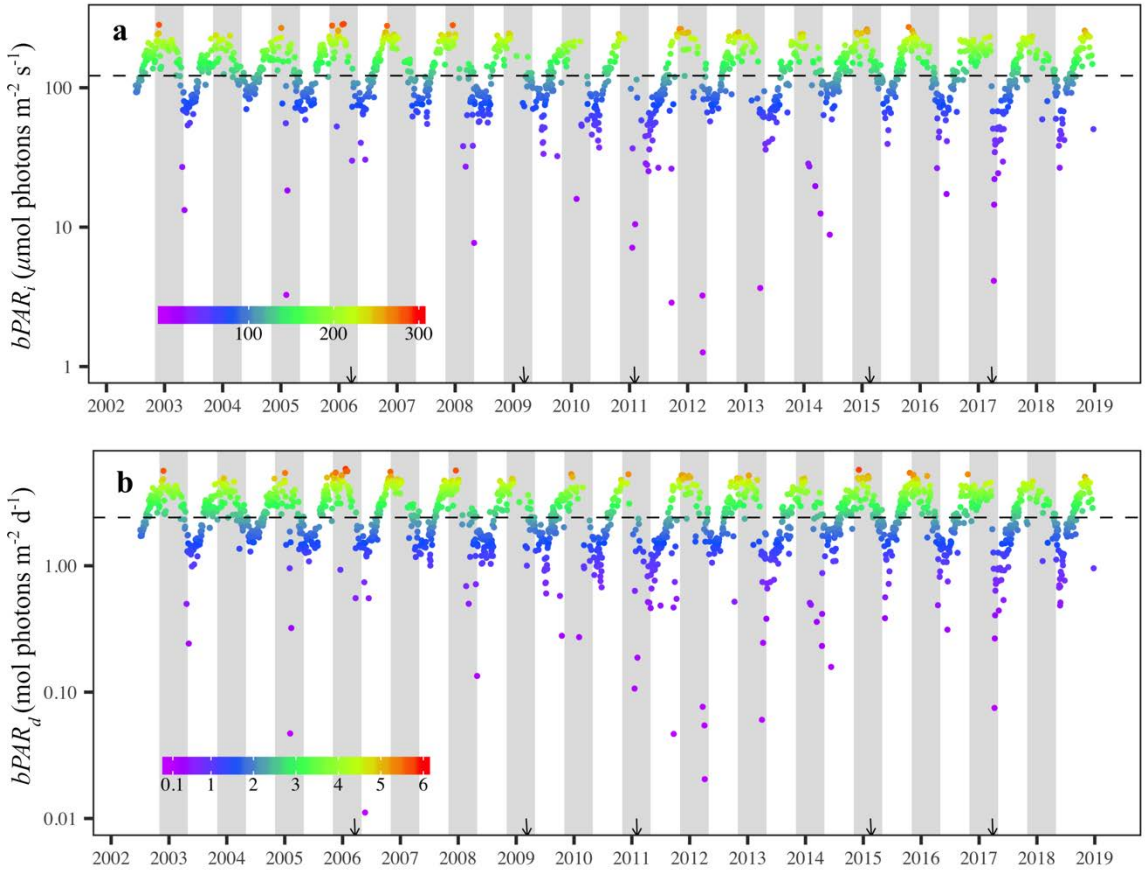

Figure 2.7. Time series plot of satellite-derived (a) instantaneous benthic PAR, $bPAR_i$, and (b) daily integrated benthic PAR, $bPAR_d$, for the Yongala test region from July 2002 to December 2018. The colour gradient indicates bPAR values while the dashed horizontal line indicates the median value of the entire time series data for each parameter, overlaid for reference. The greyed-out areas indicate the austral wet season months (extending from November to April of the following calendar year). Downward pointed black arrows on the x-axes denote occurrences of selected severe tropical cyclones that hit the eastern Australian coast. Note that vertical axes are on a logarithmic scale.

2.5.4 Time series case study

The 16+ year time series of satellite-derived benthic PAR values for the Yongala site exhibits strong seasonality (Figure 2.7). Lower values (purple to blue spots below the median lines) coincide at the end of austral wet season months (which extends from November to April the following calendar year, denoted as grey areas on both panels of Figure 2.7) and beginning of the austral dry season (May to October). Relatively higher values (green to red spots above the median lines) were derived for most of

the austral dry season towards the proper austral wet season. This temporal pattern agrees with the variability of satellite-derived photic depth data previously obtained for the GBR (Weeks et al., 2012). This time series provides insight into the influence of local events or phenomena that can drive variability of the underwater light field. As an example, decreased benthic light values are seen to coincide with tropical cyclones events (downward arrows in Figure 2.7). Indeed, the future near-synoptic, high-temporal resolution output of this model, which will be the first of its kind for the GBR, will provide a critical dataset that will allow us to further explore and understand how light availability varies both in space and time and in relation to the presence of important benthic organisms that is found within the GBR.

2.5.5 Understanding the effects of tide on instantaneous benthic PAR estimates

Both "3D-GBR" and "*pressure*" models show good temporal coincidence with the observed instantaneous benthic PAR values (Figure 2.8 (a) and (b)). For the purpose of this exercise, a large difference between the satellite-derived $bPAR_i$ values (for either model) would mean it is necessary to correct the original 3D-GBR bathymetry data for tidal effects. Otherwise, we can reasonably assume minimal tidal influence in the results of our new benthic irradiance model, but sentient of caveats when interpreting results.

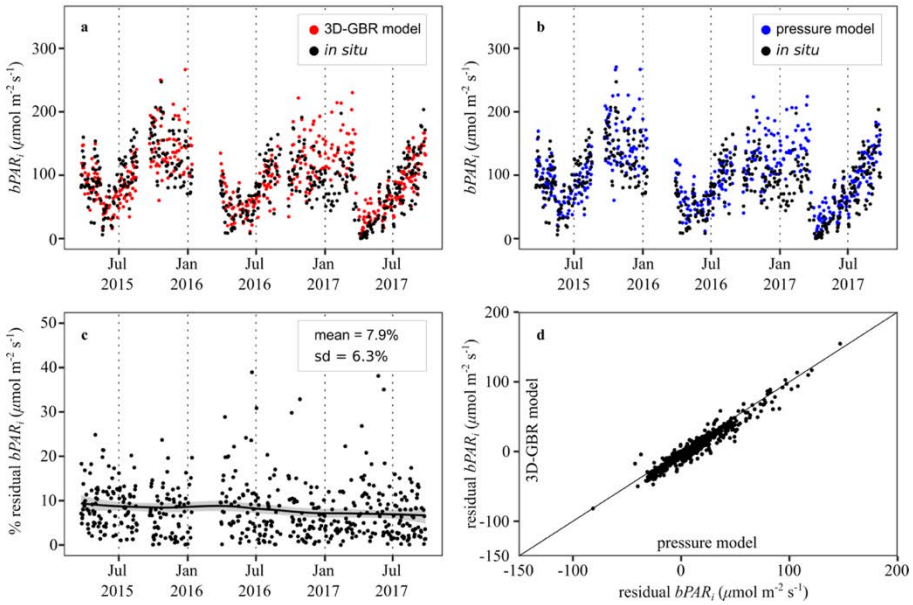

Figure 2.8. Depth sensitivity analysis and model results comparison at the Yongala test site. (a) plot of satellite-derived instantaneous benthic PAR values modelled using Beaman 3D-GBR bathymetry as z (red, 3D-GBR model) with in situ instantaneous benthic PAR (black); (b) plot of satellite-derived instantaneous benthic PAR values modelled using in situ pressure data as z (blue, pressure model) with in situ instantaneous benthic PAR (black); (c) unbiased percent difference between $bPAR_i$*, calculated as* $|(bPAR_{3D\text{-}GBR} - bPAR_{pressure})|/(0.5*bPAR_{3D\text{-}GBR} + 0.5*bPAR_{pressure})*100$*; and (d) scatterplot of the residuals (against in situ values) of the two models where diagonal black solid line denotes the 1:1 line. Gaps in plots a-c indicate periods where there were no in situ data available for validation.*

Results of the comparison showed a mean UPD of 7.9 % between the two models, equivalent to ~7 μmol photons m^{-2} s^{-1} (roughly 0.6 mol photons m^{-2} d^{-1}) (Figure 2.8(c)). Scatterplots of residuals between the two satellite-derived $bPAR_i$ values against *in situ* values (Figure 8(d)) also show good agreement. This difference is relatively small compared to the published ecologically-relevant minimum irradiance value required to maintain autotrophic health, which depending on the benthic organisms considered may vary between 0.4 to 5.1 mol photons m^{-2} d^{-1} [1]. We concede that the tidal influence will vary depending on a location's known bathymetry and range of daily tidal fluctuations such that effects will be greater in areas with shallow depths and bigger tides. We note, however, that our model does not consider intertidal regions of the GBR or locations where MSL bathymetry is less than 5 m and where the influence of the bottom can be significant (Barnes et al., 2013).

2.6 Conclusion

Here we have demonstrated that our simple benthic irradiance model can be employed to estimate realistic benthic PAR values within the GBR with good accuracy. We emphasise once again that although our results were reported in terms of a single broadband PAR irradiance, our approach does not utilize K_d(PAR). Instead, our model resolved $K_d(\lambda)$ by carrying out all calculations spectrally, where the full spectral variability of $E_b(\lambda)$ in Equation (2.1) has been retained in the process. Thus, aside from its simplicity, the key strength and novelty of our benthic irradiance model mean it can be easily extended to other ocean colour sensors. In particular, we expect that model-derived estimates of *bPAR* may be improved when applied to data collected by sensors with contiguous spectral bands such as the upcoming NASA's Plankton, Aerosol, Cloud, and ocean Ecosystem mission which is scheduled to launch ca. 2022. In addition, the *bPAR* model should also be extendable to other coastal waters for which high-resolution bathymetry data exists and where spectral IOPs can be obtained accurately.

Overall, the validation exercise using four optically diverse test sites proved that our model was able to estimate both $bPAR_i$ and $bPAR_d$ values from MODISA remote sensing data with good skill as indicated by small bias and low MAE (within ~25%) compared to the observed "true" *bPAR* values. This suggests that our benthic irradiance model is robust to variation in optical water types found in the optically complex and shallow GBR lagoon. We do note that during extreme seasonal events, such as sediment-laden flood plumes, where acute optical stratification is present (i.e., buoyant turbid freshwater lens) the model's assumption of an optically homogenous water column is violated. Indeed, the validation results revealed that season retrievals of *bPAR* for the Yongala site, which is adjacent to the Burdekin River mouth, deviated from *in situ* observations.

We also acknowledge that the baseline *bPAR* model presented here has some limitations that if addressed, may further improve the model in the future. Firstly, our model assumed clear skies and that our validation data were generally obtained during cloud-free days, yet cloud cover variability modulates $E_s(\lambda)$ (Kirk, 2011). This assumption proved to be satisfactory for instantaneous $bPAR_i$

estimates but may have significant consequences for deriving daily integrated $bPAR_d$ values; particularly in locations where temporal variation in cloud cover may be high. We concede that cloud variability should be considered when computing $bPAR_d$, however, it is challenging to generate a cloud climatology dataset to correct our $bPAR_d$ data. A future enhancement may include statistically quantifying the effect that clouds have upon $bPAR_d$ by using *in situ* surface and sub-surface PAR datasets to empirically tune the model, both regionally and seasonally (e.g., as a cloud cover climatology). We note that parallel efforts are underway to include this as a future enhancement of our benthic irradiance model. Secondly, the atmospheric model used to obtain $E_s(\lambda)$ did not include diffuse sky irradiance. Future work to improve the *bPAR* model may include using a two-component "clear sky" and "cloud layer" model similar to Frouin and McPherson (2012). Thirdly, contributions of a wind-roughened sea surface to reflectance/transmittance across the interface may also be accounted for following Haltrin et al. (2000) and Haltrin et al. (2002), provided appropriate ancillary wind data that matches our model input datasets can be obtained. Lastly, the applicability of our model may also be limited in areas where tidal fluctuations are much higher than what our DSA has tried to address. The bottom topography and physical processes that drive the oceanography of the entire GBR are complex and therefore cannot be easily generalised. Fine-tuning the water column depth in shallow locations or in regions where tides vary significantly (e.g., Broad Sound located at the southern GBR) may also improve benthic irradiance estimates for these locations.

Despite the above limitations, the model results we have presented are very promising and can be implemented to the entire GBR region using near-daily MODISA data collected over the last 16+ years. This will allow for a spatiotemporally rich benthic PAR dataset to be generated for the first time at this scale. Given the importance of light availability for the health of benthic ecosystems, our model results can now be used to explore the spatial and temporal variability of benthic light in the GBR region (see Figure 2.9). The resulting benthic light datasets will provide the information needed to assess habitat quality for corals and seagrasses. Specifically, GBR-wide maps of light thresholds (i.e., minimum light requirements for optimal system function) for these organisms can be developed from the benthic PAR values derived using this model and form the basis of a new GBR water quality index based on light.

Whilst we have outlined some limitations of the *bPAR* model, it is important to recognize that we do not necessarily anticipate that the satellite-derived benthic irradiance data presented here will become a standalone solution for monitoring water quality and ecosystem health in the GBR. Instead, we expect the *bPAR* model will complement existing monitoring tools such as the eReefs hydrodynamic model (Baird et al., 2016), the Q-IMOS mooring array, and the routine *in situ* water quality sampling programs. There is great potential for the uptake of the *bPAR* model in developing additional management criteria for monitoring water quality in the GBR based on light availability, as well as exploring the effects of long-term patterns of benthic light availability on corals and/or seagrasses which has not been possible before now.

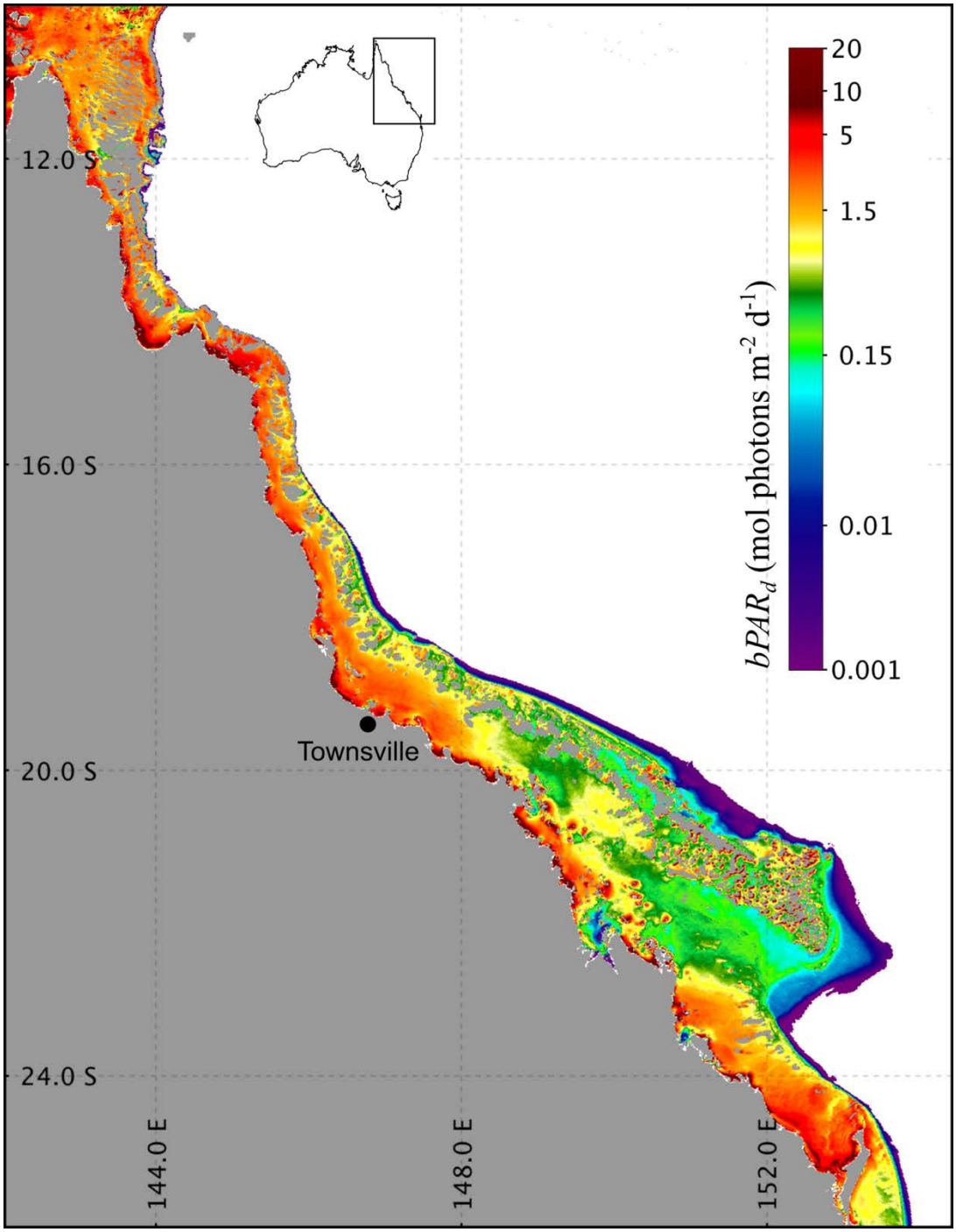

Figure 2.9. Map of 2016 annual mean of daily integrated benthic PAR ($bPAR_d$) for the Great Barrier Reef region. Colour gradient indicates values in mol photons m^{-2} d^{-1}.

"All knowledge and understanding of the Universe was no more than playing with the stones and shells on the seashore of the vast imponderable ocean of truth" – Sir Isaac Newton (1642 – 1726)

3 Temporal and spatial variations of benthic photosynthetically active radiation (bPAR) in the Great Barrier Reef, Australia

Abstract

Light, specifically the irradiance within the visible range (400 – 700 nm wavelengths) known as the photosynthetically active radiation (PAR), is fundamental for the productivity of coral reef ecosystems including the Great Barrier Reef. The impact of light availability on the health of corals and seagrasses is an adequate motivation to fully understand spatial and temporal variability in benthic light. We used 16.5 years of MODIS satellite-derived daily benthic PAR dataset to characterise the long-term spatial and temporal distribution and variability of benthic light within the GBR and its different natural resource management regions and water bodies. We found that bPAR varies strongly within the GBR as a response to the different conditions and processes that surround and operate on the shelf, with long-term means varying over 50-fold. Baseline mean bPAR values decrease from north to south, and from offshore to inshore. Values were higher during austral spring and summer than autumn and winter seasons. These data on benthic light variation across the GBR will be useful in identifying areas that experience specific light regimes and further provide insights on the exposure of benthic habitats to stresses from not just low or high but also variable benthic irradiance levels.

3.1 Introduction

Light is fundamental for the productivity of coral reef ecosystems including the Great Barrier Reef (GBR). Photosynthesis by benthic organisms, driven by the availability of light energy, supports growth and maintains health of benthic ecosystems (Dubinsky and Falkowski, 2011; Dubinsky and Iluz, 2016). Therefore, the impact of light availability on the health of corals and seagrasses is a sufficient motivation to fully understand how light varies across the benthic ocean and its role for benthic primary production (Gattuso et al., 2006; Gattuso et al., 2020), upper ocean heat transfer (Dickey and Simpson, 1983), and its strong link to water clarity and quality (Yentsch et al., 2002).

It is important to determine patterns in both space and time and quantify the changes in light availability, because such knowledge is fundamental to understanding ecological outcomes, potentially assisting managers to develop solutions to stressors affecting benthic habitats in the GBR (e.g., water quality degradation). However, the physical environment defining habitats and oceanic processes (Foster et al., 2014) can vary over wide spatial and temporal scales, ranging from sustained phenomena over long time periods to episodic events, and spanning from small to large spatial scales (Hatcher, 1997). In the GBR, the large and varied geographic settings and surrounding oceanographic conditions impart complex physical, biological, chemical and optical processes on the shelf including those that affect the distribution and availability of light across the benthic ocean.

The temporal and spatial variation in the amount of light reaching the seafloor is not homogenous across the ocean benthos. Firstly, the amount of solar irradiance reaching the ocean surface varies due to a range of factors. Light intensity is significantly reduced as it passes through the atmosphere, and fluctuates diurnally and seasonally due to solar elevation, sun angle, clouds and day length (Kirk, 2011). Second, benthic habitats are subjected to additional variations in benthic light levels in response to turbidity, coloured dissolved materials, and tides, especially in coastal waters (Anthony et al., 2004). Sediment resuspension and nutrient enrichment from river runoff strongly contributes to light attenuation and is highly seasonal (e.g., in the GBR most significant during the austral wet season; (Devlin et al., 2001)).

Although changes in light may cause perturbation of dependent ecosystems, the effects of reduced light on benthic habitats (e.g., due to increased water column turbidity or poor water quality) are not always harmful. For example, it has recently been suggested that turbidity may help to moderate coral bleaching (Sully and van Woesik, 2020) and that reefs that are often exposed to poor water quality may be more resilient against coral bleaching (MacNeil et al., 2019). However, exposure to suboptimal water quality conditions may also reduce recovery success in coral reefs and increase susceptibility to coral diseases and outbreaks frequencies of crown-of-thorns starfish (MacNeil et al., 2019). These complex connections related to light variability should motivate efforts to increase baseline knowledge of the spatial and temporal distribution and variability of benthic light/irradiance. In addition, successive mass

coral bleaching events (Hughes et al., 2017) continue to pose a significant threat to the health of coral reef ecosystems and high irradiance levels have already been implicated in increasing coral bleaching risk during thermal stress (Lesser and Farrell, 2004; Lesser, 2011; Leahy et al., 2013). An understanding of benthic light variation across the GBR will be useful in identifying areas that experience specific light regimes, either as acute or chronic events, and further provide insights on the potential extent of exposure of benthic habitats to stresses from not just low or high but also variable benthic irradiance levels.

Despite the known ecological importance of benthic irradiance, *in situ* data do not currently exist at relevant GBR-wide scales. Fortunately, repeatable quantitative tools (Dierssen et al., 2010) from remote sensing offer a key to characterising benthic habitats at scale. A new GBR benthic irradiance remote sensing model (Magno-Canto et al., 2019), discussed in Chapter 2, offers a synoptic dataset containing direct estimates of benthic irradiance values for every nominal 1 km^2 pixel for any location > 5 m depth within the GBR. This model allows for GBR-wide near-daily estimates of benthic irradiance (i.e., integrated to daily values within the photosynthetically active radiation (PAR) region (400 – 700 nm), hence benthic PAR or "bPAR", units: mol photons m^{-2} d^{-1}) to be derived from spectral remote sensing reflectance values, R_{rs} (units: sr^{-1}), provided other relevant input parameters can also be obtained. The opportunity to observe bPAR in space and time through remote sensing provides an overview of light availability within the GBR region.

This study aims to characterise the baseline (spatial and temporal) patterns and distribution of bPAR in the GBR, with emphasis on characterising the long-term variability (noting that 'long-term' refers here to the 16.5-year coverage of the dataset). Specific objectives of this study are: (i) to describe the baseline spatial and temporal patterns of bPAR in the GBR by mapping long term, annual, seasonal, and monthly bPAR climatology, and (ii) to quantify bPAR variability using Hovmöller plots, empirical orthogonal function (EOF) analysis, and standard deviation maps. These data will help establish some fundamental knowledge on how bPAR has varied within the whole GBR in the last 16.5 years.

This study is presented in two parts: the first part focuses on a descriptive characterisation of benthic PAR within the GBR for the last 16.5 years, using both the whole GBR-wide and in regional sub-domains relevant for GBR management (i.e., in the six Natural Resource Management (NRM) and four cross-shelf waterbody boundaries, the combination of which is referred to as 'zones'). For these zones, bPAR was also aggregated to provide satellite-derived estimates of benthic light intensities taking water depth into account. This offers a more direct understanding on the underwater light conditions in the GBR, extending insights on GBR water clarity gained using remotely-sensed photic depth data (Weeks et al., 2012; Fabricius et al., 2016). The second part of this chapter is focused on quantifying the associated variability in bPAR levels in the GBR.

3.2 Study region

For this chapter, the domain was the entire shelf region of the GBR World Heritage Area (GBRWHA: 10-26°S and 142-156°E; Figure 3.1). This domain occupies approximately 270,000 km^2 of the continental shelf along the northeast coast of Australia (Mathews et al., 2007) and is characterised by an uneven shelf width that is narrowest in the north along 14°S (measuring about 23 km) and widest in the south along 21°S (measuring ~260 km) (Davies, 2011). The GBRWHA region is composed of an intricate matrix of coral reefs and inter-reefal systems (Mathews et al., 2007) providing a complex topographic context. Along the eastern border of the GBR, the South Equatorial Current (SEC) is the main current that drives the regional circulation of the Coral Sea, which divides into strong and narrow jets as it encounters the small islands of Fiji, Vanuatu and New Caledonia (as mentioned in Choukroun et al. (2010)). Two of the resulting jets, the North Vanuatu Jet and the North Caledonia jet contributes to the major western boundary currents of the Australian shelf: (i) the northward flowing branch called the Hiri Current that feeds the North Queensland Current and dominates the circulation of the northern Coral Sea, and (ii) the southward flowing branch called the East Australian Current (EAC), a narrow swift current that typically impinges the coast further south but is also known to intrude within passages into the GBR (Andrews and Furnas, 1986; Brinkman et al., 2002; Choukroun et al., 2010). The southward flow of the EAC also drives the formation of the mesoscale eddy feature, the Capricorn Eddy, along the southern GBR in the Capricorn Channel as it interacts with the coastline leading to vortex-driven upwelling in the region which may have important consequences to local productivity (Weeks et al., 2010). Oceanic intrusions of oligotrophic clear Coral Sea waters via the open reef matrix in the central GBR (Choukroun et al., 2010) are also an important physical feature of the region associated with intrusive upwelling (Benthuysen et al., 2016) characterised by strong poleward along-shelf currents that results in intense stratification on the outer shelf which may have some implications for the transport and spread of land-derived materials, and potentially, for the availability of light in these regions.

3.3 Datasets

For this chapter, individual daily averaged satellite-derived bPAR files for the entire GBR spanning from July 2002 to December 2018 were generated using the benthic irradiance model (Magno-Canto et al., 2019; Magno-Canto et al., 2020) discussed in Chapter 2. The satellite data processing method detailed in Chapter 2 was also followed here where each daily file was quality controlled using the sensor-specific Level 2 quality flags as filters. Low-quality pixels were flagged and masked out (i.e., assigned a missing value, NaN) when any of the LAND, CLDICE, HISOLZEN, NAVFAIL, ATMFAIL, HISATZEN, and HIGLINT flags was detected on each pixel location, essentially excluding that pixel location in generating the respective final daily bPAR map. This step, as will be discussed later, is important in one of the selected data analysis methods. A complete description of the Level 2

quality flags used can be found in Robinson et al. (2003). Finally, each daily bPAR data file was geographically mapped within the study domain (see Figure 3.1) at a nominal pixel resolution of 1 km^2.

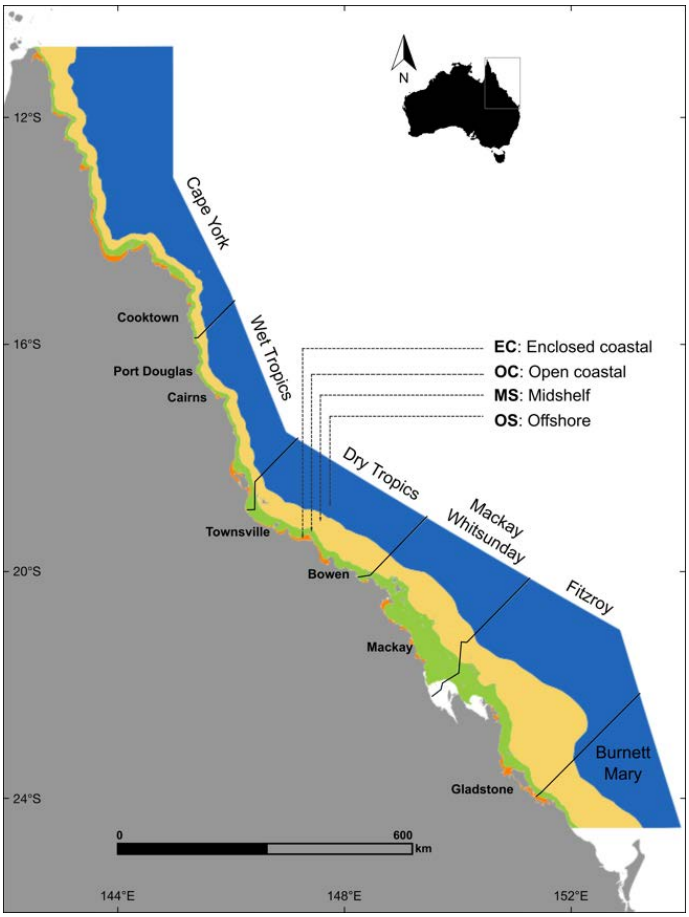

Figure 3.1. Map of the Great Barrier Reef (GBR) study region showing the entire NRM reef boundary and the boundary (black solid line) of the six individual regions from the northernmost Cape York to southernmost Burnett Mary. Cross-shelf coastal distance classes and water bodies indicated by solid colours labelled accordingly. Note that for the hovmöller diagrams detailed in Section 3.5.3, the two innermost coastal water bodies were combined as inshore locations. Land features are shown as mask in grey.

3.4 Time series generation

3.4.1 Mean GBR-wide timeseries

The daily bPAR datasets were aggregated as monthly means and processed using the NASA SeaDAS 7.5.3 Graph Processing Tool (GPT), resulting in a total of 198 monthly data files. These monthly means, were further aggregated as follows: (i) the 'long-term monthly climatology' was defined as the arithmetic mean of monthly mean values for July (N=17) or January (N=16); (ii) the 'seasonal climatology' averaged southern hemisphere seasons (e.g., austral summer: mean values of December, January, and February; austral winter: June, July, and August monthly means); (iii) the 'annual climatology' was the mean of all 12 months in each calendar year; and (iv) the 'overall long-term

climatology' (interchangeably referred to as the '16.5-year mean climatology') was the mean of all the 12 monthly long-term means as mentioned in (i). The annual climatology was not generated for the year 2002 since there were only six months of data collected by the satellite during this year. All temporal aggregations were performed using *xarray* v0.12.1 in Python 3.6 (Hoyer and Hamman, 2017). GBR-wide spatial maps were then generated to facilitate visualisation.

3.4.2 Regional global means

Spatial patterns in bPAR values were further highlighted regionally using global means aggregated for each of the six NRM reef region boundaries further subdivided using the four cross-shelf waterbody boundaries (see Figure 3.1) comprising 24 zones. The aggregation for the individual 24 zones also included spatially averaged bPAR values of: (i) monthly climatology; (ii) seasonal climatology; (iii) annual climatology, and (iv) 16.5-year mean climatology. These time series were presented as tables and/or graphs.

3.5 Quantifying spatial and temporal variability in bPAR

3.5.1 Hovmöller Diagrams

Two-dimensional time series Hovmöller diagrams were used to generate cross-shelf averages (i.e., all pixels along a latitude) for each of the 198 monthly-mean bPAR datasets over focused areas with boundaries defined by the polygons of the different water bodies across the shelf (see Figure 3.1). Here, the latitude coordinates were assigned to the vertical axis, with the horizontal dimension (x-axis) representing time (i.e., month and year) and the averages presented using a colour gradient. Thus, Hovmöller diagrams depict the evolution of benthic PAR across time and (defined) space within the GBR. Before calculating averages, land and reef pixels as well as those pixels with depth ≤ 5 m were masked out (i.e., set to NaN) and ignored in the calculation of averages. Note that no interpolation was conducted on the time series used for generating these diagrams. To obtain a single value per latitude-month, each of the 198 monthly mean benthic PARs under each of the polygon masks was averaged using an m x n domain where m is months on the x-axis and n is row along the latitude coordinate on the y-axis. Hovmöller diagrams were generated using a computer program written and executed in IDL 8.7.2 (Exelis Visual Information Solutions).

3.5.2 Empirical orthogonal function (EOF) analysis

The 198 monthly-mean bPAR datasets were further analysed using Empirical Orthogonal Function (EOF) analysis, a powerful and widely used statistical technique in oceanography (Preisendorfer and Mobley, 1988) which decomposes a set of spatio-temporal data into few dominant modes of variability. These modes or orthogonal functions, describe the spatial patterns and the associated temporal variation

contained in the dataset that may be linked to possible dynamical mechanisms (Emery and Thomson, 2001). In EOF analysis, the relative importance to the full pattern of variability of the original data is typically contained in the first few leading modes.

Although EOF is a robust technique for analysing large spatio-temporal datasets, it does have a limitation in handling missing data (i.e., the method will entirely ignore a pixel that has a missing value at any one instance in the input data time series). To minimise this constraint, each monthly mean bPAR file was spatially interpolated using the *inpaint_nans* function version 1.1.0.0 (D'Errico, 2021) in Matlab (R2017a). Only pixels with NaN values (flagged during satellite data processing as discussed in Section 3.3) were interpolated, ensuring that pixels with 'good' data remain unchanged. Lastly, a mask was also applied to each monthly bPAR file to exclude any pixels pertaining to land, reef, and shallow water (i.e., with depth ≤ 5 m) during interpolation. The latter is a common practice in remote sensing studies to minimise the influence of bottom reflectance signals that might contaminate a satellite-derived variable-of-interest in such locations (Barnes et al., 2013).

The chosen EOF analysis uses the singular value decomposition method, which is discussed in detail for example by Emery and Thomson (2001). Before running EOF, the three-dimensional dataset (i.e., longitude, latitude and time dimensions) was reorganised into a two-dimensional matrix where the columns represent the time series at each pixel location. The temporal mean and any linear trend was then subtracted from each of the time series records at each pixel location. Finally, each de-meaned and de-trended time series was normalised by dividing each data series by the standard deviation of the full time series to ensure that the variance from no individual pixel location will dominate the analysis, i.e., each location has an equal contribution to the total variance. EOF analysis was finally performed using the singular value decomposition (SVDC) procedure in IDL 8.7.2 (Exelis Visual Information Solutions) to obtain the eigenfunctions (spatial amplitude) and time-varying eigenvectors (principal component) for each pixel.

3.5.3 Standard deviations relative to long-term monthly mean benthic PAR

To quantify the magnitude and spatial distribution of bPAR variability across the whole GBR shelf, the standard deviation (σ) of monthly-averaged bPAR values was mapped at each location. Here, standard deviation represents the departure of bPAR for a particular month from the long-term monthly mean, which covers the period from July 2002 to December 2018. Two sets of maps were generated containing the: (1) full 16.5-year climatology of bPAR standard deviations and (2) climatology of standard deviations for each month. These maps identify the locations on the shelf that experience strong variation in bPAR values on a monthly scale which potentially are also locations most exposed to drivers of turbidity and variable light along the extent of the GBR. Global means of standard deviations were also calculated for each zone to facilitate comparisons between relevant NRM regions and water bodies.

3.6 Results and Discussion

3.6.1 Characterising the spatial and temporal patterns in bPAR

The GBR-wide climatologies using the different temporal aggregations (i.e., 16.5-year mean, annual, seasonal, and monthly) captured the important aspects of variations in the intensities of light reaching the GBR seafloor. The most prominent spatial pattern of the benthic light levels was primarily determined by the depth of the pixel, and secondly, by the amount of incident surface radiation as a function of solar angle and day length. Additionally, many other interesting features were highlighted by each of the maps, as described in the following section.

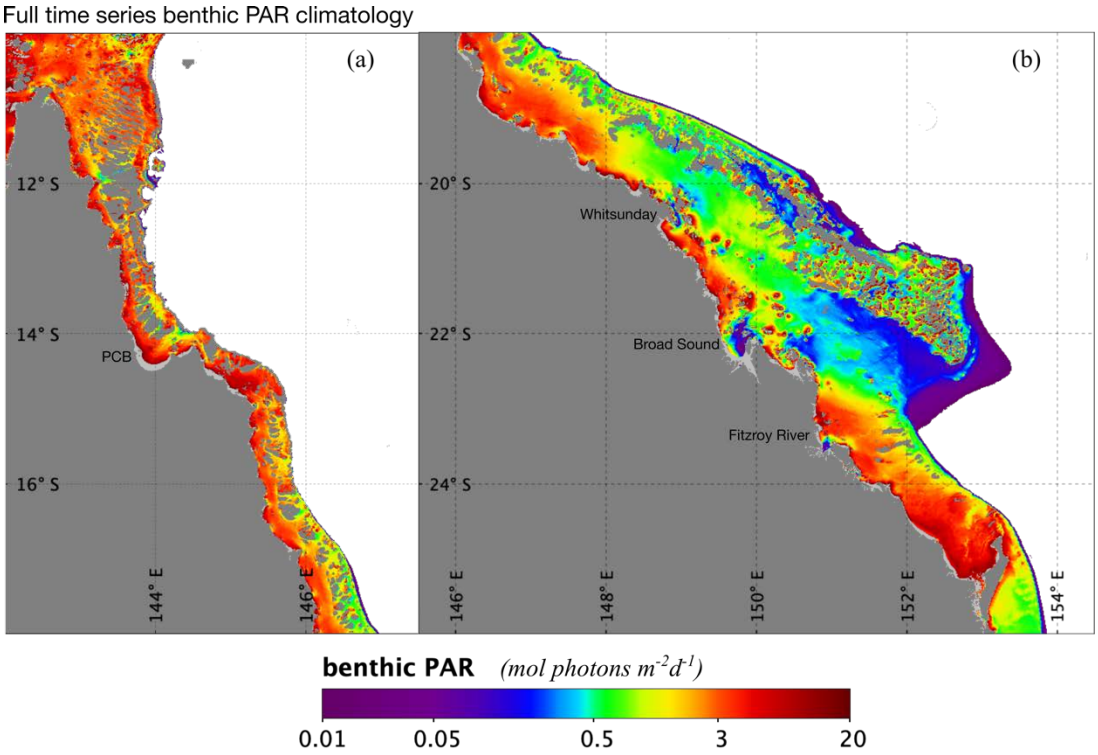

Figure 3.2. Map of the 16.5-year mean climatology of bPAR within the GBR extending from July 2002 to December 2018. (a) northern section with limits 10 to 18°S and 142 to 147.5°E; (b) southern section with limits 18 to 26°S and 145.5 to 154.5°E. Dark grey areas indicate either land or reef pixels while light grey areas indicate locations with depth ≤ 5 m. Colour gradient indicates bPAR displayed as logarithmic values. Abbreviation: PCB – Princess Charlotte Bay.

3.6.1.1 The full 16.5-year benthic PAR climatology

The full 16.5-year climatology highlighted a strong spatial variability of bPAR within the GBR (Figure 3.2). The northern section with its narrower shelf showed mostly high benthic light (red-coloured pixels in Figure 3.2a). In the southern GBR section (Figure 3.2b), bPAR was high in the shallow nearshore area, but declined to generally low values along the deep offshore shelf edge. The cross-shelf gradient

in bPAR appeared much weaker in the northern section, especially north of Latitude 16°. A north to south decline in the long-term climatology of bPAR was also apparent along the mid-shelf region (i.e., Figure 3.2b). Several nearshore locations that have chronically low benthic light values ("dark pixels", purple colours) over the last 16.5 years are also apparent in Figure 3.2b. These include, for example, the shoal around the Broad Sound where bPAR ranges from only 0.01-0.30 mol photons m^{-2} d^{-1}, south of The Keppel Islands near the mouth of the Fitzroy River, and around the southeastern tip of the Conway National Park in the Whitsunday region. Other dark pixels (dark blue to purple colours) highlighted in Figure 3.2b are in deeper regions along the outer shelf edge or slope, and the deep channels between the reef matrices.

Table 3.1. Global means of long-term (16.5 years) bPAR climatology values for the whole Great Barrier Reef (GBR) study region (numbers in bold) and the 24 zones (Region + Waterbody combination). Abbreviations are EC – enclosed coastal, OC – open coastal, MS – mid-shelf, OS – offshore, and AWB – across water bodies. Lowest (red) and highest (grey highlight) values at each water body are also indicated.

Region	bPAR (mol photons m^{-2} d^{-1})				
	EC	OC	MS	OS	AWB
Whole GBR	**4.5**	**3.7**	**1.8**	**1.3**	**2.8**
Cape York	5.9	5.6	3.2	2.8	4.4
Wet Tropics	3.9	4.8	3.0	1.6	3.3
Dry Tropics	4.0	4.0	2.3	1.2	2.8
Mackay Whitsunday	5.0	3.1	**0.8**	**0.8**	2.5
Fitzroy	**1.7**	**2.3**	1.0	1.1	**1.5**
Burnett Mary	6.7	5.4	2.7	0.1	3.7

The bPAR climatology averaged across each zone showed important patterns, with long-term means varying by over 50-fold (Table 3.1). The whole enclosed coastal region of the GBR averaged 4.5 mol photons m^{-2} d^{-1}, while means in the offshore waterbody were 70% lower (1.3 mol photons m^{-2} d^{-1}). Of the 24 zones, the Fitzroy and Mackay Whitsunday NRM regions consistently showed the lowest long-term mean bPAR values, with the single exception of the enclosed coastal waterbody of Mackay Whitsunday NRM (Table 3.1), while Cape York NRM showed the consistently highest bPAR values. Across water bodies for each NRM region, the averaged bPAR climatology also clearly revealed a latitudinal gradient that represents about 66% decline from Cape York to Fitzroy NRM regions. The latter was also markedly lower from the mostly clear Burnett Mary NRM which is nearly 60% 'brighter' on average across the shelf.

3.6.1.2 Annual climatology

The annual means of bPAR from 2003 to 2018 showed the year-to-year variation of bPAR within the GBR (Figure 3.3, Table 3.2). Strong spatial variability was also evident, characterised by the cross-shelf and north-south patterns, similar to that described in Section 3.6.1.1. In addition, the annual spatial

maps also displayed strong interannual differences in bPAR. This progression highlighted some 'dark' years with low local bPAR (e.g., Whitsundays region boxed in Figure 3.3a), potentially of interest for exploring ecological consequences of chronic low light in these years. In the location highlighted, the extent of blue-coloured pixels (signifying lower bPAR values) was clearly expanded in some years, especially between 2008 to 2013, and particularly 2010 and 2011. These darker years coincided with above-average rainfall and several severe tropical cyclones, which exposed the reefs to high loads of suspended sediments via river plumes and subsequent resuspension (Alvarez-Romero et al., 2013; Fabricius et al., 2016) from one of the largest river systems in the Dry Tropics NRM (the Fitzroy River) located south (given that the net wind-driven (Ekman) transport of materials is northward on this southern hemisphere coastline). Cyclones also resuspend existing sediments from the benthos and mix the water column vertically over sometimes large areas, bringing nutrients to the surface.

The calculated global means (Table 3.2, Figure 3.3b) revealed that throughout the period considered (2003 to 2018), 2011 was the 'darkest' year with a GBR-wide annual bPAR mean of 1.6 mol photons m^{-2} d^{-1}, i.e., 43% lower compared to the long-term mean (Table 3.1), and 24% lower than the 'brightest' years in the series (highest annual bPAR of 2.1 mol photons m^{-2} d^{-1} calculated for 2005 and 2007). The GBR-wide annual mean for 2010 was also comparably low at 1.7 mol photons m^{-2} d^{-1}. The 2010 – 2011 marks the wettest two-year period on record associated with the strongest La Niña event that affected Australia (National Climate Centre - BOM, 2012). Overall, the GBR-wide annual mean showed an undulating pattern, with peaks noted in 2005 and 2014 and troughs in 2011 and 2018 (Figure 3.3b). The annual progression of bPAR using the whole GBR means was almost similar for the mid-shelf and offshore water bodies but showed steeper variations in the two inshore coastal water bodies (Figure 3.3b). It was notable that the strong decline in the annual bPAR values in 2011 relative to 2010 was slightly subtle in the mid-shelf and offshore water bodies (average percent difference: -0.3%) compared to the two coastal water bodies (average percent difference: -7%), which might suggest that perhaps the impact of land-derived pollutants during the 2010-2011 event affected inshore regions the most.

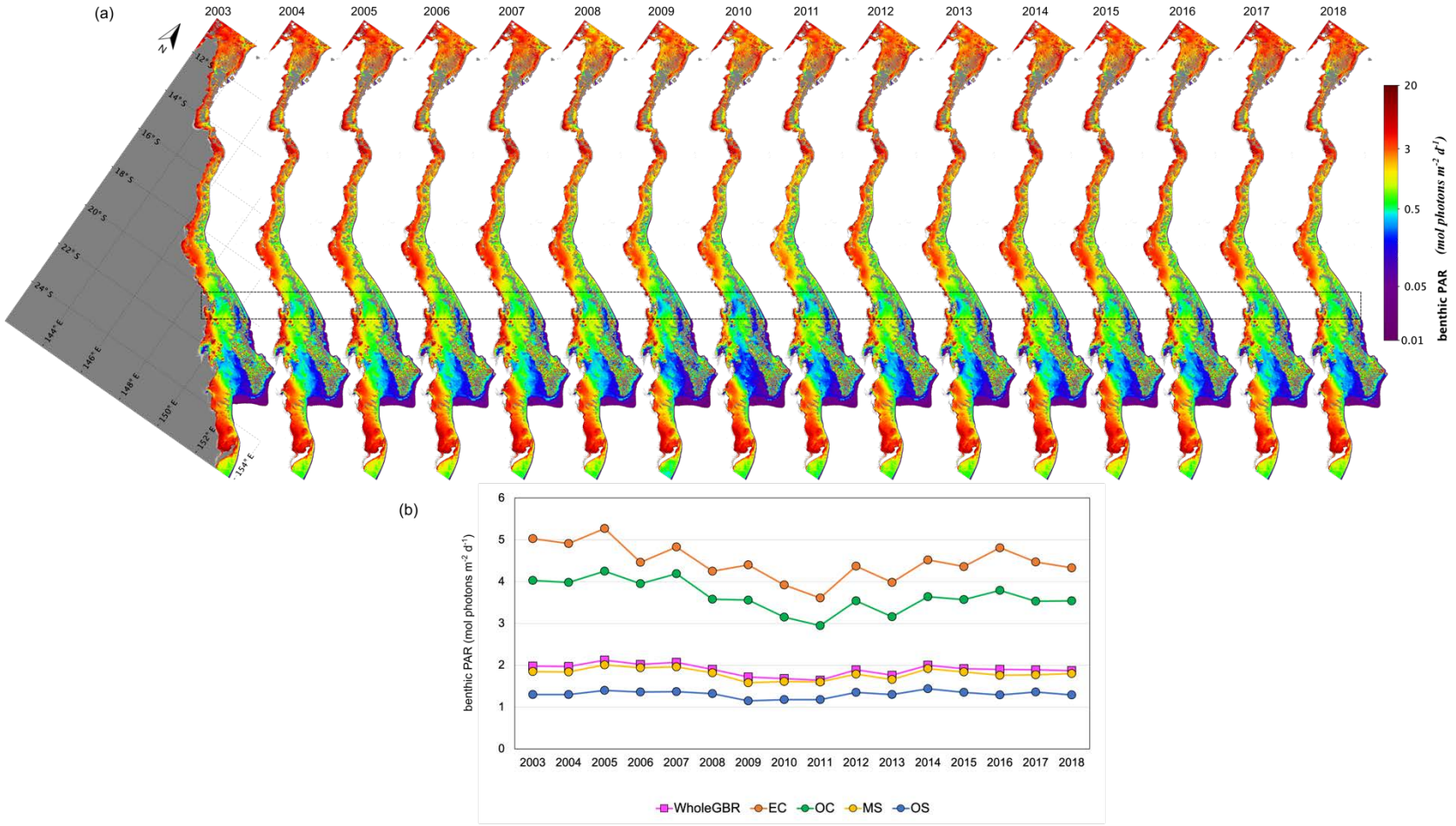

Figure 3.3. Annual means of bPAR from 2003 to 2018. (a) spatial maps; (b) line plots of annual means for the whole GBR shelf and water bodies. Black box across the spatial maps in (a) highlight a sample region of marked decline in annual bPAR especially between 2008 and 2013. Dark grey areas in (a) are either land or reef pixels while light grey areas indicate locations with depth ≤ 5m. Note that the maps have been rotated (by 35°) to facilitate visualisation. Colour gradient indicates bPAR displayed as logarithmic values. Abbreviations in (b) are for the four waterbody boundaries: EC – enclosed coastal, OC – open coastal, MS – mid-shelf, and OS – offshore.

Table 3.2 Annual mean bPAR values for the whole Great Barrier Reef (GBR), whole GBR north to south length per waterbody, and the 24 zones. Only years with full 12 monthly data were considered, hence 2002 was excluded. Shaded cells indicate the zone with the maximum (cyan) and minimum (grey) bPAR values for each year, including bPAR within 3% of the maximum or minimum. The annual values for the (mostly deep water) Burnett Mary offshore waterbody (last row) were excluded in calculations of the minimum bPAR for each year to ensure the highlighted lowest bPAR value is due to factors other than the depth of the water. Abbreviations are for waterbody boundaries: EC – enclosed coastal, OC – open coastal, MS – mid-shelf, and OS – offshore.

Region	Waterbody	2003	2004	2005	2006	2007	2008	2009	2010	2011	2012	2013	2014	2015	2016	2017	2018	min	max	ratio (%)
Whole GBR		2.0	2.0	2.1	2.0	2.1	1.9	1.7	1.7	1.6	1.9	1.8	2.0	1.9	1.9	1.9	1.9	1.6	2.1	78
Whole GBR: length North to South	EC	5.0	4.9	5.3	4.5	4.8	4.2	4.4	3.9	3.6	4.4	4.0	4.5	4.4	4.8	4.5	4.3	3.6	5.3	69
	OC	4.0	4.0	4.2	3.9	4.2	3.6	3.6	3.1	2.9	3.5	3.2	3.6	3.6	3.8	3.5	3.5	2.9	4.2	69
	MS	1.9	1.8	2.0	1.9	2.0	1.8	1.6	1.6	1.6	1.8	1.7	1.9	1.8	1.8	1.8	1.8	1.6	2.0	79
	OS	1.3	1.3	1.4	1.4	1.4	1.3	1.1	1.2	1.2	1.3	1.3	1.4	1.3	1.3	1.4	1.3	1.1	1.4	80
Cape York	EC	6.4	6.3	6.8	5.2	6.1	5.4	6.1	5.6	5.4	6.6	5.3	5.9	5.7	6.0	5.8	5.6	5.2	6.8	77
	OC	5.8	5.8	6.1	5.1	6.0	5.2	5.6	5.3	5.1	6.0	5.2	5.6	5.4	5.9	5.5	5.4	5.1	6.1	84
	MS	3.3	3.1	3.4	3.0	3.6	2.9	3.0	3.0	2.9	3.3	3.0	3.2	3.1	3.1	3.2	3.1	2.9	3.6	82
	OS	2.8	2.8	3.0	2.7	2.9	2.8	2.7	2.7	2.6	2.9	2.8	2.8	2.9	2.7	2.9	2.8	2.6	3.0	89
Wet Tropics	EC	4.7	4.1	4.7	4.1	3.8	3.6	3.5	3.6	2.7	3.7	4.0	4.2	4.2	4.5	3.9	3.4	2.7	4.7	58
	OC	5.3	5.0	5.4	4.7	5.3	4.7	4.5	4.6	3.2	4.7	4.5	5.1	4.9	5.5	5.2	4.5	3.2	5.5	59
	MS	3.1	3.1	3.3	3.1	3.3	3.0	2.6	2.8	2.0	3.0	2.8	3.3	3.0	3.2	3.1	2.8	2.0	3.3	61
	OS	1.6	1.6	1.8	1.7	1.6	1.6	1.4	1.5	1.2	1.6	1.5	1.8	1.7	1.6	1.6	1.6	1.2	1.8	65
Dry Tropics	EC	4.7	4.7	3.9	4.5	4.4	3.8	2.8	2.8	2.5	3.4	3.5	3.7	3.8	4.8	4.4	4.0	2.5	4.8	52
	OC	4.3	4.3	4.4	4.6	4.5	3.9	3.5	3.5	2.8	3.9	3.2	3.8	4.0	4.4	4.0	3.8	2.8	4.6	60
	MS	2.3	2.4	2.5	2.7	2.5	2.3	2.0	2.0	1.7	2.3	2.1	2.4	2.4	2.3	2.3	2.2	1.7	2.7	64
	OS	1.1	1.1	1.2	1.3	1.2	1.2	1.0	1.0	0.9	1.1	1.1	1.3	1.2	1.2	1.2	1.1	0.9	1.3	71
Mackay Whitsunday	EC	5.2	5.5	6.9	5.3	5.2	4.8	4.8	3.1	3.5	4.0	4.1	5.4	5.0	5.7	4.9	5.0	3.1	6.9	46
	OC	3.6	3.6	3.8	3.7	3.7	3.0	3.1	2.2	2.6	3.0	2.6	3.0	3.0	3.1	2.8	3.0	2.2	3.8	58
	MS	0.8	0.9	1.0	1.1	0.9	0.9	0.7	0.6	0.8	0.9	0.7	0.9	0.8	0.8	0.8	0.8	0.6	1.1	54
	OS	0.8	0.9	0.9	0.9	0.9	0.9	0.7	0.7	0.7	0.9	0.8	1.0	0.8	0.8	0.9	0.8	0.7	1.0	69
Fitzroy	EC	1.9	1.8	2.2	1.8	2.1	1.6	2.0	1.5	1.3	1.1	1.3	1.5	1.4	1.5	1.4	1.7	1.1	2.2	50
	OC	2.7	2.6	2.8	2.6	2.8	2.3	2.3	2.0	1.9	1.9	1.9	2.3	2.2	2.2	2.1	2.2	1.9	2.8	66
	MS	1.0	1.0	1.1	1.0	1.1	1.0	0.8	0.8	0.9	0.9	0.8	1.0	0.9	0.9	0.9	0.9	0.8	1.1	71
	OS	1.0	1.0	1.1	1.1	1.1	1.1	0.9	0.9	1.0	1.1	1.1	1.2	1.1	1.1	1.1	1.0	0.9	1.2	72
Burnett Mary	EC	7.6	7.4	8.2	7.6	8.4	7.3	7.5	5.4	4.6	5.0	4.6	7.0	6.3	6.5	6.1	6.6	4.6	8.4	55
	OC	5.7	5.8	6.5	6.2	6.3	5.8	5.3	4.8	4.2	4.2	4.0	5.7	5.6	5.4	5.0	5.5	4.0	6.5	62
	MS	2.7	2.7	2.9	2.8	2.7	2.7	2.3	2.6	2.8	2.5	2.5	3.0	2.8	2.4	2.5	2.8	2.3	3.0	77
	OS	*0.1*	*0.1*	*0.1*	*0.1*	*0.1*	*0.1*	*0.1*	*0.1*	*0.1*	*0.1*	*0.1*	*0. 1*	*0.1*	*0.1*	*0.1*	*0.1*	*NA*	*NA*	*NA*

The calculated global annual means for each zone also highlighted other differences that might be related to factors other than depth (Table 3.2). The calculated annual global means for each zone reflect an overall latitudinal gradient characterised by declining bPAR values towards the southern portion of the GBR before improving again in the Burnett Mary NRM region. Overall, the highest annual bPAR means across the years and water bodies considered were almost always noted in either the Cape York or Burnett Mary NRM regions (cyan shaded cells in Table 3.2). Specifically, the mid-shelf and offshore waters of the Cape York NRM region consistently showed the highest annual bPAR means with a range of 2.9 to 3.6 mol photons m^{-2} d^{-1} and 2.6 to 3.0 mol photons m^{-2} d^{-1}, respectively, highlighting a very narrow difference between the years with minimum and maximum annual bPAR. The brightest waters in the two inshore water bodies were mostly noted in the Burnett Mary NRM region although from 2010 to 2013, the Cape York enclosed coastal and open coastal water bodies showed on average (across the four years) 14% and 20% higher annual bPAR, respectively. The 2010 to 2011 water year is considered one of the wettest wet seasons on record when nearly all of the rivers along the GBR coastline experienced a degree of flooding and flow conditions above the long-term mean flow likely causing elevated turbidity in the nearshore waters of the GBR lagoon (including the southern GBR along the Burnett Mary region) and decreased bPAR levels during these years. The lowest annual bPAR values in the two inshore coastal water bodies were noted in the Fitzroy NRM region. Relative to the maximum local bPAR per zone, the Fitzroy NRM's enclosed coastal waterbody recorded a 50% lower annual bPAR value in 2012 (i.e., 1.1 mol photons m^{-2} d^{-1} relative to 2.2 mol photons m^{-2} d^{-1} in 2005) whereas the open coastal waterbody recorded 32% lower annual bPAR value in 2011 (i.e., 1.9 mol photons m^{-2} d^{-1} compared to 2.8 mol photons m^{-2} d^{-1} in 2007). In the mid-shelf and offshore water bodies, the lowest annual bPAR values (grey shaded cells in Table 3.2) were consistently noted for the Mackay Whitsunday NRM region although the annual values calculated in the Fitzroy NRM region were also comparably low. The range for the Mackay Whitsunday and Fitzroy NRM regions mid-shelf waterbody (i.e., 0.6 to 1.1 mol photons m^{-2} d^{-1} and 0.8 to 1.1 mol photons m^{-2} d^{-1}, respectively) were comparable but indicated about 25% lower annual value in the Mackay Whitsunday region in 2010 when the lowest annual value occurred. In most years, the annual bPAR for the Fitzroy mid-shelf waterbody were either equally lowest or within ~3% of the lowest values obtained for Mackay Whitsunday NRM, highlighting that these two southern NRM regions consistently had poor bPAR levels compared to the three other NRM regions in the north or relative to Burnett Mary NRM region. Note that the offshore waterbody of the deep Burnett Mary, which showed an annual mean bPAR of 0.1 mol photons m^{-2} d^{-1} throughout the time series, were not considered in determining the lowest annual bPAR to highlight low bPAR pattern that is not wholly due to deep water. The global annual bPAR means for the Wet and Dry Tropics NRM regions showed values that were generally intermediate relative to the extremes discussed. However, in some years (e.g., 2004 to 2006, 2008, and 2014 to 2017), annual bPAR means in the Wet Tropics mid-shelf waterbody were marginally higher than the Cape

York NRM region or is within ~3% of the Cape York region's maximum annual bPAR mean, highlighting some historical 'bright' years in this tropical water body. The Wet and Dry Tropics NRMs are the two tropical regions that receive large amount of discharge from nearby catchments. The years where the annual bPAR means in Wet Tropics were comparably high as that of the Cape York region may be related to decline in river flow and thus, input loads that allowed more light penetration and higher annual bPAR estimates in this zone.

3.6.1.3 Seasonal climatology

Strong seasonal differences in bPAR were highlighted in the maps (Figure 3.4) and the global means calculated for the whole GBR and the different zones (Table 3.3 and Figure 3.5). Strong spatial gradients in seasonally aggregated bPAR values varied particularly from ~18°S to 23°S. The time series (Figure 3.4b) for some selected pixels (see locations indicated on the fourth map of Figure 3.4a) clearly demonstrated this seasonal and spatial variability. The selected locations were distributed across the shelf and included the four optically diverse sites used for the benthic irradiance model validation (Section 2): the Palm Passage (PPS) and Myrmidon (MYR) which are deep, clear oceanic stations; the seasonally turbid, inshore water-influenced mid-shelf station in Yongala (YON); and the clear mid-shelf station in south Heron Island (HER). Within sample locations, the inter-seasonal differences in percent (calculated as the difference between the maximum and minimum values between seasons) ranged from 8% (MYR) to almost 500% (pixel location 3). These differences and strong fluctuations in bPAR values were also evident between locations during each austral season further highlighting the abovementioned spatial gradient.

The seasonal global means obtained for the whole GBR and the individual water bodies offered the same overview of the inter-seasonal variability of bPAR values on the shelf. In addition, Figure 3.5a also highlighted the latitudinal and cross-shelf gradients such that clear historical (seasonal) decreases in bPAR were evident especially on the mid-shelf waterbody of the two southern NRM regions, Mackay Whitsunday and Fitzroy, although the latter has a marginally higher bPAR values (Table 3.3).

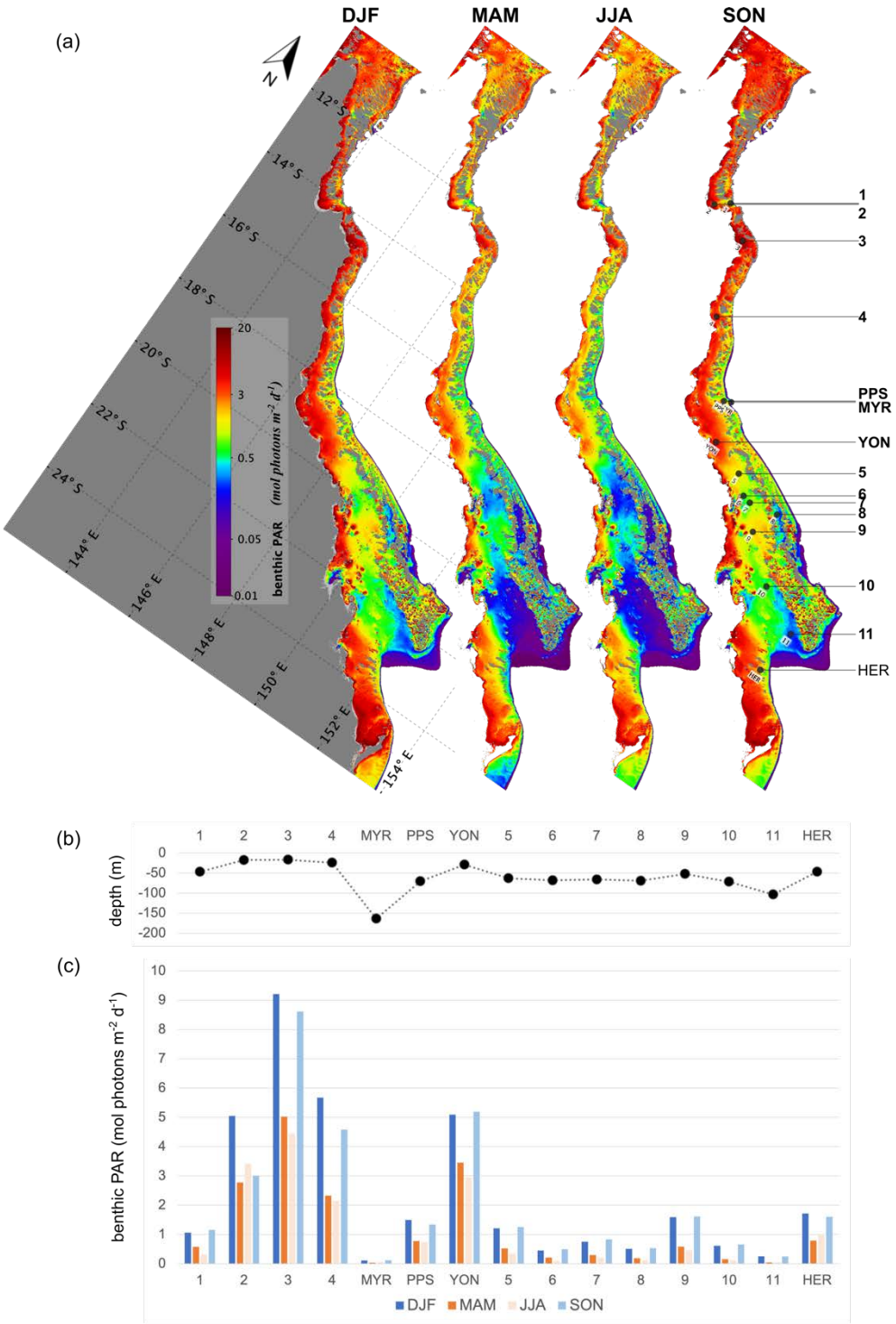

Figure 3.4. Long-term seasonal means of bPAR in the Great Barrier Reef. (a) spatial maps of four long-term seasonal means; and (b) depth in metres and (c) bar plot time series for some selected locations indicated in (a) including the model validation test sites: YON – Yongala, MYR – Myrmidon, PPS – Palm Passage and HER – Heron Island. Note that the maps were rotated (by 35°) to facilitate visualisation. Also indicated are land pixels (dark grey) and locations with depth ≤ 5 m (light grey) on the first map while reef pixels (dark grey) on all maps. The colour gradient indicates bPAR displayed as logarithmic values on the spatial maps. Abbreviations in (c) indicate the first letter of months in each seasonal group (e.g., DJF – December, January, and February, and so on).

Table 3.3. Long term seasonal mean bPAR values for the whole Great Barrier Reef, the 24 zones, and the north to south length of the GBR per waterbody for the full dataset spanning July 2002 to December 2018. Shaded cells indicate the maximum (cyan) and minimum (grey) bPAR for each zone and season, the latter excluding the offshore Burnett Mary NRM (last row). Abbreviations are EC – Enclosed Coastal; OC – Open Coastal; MS – Mid-shelf; OS – Offshore.

Region	Waterbody	DJF	MAM	JJA	SON
Whole GBR		**2.7**	**1.5**	**1.4**	**2.5**
Whole GBR: length North to South	EC	7.2	3.7	3.2	5.5
	OC	5.5	3.0	2.7	4.6
	MS	2.6	1.4	1.3	2.4
	OS	1.8	1.0	1.0	1.7
Cape York	EC	9.4	4.5	4.5	7.4
	OC	8.7	4.2	4.4	6.9
	MS	4.5	2.4	2.3	4.2
	OS	3.2	2.4	2.3	3.5
Wet Tropics	EC	6.4	3.2	2.7	4.8
	OC	7.9	3.6	3.6	5.8
	MS	4.4	2.3	1.9	3.8
	OS	2.1	1.3	1.0	2.1
Dry Tropics	EC	6.9	3.6	2.8	4.1
	OC	6.1	3.3	2.9	4.6
	MS	3.2	1.9	1.5	3.1
	OS	1.6	0.9	0.8	1.5
Mackay Whitsunday	EC	8.4	4.2	2.8	6.7
	OC	4.7	2.6	2.1	4.0
	MS	1.3	0.6	0.4	1.3
	OS	1.2	0.6	0.5	1.2
Fitzroy	EC	2.3	1.7	1.1	2.0
	OC	3.1	2.1	1.5	3.0
	MS	1.4	0.7	0.6	1.4
	OS	1.6	0.7	0.8	1.4
Burnett Mary	EC	8.6	6.5	4.5	8.3
	OC	6.9	4.8	4.0	6.9
	MS	3.8	1.9	2.3	3.4
	OS	*0.2*	*0.0*	*0.1*	*0.1*

3.6.1.4 Monthly climatological composites

The monthly climatological means revealed additional details of the spatio-temporal variability of bPAR within the GBR. The spatial maps shown in Figure 3.6 also highlighted the strong spatial gradient but with clear differences between months. Overall, the long-term pattern includes relatively higher values between September to February and much lower values (with gradual temporal decrease) beginning March to August. The May, June, and July monthly climatologies showed the lowest benthic light intensities in some locations (e.g., the coverage of the "dark pixels" (blue to deep purple colours) were noticeably more extensive, particularly at the widest portion of the shelf along the central to southern GBR). The inshore coastal locations during these months also notably have lower long-term benthic light values compared to other months.

The global means of the monthly climatologies presented in Table 3.4, as well as the additional visualisation of the same global means shown in Figure 3.7, provided overviews of the monthly long-term patterns of bPAR at the whole GBR extent and at each zone. The whole GBR global means reflected the mesoscale regional pattern in bPAR related to the expected amount of solar radiation received at the surface during each month. That is, the long-term mean value for December (3.03 mol photons m^{-2} d^{-1}) is about 40% higher than that for June (1.16 mol photons m^{-2} d^{-1}).

The whole-GBR long-term monthly means calculated for each waterbody (rows 2 to 5 in Table 3.4) showed about the same difference between the highest and lowest long-term monthly mean values (i.e., varying at 36%, 38%, 35% and 43%, respectively at each waterbody from the most inshore). However, the minimum values were noted one month earlier (i.e., May) for the two inshore coastal water bodies and a month later (i.e., June) for the mid-shelf and offshore water bodies. May and June mark the beginning of the austral dry season and are typically associated with the cessation of river discharges. The timing of the minimum long-term monthly mean bPAR value suggests that the impacts of the preceding wet season-derived materials extend well into winter dry season months, depending on the distance from the coast (i.e., May for the two coastal water bodies, and up to June for the mid-shelf and offshore water bodies, noting that the values between these two months do not differ very much in these water bodies, except for the enclosed water body). Fabricius et al. (2016) indeed showed that poor water clarity in the GBR waters can extend 4-8 months after a major flood event.

Differences between the NRMs were also detected (Figure 3.7a, Table 3.4). The lowest long-term monthly mean values for the two inshore coastal water bodies were consistently noted in the Fitzroy NRM region while the lowest long term mean values for the offshore water bodies were consistently noted in the Mackay Whitsunday NRM region (note that in determining the months with the minimum values for the offshore water body, values obtained on the Burnett Mary NRM were ignored since this zone has largely deep water pixels and hence expected to have very low mean bPAR values nonetheless). The Mackay Whitsunday NRM region also showed the lowest monthly long-term bPAR values on the mid-shelf waterbody except in November and December months when lower values (but only marginally) were obtained in the Fitzroy NRM region.

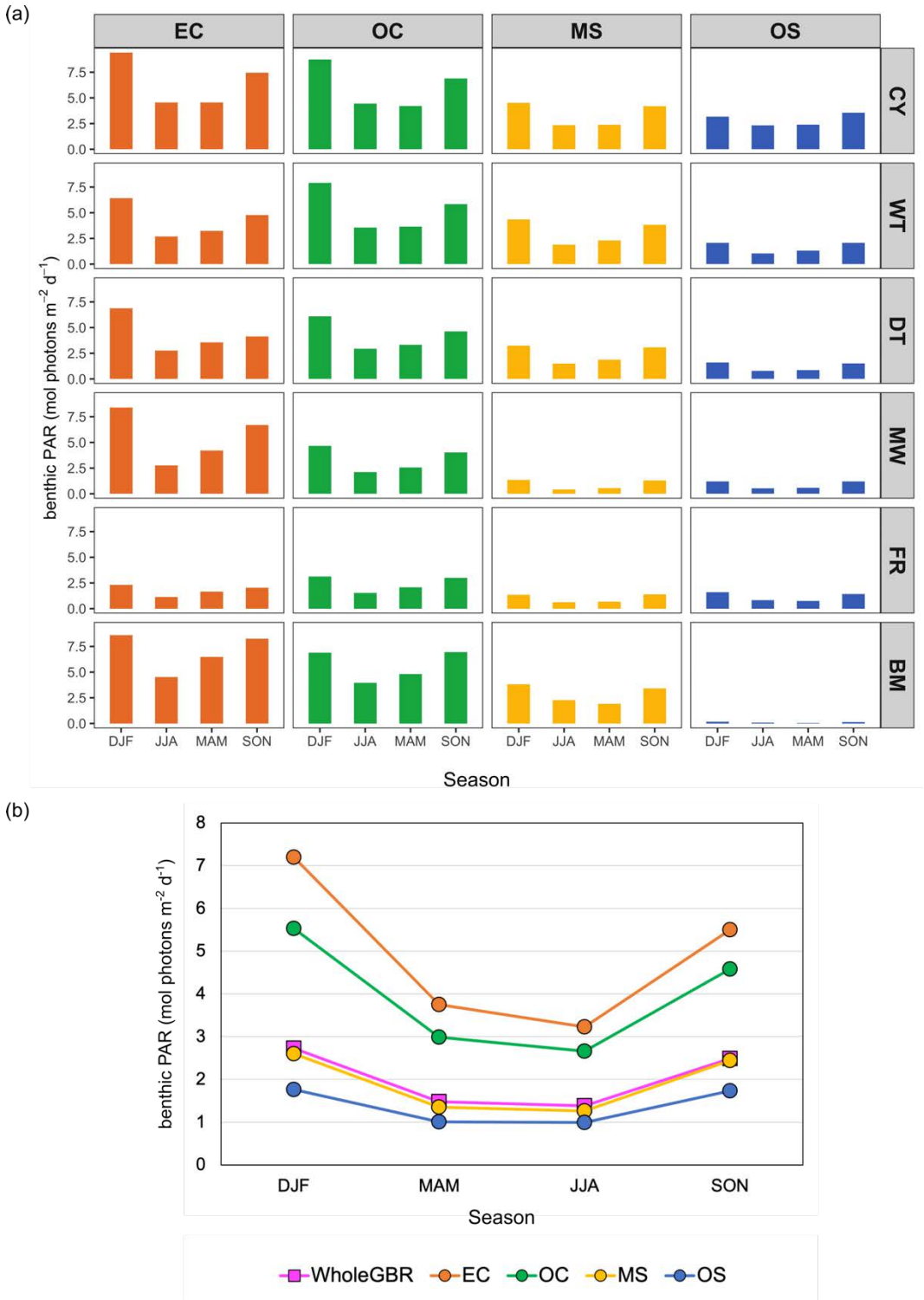

Figure 3.5. Seasonal long term mean bPAR for (a) each zone (NRM region + water body) and (b) the whole GBR (entire shelf and per waterbody) showing inter-seasonal differences and overall spatial (shelf) variability due to seasons. These means were calculated as a single averaged value for all valid pixels within a zone using the full 16.5 years dataset spanning from July 2002 to December 2018. Abbreviations in both are for the four water body boundaries: EC – enclosed coastal, OC – open coastal, MS – mid-shelf, and OS – offshore; and NRM regions: CY – Cape York, WT – Wet Tropics, D T – Dry Tropics, MW – Mackay Whitsunday, FR – Fitzroy, BM – Burnett Mary. Horizontal axes labels indicate month names (e.g., DJF – December, January, February, and so on).

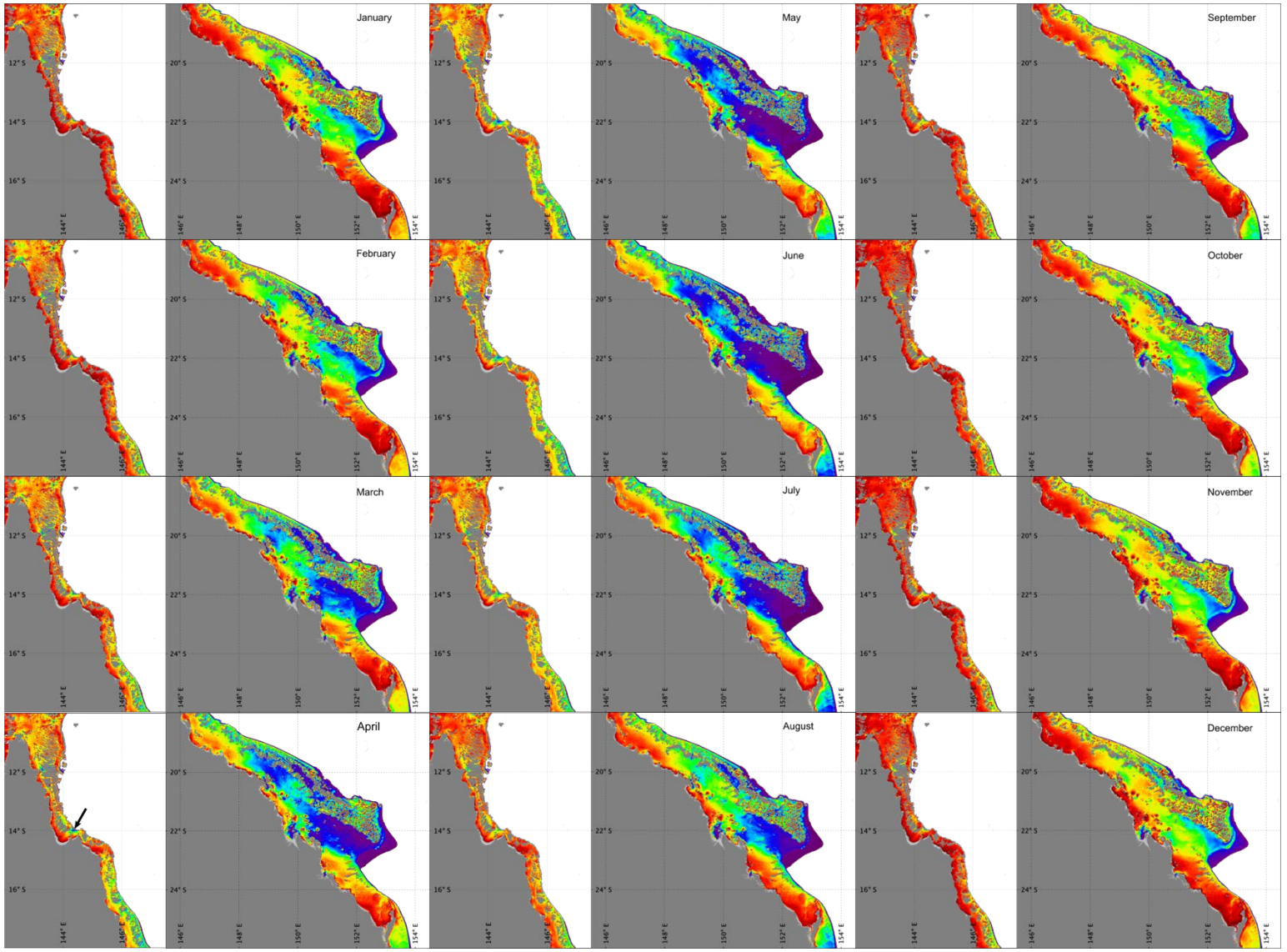

Figure 3.6. Map of the monthly mean climatology of benthic PAR within the GBR encompassing July 2002 to December 2018. For each month, the left image of the pair shows the northern GBR section (limits: 10 to 18°S and 142 to 147.5°E) while the right image shows the southern GBR section (limits: 18 to 26°S and 145.5 to 154.5°E), partitioned to facilitate visualisation. Land or reef pixels (dark grey) and locations with depth ≤ 5 m (light grey) are also indicated. Colour gradient indicates benthic PAR displayed as logarithmic values as in Figure 3.2.

Table 3.4. Long-term monthly mean bPAR values (on cloud-free days) for the whole Great Barrier Reef (GBR), the 24 zones (Region + Waterbody combination), and the north to south length of the GBR per waterbody for the full dataset spanning July 2002 to December 2018. Shaded cells indicate the maximum (cyan) and minimum (grey) bPAR for the zone and month (except the whole GBR cases). As per Table 3.2, values for the offshore waterbody of the Burnett Mary NRM region (last row) were excluded in identifying minimum bPAR values in each month. Abbreviations are for the four waterbody boundaries: EC – enclosed coastal, OC – open coastal, MS – mid-shelf, and OS – offshore.

Region	Waterbody	J	F	M	A	M	J	J	A	S	O	N	D
Whole GBR		**2.7**	**2.3**	**1.7**	**1.4**	**1.2**	**1.2**	**1.4**	**1.8**	**2.3**	**2.5**	**2.8**	**3.0**
Whole GBR: length North to South	EC	7.1	5.6	3.9	3.1	3.0	3.4	3.5	4.3	4.6	5.3	7.2	8.4
	OC	5.6	4.5	3.3	2.6	2.4	2.4	2.8	3.6	4.2	4.5	5.4	6.2
	MS	2.6	2.2	1.6	1.3	1.0	1.0	1.2	1.7	2.3	2.5	2.7	2.9
	OS	1.8	1.5	1.2	1.0	0.9	0.8	0.9	1.2	1.6	1.8	1.9	1.9
Cape York	EC	9.3	8.3	6.0	4.6	3.9	4.1	4.1	5.3	6.2	7.5	9.1	10.2
	OC	8.9	8.1	6.1	4.5	3.7	3.7	3.9	4.9	6.0	7.0	8.0	9.1
	MS	4.4	4.1	3.1	2.3	2.0	2.0	2.2	2.9	3.7	4.4	4.6	4.9
	OS	3.0	2.9	2.4	2.3	2.2	2.1	2.3	2.8	3.4	3.7	3.6	3.5
Wet Tropics	EC	6.0	4.8	3.1	2.4	2.6	2.9	3.0	3.6	4.0	4.6	6.4	7.7
	OC	7.5	6.6	4.7	3.3	3.1	3.0	3.3	4.4	5.2	5.6	7.4	9.0
	MS	4.3	3.7	2.7	1.7	1.6	1.6	2.1	3.0	3.6	3.7	4.4	4.9
	OS	2.1	1.8	1.4	1.0	0.9	0.9	1.2	1.6	2.0	2.0	2.2	2.3
Dry Tropics	EC	7.2	4.2	3.1	2.3	3.0	3.7	3.7	3.3	3.0	3.4	6.4	8.6
	OC	6.3	4.5	3.6	2.8	2.7	2.7	3.2	3.9	4.2	4.3	5.8	7.2
	MS	3.3	2.6	1.9	1.4	1.3	1.3	1.8	2.4	2.9	3.0	3.4	3.7
	OS	1.6	1.3	1.0	0.8	0.7	0.7	0.8	1.1	1.4	1.5	1.7	1.8
Mackay Whitsunday	EC	7.4	5.6	3.1	2.5	2.7	2.9	3.8	5.5	5.6	6.3	9.1	11.2
	OC	4.7	3.6	2.6	2.1	1.9	2.0	2.4	3.1	3.7	3.9	4.7	5.4
	MS	1.3	1.0	0.6	0.4	0.3	0.3	0.5	0.8	1.2	1.3	1.5	1.6
	OS	1.2	1.0	0.7	0.5	0.5	0.4	0.5	0.8	1.1	1.2	1.4	1.4
Fitzroy	EC	2.3	1.4	1.3	1.1	1.1	1.3	1.5	2.0	1.8	2.1	2.5	2.6
	OC	3.2	2.3	1.7	1.5	1.5	1.6	2.0	2.5	2.9	2.8	3.3	3.7
	MS	1.3	1.1	0.8	0.6	0.5	0.5	0.6	0.9	1.3	1.4	1.5	1.6
	OS	1.7	1.4	1.1	0.9	0.7	0.6	0.7	0.9	1.2	1.5	1.7	1.7
Burnett Mary	EC	8.4	5.7	3.6	4.6	5.0	5.0	6.3	7.7	7.6	7.7	10.5	10.9
	OC	7.1	5.4	4.0	4.0	3.9	3.7	4.6	5.9	6.7	6.7	7.7	8.0
	MS	4.0	3.6	2.8	2.3	1.8	1.5	1.7	2.4	3.1	3.5	3.8	3.9
	OS	*0.2*	*0.2*	*0.1*	*0.1*	*0.1*	*0.0*	*0.0*	*0.1*	*0.1*	*0.1*	*0.2*	*0.2*

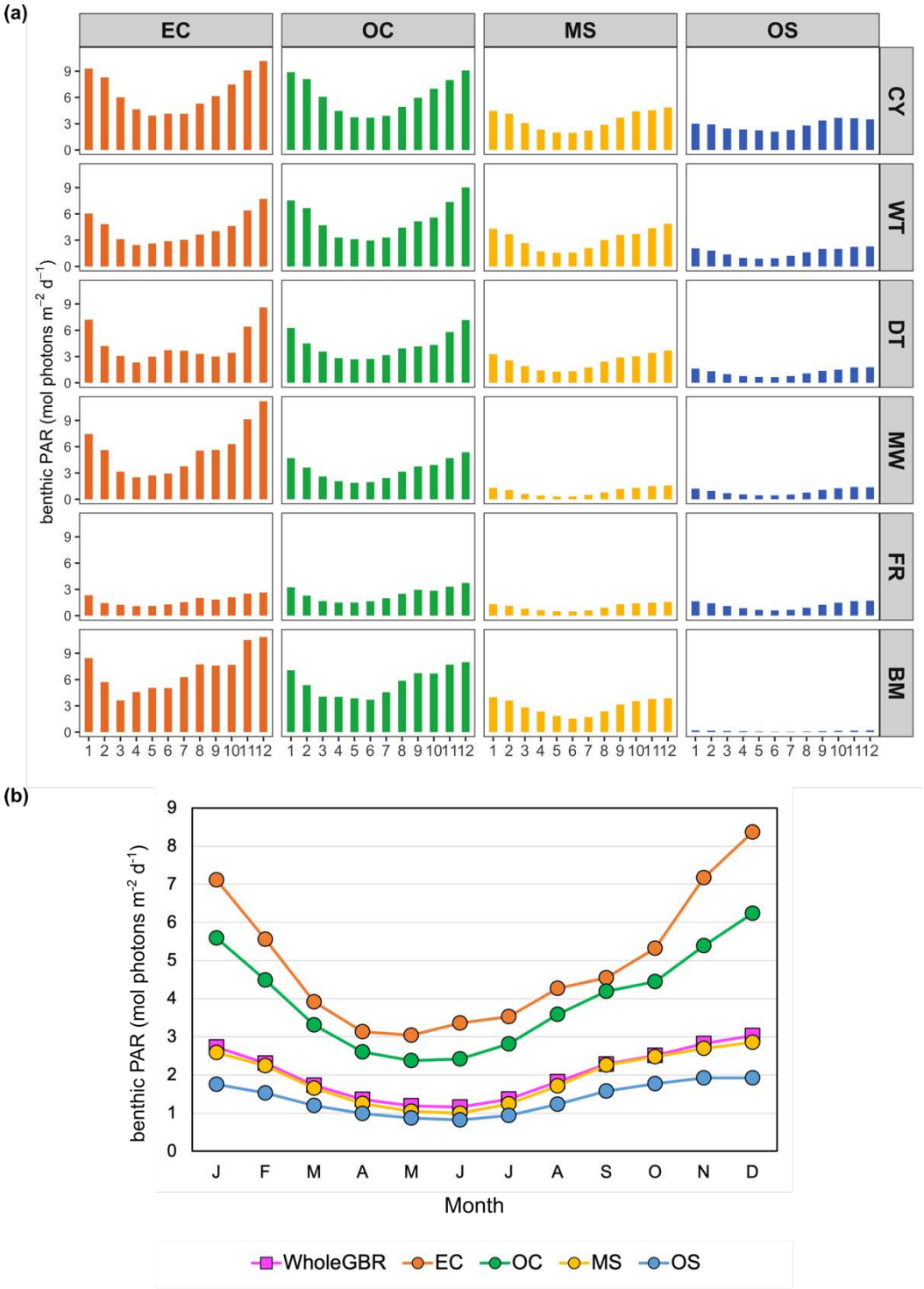

Figure 3.7. Long term monthly mean bPAR values for the (a) different zones (NRM region + water body) and (b) whole GBR (entire shelf and per waterbody) showing strong seasonality and overall spatial variability. These means were calculated using the full 16.5 years dataset spanning from July 2002 to December 2018. Abbreviations in both figures are for the four waterbody boundaries: EC – enclosed coastal, OC – open coastal, MS – mid-shelf, and OS – offshore; NRM regions: CY – Cape York, WT – Wet Tropics, D T – Dry Tropics, MW – Mackay Whitsunday, FR – Fitzroy, BM – Burnett Mary.

3.6.2 Quantifying spatial and temporal patterns of variability in bPAR

3.6.2.1 Hovmöller diagrams

Hovmöller diagrams were used to examine the evolution and spatio-temporal variability of bPAR over the GBR. Figure 3.8 shows monthly mean values for latitudinal bands averaged over (a) the whole shelf; (b) the inshore region, including both the enclosed coastal and open coastal water bodies defined earlier; (c) the mid-shelf; and (d) the offshore regions. Gaps (e.g., white holes) in the diagrams indicate locations with data that were masked or ignored either due to the bathymetry-based mask (excluding land and reef pixels) or the quality control procedure described in Section 3.3 (i.e., when any of the Level 2 quality flags were detected on the pixel).

The Hovmöller diagrams clearly show the temporal evolution of benthic light values across the GBR over the last 16.5 years. Overall, the diagrams highlighted three prominent features that can be summarised as: (i) distinct north to south differences, (ii) distinct horizontal and vertical structures ('events'), and (iii) pronounced horizontal cyclical features. All four diagrams showed that bands of high bPAR values were more apparent in low latitude areas (i.e., in the north) and account for most of the latitudinal variance in bPAR within the GBR. For example, locations between 14 to 15°S revealed substantially higher bPAR (e.g., range: 0.4 to 11.4 mol photons m^{-2} d^{-1}, mean: 4.8 mol photons m^{-2} d^{-1}, median: 4.5 mol photons m^{-2} d^{-1}) across the study period as opposed to locations further south at 19.5 to 20.5°S (e.g., range: 0.1 to 3.1 mol photons m^{-2} d^{-1}, mean: 1.2 mol photons m^{-2} d^{-1}, median: 1.1 mol photons m^{-2} d^{-1}) or at 22 to 23°S (e.g., range: 0.0 to 3.0 mol photons m^{-2} d^{-1}, mean: 0.7 mol photons m^{-2} d^{-1}, median: 0.6 mol photons m^{-2} d^{-1}) latitudes across the whole shelf (Figure 3.8a). The diagrams for the inshore, mid-shelf and offshore water bodies also effectively highlighted the cross-shelf gradient characterised by generally lower bPAR on the offshore relative to inshore areas at similar latitudes.

The diagrams also revealed some interesting features beyond those shown by the global means or temporally aggregated averages in the previous section. Distinct horizontal bands, the width of which potentially indicate the duration and extent of an 'event' throughout the available time series, differed strongly between years. The temporal oscillation (via alternating bands of low and high bPAR along the horizontal axis) highlighted the seasonal behaviour of bPAR with markedly higher values during austral spring and summer than in austral autumn and winter. In some years, the width of the lower-bPAR (blue to purple) bands was expanded, for example between latitudes 15°S and 19.5°S (Figure 3.8c), particularly during the beginning of the 2010 austral wet season to almost the latter part of 2011. This specific progression was an indication of the strong response of light availability to a major flood event (or to the storm event that produced this flood) during this period.

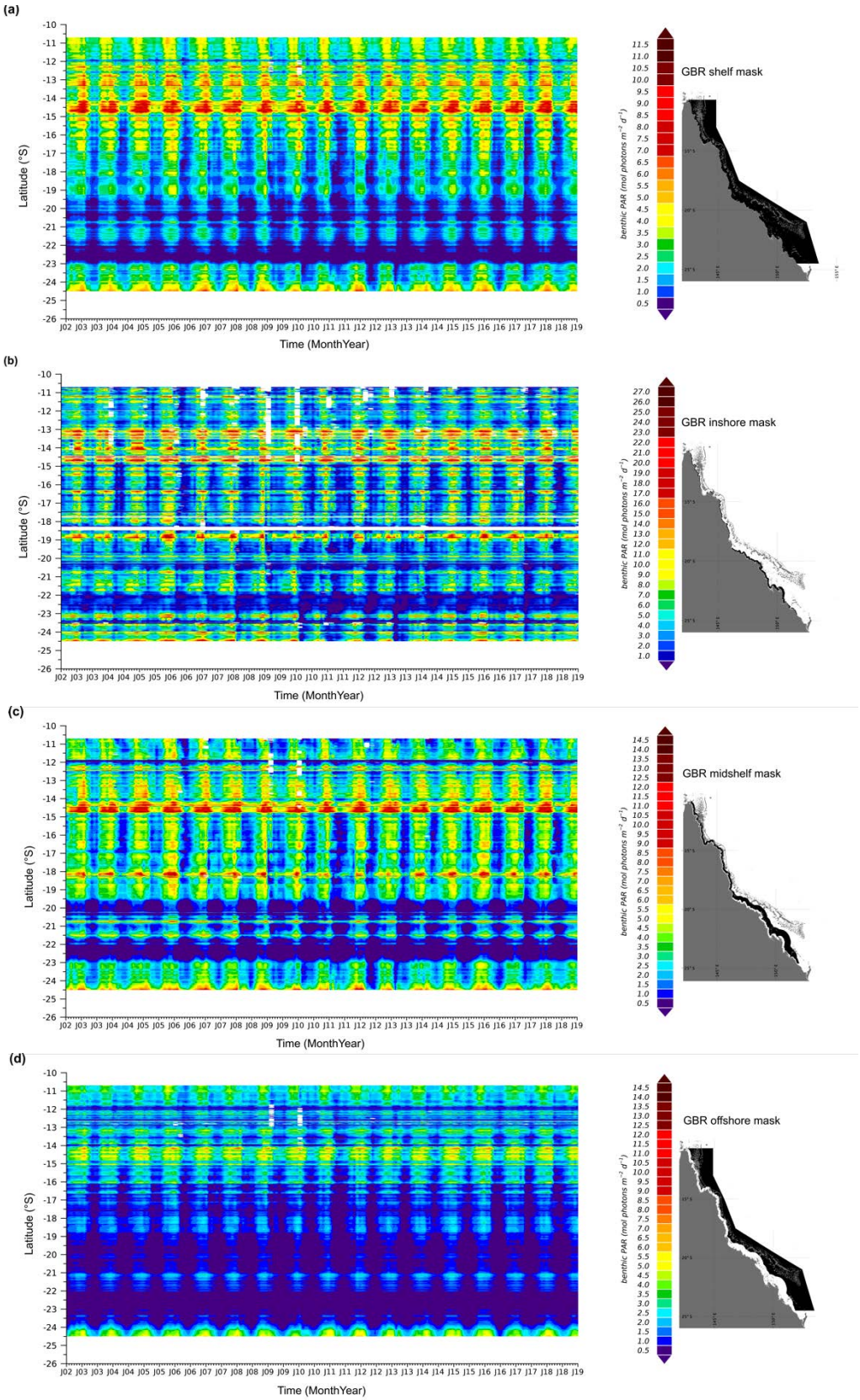

Figure 3.8. Time versus latitude Hovmöller diagrams of monthly bPAR from July 2002 to December 2018 for the (a) whole shelf, and the (b) inshore (c) mid-shelf, and (d) offshore water bodies. Each column in these diagrams represents the monthly mean bPAR. Gaps indicate missing data either due to the L2 quality flag applied during satellite data processing or due to bathymetry masking. Note different scales for each diagram.

3.6.2.2 Empirical orthogonal function (EOF) analysis of monthly bPAR

The EOF analysis of monthly bPAR data showed that the first dominant mode contained 56.5% of the variance with a spatially homogenous pattern across the GBR shelf (Figure 3.9a). The associated principal components of Mode 1 (Figure 3.9c) indicated a regular pattern of fluctuations in time that repeats over a period of several months suggesting that the variance captured in Mode 1 is due to seasonal variability related to the overall solar radiation received at the surface. In EOF analysis, the product of the spatial eigenfunction and the principal component reconstructs the full pattern (e.g., correct polarity and the variance) captured by each mode (Deser et al., 2010). As expected, due to differences in day length, bPAR was higher during austral spring to austral summer months and lower during austral autumn to austral winter months. Both positive spatial eigenfunctions and positive principal components for all the months from September 2002 to February 2003, for example, denote positive product and thus high bPAR values. Similarly, positive spatial eigenfunction values and negative principal components for the months of March to July 2003, for example, denote negative product, thus low bPAR values (Figure 3.9a and Figure 3.9c). Interestingly, the temporal pattern depicted in Mode 1 also showed an overall trend (blue solid line in Figure 3.9c) that was relatively lower from around the period 2008 to 2013 but suggested recovering bPAR towards the latter part of the study period.

The second mode, which showed a pattern separate from the seasonal variability, contained 6.2% of the variance. Mode 2 showed a spatial structure that is out of phase between some locations (red coloured pixels vs. blue coloured pixels in Figure 3.9b), suggesting a process (or processes) that affects these locations differently. The principal components for Mode 2 (Figure 3.9d) showed that there was also some seasonal variability associated with the out of phase spatial structure which indicated lower bPAR over most of the shelf and the Cape York region in the north (red coloured pixels in Figure 3.9b) during austral summer months that persists between 4 to 6 months. In contrast, during the same period, higher bPAR values were instead noted in locations along the edge of the shelf, in the vicinity of the Swains and the Capricorn Channel at the southern portion of the study region, and on the inner shelf of PCB (blue coloured pixels in Figure 3.9b).

The patterns revealed by Mode 2 may be related to physical processes within the GBR shelf. The lower bPAR values continuing from the austral summer months may indicate the impact of seasonal runoff from the numerous rivers with catchments that drain into the Reef resulting in elevated turbidity, whereas the higher bPAR values along the shelf edge (and other locations previously discussed) may be a direct consequence of mesoscale oceanographic processes on the GBR, particularly along the eastern seaboard. Along the southern half of the GBR, the EAC is known to intensify and flow poleward close to the continental slope with speeds greater than 50 cm s^{-1} (Choukroun et al., 2010) during austral spring and summer months, setting the connectivity of the GBR shelf waters to the clear oligotrophic water mass of the southern Pacific. The spatial distribution of the negative spatial eigenfunctions in

Figure 3.9b clearly coincides with locations along the path of the EAC. The similar pattern observed in the vicinity of the PCB (location indicated in Figure 3.9a) is of another feature of interest although the oceanographic mechanism is different and may be due to oceanic inflow generated by southeast trade winds (Wolanski and Lambrechts, 2020) flowing from the narrow channel further south of the PCB and potentially affords the closest connectivity between the Cape York region (in the far north GBR) and the rest of the GBR (in the south).

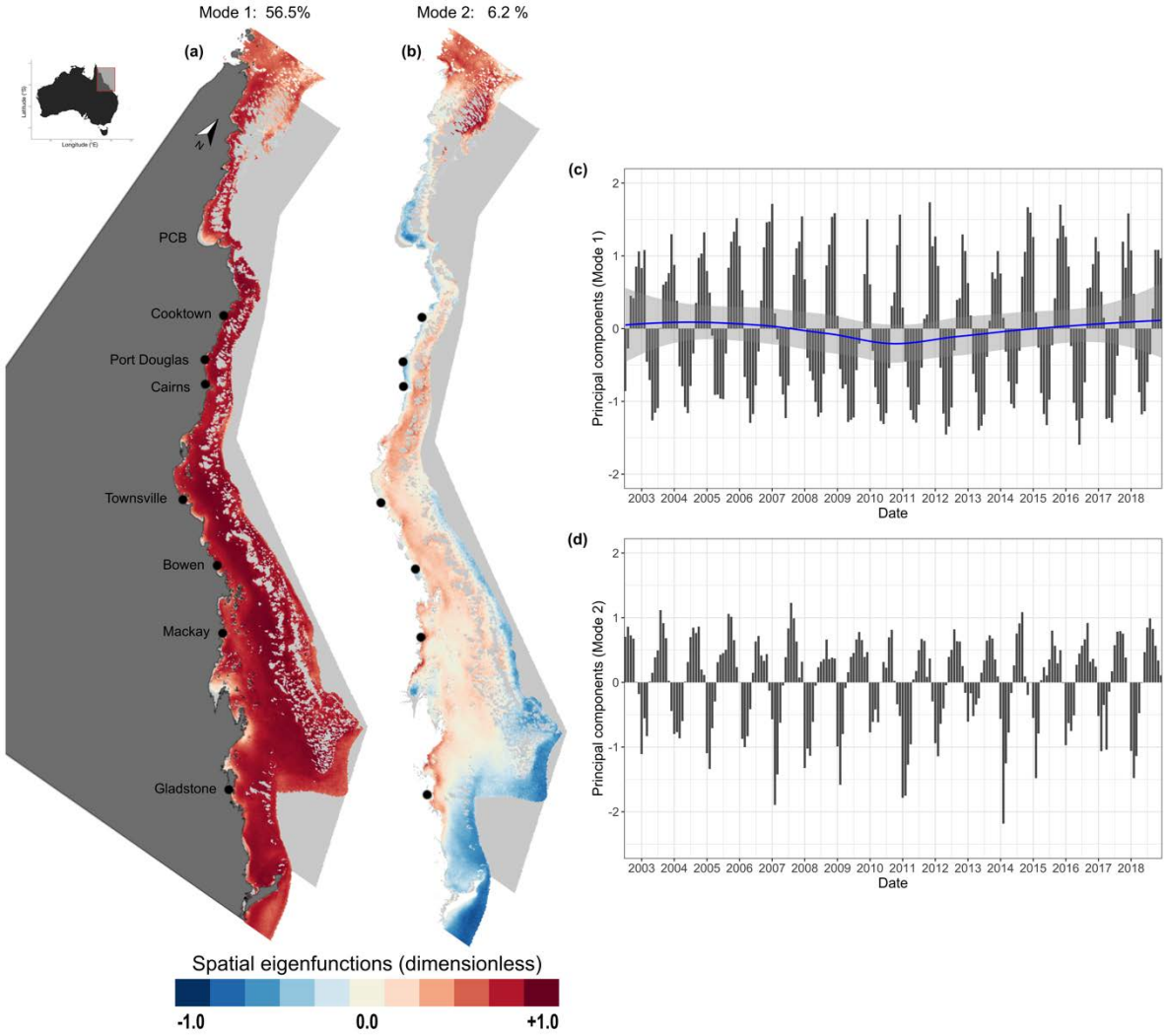

Figure 3.9. Empirical orthogonal function (EOF) analysis of the monthly bPAR variability for the whole GBR shelf region. Shown are the results for the two most dominant modes that contained 62.7% of the variance of the dataset. (a, b) Spatial Eigenfunctions of Mode 1 and Mode 2 and (c, d) the Principal Components of Mode 1 and Mode 2 showing the temporal variation of the corresponding spatial features. Blue solid line in (c) denotes the mean trend in monthly bPAR detected for Mode 1 with the 95% confidence interval (shaded area in grey). Note different scales in vertical axes in (c) and (d).

3.6.2.3 Standard deviations

The full climatology σ distribution (Figure 3.10) highlighted a strong spatial gradient whereby the variability in the satellite-derived bPAR values was generally higher at inshore locations and decreases towards the offshore. Maximum values of the bPAR standard deviations at inshore locations exceeded 3 mol photons m^{-2} d^{-1} while most of the offshore locations showed standard deviation values between 0 to 1 mol photons m^{-2} d^{-1}.

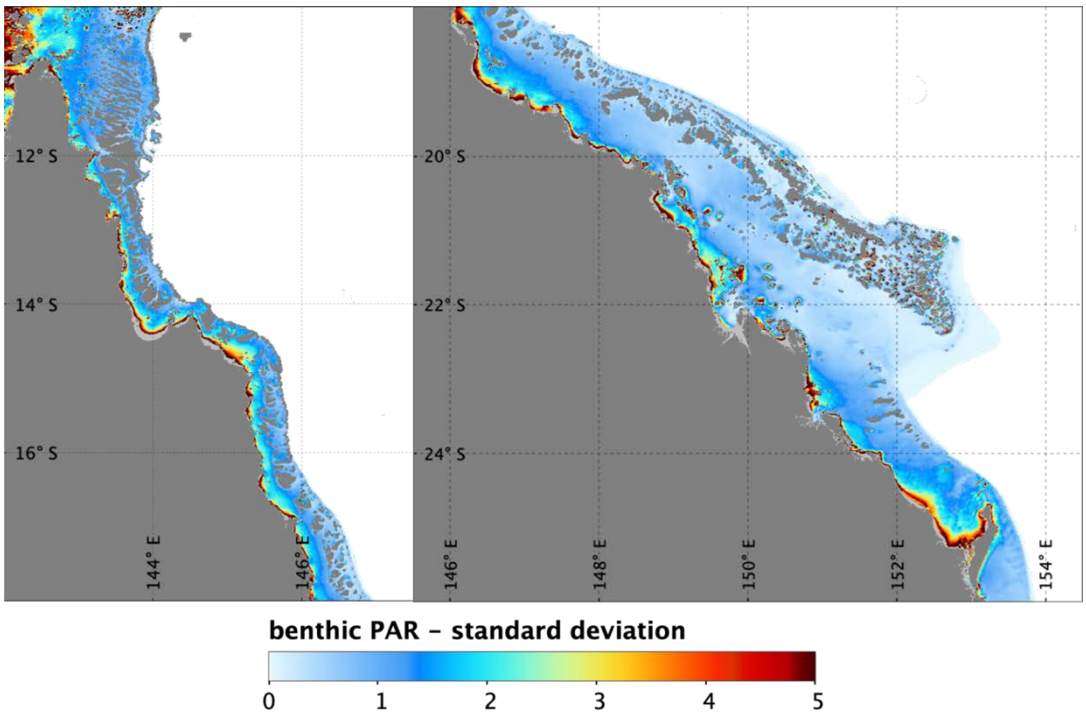

Figure 3.10. Map of the 16.5-year (July 2002 to December 2018) climatological standard deviation of bPAR within the GBR. Left image: northern section with limits 10 to 18°S and 142 to 147.5°E. Right image: southern section with limits 18 to 26°S and 145.5 to 154.5°E. Dark grey areas are either land or reef pixels while light grey areas indicate locations with depth less than or equal to 5 m. Colour gradients indicate standard deviation values.

The global mean σ values for the whole GBR and the different zones indicated the strong variability in the bPAR (Table 3.5). The standard deviations obtained for the whole GBR showed seven times higher variability in the enclosed coastal compared to the offshore waterbody (i.e., 4.0 mol photons m^{-2} d^{-1} vs. 0.6 mol photons m^{-2} d^{-1}, respectively). Between NRM regions, the overall cross-shelf gradient also showed decreasing standard deviation values toward the offshore locations while depending on the distance from the coast, north-south gradient showed higher climatological standard deviation values in the central GBR NRM regions (for inshore water bodies) and lower latitude NRM regions for the mid-shelf and offshore water bodies. The Fitzroy NRM region consistently showed the overall lowest standard deviation values across all water bodies although the Mackay Whitsunday mid-shelf and offshore water bodies were also comparably low.

Table 3.5. Climatological (16.5 years) standard deviation of bPAR and coefficient of variation (in percent, calculated as the ratio of the standard deviation to the mean) for the whole Great Barrier Reef (GBR) and the 24 zones (Region + Waterbody combination). Abbreviations in (b) are for the four waterbody boundaries: EC – enclosed coastal, OC – open coastal, MS – mid-shelf, OS – offshore, and AWB – across water bodies.

Region	Standard deviation (mol photons m^{-2} d^{-1})					Coefficient of variation (%)				
	EC	OC	MS	OS	AWB	EC	OC	MS	OS	AWB
Whole GBR	4.0	2.0	0.7	0.6	1.8	89	55	40	43	65
Cape York	4.0	2.4	1.2	0.9	2.1	68	42	38	32	48
Wet Tropics	4.0	2.9	1.2	0.7	2.2	103	60	40	41	66
Dry Tropics	4.6	2.2	0.8	0.5	2.0	115	56	35	39	72
Mackay Whitsunday	4.8	1.9	0.5	0.5	1.9	96	60	60	58	76
Fitzroy	2.8	1.5	0.5	0.5	1.3	164	66	46	48	88
Burnett Mary	5.2	2.6	0.8	0.1	2.2	77	47	30	66	58

The climatological monthly standard deviation was also calculated as the averaged standard deviation at each pixel location for each month during the entire 16.5 years and is presented as categorised maps (Figure 3.11). Warm (red) colours indicate higher standard deviations (or higher variability) while cool (blue) colours represent values that are relatively stable or close to the mean bPAR value (thus, lower variability) at a location during the period covered by the entire bPAR dataset. For ease of comparison and discussion, global means of climatological monthly standard deviation were also shown in Table 3.6.

The categorised maps (Figure 3.11) and the corresponding global means of climatological monthly standard deviation (Table 3.6) revealed additional spatial and temporal details into the variability of bPAR. Figure 3.11 highlighted standard deviations of > 2 mol photons m^{-2} d^{-1} outlining the coastline along the length of the GBR with offshore/cross-shelf extension (i.e., defining the width of the band) that varies between each month, and hence seasonally. The width of these bands also indicated the amount of variability. Stronger variability was apparent for months coinciding with the austral wet season (November to April) and perhaps also during the two preceding months (September and October which mark the end of austral dry season). Along the central GBR (latitudes between 16°S to 20°S) in particular, moderate standard deviation values between 1 and 2 mol photons m^{-2} d^{-1} were also noted on the mid-shelf location and similarly coincided with the austral wet season months. Similar patterns of variability were also noted for the southern GBR region (latitudes between 16°S to 20°S). Nonetheless, still much of the study region showed <1 mol photons m^{-2} d^{-1} standard deviation values (e.g., pixels at offshore deep locations).

During the austral summer, the enclosed coastal regions in the Burnett Mary NRM region showed the highest standard deviation values eight out of 12 months (i.e., 67% of the time), while during the austral winter months of June and July the Dry Tropics showed the highest standard deviation values (Table 3.6). For the open coastal region, the highest standard deviations were noted in the Wet Tropics almost

consistently across all 12 months except January. For the mid-shelf, the standard deviations were highest for the Cape York Region except for the months of January to March where the highest values were noted in the adjacent south NRM region, the Wet Tropics. In the offshore, the Cape York NRM region recorded the highest standard deviation values across all 12 months. Meanwhile, the lowest standard deviations in bPAR across the 12 months were consistently noted in the Fitzroy NRM for the two inshore water bodies, in the Burnett Mary NRM for the offshore waterbody , and in the Fitzroy and Mackay Whitsunday NRM regions for the mid-shelf waterbody .

While standard deviation provided a clear measure of bPAR variability, the overall results obtained also highlighted that the bPAR 16.5-year means vary greatly within the large spatial extent and complex physical setting of the GBR. Hence, the coefficient of variation (CV) which indicates the relative dispersion of the data around the mean was also calculated as the ratio of the standard deviation to the mean expressed in percent. CV was therefore also used as a measure of bPAR variability at each zone. Table 3.5 includes the corresponding CV for the 16.5-year climatology (also graphically presented in Figure 3.12) while Figure 3.13 shows the CV for the monthly climatology (with the corresponding table of values provided in the thesis Appendix 7.2 section).

The CV values underscored the strong variability of bPAR especially in the enclosed coastal waterbody across all NRM regions, both in the 16.5-year climatology (Figure 3.12) and monthly climatology (Figure 3.13). This variability was greatest in the Fitzroy NRM (Figure 3.13e) and smallest in the Cape York NRM (Figure 3.13a). Temporally, the greatest variability was noted during austral autumn with peak in April in the Mackay Whitsunday (Figure 3.13d) and Fitzroy (Figure 3.13e) NRM regions. The variability in the NRM regions to the north showed a bimodal pattern that is most prominent in the Dry Tropics NRM (Figure 3.13c) with peaks occurring in March and September and trough in December and/or June. The Dry Tropics (Figure 3.13c) and the Burnett Mary (Figure 3.13f) NRM regions are the only two regions where the variability of bPAR in the offshore waterbody were comparable to variability in the open coastal waterbody, suggesting a response to physical processes that directly affect the offshore locations as discussed in the EOF analysis section.

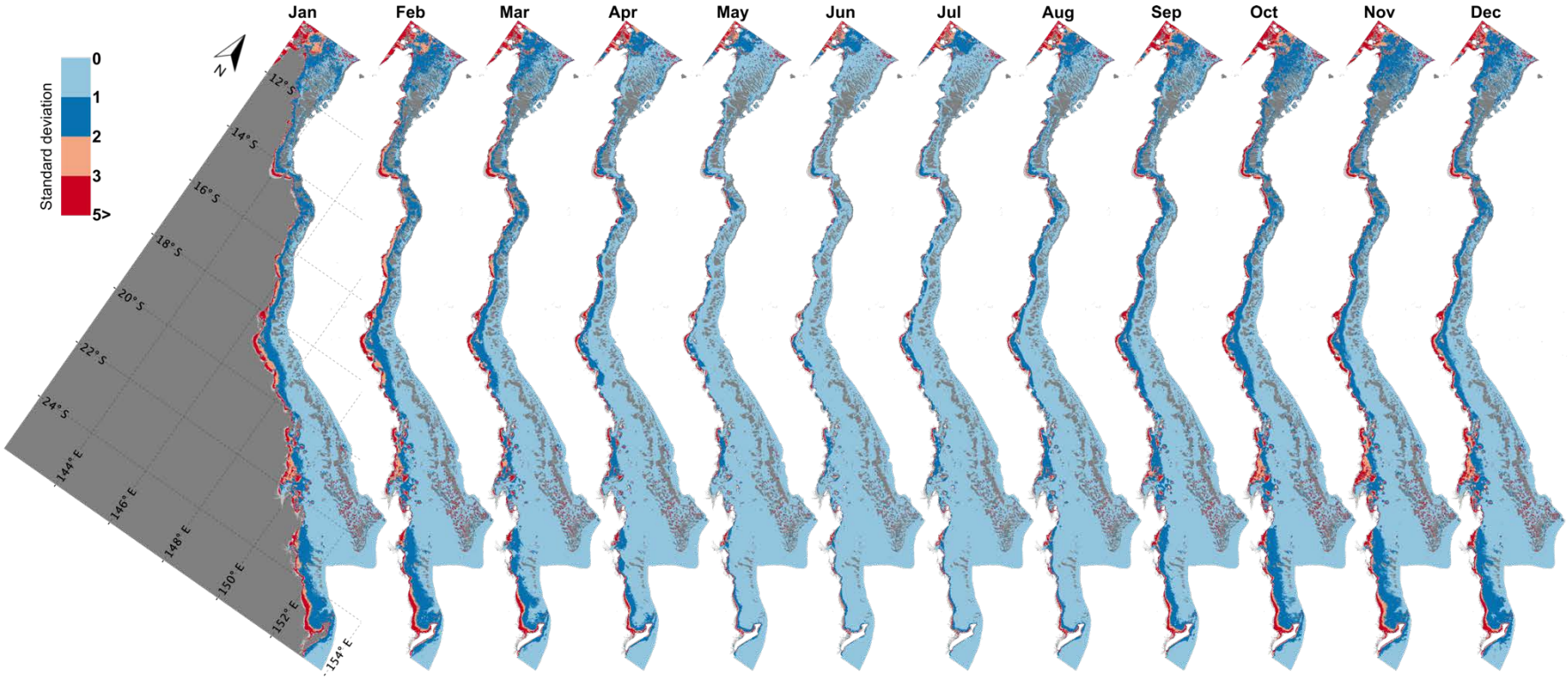

Figure 3.11. Maps of climatological monthly standard deviations for the full duration of the bPAR dataset (July 2002 to December 2018) categorised as per intervals denoted by the colour bar. Land (in January map only) or reef pixels (dark grey) and locations with bathymetry ≤5 m (light grey) are also indicated. The fluctuations of the bPAR values relative to the long-term climatology captured strong seasonality and spatial variation which coincide with the austral wet season (November to April).

Table 3.6. Climatological monthly standard deviation means of bPAR values for the whole Great Barrier Reef, the 24 zones, and the whole GBR (north to south length per zone) for the full dataset spanning July 2002 to December 2018. Shaded cells indicate the maximum (cyan) and minimum (grey) standard deviation values for the zone and month, excluding both whole GBR cases and offshore Burnett Mary NRM (last row). Abbreviations are: EC – Enclosed Coastal; OC – Open Coastal; MS – Mid-shelf; OS – Offshore.

Region	Waterbody	J	F	M	A	M	J	J	A	S	O	N	D
Whole GBR		1.2	1.1	1.0	0.7	0.6	0.5	0.6	0.7	0.9	1.1	1.1	1.1
Whole GBR: length North to South	EC	5.3	4.5	3.7	3.1	2.9	2.8	3.0	3.6	3.9	4.6	5.4	5.6
	OC	2.7	2.5	2.2	1.7	1.4	1.3	1.4	1.7	2.0	2.4	2.5	2.5
	MS	1.0	1.0	0.8	0.6	0.4	0.4	0.4	0.6	0.7	0.9	0.9	0.9
	OS	0.7	0.7	0.6	0.5	0.4	0.3	0.4	0.5	0.6	0.7	0.7	0.7
Cape York	EC	4.7	4.6	4.1	3.4	2.9	2.7	2.8	3.5	4.2	5.1	5.1	4.9
	OC	2.5	2.8	2.9	2.2	1.8	1.7	1.8	2.0	2.3	2.9	2.7	2.5
	MS	1.4	1.6	1.5	1.0	0.8	0.8	0.9	1.0	1.2	1.5	1.4	1.4
	OS	1.0	1.1	1.0	0.9	0.7	0.6	0.7	0.8	0.9	1.1	1.1	1.0
Wet Tropics	EC	5.2	4.6	3.2	2.8	2.7	2.7	3.0	3.9	4.2	4.8	5.4	5.7
	OC	3.8	3.7	3.2	2.5	2.2	1.9	2.1	2.4	2.8	3.2	3.3	3.3
	MS	1.7	1.8	1.5	1.0	0.8	0.7	0.9	1.0	1.2	1.4	1.3	1.3
	OS	0.8	0.8	0.8	0.6	0.5	0.4	0.5	0.5	0.7	0.7	0.8	0.7
Dry Tropics	EC	6.8	5.3	4.0	3.0	3.4	3.6	3.6	3.8	3.8	4.3	6.4	7.2
	OC	3.1	2.9	2.3	1.9	1.6	1.4	1.6	1.8	2.1	2.4	2.7	2.7
	MS	1.1	1.2	0.9	0.7	0.6	0.5	0.5	0.6	0.8	1.0	0.9	0.9
	OS	0.6	0.6	0.5	0.4	0.3	0.3	0.3	0.4	0.5	0.6	0.6	0.6
Mackay Whitsunday	EC	7.0	5.9	3.8	3.2	3.1	2.9	3.4	4.1	4.6	5.5	7.1	7.2
	OC	2.5	2.4	1.9	1.5	1.2	1.1	1.2	1.5	1.8	2.2	2.5	2.5
	MS	0.6	0.7	0.5	0.3	0.2	0.2	0.3	0.4	0.6	0.6	0.7	0.7
	OS	0.6	0.6	0.5	0.4	0.3	0.2	0.3	0.4	0.5	0.6	0.6	0.6
Fitzroy	EC	3.8	2.2	2.4	2.4	2.1	2.3	2.3	2.8	2.7	3.1	3.4	4.1
	OC	2.2	1.8	1.5	1.2	1.0	0.9	1.0	1.2	1.6	1.7	2.0	2.1
	MS	0.7	0.6	0.5	0.3	0.2	0.2	0.2	0.3	0.5	0.6	0.7	0.7
	OS	0.7	0.7	0.6	0.4	0.3	0.3	0.3	0.4	0.5	0.6	0.7	0.7
Burnett Mary	EC	7.5	6.0	4.6	4.4	3.6	3.2	3.2	4.0	5.1	6.0	7.1	7.6
	OC	3.8	3.5	2.9	2.4	1.8	1.5	1.5	1.7	2.4	3.0	3.0	3.2
	MS	1.1	1.1	0.9	0.7	0.5	0.5	0.4	0.5	0.8	1.0	1.1	1.0
	OS	*0.1*	*0.1*	*0.1*	*0.1*	*0.0*	*0.0*	*0.0*	*0.0*	*0.1*	*0.1*	*0.1*	*0.1*

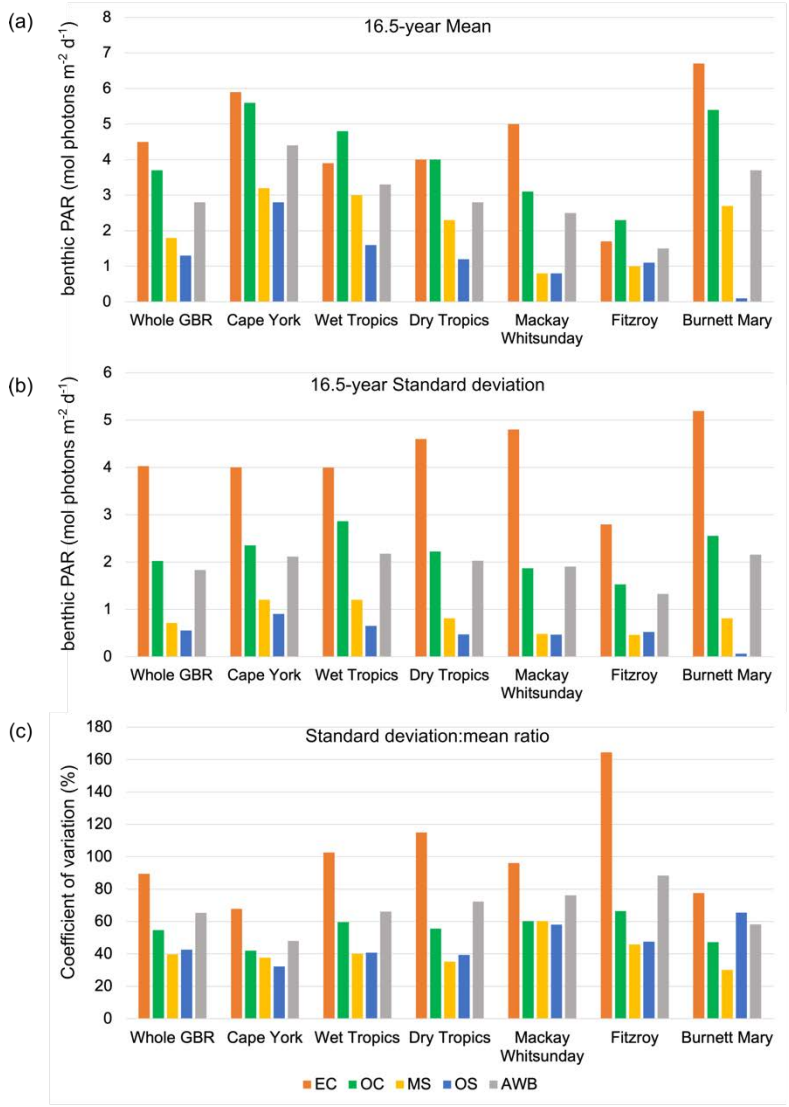

Figure 3.12. Bar plots summarising the climatological variability of bPAR in the different zones with (a) global 16.5-year mean, (b) global 16.5-year standard deviation, and (c) coefficient of variation calculated as the ratio of the standard deviation to the mean expressed in percent. Abbreviations as in Table 3.5.

3.7 Conclusion

This analysis of spatiotemporal patterns of benthic PAR in the GBR has highlighted the strong control of depth and the seasonally-varying amount of incident surface radiation, with long-term means varying by 50-fold between zones. The 16.5-year climatology highlighted a strong spatial variability (from north to south) with almost spatially homogenous high bPAR in the northern GBR (where the shelf is narrow) and a more variable bPAR for the southern GBR (where the shelf can be as wide as ~260 km). The annual means of bPAR showed the year-to-year variation of bPAR within the GBR from 2003 to 2018, which revealed 2011 was the 'darkest' year on record with a GBR-wide annual bPAR mean of 1.6 mol photons m^{-2} d^{-1}. They also revealed differences that may directly be attributed to the impacts of river

runoff, which introduce high concentrations of optically active components (particulate suspended sediments, coloured dissolved organic matter (CDOM)) and elevated nutrient concentrations that can result in phytoplankton blooms) and change the character and intensity of light reaching the ocean benthos.

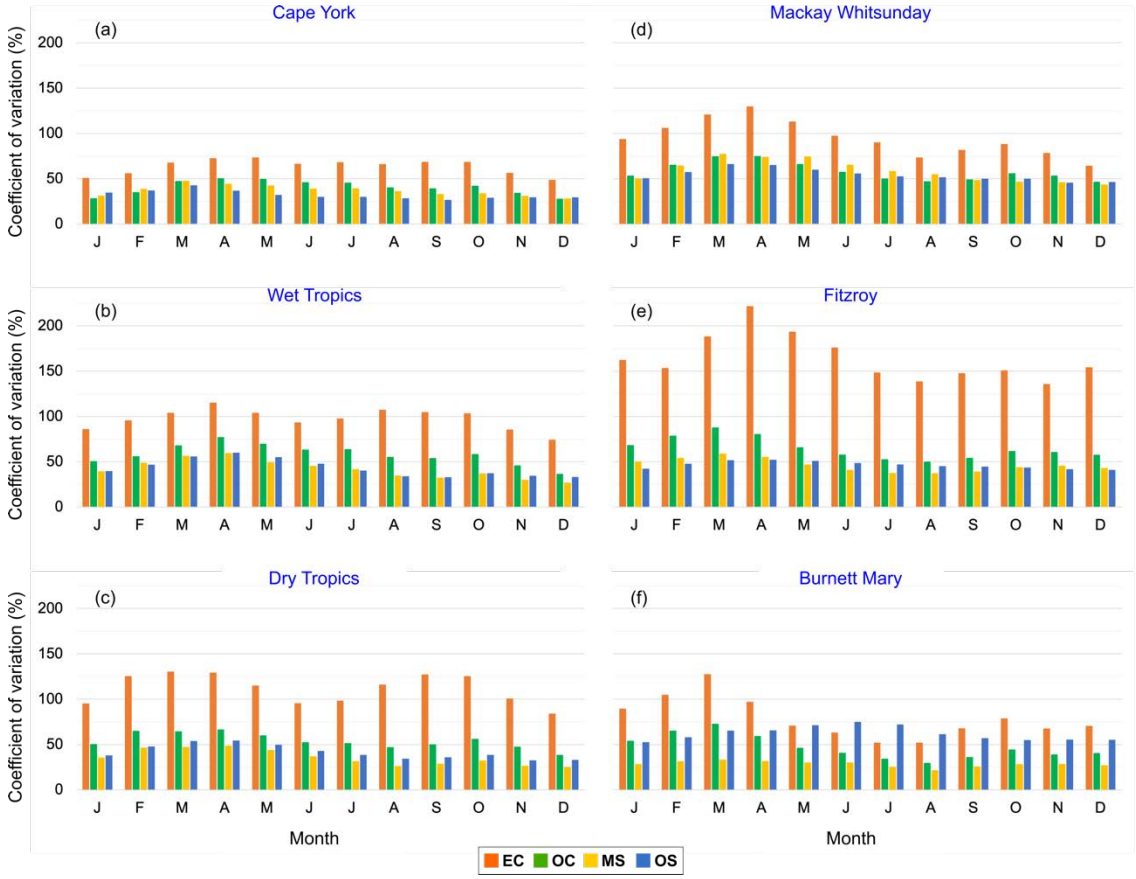

Figure 3.13. Coefficient of variation (%) of monthly bPAR climatology for each NRM region and waterbody (indicated by the colour gradient). Abbreviations are for the cross-shelf waterbodies: EC – enclosed coastal, OC- open coastal, MS – mid-shelf, and OS – offshore.

This study is the first to demonstrate bPAR variability at a scale of the whole GBR region using realistic estimates of benthic PAR values. The relationship between bPAR and river runoff is the motivation for Chapter 4 of this thesis. Baseline values calculated here for the different NRM regions and water bodies can be used as a guide for GBR monitoring programs, to detect spatial and temporal changes in water quality in addition to parameters already being used. The patterns of benthic PAR obtained here justify the potential of the bPAR dataset for developing a water quality index based on light availability (as presented in Chapter 5).

"The sea, once it casts its spell, holds one in its net of wonder forever" – Jacques-Yves Cousteau (1910 – 1997)

4 Drivers of benthic light variability within the Great Barrier Reef

Abstract

The diffuse light attenuation coefficient for the downwelling plane irradiance, K_d (m^{-1}), can be used to estimate light intensity at depth and explore the variability of light in the benthic ocean. The variation in K_d is wavelength-dependent and is determined by the optically active constituents in the water column, including water, phytoplankton, coloured dissolved organic matter (CDOM), and suspended non-algal particulate (NAP) materials which may originate from terrestrial and river runoffs. We used a random forest model (RFM) analysis to understand how these constituents and other environmental predictors affect spectral light attenuation, and hence light availability and variability, in the different water bodies within the shelf region of the Great Barrier Reef (GBR). We found that predictors reflecting terrestrial and anthropogenic inputs (CDOM and NAP) strongly influence variations of K_d in the inshore coastal water bodies. In contrast, the RFM results showed that K_d variability in the offshore waterbody was consistent with the inherent optical properties in clear oceanic conditions dominated by variations in Chlorophyll *a* (Chl *a*) concentration. K_d variability in the mid-shelf reflects the potential combined influence of variations in chlorophyll *a* concentration driven by land-derived nutrient inputs and local oceanography within the shelf, temporally consistent with the known seasonal dynamics of extreme rainfall and flood events and oceanic intrusions and upwelling, respectively. In optically complex coastal waters like the GBR shelf region, information on drivers of light variability is crucial to better manage and address the pressures affecting the vast and vital benthic marine ecosystems, including corals and seagrasses that it supports.

4.1 Introduction

Information about light attenuation can be used to explore the variability of light in the benthic ocean. The diffuse light attenuation coefficient for the downwelling plane irradiance, K_d (m^{-1}), is an important apparent optical property that determines the penetration of solar radiation into natural waters (Smith and Tyler, 1976; Kirk, 1981) and hence can be used to estimate light intensity at depth. Absorption and scattering processes (collectively, attenuation) determine $K_{d,}$ which varies with depth (Mobley, 1994; Kirk, 2011). The most common constituents responsible for the attenuation of light in water include: (i) the water itself, which absorbs photons strongly in the red end of the spectrum (Kirk, 1977); (ii) phytoplankton, which scatters light but absorbs relatively more light especially in the blue and red wavelengths (Kirk, 1977; O'Reilly et al., 1998); (iii) coloured dissolved organic matter (CDOM, historically also referred to as "yellow substances", Gelbstoff or "gilvin" (Kirk, 1980; Kirk, 2011)), which does not scatter but absorbs light most strongly in the UV and blue regions from leached soluble humic substances from soils (and indirectly from vegetation) with large fraction in the marine environment coming from land and river discharge (Kirk, 2011). CDOM may also include degradation components of phytoplankton cells and other organic particles, especially in productive water bodies (IOCCG, 2000); and (iv) non-living particulate suspended matter, which may include mineral particles, organic detritus and suspended sediments transported from river outflows or bottom resuspension, which does not absorb light strongly but scatters light intensely, increasing the path length of light propagation and hence the potential for light absorption (Kirk, 1980; Kirk, 2011). These constituents affect the character and intensity of light at different wavelengths (Kirk, 1997; Brando et al., 2012) and contribute correspondingly to the inherent optical properties (IOPs) of the water. The IOPs, "total spectral absorption coefficient", $a(\lambda)$ (m^{-1}) and "total spectral backscattering coefficient", $b_b(\lambda)$ (m^{-1}), link the light attenuation to a particular optical property (Mascarenhas and Keck, 2018).

The Great Barrier Reef (GBR) is located on a shallow continental shelf and has a complex mixture of water types ranging from clear oceanic offshore waters to turbid inshore waters (Schroeder et al., 2012). CDOM from river outflows along the GBR coastline strongly influences light attenuation in the inland coastal waters of the GBR (Lønborg et al., 2021). River plumes carrying suspended sediments from eroded topsoil and wave-resuspension of marine and terrestrial sediments from the seafloor (Orpin and Ridd, 2012) elevate turbidity in inshore coastal waters. The offshore waters, which are typically minimally exposed to coastal and riverine influences because of physical distance from sources, are generally clear oceanic (Case I) waters with optical properties that predominantly covary with concentrations of the phytoplankton pigment Chlorophyll-*a* (Chl *a*) (Morel, 1988) so for these water bodies, phytoplankton that both absorbs and scatters light may be most important aside from the natural attenuation of light due to water and depth. In the mid-shelf, it will be helpful to ascertain the primary driver of light variability, including to what extent inshore coastal processes also reach and affect the mid-shelf.

Pollutants and other land-derived materials transported into the GBR lagoon from nearby developed catchments and river systems have substantially increased since European settlement (Brodie et al., 2012; Joo et al., 2012; Kroon, 2012). Nutrient enrichment (or eutrophication) is considered a significant threat to the GBR (Schaffelke et al., 2017) and presents a compelling reason to address the consequence of anthropogenic influences in the marine environment. This does not imply that GBR waters are eutrophic in the sense of being high in nutrients relative to other coastal waters. Information on changes in K_d in the different water bodies of the GBR and their drivers is crucial because it can improve the capacity to monitor and manage impacts from land-use throughout the GBR.

The fate, spatial extent relative to point source location and biological effects of anthropogenic pollutants in GBR coastal waters are relatively well understood (Brodie et al., 2007; Brodie et al., 2010; Brodie et al., 2012; Devlin et al., 2012; Alvarez-Romero et al., 2013; Fabricius et al., 2016). However, GBR-wide and long-term assessments of spectral light attenuation to identify the main optical component that defines light variability and availability have been limited. To better understand the contributions of the various optically active components to the variability of the underwater light field, it is essential to consider spectral variation as these effects are wavelength dependent. This study of spectral light attenuation, $K_d(\lambda)$, investigates the role of these constituents in driving light attenuation and thus light availability and variability within the scale of the whole GBR.

The objectives of this study are (i) to analyse the regional and temporal variability in K_d spectral quantities encountered in the complex waters of the GBR; and (ii) to identify the K_d characteristics of some of the GBR surface water masses as a function of various optical and physical variables, including Chlorophyll-*a* concentration (Chl *a*), CDOM, non-algal particles (NAP), sea surface temperature (SST), total river discharge, southern oscillation index (SOI), wave height, depth, *across* and *along* distances (more details in (De'ath and Fabricius, 2010)) from the coast as well as *water year*, *season block* (early wet, late wet, early dry, and late dry), and the natural resource management (NRM) region as categorical variables.

4.2 Dataset and Methods

4.2.1 Remote sensing datasets

4.2.1.1 Spectral vertical diffuse light attenuation coefficient, $K_d(\lambda)$

Daily spectral values of $K_d(\lambda)$ (m^{-1}) were obtained from implementing the benthic irradiance model described in Chapter 2 for the study region shown in Figure 4.1a. Recall that IOP-based $K_d(\lambda)$ values were calculated at each of the ten MODIS Aqua wavelengths (nm) (412, 443, 469, 488, 531, 547, 555, 645, 667, and 678) to estimate the benthic irradiance values at each pixel within the GBR study domain (note that these spectral K_d values are instantaneous values, i.e., coincident to MODIS satellite

overpass). Satellite data processing methods described in Chapters 2 and 3 were also applied to the $K_d(\lambda)$ data used in this chapter. The temporal coverage of $K_d(\lambda)$ was extended to include the period until December 2019 from July 2002 (one year more worth of data than the bPAR dataset presented in Chapter 3). Daily spectral values were aggregated temporally to monthly data, resulting in 210 individual NetCDF (Unidata, 2021) data files for each wavelength.

4.2.1.2 Chlorophyll-a pigment concentrations

Observations of Chl *a* (mg m^{-3}) were derived from remote sensing reflectances, R_{rs} (sr^{-1}), recorded by the MODIS-Aqua satellite sensor and obtained from the NASA OBPG website (https://oceandata.sci.gsfc.nasa.gov). The Chl *a* product was derived using the standard OCI algorithm, specifically, the ocean colour index algorithm of Hu et al. (2012). Although this algorithm was also developed for clear waters with low chlorophyll concentration, it offers improved performance over the old OC4 algorithm (O'Reilly, 2000) in that it is more tolerant to perturbations due to hardware and residual processing errors (Hu et al., 2012). Nonetheless, the OCI algorithm may be challenged in the nearshore coastal zones where the presence of other optically active constituents may contribute to the signal measured by the satellite (Brando et al., 2012). The daily Level 2 data was then quality controlled and tuned locally to GBR conditions using L2 quality flags: LAND, CLDICE, ATMFAIL, HILT, HISATZEN, CHLFAIL, NAVFAIL, NAVWARN, LOWLW, HISOLZEN, CHLWARN, and MAXAERITER (Robinson et al., 2003) to minimise these shallow water effects. The daily Chl *a* data files that were not flagged during the processing were then mapped to the same nominal 1 km^2 pixel resolution and aggregated to monthly temporal resolution resulting in 210 NetCDF (Unidata, 2021) data files.

4.2.1.3 Sea Surface Temperature

The SST data recorded by both the MODIS Aqua and Terra satellite sensors were also obtained from the NASA OBPG website (https://oceandata.sci.gsfc.nasa.gov). Both the respective day- and night-time SST files were quality-controlled and merged to generate the final daily SST files. The L2 flags used in data processing include LAND, HISATZEN, HISOLZ, and NAVWARN. Each Level 3 data file was then mapped to the same nominal spatial resolution of 1 km^2. Like Chl *a*, the resulting daily SST files were also temporally averaged to monthly resolution resulting in 210 NetCDF (Unidata, 2021) data files. SST does not affect light attenuation but here was used as a proxy for surface upwelling that can influence the concentrations of optically active components in the water column.

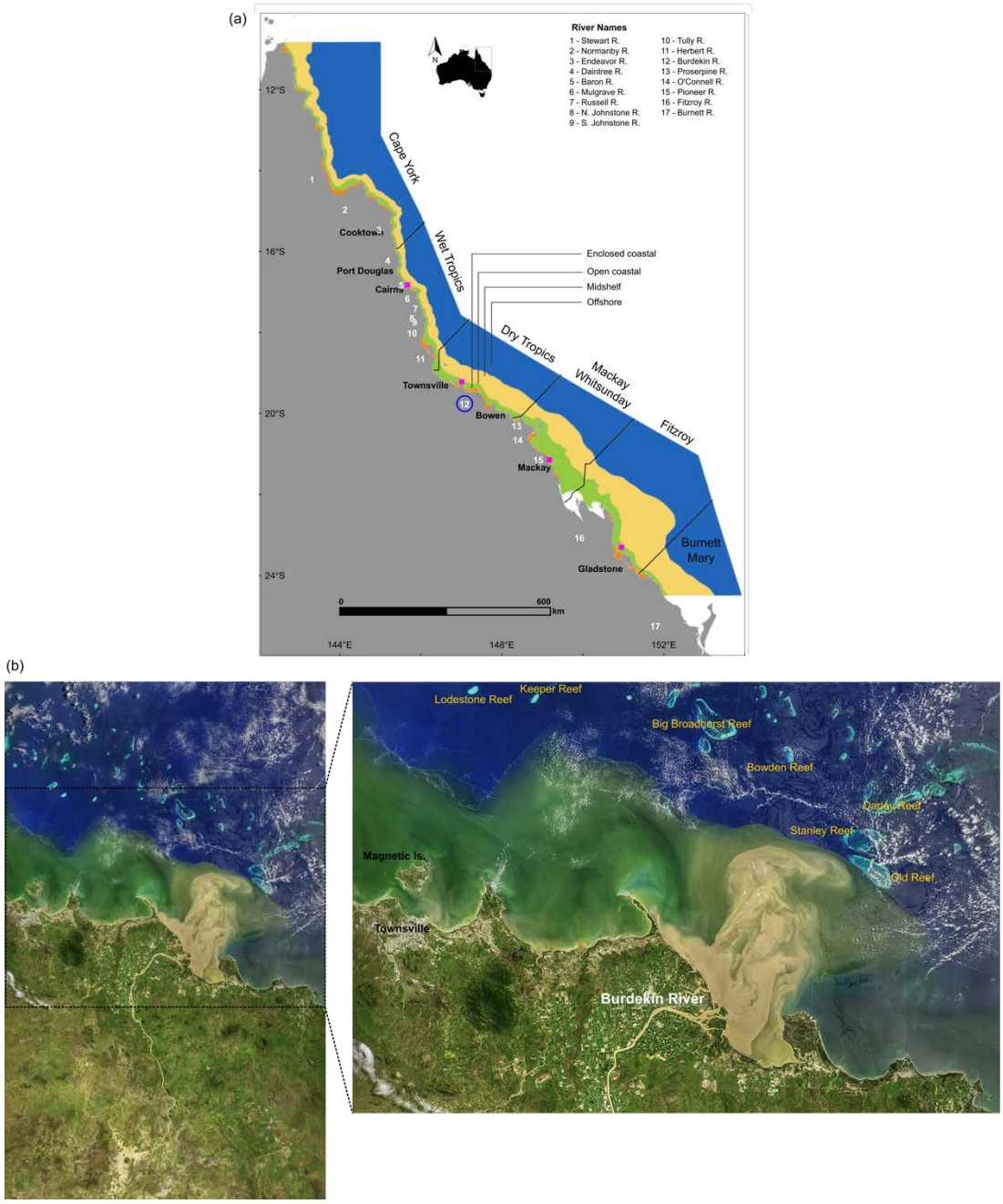

Figure 4.1. (a) Map of the study region including the boundaries of the NRM regions (solid black lines) and cross-shelf water bodies (solid green lines). Also shown are the locations of major rivers (indicated by numbers), major cities (black-filled circles), and wave monitoring sites (magenta-filled squares). Colour gradients indicate water body boundaries labelled accordingly. (b) Landsat 8 satellite image of the Burdekin River floods taken on the 9th of February 2019 (referred to later in the manuscript) courtesy of the Ocean Biology Processing Group (OBPG), NASA Goddard Space Flight Centre (https://oceancolor.gsfc.nasa.gov/gallery/). The blue-circled number in (a) indicates the relative location of the Burdekin River.

4.2.1.4 Coloured dissolved organic matter (CDOM) and non-algal particle (NAP)

Monthly data files containing the satellite-derived absorption coefficients due to CDOM (m^{-1}) at 440 nm and total suspended solids (or non-algal particles, NAP) (g m^{-3}) were obtained from the eReefs

ocean colour data products available from the Bureau of Meteorology (BoM) (http://ereeftds.bom.gov.au/ereefs/tds/catalog/ereef/mwq/P1M, Accessed 19th May 2021). A detailed description of the inversion process for the estimation of these products from remote sensing reflectance is available in Brando et al. (2012). The CDOM and NAP data files cover a smaller spatial domain (10 to 24.5°S and 142 to 156°E) and pixel resolution than the K_d dataset. Hence, each NetCDF (Unidata, 2021) data file was remapped to the same spatial extent (using the above domain limits) and resolution to that of the K_d dataset using the Climate Data Operator (CDO) version 1.9.3 (i.e., *remapbil* operator) (Schulzweida, 2020) to allow direct comparison at each pixel location.

Table 4.1 Summary of relevant streamflow monitoring stations used to estimate total river discharge at each NRM region adapted with some modifications from Fabricius et al. (2016) where the northern and southern segments of the Wet Tropics NRM were combined in this study. The percentage of estimated cumulative end-of-river freshwater discharge from the Burdekin River for the three northern NRM regions used in Fabricius et al. (2016) is also shown. The corresponding wave monitoring site assigned for each NRM region is also shown in the last column. See Figure 4.1a for the location of sites within the study area.

NRM region	Streamflow monitoring stations	Wave monitoring sites
Cape York	Normanby, Endeavour, Stewart	Cairns
Wet Tropics (WT): (North WT + South WT)	(North WT): Daintree, Barron, Russell, Mulgrave, Johnstone, Burdekin (30% of freshwater discharge) (South WT): Russell, Mulgrave, Johnstone, Tully, Herbert, Burdekin (50% of freshwater discharge)	Cairns
Dry Tropics	Burdekin (100% of freshwater discharge)	Townsville
Mackay-Whitsunday	Proserpine, O'Connell, Pioneer	Mackay
Fitzroy	Fitzroy	Emu Point
Burnett-Mary	Burnett	Emu Point

4.2.2 Other datasets and environmental predictors

4.2.2.1 Total river discharge

Monthly streamflow data from July 2002 to December 2019 for relevant monitoring stations along the GBR coastline were downloaded from the Queensland State Government's Water Monitoring Information Portal (https://water-monitoring.information.qld.gov.au). The total river discharge for each NRM region was then estimated as the sum of the streamflow for a combination of relevant stations that measure the stream height and flow values from respective rivers (Table 4.1). The grouping of relevant river stations for each NRM was adapted from the methods of Fabricius et al. (2016) with some modifications, particularly in the Wet Tropics NRM region, here combining its northern and southern

segments. The regional monthly total river discharge was assigned at each pixel location within an NRM region boundary, and a uniform zonal monthly total discharge was used for each region.

Table 4.2 Details of predictors used in the random forest model.

Variable / Predictor	Description	Temporal resolution	Spatial resolution
across	normalised distance from the coast (normal to the coastline)	uniform value over the study period	unique value per pixel
along	normalised distance from the coast (parallel to the coastline)	uniform value over the study period	unique value per pixel
depth	pixel bathymetry (m)	uniform value over the study period	unique value per pixel
river discharge	aggregated river outflows from rivers relevant to each NRM region	monthly value over the study period	uniform value per NRM boundary
wave height	observed wave height at selected stations relevant to each NRM region	monthly value over the study period	uniform value per NRM boundary
SOI	index for El Niño or La Niña to account for large scale ocean-atmosphere driver of variability	monthly value over the study period	uniform value over whole GBR
SST	MODIS (Aqua and Terra) Sea surface temperature	monthly value over the study period	unique value per pixel
Chlorophyll *a*	MODIS (Aqua) Chlorophyll *a* pigment concentration	monthly value over the study period	unique value per pixel
CDOM	MODIS (Aqua) – derived absorption due to coloured dissolved organic matter; eReefs, aLMI (Brando et al., 2012))	monthly value over the study period	unique value per pixel
NAP	MODIS (Aqua) – derived non-algal particle concentration, a proxy for total suspended solids (TSS); eReefs, aLMI (Brando et al., 2012)	monthly value over the study period	unique value per pixel
water year	defined as 01 October to 30 September of the following calendar year following Waterhouse et al. (2017)	unique value per year over the study period	uniform value over whole GBR
season	block of three months based on the definition of water years as follows: Late Wet (LW) – February, March, April Early Dry (ED) – May, June, July Late Dry (LD) – August, September, October Early Wet (EW) – November, December, January	categorised value quarterly over the study period	uniform value over whole GBR
region	NRM region	uniform over the study period	uniform value per NRM boundary

4.2.2.2 Southern Oscillation Index and wave height data

Inter-annual or longer time scale variations of climate and influences are also an important feature of average spatiotemporal conditions that operate on the GBR. For example, water quality parameters that affect light availability not only vary along cross-shelf, seasonal and latitudinal gradients but may also

exhibit high variability between years driven by La Nina and El Nino cycles. To account for some of these influences on the variability of K_d, monthly southern oscillation index (SOI) data for the coincident period (July 2002 to December 2019) were downloaded from the Australian Bureau of Meteorology website (http://www.bom.gov.au/climate/enso/soi/).

In addition, daily data on wave heights (m) were downloaded from the Queensland State Government's, Department of Environment and Science website (https://www.qld.gov.au/environment/coasts-waterways/beach/monitoring/waves-sites) to account for short-term high-frequency fluctuations of physical processes in the ocean that can affect K_d values. The Environment, Land, and Water group of the department maintains a network of wave monitoring sites along the Queensland coast, including the four wave monitoring buoys used (Table 4.1). The daily maximum wave height for each site was then aggregated monthly and assigned to pixels within the relevant zone.

4.2.2.3 Depth and distance across and along the shelf

Some spatial attributes of the study area were also obtained. These include depth (m) and relative distance *across* and *along* the GBR shelf. Depth, which defines the vertical distance that light would travel from the surface to the seafloor, was obtained from the high-resolution digital elevation model (DEM) for the GBR (Beaman, 2010b). This DEM was the same dataset used in the benthic irradiance model detailed in Chapter 2 (Figure 2.1). Distances from the coastline in the across (normal) and along (parallel) directions were also calculated using the *acrossAlong* package in R version 3.0 (De'ath and Fabricius, 2010; De'ath and Venables, 2013) and the pixel geographic coordinate locations (Latitude and Longitude). Following De'ath and Fabricius (2010), the distance *along* the shelf was set to 0 in the south and 1 in the north, and the distance *across* the shelf was set to 0 at the coast and 1 at the outer edge of the continental shelf.

4.2.3 Random Forest model analysis

The Random Forest algorithm (Breiman, 2001) was used in the analysis to understand and explore the variability in spectral K_d within the GBR. A Random Forest algorithm is a bootstrap aggregation-type algorithm where multiple regression (or classification in the case of categorical variable problems) decision trees are grown, pruned, and aggregated to understand the variability of a dataset. It also allows to predict the desired variable(s) based on the set of predictor variables used to train the model. One powerful feature of RFM is its ability to provide insight into variables of most importance when building the model, which can be used as a data exploration tool. Here, Random Forest models (RFMs) were constructed as a function of 12 predictors (see Table 4.2 and Sections 4.2.1 to 4.2.2 for details) using the *randomForest* package (Liaw and Wiener, 2002) in R version 4.0.5 (2021-03-31) (R Core Team, 2021).

One RFM was constructed for each combination of spectral K_d time series (i.e., each of the ten wavelengths) and cross-shelf waterbody boundary: enclosed coastal, open coastal, mid-shelf and offshore (i.e., 40 RFMs in total). Each model was required to build a minimum of 500 decision trees, and each tree was limited to a maximum of five terminal nodes (or leaves of the tree) and six predictors, randomly sampled from the full set of candidate predictors, at each split in a tree. Random Forests offer improved predictive performance by building decorrelated trees where the number of trees needs to be large enough to stabilise the prediction error rate. More trees provide more robust and stable error estimates and variable importance measures (James et al., 2013). In this study, 500 decorrelated trees were deemed large enough to ensure convergence and produce a single (averaged) consensus prediction while also using reasonable computing resources. The node size defines the depth or complexity of the trees, while the number of randomly selected predictors ensure a low correlation between trees. Together, the node size and the number of predictors help prevent over-fitting. The analysis included datasets that extend from July 2002 to December 2019.

The relative importance of the variables included in the individual models was evaluated using the model output called the 'percent increase in mean squared error' (% IncMSE) which indicates the mean increase in the model prediction error if the variable is omitted in the model (Liaw and Wiener, 2002). The higher the associated % IncMSE, the greater the error in model predictions of the spectral K_d if the variable is excluded as a model predictor, thus the greater the importance of that predictor in predicting the variability of the variable being modeled (in this case, K_d).

4.3 Results

Table 4.3. Summary statistics of monthly averaged light attenuation coefficients (K_d) for each wavelength calculated over the whole GBR, including in the turbid inshore locations encompassing the study period between July 2002 and December 2019. Long-term monthly time series calculated for each zone (NRM region and waterbody combination) and wavelength are provided in the Thesis Appendix 7.3. The number in parentheses after K_d indicate the wavelength in nanometres.

Variable	mean (m^{-1})	minimum (m^{-1})	maximum (m^{-1})	median (m^{-1})
$K_d(412)$	0.15	0.02	5.86	0.08
$K_d(443)$	0.12	0.02	5.25	0.07
$K_d(469)$	0.10	0.02	4.83	0.06
$K_d(488)$	0.09	0.02	4.56	0.06
$K_d(531)$	0.09	0.05	3.66	0.07
$K_d(547)$	0.10	0.06	3.45	0.08
$K_d(555)$	0.11	0.00	3.36	0.09
$K_d(645)$	0.42	0.35	3.59	0.41
$K_d(667)$	0.55	0.46	3.71	0.54
$K_d(678)$	0.58	0.49	3.73	0.57

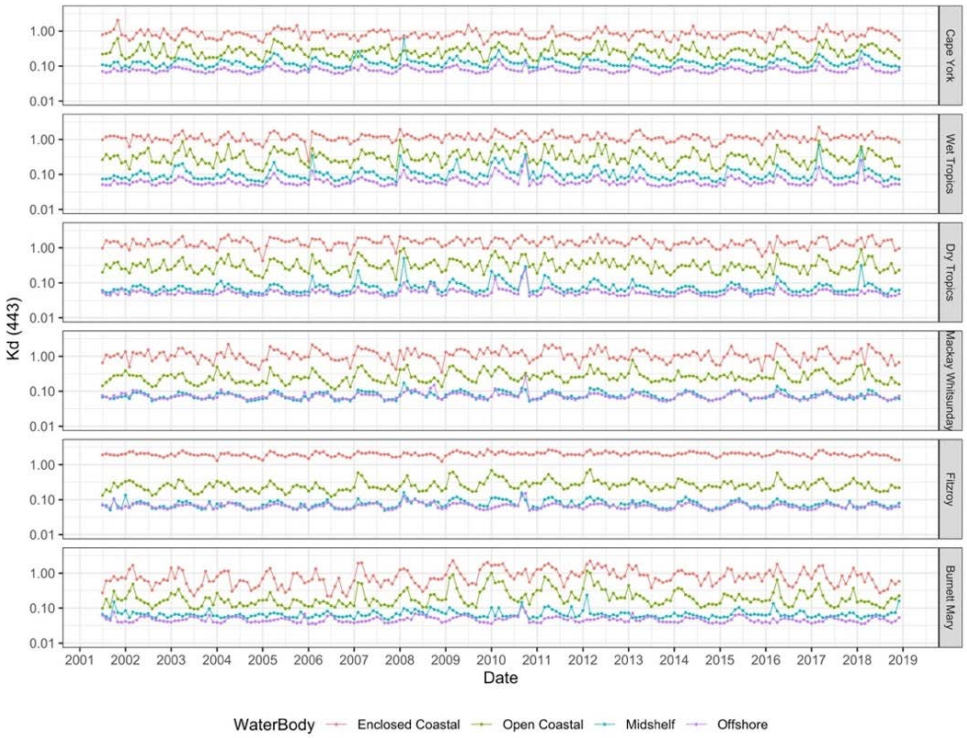

Figure 4.2. Monthly time series of light attenuation coefficient (K_d) at 443 nm summarised for each NRM region arranged from north to south (rows) and each cross-shelf waterbody denoted by colour. Note that the y-axis is on a logarithmic scale with limits from 0.01 to 4.0 m^{-1}.

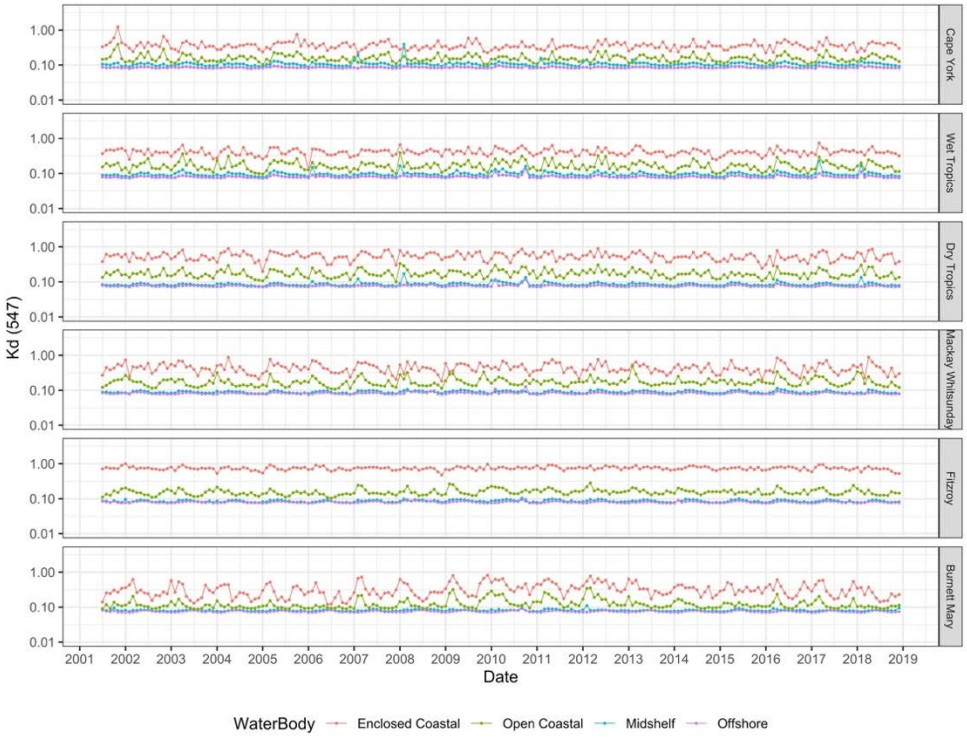

Figure 4.3. Same as Figure 4.2 but for (K_d) at 547 nm.

4.3.1 Characteristics of light attenuation coefficient, $K_d(\lambda)$, within the GBR

Long-term monthly light attenuation coefficient (K_d) values averaged over the whole GBR region and the whole time series (July 2002 to December 2019) are shown in Table 4.3. Overall, mean calculated K_d ranged from 0.09 m^{-1} for $K_d(488)$ and $K_d(531)$ to 0.58 m^{-1} for $K_d(678)$. Mean light attenuation was highest in the red wavelengths and comparably low in the blue and green (Table 4.3). However, for some wavelengths, especially in the blue wavelengths, maximum light attenuation values were as high as 4.56 m^{-1} (i.e., $K_d(488)$) and 5.86 m^{-1} (i.e., $K_d(412)$). The monthly time series for this 17.5-year dataset, summarised for each zone (combination of NRM region and cross-shelf waterbody), showed strong temporal and spatial variability (representative wavelengths for blue, green, and red are shown in Figure 4.2, Figure 4.3, and Figure 4.4, respectively; plots and table of long term monthly K_d values for the other remaining wavelengths are provided in the Thesis Appendix 4).

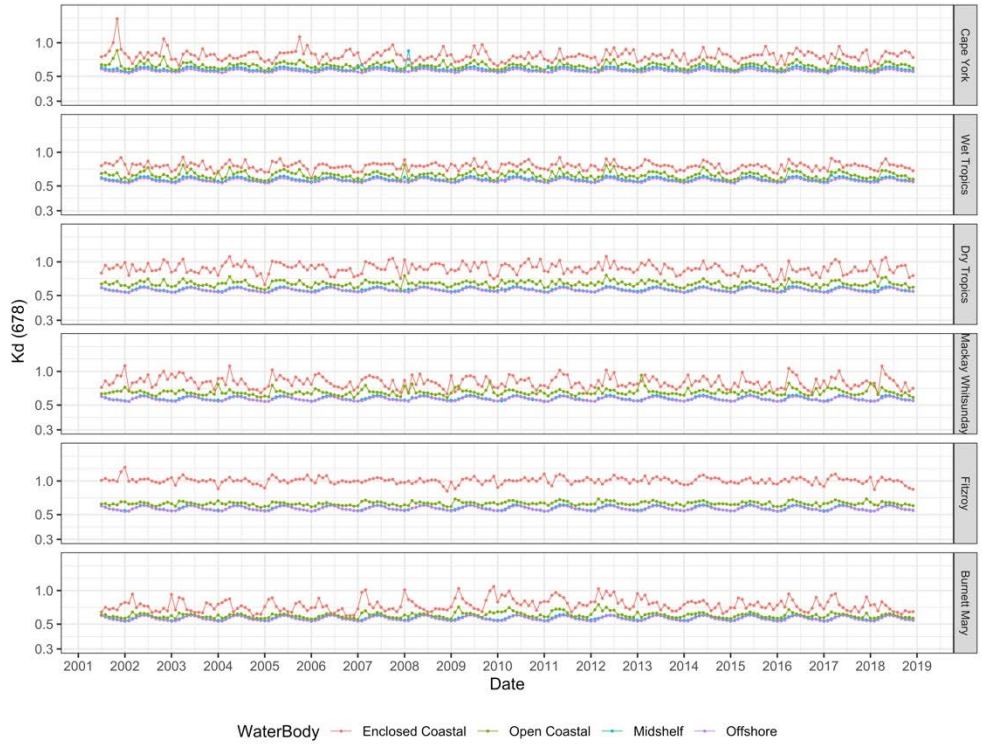

Figure 4.4. Same as Figure 4.2 but for (K_d) at 678 nm. Note that the y-axis is on a logarithmic scale with limits from 0.3 to 2.0 m^{-1}.

K_d values obtained for the enclosed coastal and open coastal water bodies were consistently higher than the mid-shelf and offshore values, and the enclosed waterbody values were consistently higher than the open coastal waterbody, especially in the Fitzroy NRM region. The mid-shelf and offshore water bodies had similar K_d in terms of the range of values and overall variability. However, several peaks through the time series were discernible in the mid-shelf waterbody, especially in the blue wavelength (Figure 4.2), not visible in the offshore K_d values. In most regions, for example, the mid-shelf $K_d(443)$ was

higher than offshore (except in the Mackay Whitsunday and Fitzroy NRM regions where the shelf is much wider).

4.3.2 Random Forest Analysis

4.3.2.1 Enclosed and open coastal water bodies

The RFM results for the two inshore coastal water bodies (enclosed and open) are shown in Figure 4.5 and Figure 4.6. In the enclosed coastal waterbody, NAP was the most important predictor of variability in K_d across all wavelengths (Figure 4.5b to j) indicated by an average of 32% IncMSE (Table 4.4) except in K_d(412), where CDOM was the best predictor (Figure 4.5a) with a 29% IncMSE (Table 4.4). Across all the other wavelengths (except the 412 nm), CDOM followed NAP as the next best predictor with an average of ~20% IncMSE (Table 4.4). The Chl *a* and categorical variable Region also showed some importance across the blue wavelengths and the two shorter green wavelengths (Figure 4.5a to f), both with >10% IncMSE values. In the red wavelengths, variables Region and *along* distance were third and fourth in importance (both with >10% IncMSE). River discharge showed increasing importance from the blue (~2% IncMSE) to green (~6% IncMSE) and red wavelengths (8% IncMSE) while the other remaining predictors used showed generally low importance (mostly between 0 and 5% IncMSE) in explaining the spectral K_d variability in the enclosed coastal waterbody.

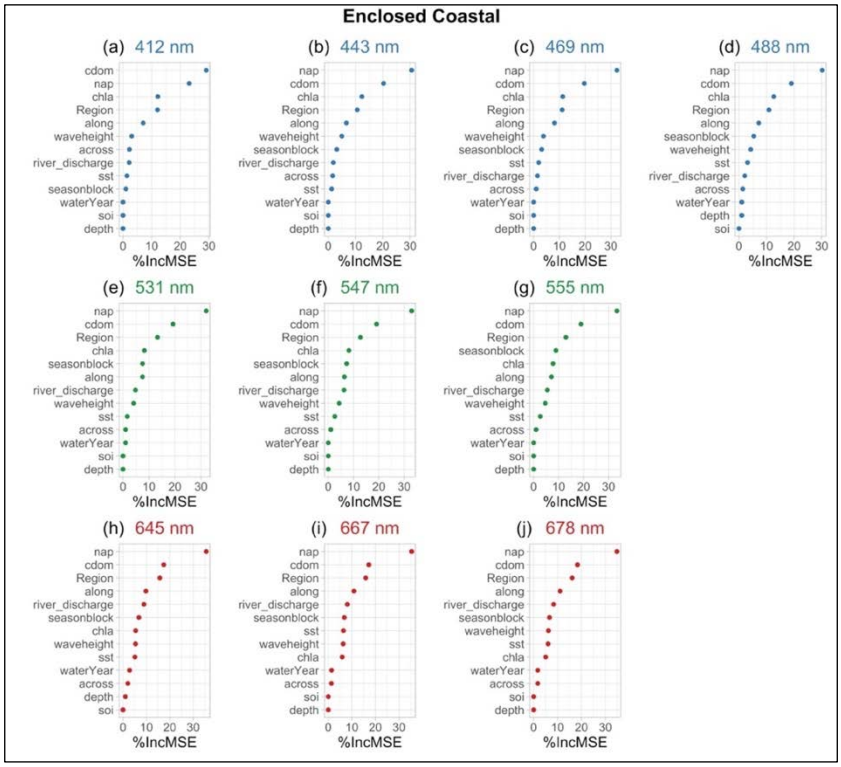

Figure 4.5. Importance of variables included in the random forest model in predicting the spatial and temporal change in spectral K_d on the enclosed coastal waterbody. Variable importance on the horizontal axis is indicated as the 'percent increase in mean squared error' (% IncMSE), the model prediction error if any of the variables on the vertical

y-axis is removed from the model. The wavelength of the respective K_d time series analysed is indicated in nm units at the top of each plot. Colours of filled dot points denote the wavelength region.

NAP was also the single best predictor of variability in light attenuation across all wavelengths in the open coastal waterbody (Figure 4.6) with a mean of 33% IncMSE (Table 4.5). In this waterbody, the variables Chl *a*, CDOM, and depth were consistently the next (consecutive) three important predictors in the blue and green wavelengths with importance ranging from about 10 to 25% IncMSE (Figure 4.6a to g). In the red wavelengths, Chl *a* and season block (quarterly) also followed NAP as important predictors of K_d variability in this region (Figure 4.6h to j). River discharge showed some importance with values ranging from 0 to 5% IncMSE across the ten wavelengths, highest in the shortest blue wavelength, while the variables indicating the distance from the coast, *across* and *along*, indicated comparable importance with an average of 5 and 4% IncMSE across the ten wavelengths, respectively. The remaining predictors in the RFMs for open coastal waterbody did not contribute much to explaining the variability of K_d.

Table 4.4. Summary statistics of the importance of predictors (i.e., % IncMSE) used in the random forest model constructed for the enclosed coastal waterbody and summarised per wavelength region and across all wavelengths. Statistics calculated across specified wavelength interval and predictor are as follows: mean = average of % IncMSE; min = minimum % IncMSE; and max = maximum % IncMSE.

	Wavelength region	Blue			Green			Red			Across all		
	Summary variable of importance	mean	min	max	mean	min	max	mean	min	max	mean	min	max
Model predictors	Region	11.2	10.6	12.0	13.0	12.7	13.3	15.9	15.8	16.1	13.1	10.6	16.1
	Water year	0.3	0.0	1.0	0.3	0.0	1.0	2.0	1.4	2.8	0.8	0.0	2.8
	Season block	3.2	1.0	5.4	7.9	7.3	8.9	6.7	6.6	6.8	5.6	1.0	8.9
	Across	1.6	1.0	2.2	1.0	1.0	1.0	1.7	1.3	2.1	1.4	1.0	2.2
	Along	7.2	6.6	8.1	7.0	6.4	7.5	10.6	9.8	11.1	8.2	6.4	11.1
	Depth	0.3	0.0	1.0	0.0	0.0	0.0	0.3	0.0	1.0	0.2	0.0	1.0
	Wave height	4.0	3.0	5.0	4.3	4.1	4.6	5.9	5.3	6.3	4.7	3.0	6.3
	River discharge	1.9	1.5	2.1	5.5	4.8	6.2	8.4	8.1	8.9	4.9	1.5	8.9
	SOI	0.0	0.0	0.0	0.0	0.0	0.0	0.0	0.0	0.0	0.0	0.0	0.0
	SST	1.9	1.2	3.1	2.3	1.6	2.6	5.8	5.1	6.4	3.2	1.2	6.4
	Chl a	12.1	11.3	12.6	8.1	7.8	8.2	5.5	5.1	5.9	8.9	5.1	12.6
	NAP	**29.0**	**23.1**	**32.3**	**32.8**	**32.1**	**33.3**	**35.2**	**34.8**	**35.6**	**32.0**	**23.1**	**35.6**
	CDOM	22.0	19.0	29.1	19.1	18.9	19.3	17.6	17.2	18.3	19.8	17.2	29.1

Table 4.5. As per Table 4.4 but for the open coastal waterbody.

	Wavelength region	Blue			Green			Red			Across all		
	Summary variable of importance	mean	min	max	mean	min	max	mean	min	max	mean	min	max
Model predictors	Region	2.0	1.5	2.5	2.9	2.6	3.2	5.4	4.1	6.9	3.3	1.5	6.9
	Water year	0.0	0.0	0.0	0.0	0.0	0.0	0.0	0.0	0.0	0.0	0.0	0.0
	Season block	1.8	1.4	2.6	0.5	-0.8	1.3	16.7	12.3	19.9	5.9	-0.8	19.9
	Across	4.9	4.6	5.1	5.0	4.7	5.2	4.1	3.4	4.8	4.7	3.4	5.2
	Along	3.6	3.0	4.2	5.8	5.1	6.3	3.1	2.3	3.8	4.1	2.3	6.3
	Depth	11.3	9.4	12.4	10.4	10.2	10.7	12.0	10.8	13.1	11.2	9.4	13.1
	Wave height	1.7	1.0	2.2	3.6	3.2	4.1	4.7	4.3	5.4	3.2	1.0	5.4
	River discharge	3.3	1.9	4.9	0.4	0.0	1.3	3.2	2.6	4.3	2.4	0.0	4.9
	SOI	0.3	0.0	1.0	0.0	0.0	0.0	0.0	0.0	0.0	0.1	0.0	1.0
	SST	2.0	1.4	2.4	1.3	1.0	1.8	8.9	7.7	11.0	3.8	1.0	11.0
	Chl a	22.4	21.1	24.0	20.7	18.6	22.9	18.8	17.6	20.0	20.8	17.6	24.0
	NAP	**31.1**	**27.7**	**35.4**	**32.8**	**32.2**	**34.0**	**34.2**	**33.1**	**35.6**	**32.5**	**27.7**	**35.6**
	CDOM	18.9	18.5	19.9	13.9	13.6	14.3	12.5	12.3	12.8	15.5	12.3	19.9

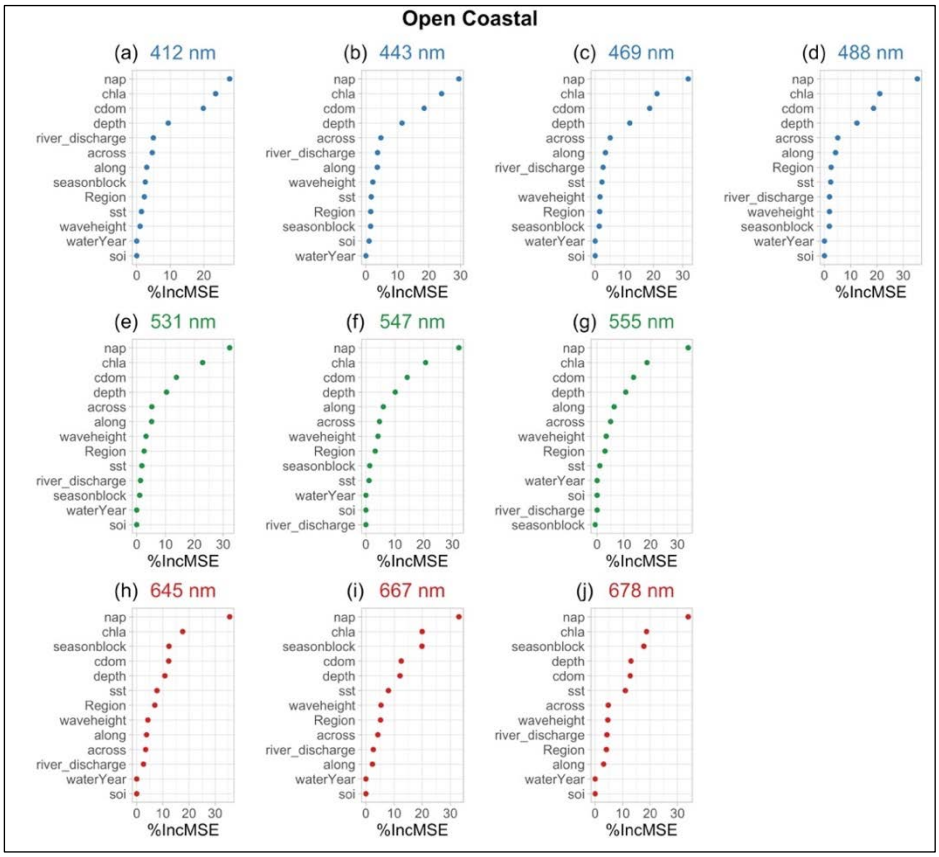

Figure 4.6. Same as Figure 4.5 but for the open coastal waterbody.

4.3.2.2 *Mid-shelf waterbody*

In the mid-shelf waterbody, the results of the RFMs are somewhat similar to that obtained in the offshore waterbody in that (i) Chl *a* was also identified as the best predictor of K_d variability across the blue (Figure 4.7a to d) and green (Figure 4.7e to g) wavelengths with a respective average of 38% IncMSE and 37% IncMSE (Table 4.6); and (ii) the season block was clearly most important in the red wavelengths (Figure 4.7h to j) with the same level of variable importance (37% IncMSE, Table 4.6). However, in the mid-shelf, CDOM came up as the second-best predictor in the blue and NAP in the green spectra (Figure 4.7), with about the same importance of 21% IncMSE (Table 4.6). Chl *a*, NAP, CDOM and SST showed almost equal importance after *season block* in predicting changes in K_d in the red wavelengths (Figure 4.7h to j). Interestingly, river discharge showed some importance in predicting K_d variability in the blue wavelengths (Figure 4.7a to d), with variable importance slightly higher in the 412 nm wavelength (>10% IncMSE), comparable with the mean variable importance noted for river discharge in the enclosed coastal waterbody (Figure 4.5h to j). However, river discharge showed less importance in the green and red wavelengths with a range of 3 to 5% IncMSE and 5 to 6% IncMSE, respectively. The other predictors with spatially uniform values across much of the study area, including wave height, water year, and SOI, did not contribute much to the changes in light attenuation values in this study.

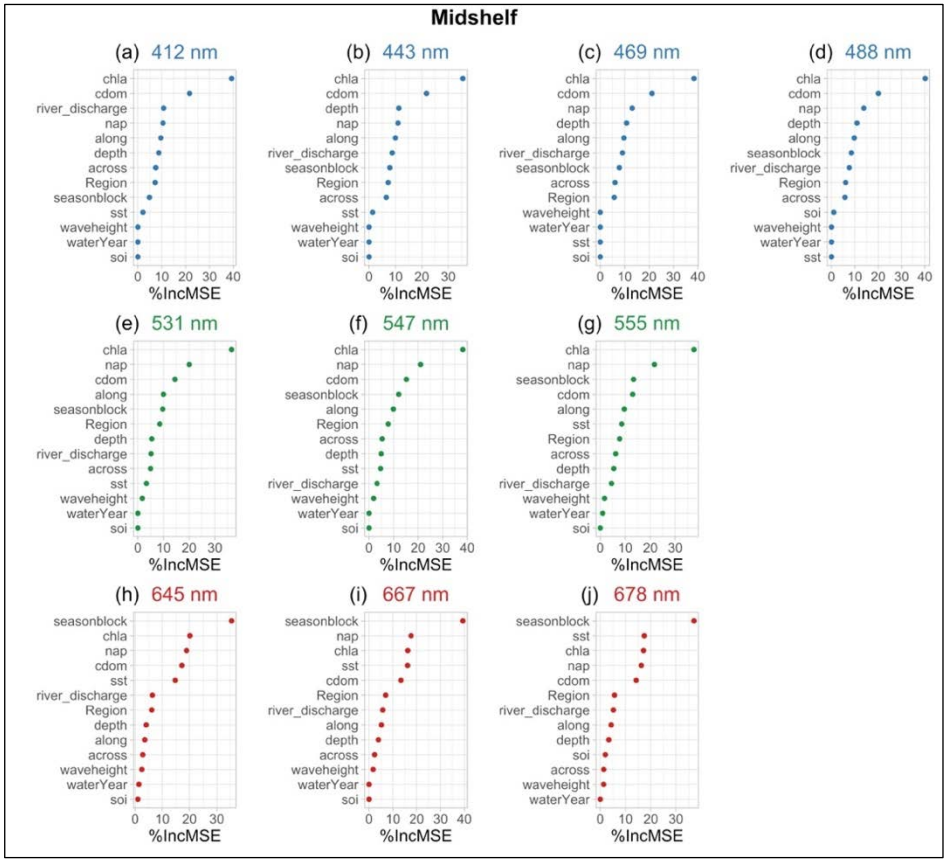

Figure 4.7. Same as Figure 4.5 but for the mid-shelf waterbody.

Table 4.6. As per Table 4.4 but for the mid-shelf waterbody.

	Wavelength region	Blue			Green			Red			Across all		
	Summary variable of importance	mean	min	max	mean	min	max	mean	min	max	mean	min	max
Model predictors	Region	6.6	5.7	7.2	8.0	7.8	8.5	6.2	5.6	7.0	6.9	5.6	8.5
	Water year	0.0	0.0	0.0	0.3	0.0	1.0	0.5	0.0	1.4	0.2	0.0	1.4
	Season block	7.3	4.8	8.6	11.7	9.7	13.3	**37.3**	**35.4**	**39.4**	17.6	4.8	39.4
	Across	6.4	5.7	7.5	5.5	4.9	6.2	2.2	1.4	2.8	4.9	1.4	7.5
	Along	9.8	9.6	10.0	9.8	9.6	10.0	4.4	3.6	5.2	8.2	3.6	10.0
	Depth	10.4	8.7	11.3	5.3	4.9	5.4	3.8	3.4	4.0	6.9	3.4	11.3
	Wave height	0.0	0.0	0.0	1.8	1.7	1.9	1.8	1.4	2.5	1.1	0.0	2.5
	River discharge	9.1	7.6	10.8	4.3	3.3	5.2	5.8	5.2	6.3	6.6	3.3	10.8
	SOI	0.3	0.0	1.0	0.0	0.0	0.0	1.0	0.0	2.0	0.4	0.0	2.0
	SST	0.9	0.0	2.2	5.5	3.3	8.6	16.1	14.7	17.4	6.8	0.0	17.4
	Chl a	**38.3**	**35.5**	**40.1**	**37.4**	**36.5**	**38.2**	17.8	16.2	20.1	**31.9**	**16.2**	**40.1**
	NAP	12.1	10.5	13.8	20.9	20.0	21.6	17.6	16.2	18.9	16.4	10.5	21.6
	CDOM	21.1	20.1	21.8	14.2	13.0	15.2	14.9	13.4	17.2	17.2	13.0	21.8

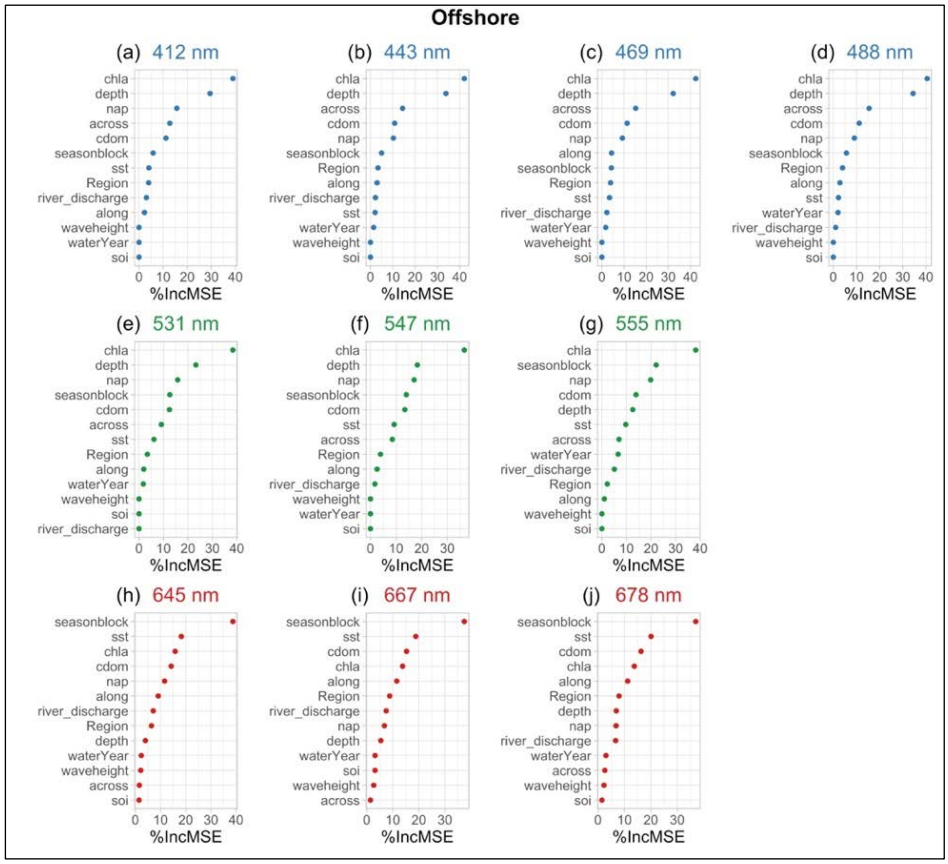

Figure 4.8. Same as Figure 4.5 but for the offshore waterbody.

Table 4.7. As per Table 4.4 but for the offshore waterbody.

	Wavelength region	Blue			Green			Red			Across all		
	Summary of variable importance	mean	min	max	mean	min	max	mean	min	max	mean	min	max
Model predictors	Region	3.8	3.4	4.0	3.2	2.2	3.9	7.7	6.4	8.8	4.8	2.2	8.8
	Water year	1.3	0.0	2.0	2.8	0.0	6.6	2.9	2.4	3.2	2.2	0.0	6.6
	Season block	5.2	4.3	5.8	16.2	12.6	22.1	**37.7**	**37.0**	**38.7**	18.3	4.3	38.7
	Across	14.5	12.8	15.4	8.2	7.0	9.2	1.9	1.4	2.6	8.8	1.4	15.4
	Along	3.1	2.3	4.4	1.8	1.0	2.6	10.6	9.1	11.5	5.0	1.0	11.5
	Depth	32.5	29.5	34.4	18.0	12.6	23.3	5.4	4.0	6.9	20.0	4.0	34.4
	Wave height	0.0	0.0	0.0	0.0	0.0	0.0	2.4	2.2	2.7	0.7	0.0	2.7
	River discharge	2.1	1.0	3.1	2.3	0.0	5.1	7.1	6.7	7.4	3.7	0.0	7.4
	SOI	0.0	0.0	0.0	0.0	0.0	0.0	2.0	1.5	3.2	0.6	0.0	3.2
	SST	3.0	2.1	4.1	8.4	6.1	9.7	19.1	18.3	20.1	9.4	2.1	20.1
	Chl a	**41.0**	**38.9**	**42.4**	**37.7**	**36.6**	**38.4**	14.4	13.8	15.8	**32.0**	**13.8**	**42.4**
	NAP	11.1	9.1	15.7	17.6	15.8	19.8	8.4	6.8	11.6	12.2	6.8	19.8
	CDOM	11.1	10.8	11.4	13.2	12.5	13.9	15.3	14.2	16.3	13.0	10.8	16.3

4.3.2.3 Offshore waterbody

In the offshore waterbody, the RFM results clearly showed Chl *a* as the best predictor of K_d variability across the blue (Figure 4.8a to d) and green (Figure 4.8e to f) wavelengths with an average of 41% IncMSE and 38% IncMSE, respectively (Table 4.7). Depth was noted as the second-best predictor in the blue and green wavelengths, and a mean 33% IncMSE indicated the sensitivity of the blue light spectrum to changes in depth, and in the green by a mean 18% IncMSE (Table 4.7). In the red wavelength, the season block showed strong dominance with a mean 39% IncMSE, while SST, the second-best predictor in the red region, showed relatively high importance (with a mean 20% IncMSE) for the first time.

4.3.2.4 Exploring temporal differences

The partial dependence plots of the season block predictor were summarised to get more specific information about potential temporal differences that can be used to interpret the important predictors obtained for each waterbody, especially in the mid-shelf. These results are important because some physical processes that operate within the GBR shelf, which may drive light variability, occur at specific times of the year. The partial dependence plot shows the marginal effect of the predictor on the outcome of the model or even the type of relationship (i.e., linear) between the predictor and the target variable being modelled. The categorised partial dependence of *season blocks* (see Table 4.2 for the definition and relevant details) for each waterbody and wavelength highlighted a temporal gradient that may

influence the variability of spectral light attenuation across the shelf (Figure 4.9). Based on Figure 4.9, the enclosed coastal waterbody has high K_d variability during late dry (August, September, October) to early wet (November, December, January) seasons, while the late wet season (February, March, April) was marked by high K_d variability in the open coastal waterbody. In the mid-shelf and offshore water bodies, K_d variability in the green and red wavelengths was most notable during the early dry season (May, June, July) and typically during late wet (especially in the blue wavelengths) and late dry seasons.

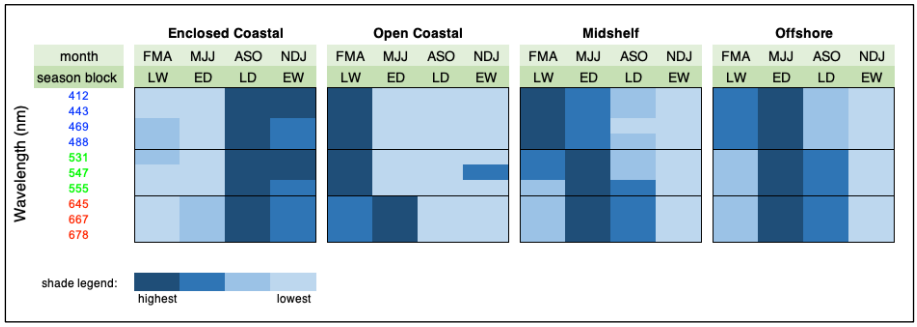

Figure 4.9 Summary of partial dependence of season blocks at each cross-shelf waterbody and wavelength showing how much season affects the variability of spectral K_d. Abbreviations: (season blocks) LW – Late Wet, ED – Early Dry, LD – Late Dry, EW – Early Wet; (month) FMA – February, March, April; MJJ – May, June, July; ASO – August, September, October; NDJ – November, December, January.

4.3.2.5 Reduced random forest models for the mid-shelf waterbody

The importance of Chl *a* in the mid-shelf waterbody based on the full models presented in Section 4.3.2.2 imply strong variability and potentially high concentrations (Figure 4.10) contrary to typically low values reported in Brodie et al. (2007). Hence, this motivated further investigation using a reduced form of the original random forest models; this time focused on each season block and wavelength to narrow down the associated temporal aspect of the Chl *a* signal which may aid in interpreting this result. Reduced models excluded the early wet season block since the categorised partial dependence plots (Figure 4.9) indicated this season block was least important in the mid-shelf.

The reduced RFMs confirmed Chl *a* as the best predictor of light attenuation in the mid-shelf waterbody across the seasons considered (Figure 4.11 to Figure 4.13) with 35 to 40% IncMSE, except in the late wet season's 667 nm and 678 nm wavelength models, where SST showed a marginally higher variable importance than Chl *a* (Figure 4.11i to j). Of the three reduced RFMs, river discharge showed relatively higher mean variable importance in the late wet season block (Figure 4.11) with an 11% IncMSE across all wavelengths (Table 4.8) but with almost negligible variable importance in the dry season blocks (2 and 4% IncMSE for early and late dry, respectively). Along with river discharge in the late wet season block, CDOM also showed moderate importance in the blue and green wavelengths (with respective mean of 19% IncMSE and 16% IncMSE) as well as NAP with comparable importance in the green and red wavelengths (respective mean of 25% IncMSE and 22% IncMSE) (Figure 4.11).

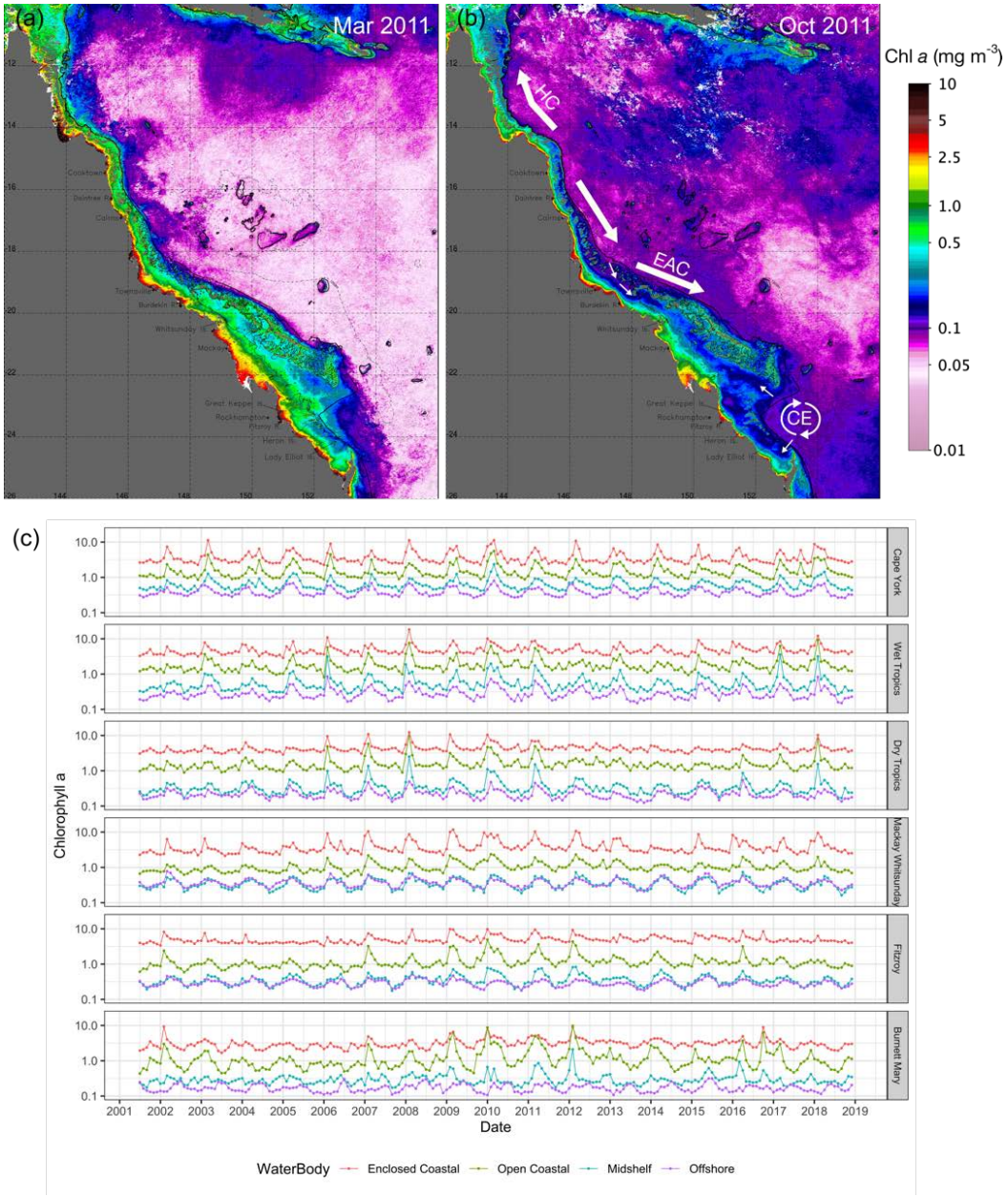

Figure 4.10. Monthly Chl a concentration in the Great Barrier Reef from remote sensing with example spatial maps for months during the (a) late wet season highlighting the overall high surface concentrations within the shelf and (b) early dry season showing the surface signal of oceanic intrusions (white arrows) in the central GBR and the narrower spatial extent of high surface Chl a concentration; and (c) monthly time series of Chl a summarised for each NRM region arranged from north to south (rows) and each cross-shelf waterbody denoted by colour. Note that the y-axis is on a logarithmic scale with limits from 0.01 to 10.0 mg m^{-3}. HC – Hiri Current, EAC – East Australian Current, CE – Capricorn Eddy (Weeks et al., 2012).

In the late dry season (Figure 4.13), NAP showed moderate to high importance after Chl *a* (with mean 16, 23, and 29% IncMSE in blue, green, and red wavelengths, respectively) along with high SST importance in the red wavelengths (25% IncMSE). CDOM indicated about 14% IncMSE importance in the red wavelengths during the late dry season with the remaining predictors contributing minimally to the model predictions.

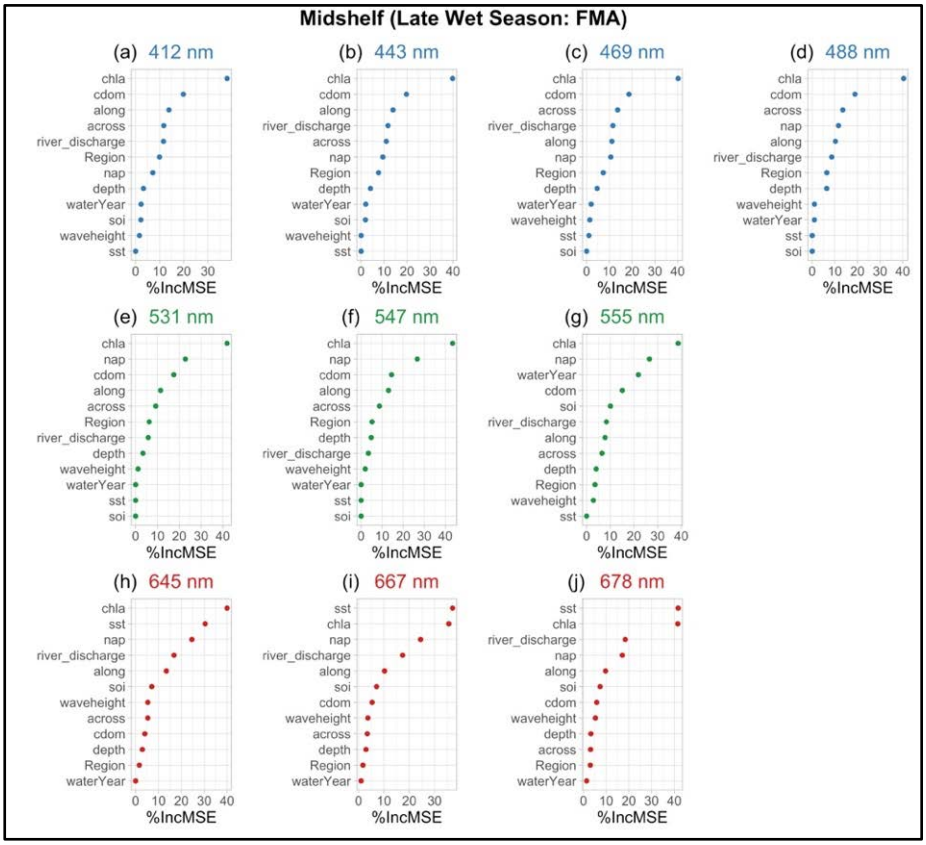

Figure 4.11. Importance of variables included in the reduced random forest model in predicting the spatial and temporal change in spectral K_d in the mid-shelf waterbody during the late wet season block for each wavelength region: (a to d) blue, (e to g) green, and (h to j) red.

Table 4.8. As per Table 4.4 but for the mid-shelf waterbody and late wet season block (February, March, and April).

	Wavelength region	Blue			Green			Red			Across all		
	Summary of variable importance	mean	min	max	mean	min	max	mean	min	max	mean	min	max
Model predictors	Region	7.8	6.5	9.9	5.0	3.5	6.2	2.1	1.6	3.1	5.3	1.6	9.9
	Water year	1.8	1.0	2.2	7.3	0.0	21.9	0.8	0.0	1.4	3.2	0.0	21.9
	Across	12.4	10.9	13.6	8.1	6.5	9.2	4.0	3.2	5.3	8.6	3.2	13.6
	Along	12.3	10.3	13.9	10.7	7.8	13.0	11.1	9.7	13.4	11.5	7.8	13.9
	Depth	4.6	3.3	6.4	4.1	3.4	4.8	3.1	2.9	3.3	4.0	2.9	6.4
	Wave height	1.0	0.0	1.6	2.0	1.1	2.9	4.8	3.7	5.3	2.4	0.0	5.3
	River discharge	10.8	8.6	11.7	5.9	3.4	8.3	17.5	16.8	18.4	11.4	3.4	18.4
	SOI	1.0	0.0	2.2	3.4	0.0	10.1	7.2	7.1	7.3	3.6	0.0	10.1
	SST	0.3	0.0	1.0	0.0	0.0	0.0	36.4	30.4	41.7	11.0	0.0	41.7
	Chl *a*	**39.6**	**38.0**	**40.4**	**41.3**	**38.7**	**43.4**	**39.0**	**35.6**	**41.5**	**40.0**	**35.6**	**43.4**
	NAP	9.7	7.2	11.6	25.3	22.8	26.6	22.1	17.1	24.6	18.1	7.2	26.6
	CDOM	19.3	18.6	19.8	15.7	14.4	17.5	5.1	4.0	5.9	13.9	4.0	19.8

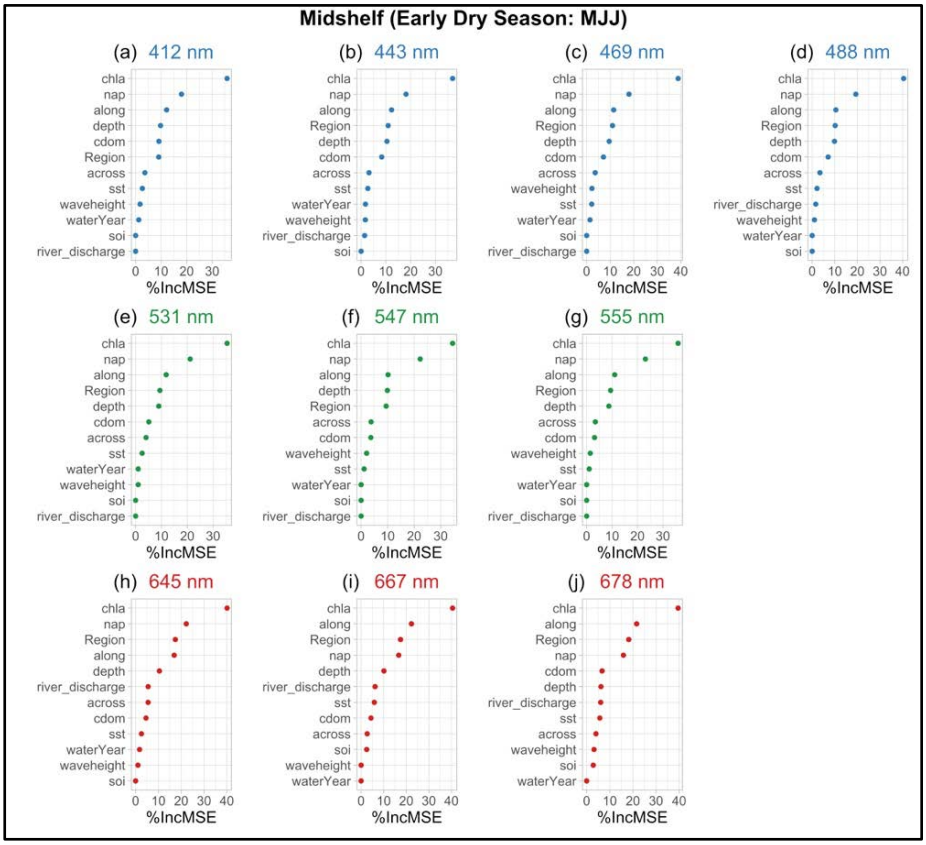

Figure 4.12. Same as Figure 4.11 but for the early dry season block.

Table 4.9 As per Table 4.4 but for the mid-shelf waterbody and early dry season block (May, June, and July).

	Wavelength region	Blue			Green			Red			Across all		
	Summary of variable importance	mean	min	max	mean	min	max	mean	min	max	mean	min	max
Model predictors	Region	10.3	9.1	11.0	9.4	9.4	9.4	17.7	17.4	18.2	12.2	9.1	18.2
	Water year	1.1	0.0	1.7	0.3	0.0	1.0	0.6	0.0	1.7	0.7	0.0	1.7
	Across	3.5	3.2	3.6	3.7	3.4	4.0	4.1	2.7	5.5	3.7	2.7	5.5
	Along	11.6	10.5	12.3	11.0	10.2	11.8	20.3	16.9	22.3	14.0	10.2	22.3
	Depth	9.9	9.6	10.4	9.2	8.7	9.9	8.9	6.2	10.4	9.4	6.2	10.4
	Wave height	1.7	1.0	2.2	1.5	1.0	2.1	1.4	0.0	3.2	1.5	0.0	3.2
	River discharge	0.7	0.0	1.6	0.0	0.0	0.0	5.9	5.5	6.2	2.1	0.0	6.2
	SOI	0.0	0.0	0.0	0.0	0.0	0.0	1.8	0.0	2.9	0.5	0.0	2.9
	SST	2.4	2.1	2.7	1.6	1.0	2.5	4.7	2.6	5.8	2.8	1.0	5.8
	Chl *a*	**38.0**	**35.8**	**40.5**	**35.3**	**34.5**	**36.0**	**40.0**	**39.5**	**40.5**	**37.8**	**34.5**	**40.5**
	NAP	18.3	18.0	19.3	22.2	21.1	23.1	18.2	15.9	22.2	19.5	15.9	23.1
	CDOM	7.9	7.1	9.1	4.0	3.1	5.1	5.2	4.4	6.7	5.9	3.1	9.1

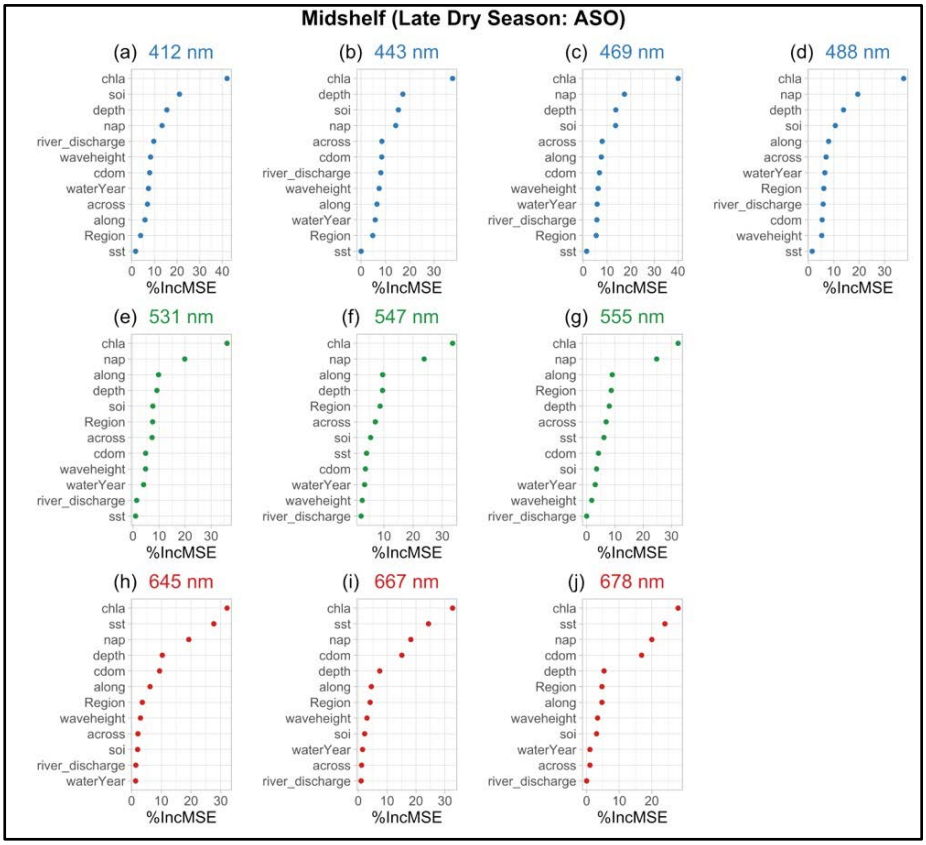

Figure 4.13. Same as Figure 4.11 but for late dry season block.

Table 4.10. As per Table 4.4 but for the mid-shelf waterbody and late dry season block (August, September, and October).

	Wavelength region	Blue			Green			Red			Across all		
	Summary of variable importance	mean	min	max	mean	min	max	mean	min	max	mean	min	max
Model predictors	Region	5.0	3.9	6.1	8.3	7.5	8.7	4.1	3.6	4.7	5.7	3.6	8.7
	Water year	6.4	5.8	7.3	3.5	3.0	4.1	1.3	1.0	1.5	4.0	1.0	7.3
	Across	7.6	6.9	8.5	7.1	6.9	7.3	1.4	1.0	2.1	5.6	1.0	8.5
	Along	7.0	5.8	7.9	9.5	9.0	9.8	5.2	4.5	6.2	7.2	4.5	9.8
	Depth	15.0	13.7	17.2	8.9	8.0	9.5	7.7	5.3	10.3	11.0	5.3	17.2
	Wave height	6.8	5.3	8.3	3.1	1.8	4.8	3.1	3.0	3.3	4.6	1.8	8.3
	River discharge	7.3	5.7	9.7	1.2	0.0	2.2	0.8	0.0	1.4	3.5	0.0	9.7
	SOI	15.1	10.6	21.0	5.5	3.5	7.6	2.4	2.0	3.0	8.4	2.0	21.0
	SST	1.1	0.0	1.7	3.7	1.0	6.1	25.3	24.0	27.7	9.2	0.0	27.7
	Chl *a*	**39.3**	**37.5**	**42.1**	**34.0**	**32.4**	**36.1**	**31.0**	**28.1**	**32.7**	**35.2**	**28.1**	**42.1**
	NAP	16.1	13.3	19.4	22.8	19.9	24.8	19.1	18.2	20.0	19.0	13.3	24.8
	CDOM	7.1	5.4	8.5	4.2	3.7	4.8	13.8	9.4	16.9	8.3	3.7	16.9

4.4 Discussion

This study determined the main drivers of the variability in light attenuation within the different water bodies in the GBR. The results highlighted strong variation in the dominant driver of spectral K_d variability depending on the wavelength and location within the shelf (i.e., enclosed and open coastal, mid-shelf or offshore water bodies), reflecting the inherent optical properties of the respective waterbody, their proximity to sources (of terrigenous material and upwelling), climate and oceanographic influences, and temporal variability.

The dominant predictors of spectral K_d variability within the inshore coastal and offshore water bodies align with the expected optical constituents at these regions. The nearshore GBR region is typically exposed to river plumes that carry significant amounts of materials of both particulate and dissolved nature (Furnas, 2003b; Devlin et al., 2012; Alvarez-Romero et al., 2013; Devlin et al., 2015). NAP and CDOM were the essential constituents driving light attenuation in the two inshore coastal water bodies. NAP, which includes suspended sediment material from rivers, does not absorb light strongly but scatters light intensely, increasing a photon's effective path length and potential for light absorption, thus light attenuation (Kirk, 2011). CDOM, on the other hand, is an intense light absorber in the UV and short wavelengths and is highest in inland waters proximal to river mouths (Kirk, 2011), which may explain its highest importance in the variability of K_d(412) in the enclosed coastal waterbody. The influence of these two components on light attenuation explains the high K_d values consistently found in the two inshore coastal water bodies across all NRM regions, but especially in the Fitzroy NRM region, which generally have higher suspended sediment concentrations (Furnas and Mitchell, 2001). This result underscores the relative exposure of the nearshore coastal areas to land-based pollution, providing further justification for the ongoing investments (State of Queensland, 2013, 2018) to manage and minimise the impact of anthropogenic influences on the GBR coastal marine ecosystem.

In the offshore waterbody, the high importance of Chl *a* and depth in the blue and green wavelengths, and *season block* (and SST to an extent) in the red wavelengths, align with the characteristics of clear oceanic waters and their optical signatures. In these waters, the attenuation (i.e., absorption and scattering) due to varying biological components, the phytoplankton and associated pigments (Morel, 1997), and related CDOM and detritus degradation products (Mobley et al., 2004) adequately describe the optical properties aside from the steep selective attenuation of seawater itself in the red wavelengths. Oceanic waters, compared to coastal waters, have typically low concentrations of Chl *a* (less than 0.5 mg m^{-3}, although a mean value for the global ocean is lower at 0.2 mg m^{-3} (Morel and Gentili, 2009)), but the blue and green regions of the light spectrum are sensitive to even slight changes in Chl *a* concentration (Moore et al., 2014). The sensitivity of the K_d values to depth, especially in the blue region, may reflect the contribution of some shallow pixels within the offshore waterbody, where the increased variability is due to changes in the physical depth of the pixel. The importance of *season block* (along with SST, Chl *a*, and CDOM) in the red wavelengths suggests that the mechanism which

sustains the variability of Chl *a* concentration in the offshore waterbody varies temporally. Here, internal recycling of nutrients and reintroduction from subsurface mixing and upwelling supports the phytoplankton growth (Furnas and Mitchell, 1996; Bristow et al., 2017), controlled by the local dynamics (i.e., oceanography), which may also have temporal variation.

The importance of Chl *a* in the K_d variability was also noted in the mid-shelf waterbody. First and foremost, this implies that Chl *a* concentration in the mid-shelf fluctuates seasonally, as highlighted in Figure 4.10. This result is also intriguing because it invokes the question as to the potential mechanism that drives the seasonal variability or which can support phytoplankton blooms in this part of the shelf leading to high concentrations. Central to this is thus the question of source (or sources) of nutrients that can fuel blooms (e.g., large enough to be detected through ocean colour remote sensing, such as the Chl *a* dataset used in this analysis). Some mechanisms can be explored depending on how connected the mid-shelf waterbody is to the rest of the GBR shelf regions.

Firstly, a mechanism that may play the role of supplying the required nutrients that limit growth (Bristow et al., 2017) is upwelling (Furnas and Mitchell, 1996). Upwelling is the upward movement of water that brings deep, cold, and nutrient-rich waters towards the sunlit surface layer of the water column (Garrison and Ellis, 2016) leading to elevated nutrient concentrations and a broad temperature difference as deep water rises. Within the central GBR, intrusions of oceanic (Coral Sea) waters have been suggested to induce upwelling events (Andrews and Furnas, 1986; Furnas and Mitchell, 1996) and may be detected by remote sensing datasets as a tongue of low chlorophyll surface waters moving onshore from along the continental edge (Figure 4.10b). These oceanic intrusions occur along the narrow passages in the outer reef matrix, often coinciding with the poleward intensification of the East Australian Current (Ridgway, 2007) along the eastern coastline of Australia during austral summer, but significant intrusion events are most often observed between October to May and can spread onshore (e.g., by 50 km over one week or 100 km over several weeks) (Andrews and Furnas, 1986).

Using combined *in situ* datasets obtained from the moorings deployed in Palm Passage on the outer-shelf (~70 m depth) and Myrmidon Reef on the shelf-slope (~205 m depth) and results from the eReefs hydrodynamic model (Sparse Hydrodynamic Ocean Code (SHOC), (Herzfeld, 2006)), Benthuysen et al. (2016) recently showed that cool water intrudes onto the shelf along the seafloor during weak equatorward winds or strong poleward winds and an intensified poleward-flowing EAC. Although the generation of this intrusive upwelling was found in the outer-shelf, the along-shelf and onshore spatial extent of SST from the intrusions do reach the mid-shelf (e.g., onshore propagation of 1-3°C cooler bottom waters near Palm Passage to over 70 km from the shelf break, (Benthuysen et al., 2016)). Thus, the resulting change in nutrient supply at the sunlit upper layers from these oceanic intrusions can potentially drive the biological production even in the mid-shelf, supporting the RFM results presented for this waterbody. Temporally, the reduced RFMs showed that the importance of Chl *a*, along with SST, NAP and CDOM (parameters that could be related to upwelling and phytoplankton cells),

especially in the red wavelengths, coincide with the late dry *season block,* which includes the month of October when oceanic intrusions begin to occur (Andrews and Furnas, 1986) with also visible surface manifestation (see Appendix 7.5 for example monthly GBR image of MODIS Aqua-derived Chl *a* concentrations showing an example of oceanic intrusions). The near-surface expression of the cooling events from the uplift of thermocline during intrusions is not necessarily reflected on the near-surface temperature, which may continue to increase on the surface (Benthuysen et al., 2016) as would happen during the austral summer due to seasonal variability, despite simultaneous cooling of bottom temperatures.

Upwelling events have also been observed in the northern GBR. Here, the upwelling is tidal jet-driven resulting from strong currents flowing through narrow passages within the barrier reefs during the rising tide (Wolanski et al., 1988). A tidal jet-vortex system also develops, propagating nutrient-rich upwelled waters inshore of the barrier reefs (Wolanski et al., 1988; Drew, 2000). This type of upwelling in the northern GBR has been proposed as the reason for the development of and thriving *Halimeda* meadows within a few kilometres inshore of the barrier reefs but may also support nutrient requirements of phytoplankton in these waters (Wolanski et al., 1988).

Secondly, the mid-shelf waterbody may not entirely be disconnected from the influences of nearshore activities and processes. Land-derived materials still have the potential to reach the mid-shelf, especially during acute events (i.e., cyclones and strong rainfall events that may result in river floods). In these cases, river discharge and flood plumes may supply the nutrients that can drive biological activity leading to phytoplankton blooms. Devlin and Brodie (2005) showed that plumes could spread away from the coast and reach the outer shelf beyond the main barrier reefs during cyclone events, noting that dissolved nutrients disperse much further than particulate materials transported in the plumes. The location and width of the shelf within the vast and complex GBR setting may also define the connection between the mid-shelf waterbody and the impacts of river inputs. For example, where the shelf is wide (e.g., as in the southern GBR), the nearshore influences and the mid-shelf may be more disconnected. Here, the mid-shelf may be considered far distant enough to be mostly spared from the direct impact of pulses of nutrient inputs from land and river runoffs further aided by the local oceanography (i.e., the Coriolis effect), which steers the overall surface layer transport northward along the coast. The net surface Ekman transport hinders the offshore spread of materials and ensures that terrigenous materials and other buoyant particles stay close and concentrated near the coastline (Alongi and McKinnon, 2005; Devlin and Brodie, 2005).

Fabricius et al. (2016) also showed that the decline in photic depth, a proxy for water clarity, due to river discharge has a cross-shelf gradient that decreased from the coast to offshore zones in the southern GBR, highlighting strong effects in the inner zones where the shelf is wide. The northern half of the GBR has a relatively narrow shelf, so the degree of connection between shelf regions is likely, and the mid-shelf may be more exposed to influences from adjacent rivers (Blondeau-Patissier et al., 2014). At

latitudes 14.5°S to 19.0°S, Fabricius et al. (2016) noted the strongest effects of river discharge on photic depth across the shelf, including >40% photic depth declines in the offshore, noting that even the offshore waterbody, hence the mid-shelf, was not isolated from riverine inputs where the shelf is narrow and river loads are high. In addition, features like the bottom nepheloid layers have been observed near the coast in Cairns (latitude 16.9°S) (Wolanski and Spagnol, 2000; Wolanski et al., 2003). Nepheloid layers are features in the water column or near the bottom boundary characterised by increased light scattering due to particles produced by biological activity but may also include high concentrations of suspended sediment materials accumulated and transported from nearby river plumes (McCave, 2009). In the GBR, observations of bottom nepheloid layers indicated that these features might also be exported offshore (e.g., ~30 km offshore from the coastal zone) (Wolanski and Spagnol, 2000; Wolanski et al., 2003) and may serve as another indication that riverine inputs have the potential to supply the nutrients required to boost biological processes in the mid-shelf waterbody.

Thirdly, other sources may still contribute to nutrients in the mid-shelf waterbody, including rain, atmospheric deposition of iron-rich dust from inland storms, biological nitrogen fixation and wind-driven resuspension of benthic sediments, which also releases pore-water nutrients into the water column (Furnas and Mitchell, 1996; Devlin and Brodie, 2005; Schaffelke et al., 2012; Bristow et al., 2017). Another physical process that may serve as an arbitrary mechanism is the formation of convergent frontal structures (Bakun, 2012), which may develop at the interface between the river plumes' fresher water mass and the receiving 'oceanic' waters. The frontal interface between the surface waters of these water masses with contrasting densities may entrain and concentrate buoyant particles (including particulate sediment materials and nutrients). During a strong river flood, e.g., the recent Burdekin floods in 2019 (which resulted from a prolonged intense rainfall event), the boundary of the plume was extended further offshore, reaching the mid-shelf boundary (see Figure 1.1b for a Landsat 8 True Colour satellite image of the floods taken on 11th February 2019 and Appendix 7.6 for the full resolution of the image), the entrained materials in the fronts may provide a transient nutrient source whose duration will be controlled by local hydrodynamics.

4.5 Conclusion

The spectral variability of light attenuation and hence benthic light availability in the GBR is influenced by a complex interplay of many factors, including the composition and optical properties of the water. The objective of this study was to determine the primary driver of light attenuation within the GBR, a piece of critical information that can be used to assess the impacts of land-based pollutants and inform management for catchment and marine ecosystem conservation in the GBR. We used RFMs on the 17.5-years of spectral K_d data and a suite of optical constituents and environmental predictors to determine what drives the variability of light attenuation within the different NRM regions and water bodies in the GBR between July 2002 and December 2019. We found that CDOM and NAP, predictors

reflecting terrestrial and anthropogenic inputs, strongly influence variations of K_d in the inshore coastal water bodies offering sound justification to ongoing management efforts focused on these regions. In contrast, K_d variability in the offshore waterbody was consistent with the inherent optical properties in clear oceanic conditions dominated by variations in Chl *a* concentration, highlighting that this region may relatively be unscathed from direct impacts of terrestrial influences and anthropogenic activities along the GBR coastline. In the mid-shelf, K_d variability reflects the potential combined influence of variations in Chl *a* concentration driven by land-derived nutrient inputs and local oceanography within the shelf, temporally consistent with the known seasonal dynamics of extreme rainfall and flood events and oceanic intrusions and upwelling, respectively. Spatially, the potential of land-derived nutrient inputs to drive the variability in Chl *a* concentrations may be higher in the northern NRM regions where the width of the shelf is narrow and the connection of the mid-shelf to the inshore influences is probable, as have been suggested by other studies (Blondeau-Patissier et al., 2014; Fabricius et al., 2016). The outcomes of this analysis may add support to the ongoing government investments to assess, monitor and adjust catchment management to mitigate or minimise the impact of exposure to land-based pollution within the GBR and allocate effort, especially in the mid-shelf.

Some limitations and caveats are inherent in the analysis that are worth highlighting. First, the datasets used as predictors of variability in spectral light attenuation values within the GBR are a combination of model, remote sensing-derived, and *in situ* values, with varying (temporal or spatial) resolutions or potentially confounding effects. The remote sensing-derived datasets (i.e., Chl *a*, CDOM, NAP, and to some extent SST), for example, were based on remote sensing reflectance measurements obtained from the same satellite sensor, MODIS-Aqua (or MODIS-Aqua + Terra in the case of SST) transformed using specific algorithms (each mentioned in the data section) to derive target values and thus represent a comparison of one data transformation to another whilst derived from the same observations. However, the potential benefit of information from this study outweighs this limitation since this is the first attempt to analyse a spatially- and temporally-rich dataset on light attenuation within the GBR. In addition, using a single satellite dataset (MODIS Aqua) serves to mitigate the introduction of inter-mission bias and uncertainties associated with differences in the design, flight, calibration, and data quality characteristics of different ocean colour satellite sensors. It would also be ideal to have these satellite datasets validated using *in situ* measurements to increase confidence in the outcome and potential applications that may arise from the analysis and should be a focus in the future.

Second, other datasets used in the analysis as a predictor were spatially coarse. The wave height and river discharge values were taken only from very few point locations that were distributed spatially to each relevant 1 km^2 pixel and thus may not necessarily be representative of the spatial variation of these variables within the GBR, which may also affect how light is attenuated spatially.

Future work should consider tidal height variation to account for short-term high-frequency fluctuations, which can be modelled with high accuracy using the existing tidal inversion scheme (i.e.,

OSU Tidal Inversion Software, OTIS) and which allow spatially relevant values. Unfortunately, it was not possible to conduct the tide-modelling during this project due to time constraints. Despite these limitations, the analysis has highlighted exciting results towards a better understanding of benthic light dynamics at the temporal and spatial scale of the whole GBR that has not been achieved before.

"People protect what they love." – Jacques-Yves Cousteau (1910 – 1997)

5 A benthic light index of water quality in the Great Barrier Reef, Australia

This chapter was published as:

Canto, M.M., Fabricius, K., Logan, M., Lewis, S., McKinna, L., and Robson, B. (2021) *A benthic light index of water quality in the Great Barrier Reef, Australia.* Marine Pollution Bulletin, 169, 112539. doi: https://doi.org/10.1016/j.marpolbul.2021.112539

Abstract

Good water quality is essential to the health of marine ecosystems, yet current metrics used to track water quality in the Great Barrier Reef are not strongly tied to ecological outcomes. There is a need for a better water quality index (WQI). Benthic irradiance, the amount of light reaching the seafloor, is critical for coral and seagrass health and is strongly affected by water quality. It therefore represents a strong candidate for use as a water quality indicator. Here, we introduce a new index based on remote sensing benthic light (bPAR) from ocean colour. Resulting bPAR index time series, based on the extent to which the observed bPAR fell short of the locally- and seasonally- specific optimum, showed strong spatial and temporal variability, which was consistent with the dynamics that govern changes in water clarity in the Great Barrier Reef. Our new index is ecologically relevant, responsive to changes in light availability and provides a robust metric that may complement current Great Barrier Reef water quality metrics.

5.1 Introduction

5.1.1 Great Barrier Reef and water quality

Coastal oceans around the world are vulnerable to the impacts of multiple stressors ranging from increased coastal developments and anthropogenic activities to extreme weather events and climate change. Unfortunately, the Great Barrier Reef (GBR) is not impervious to these stressors (Wolff et al., 2018). The GBR is one of the most diverse marine habitats on Earth and forms a critical part of the Australian economy (Deloitte Access Economics, 2013) and national natural and cultural heritage (Lucas et al., 1997). Recurrent and recent mass coral bleaching due to thermal stress (Hughes et al., 2017; Hughes et al., 2018b), pollution from agricultural runoffs (Kroon, 2012) and the associated declining quality of the water entering the GBR lagoon (Fabricius et al., 2016), and crown-of-thorns seastar (COTS) outbreaks (Fabricius et al., 2010) present current challenges in maintaining the health of the GBR. Considering these numerous environmental pressures, it is important for management agencies to have tools that can be used to identify and monitor changes that can impact the ecosystem's health. Understanding the factors driving these changes and how the ecosystems respond to both short- and long-term environmental forces (Ackleson, 2003) can help focus management actions, integrate relevant management approaches and increase the anticipated success in addressing identified challenges.

One of the main priorities for maintaining the health and resilience of the GBR ecosystems is the management of water quality flowing into the Reef since poor water quality can reduce light availability at depth. Hence, although warming ocean temperatures and rising acidity levels due to climate change (Heron et al., 2017; Hughes et al., 2018a) is considered as the greatest threat to the GBR, poor water quality is also considered a key factor for declining marine ecosystem health (Fabricius et al., 2016) and regarded as a major threat to the health of the GBR (De'ath and Fabricius, 2010; Devlin et al., 2015). The need to address the threats associated with declining quality of the water (Fabricius et al., 2016) was greatly recognised by both the Australian and Queensland Governments' and reflected on the implementation of the Reef 2050 Long-term Sustainability Plan (Reef 2050 Plan) (Commonwealth of Australia, 2015). The Reef 2050 Plan aims to preserve the heritage value of the Reef between now and 2050 and to provide support to the development and implementation of water quality improvement plans strategic to relevant catchment and coastal systems along the length of the GBR, including development of tools to inform and monitor GBR water quality.

5.1.2 The ecological importance of benthic light

Light is essential for photosynthesis, the foundation of most marine food webs and the dominant source of energy for corals and seagrasses (Kirk, 2011). For these benthic organisms, the most important part

of the light spectrum is the photosynthetically active radiation (PAR) – the amount of available solar irradiance (light) typically within the 400 to 700 nm wavelength range – and specifically, the amount of PAR reaching the sea floor or reef surfaces, known as 'benthic PAR' (bPAR, mol photons m^{-2} d^{-1}) (Magno-Canto et al., 2019; Magno-Canto et al., 2020). The spatial and temporal variability of bPAR in shallow coastal environments is a crucial control of benthic primary production and its contribution to the total primary production (Gattuso et al., 2006; Gattuso et al., 2020). It is therefore key to understanding and monitoring the dynamics and health of important benthic habitats near the coasts.

Although some species of seagrass and corals can tolerate a wide range of benthic irradiance levels, they do have light optima, and both low and high benthic light can create stress (Gattuso et al., 2006; Muir et al., 2015; Bessell-Browne et al., 2017b). Some species can tolerate short periods of reduced light intensities in shallow waters, but their photosynthesis and growth may be reduced during these periods. Some seagrass taxa are able to persist to appreciable water depths owing to effective morphological and physiological adaptations to low-light conditions (Dennison, 1987; Ralph et al., 2007). However, reduced light availability, whether chronic or acute, is a threat to seagrass meadow health (Collier and Waycott, 2009; McKenzie et al., 2012), a major driver of seagrass loss in coastal and inshore GBR (Collier et al., 2012a; Collier et al., 2012b), and can strongly alter coral communities (Muir et al., 2015; Bessell-Browne et al., 2017b).

Interactions between benthic irradiance and other stressors are also important for both corals and seagrasses. For example, turbidity-induced light reductions can result in reduced coral recruitment and diversity (Fabricius, 2005). Similarly, prolonged exposure to 'dark' (low to no light) conditions during high turbidity (e.g., near dredging locations) can cause sub-lethal bleaching in some corals (Bessell-Browne et al., 2017a; Bessell-Browne et al., 2017b) while others were able to adjust to combination of low light levels (2.3 mol photons m^{-2} d^{-1}) and elevated suspended sediment concentrations (Jones et al., 2020). Other examples include increased coral bleaching during high irradiance in the presence of thermal stress (Leahy et al., 2013) and compromised seagrass survival during limited light levels and high nutrient conditions (McKenzie et al., 2010). Further, for some seagrass species (i.e., *Halophila ovalis*), additional shading in an already-turbid low light environment can result in complete mortality, demonstrating that historical light exposure is important in maintaining the resilience and ability of seagrasses to acclimate to chronic low light regimes (Yaakub et al., 2014). Yet, there is also recent evidence that during heat-induced bleaching events some turbidity can benefit nearshore reef corals by alleviating the harmful effects of the combination of thermal stress and high irradiance (Cacciapaglia and van Woesik, 2016; Morgan et al., 2017; Fisher et al., 2019; Sully and van Woesik, 2020). These results highlight the complex role of light availability to the survival, growth and maintenance of dependent benthic organisms and hence, also underscore the need to develop a water quality metric that is not only ecologically relevant but also responsive to changes in light availability.

5.1.3 Physical controls of benthic PAR

bPAR is controlled by both water quality and water column depth (Magno-Canto et al., 2019). In shallow coastal waters, bPAR is mainly determined by the attenuation of light as it travels through the water column by optically active constituents including phytoplankton, suspended non-algal particulate matter, and coloured dissolved organic matter (CDOM) which attenuate (either by absorption and/or scattering) and change the character of light with depth (Kirk, 2011; Brando et al., 2012).

Water clarity in the GBR, a parameter related to water quality and commonly expressed as Secchi depth (Z_{sd}) or photic depth, is affected by river discharge. River flood plumes often transport high loads of fine sediments, nutrients – that can induce phytoplankton blooms – and dissolved organic matter that directly impact coastal water clarity. Previous studies indicate that tracking interannual variability is important to understand temporal variability and to develop predictive casual relationships (Fabricius et al., 2013; Fabricius et al., 2014; Fabricius et al., 2016). Metrics to calculate the exposure of GBR reef and seagrass habitats to flood plumes have been developed (Devlin et al., 2012; Petus et al., 2014; Devlin et al., 2015) using the 'colour' of water in the vicinity of the plume from enhanced True Colour satellite-imagery. These metrics have provided an integration of multiple potential impacts of flood plumes, from reduced water clarity to freshwater exposure to the potential impacts of pesticide exposure and sedimentation. As such, these exposure metrics have offered a useful estimate of risk associated with water quality that can inform targeted management of relevant catchments (Alvarez-Romero et al., 2013; Petus et al., 2018).

However, light penetration and photic depth indeed vary across the whole GBR in response to inter-annual variations in river discharge (Logan et al., 2013; Fabricius et al., 2014; Fabricius et al., 2016) which occur not only in the coastal areas adjacent to river mouths, but also in the mid- and outer-shelf areas of some regions. These effects were also not only shown to be spatially extensive but can be observed more than six months after flood plumes have dispersed, suggesting that flood plume detection is not in itself sufficient to characterise the likely spatial and temporal extent of the ecological impacts of river runoff and human activities in Queensland catchments and coastal regions.

5.1.4 The need for an improved water quality index (WQI)

A motivation for developing a benthic light-based index of water quality is the need to relate changes in bPAR to ecological outcomes such that interannual progress and variations in water quality can be tracked within the whole GBR region (i.e., within each Natural Resource Management (NRM) region and waterbody across the GBR shelf, see Figure 5.1). A WQI is a quantitative metric that provides a standardised measure of water quality indicators (examples discussed below) as compared against a threshold value (Robillot et al., 2018), defined at a level intended to help identify the need for management actions (Great Barrier Marine Park Authority, 2010b). In the GBR, the WQI is used to

generate scores for water quality which forms part of the annual GBR "Report Card" (Robillot et al., 2018) used to monitor the condition and trend of GBR ecosystem health and drivers to guide management based on a consistent science-based national strategy for managing water quality (e.g., Reef 2050 Water Quality Improvement Plan 2017-2022 (State of Queensland, 2018) as part of the Reef 2050 Long-term Sustainability Plan (Reef 2050 Plan) (Commonwealth of Australia, 2015)).

Two water quality sub-indicators (i.e., productivity and water clarity) are currently used to provide information about GBR inshore marine conditions and generate a WQI reported as part of the annual GBR Report Cards, indicated by observable measures: chlorophyll-*a* pigment concentration, Chl *a* (mg/L) as a productivity sub-indicator and Secchi depth, Z_{sd} (m) as a water clarity sub-indicator (Robillot et al., 2018). Chl *a* associated with phytoplankton biomass is a widely-used proxy for nutrient pollution in the GBR, in that annual mean concentrations above a threshold (which varies from 2.0 to 0.4 mg/L from inshore to offshore locations within the GBR) are considered an indication of water quality degradation associated with eutrophication (increased nutrient inputs, e.g., from floods or river runoffs, and a subsequent increase in phytoplankton biomass) (Schaeffer et al., 2013) and light attenuation (Platt et al., 1994). The photic depth, Z_{sd} which quantifies the depth of in-water visibility (Kirk, 2011), is a common proxy for water clarity (transparency) and is inversely related to turbidity (i.e., cloudiness/opacity of the water). Declining Z_{sd} indicates increased turbidity and reduced light. In the current GBR Report Cards, individual scores for the two water quality sub-indicators are formulated based on deviations from a benchmark (e.g., against threshold values derived from water quality guidelines), individually calculated at the level of the observations and aggregated using a nested hierarchical structure, e.g., Measures are nested within Sub-indicators which is nested in Indicators (see Robillot et al. (2018) for more details). The average of the two sub-indicator scores provide the combined marine WQI score which is converted into a simple alphanumeric grade scale used in reporting to indicate water quality status. Although indicative of changes in water quality, Z_{sd} does not directly tell us what light environments are experienced by seagrasses and corals, as the relationship varies with depth in the water column and with the colour (i.e., optical properties) of the water. Hence, while the spatial and temporal variations in Z_{sd} can be characterised using existing remote sensing data products developed for the GBR (Weeks et al., 2012), translating these variations to ecological outcomes such as the exposure to stress from low-light is not straightforward.

Using satellite-derived bPAR to provide an index of water quality instead of the WQI from combined Z_{sd} and Chl *a* indices will allow the interacting effects of complex optically active constituents that define water clarity and the spatially variable bathymetry (water depth) to be considered. This will allow, for the first time, the application of ecologically-relevant, GBR-specific light thresholds for corals, seagrasses and overall ecosystem health.

The objective of this work is therefore to use the new satellite-derived estimates of daily benthic irradiance or bPAR to develop an ecologically-relevant marine index of water quality to replace or

complement the current combined Z_{sd} – and Chl *a*–based index. The proposed benthic light index will incorporate the benthic light regimes within the GBR at spatial scales that is required by the GBR Marine Park Authority (GBRMPA) in the preparation and issue of the annual GBR Water Quality Report Cards.

5.2 Methods

5.2.1 Study Site

The GBR Marine Park lies adjacent to the Queensland coast along the north-eastern seaboard of the Australian continent. It stretches about 2300 km in length, occupying the continental shelf roughly between 9°S and 24°S. Along its length, there are 35 main river basins with catchment areas that drain into the GBR lagoon (Furnas, 2003a), and each catchment varies in its land use (Fabricius et al., 2016) and impact on the quality of the water within the lagoon. To facilitate regional comparisons consistent with recent efforts to manage and monitor the health of waters within the GBR lagoon and account for spatial differences across the shelf, we used a combination of the NRM regional GBR catchment and cross-shelf waterbody boundaries which respectively include (from North to South): the Cape York, Wet Tropics, Dry Tropics (Burdekin), Mackay-Whitsunday, Fitzroy, and Burnett Mary regions, and the (i) enclosed coastal, (ii) open coastal, (iii) mid-shelf and (iv) offshore water bodies (Great Barrier Marine Park Authority, 2010a) (see Figure 5.1). For clarity, combinations of the NRM regions and the water bodies are interchangeably referred to as "zones" throughout the manuscript.

5.2.2 Defining spatial and temporal aggregation aligned with the current GBR Report Cards

Annual GBR "Report Cards" are currently used to monitor and communicate the condition and trend of GBR ecosystem health and drivers to guide management of the Reef. The GBR reporting framework uses consistent, well-defined spatial boundaries for aggregation, which are based on a combination of the NRM regions and cross-shelf waterbody boundaries (as shown in Figure 5.1) and temporal boundaries that uses a "water year" – defined as the period between 01 October to 30 September of the following calendar year. This temporal aggregation ensures that austral wet seasons are not split across reporting years (Waterhouse et al., 2017) and is hence adapted in the present study to align with the current management, monitoring and reporting framework of water quality status in the GBR.

5.2.3 The bPAR index

The development of a bPAR index requires three components: (i) a benthic light threshold relevant to targeted benthic organisms (i.e. corals and seagrasses); (ii) robust, spatiotemporally consistent estimates of bPAR data; and (ii) a method of combining these to map benthic light stress within the entire GBR and generate an index that can inform managers and policy makers of when and where benthic light

conditions are less optimal for corals and seagrasses as a result of intermittent factors that control water clarity. The following sections provide more detail for each of these components.

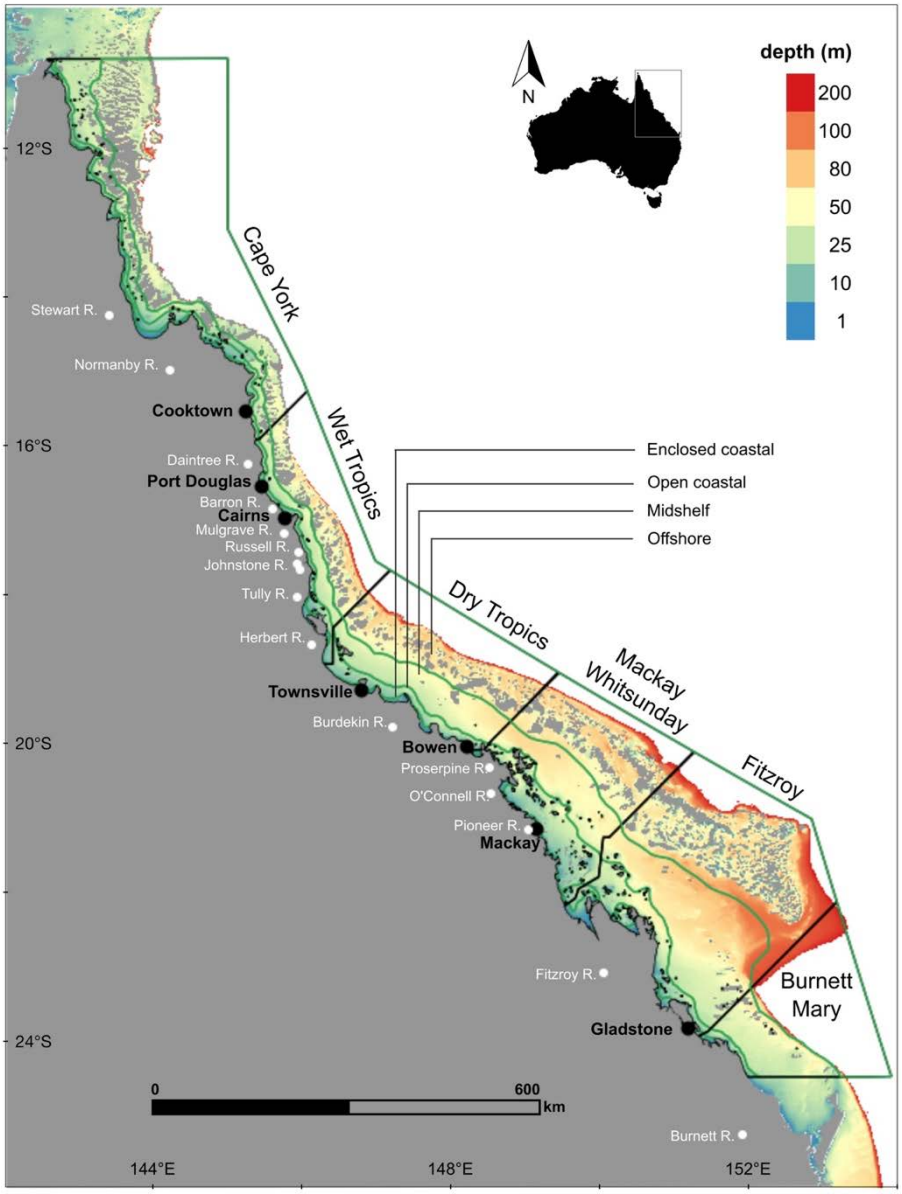

Figure 5.1. Map of the Great Barrier Reef showing the reef matrix, boundaries of the six NRM regions (N to S: Cape York, Wet Tropics, Dry Tropics, Mackay Whitsunday, Fitzroy, and Burnett Mary) and the four cross-shelf water bodies used in the analysis (Enclosed coastal, Open coastal, Mid-shelf and Offshore) with boundaries delineated by the green contour lines. Also indicated are several major cities (filled white circles) and rivers (filled red circles) along the length of the GBR.

5.2.3.1 Benthic light responses and thresholds for key GBR coral and seagrass species

Information about light responses and relevant thresholds for some key GBR coral and seagrass species was compiled from both field and laboratory/experimental data obtained from complementary laboratory studies and a review of pertinent literature. Our purpose is to determine a collective

maximum benthic light threshold that both corals and seagrasses could potentially make use of for photosynthesis and growth under varying water quality conditions.

The relationship between light intensity and photosynthesis is modelled as a photosynthesis-irradiance (P-E) curve (Sakshaug et al., 1997) which provides a measure of the efficiency of utilization of the incident light (Kirk, 2011). In a P-E curve, photosynthetic rates initially increase linearly with irradiance until the maximum photosynthetic potential, P_{max}, is reached. Further increases in irradiance then result to photosynthetic rates plateauing, until the point of light-induced reduction in photosynthetic capacity of the plant (i.e., photoinhibition) (Sakshaug et al., 1997). P-E curves thus provide the information needed to define a relevant threshold for our benthic light index.

Most of the previous studies that examined benthic light requirements have focused on determining the lowest light limits at which species are being found (e.g., (Gattuso et al., 2006; Muir et al., 2015). In contrast, we focused our index on the light needed to obtain P_{max}. As in a typical P-E curve, further increases in irradiance level after P_{max} is reached do not offer further growth benefits in terms of photosynthetic gain by relevant benthic organisms and in fact lead to photoinhibition (Kirk, 2011).

PAR requirements and responses of corals and seagrasses to light vary considerably between species and conditions (Table 5.1). For example, Muir et al. (2015) has suggested that for Acropora corals, the most important reef-building coral species found in the GBR, a winter PAR threshold of 5.2 mol photons m^{-2} d^{-1} strongly determines their depth limits, a value relatively lower than the 7 to 8 mol photons m^{-2} d^{-1} light limit for reef formation reported by (Kleypas, 1997). Considering the surface area corresponding to global coastal oceans where important benthic organisms flourish, Gattuso et al. (2006) (recently updated as (Gattuso et al., 2020)) also calculated a mean benthic irradiance of 1.2 mol photons m^{-2} d^{-1} at the maximum depth of coral colonisation as well as a mean compensation irradiance for benthic communities at a range of 0.24 to 4.4 mol photons m^{-2} d^{-1}. Gattuso et al. (2006)'s mean benthic irradiance value is comparable to benthic light threshold for reef development of ~2 mol photons m^{-2} d^{-1} estimated for Whitsunday Islands in the GBR – a region with strong water quality gradient (Cooper et al., 2007) and in the Gulf of Siam (Titlyanov and Latypov, 1991). A benthic PAR threshold for other important benthic habitats (e.g., macroalgae) has also been reported where levels below 2 mol photons m^{-2} d^{-1} were found to cause steep declines in macroalgal species richness (Hurrey et al., 2013) while other assemblages such *Lobophora*-turf and *Halimeda*/Bryopsidales have strong affinity to light thresholds of 3.6 mol photons m^{-2} d^{-1} and 4.6 mol photons m^{-2} d^{-1}, respectively.

For seagrasses, average daily irradiance (i.e., PAR) above 5.0 to 8.4 mol photons m^{-2} d^{-1} has been associated with increased seagrass abundance (i.e., cover) but prolonged exposure to conditions below 3.0 mol photons m^{-2} d^{-1} resulted in 50% seagrass cover loss (Collier et al., 2012a). More than 4 weeks of light below 5.0 mol photons m^{-2} d^{-1} also resulted in a decline in seagrass condition (i.e., biomass, shoot density and percent cover) (Chartrand et al., 2016). Hence, for seagrasses, it has been suggested

that risk of light limitation may occur when average daily benthic PAR falls below 5 to 6 mol photons m^{-2} d^{-1} (Collier et al., 2012a; Chartrand et al., 2016) although some deep-water species (e.g., *Halophila spp*.) can tolerate daily average light from 2 to 6 mol photons m^{-2} d^{-1}. The latter range is thus suggested as the lowest light threshold for managing acute impacts of light limitation on seagrasses, while 10 to 13 mol photons m^{-2} d^{-1} is the currently suggested limit for managing long term chronic impacts of light limitation on seagrasses (Collier et al., 2016a).

Recent experimental studies that investigated the different responses of key GBR coral species to different water quality gradients (Strahl et al., 2019), different daily light integral (DLI) levels at either constant or variable doses (DiPerna et al., 2018), and effects of variable light on adult and juvenile corals under increasing carbon dioxide levels (Robson et al., 2019) have also provided useful insights on coral light requirements relevant to the present study. For example, Strahl et al. (2019) highlighted that in a region with a strong water quality gradient (e.g., near the Burdekin River), *Acropora tenuis* showed reduced calcification at light levels below ~10 mol photons m^{-2} d^{-1} but exhibited high growth rates (i.e., total Chl *a* content, net photosynthesis and light and net calcification) at moderate light levels between ~14 to 16 mol photons m^{-2} d^{-1} (Table 5.1). A reduction of light by ~ 50% (e.g., from moderate to low light levels), for instance in shallow turbid inshore waters like the Burdekin River region, markedly reduced rates of net photosynthesis and light calcification although the observed variations in water quality did not have detrimental effects on *A. tenuis* (e.g., as long as light levels received are not limiting such as when there is no light).

DiPerna et al. (2018), on the other hand, showed that coral responses to constant (high or low DLI) or variable light conditions (with alternating segments of high and low DLI levels) during a 20-day laboratory experiment did not vary greatly between two morphologically different GBR reef corals, *Pachyseris speciosa* and *Acropora millepora*. Specifically, the 'shade-tolerant' *P. speciosa* showed chronic light-limitation response at low DLI of 6 mol photons m^{-2} d^{-1} and light inhibition response at high DLI of 32 mol photons m^{-2} d^{-1}, under both constant and variable light conditions (DiPerna et al., 2018). For a 'high-light tolerant' *A. millepora* exposed to the same light conditions, observed responses suggested chronic light-limitation under all conditions by the end of the experiment although growth observations noted (i.e., differences in nubbins' buoyant weight over time) in *A. millepora* also indicated that it was able to gain some advantage when exposed to constant high daily light. Relationships between incident irradiance and oxygen production (one of the parameters used to indicate photosynthetic efficiency) for *P. speciosa* and *A. millepora* at all light treatments (high, low and variable light levels) presented in the DiPerna et al. (2018) paper did not greatly differ between the coral species studied, suggesting that these corals have equivalent photosynthetic efficiency regardless of the level of instantaneous irradiance treatment received. In other words, the minimum or the maximum instantaneous light is probably less important than the total daily integrated light received as a predictor of the health and growth of these corals. This is further supported by the results obtained by

Robson et al. (2019) in their laboratory experiments that investigated the effects of variable light levels and pCO_2 (partial pressure of carbon dioxide, used in ocean acidification studies) on *Acropora sp.* reef corals. This work (Robson et al., 2019) concluded that the rate of increase in photosynthesis (as measured by the changes in the relative electron transport rate) on mature *Acropora sp.* is directly related to the total amount of light the corals received within the range of light conditions it was subjected to, highlighting the importance of cumulative amount of light received as opposed to instantaneous irradiance levels.

The above review has highlighted that light thresholds relevant to corals and seagrasses (and potentially other benthic organisms) vary widely (from ~ 2 mol photons m^{-2} d^{-1} to 16 mol photons m^{-2} d^{-1}) and that at irradiance values higher than these, there is very little additional benefit in terms of growth. In developing the benthic light limitation index, our intent is to use a parameter for benthic light stress that reflects reduced opportunity for photosynthesis due to low light, but does not consider stress (e.g., photoinhibition) due to excessively high bPAR that may be relevant during bleaching events (Mumby et al., 2001; Leahy et al., 2013) since our purpose is to produce an index of chronic light stress due to reduced water quality, which is not the cause of photo-oxidative stress during bleaching events.

5.2.3.2 Benthic PAR data

The second requirement for developing an index is a consistent and spatio-temporally rich estimate of benthic PAR. We obtained daily bPAR estimates for the GBR study region (Figure 5.1) from a benthic irradiance model (Magno-Canto et al., 2019; Magno-Canto et al., 2020) that uses ocean colour satellite observations from the National Aeronautics and Space Administration (NASA)'s Moderate Resolution Imaging Spectroradiometer (MODIS) aboard the Aqua satellite (NASA Goddard Space Flight Center). The benthic irradiance model estimates the amount of light reaching the seafloor by considering spectrally-varying vertical diffuse light attenuation, $K_d(\lambda)$, and variations in depth for each nominal 1 km^2 pixel (Magno-Canto et al., 2019; Magno-Canto et al., 2020). $K_d(\lambda)$ determines the light penetration to the bottom of the water column. We note that our source benthic irradiance model used vertically integrated $K_d(\lambda)$ values calculated using an Inherent Optical Property (IOP)-based method (Lee et al., 2005b) to estimate benthic irradiance. That is, estimates of IOPs (McKinna et al., 2015), specifically the total absorption coefficients, $a(\lambda)$, and the total backscattering coefficients, $b_b(\lambda)$, which respectively define the overall attenuation due to absorption and scattering at each pixel location were used to obtain the per pixel $K_d(\lambda)$ value. This essentially means that in calculating benthic irradiance, the contributions of both dissolved (e.g., CDOM) and suspended particulate (e.g., phytoplankton, non-algal particles, and sediments) constituents in the water column were considered in the model. Here, we used the daily integrated bPAR data product extracted over a domain within 10.7 – 24.5°S and 142 – 154°E along north-eastern Australia (Figure 5.1) between July 2002 and December 2019. Following the methods for generating the required daily bPAR data product described in Magno-Canto et al.

(2019), we obtained 6322 individual files representing 17.5 years of data. Data aggregation and water quality index calculation were then conducted in R v3.4.1 (R Core Team, 2019).

5.2.3.3 Developing the benthic light-based water quality index

Calculating total relative benthic light stress for each unmasked pixel

We first defined benthic light stress, *S*, as the cumulative stress due to benthic light levels falling below the defined bPAR threshold, *T*. The value of this threshold, 16 mol photons m^{-2} d^{-1}, forms part of the results of this study and is explained in section 3.1. For any location in each data file where the per pixel MODIS-derived daily benthic PAR value, $bPAR_d$, exceeded *T*, we capped at $bPAR_d = T$ on that pixel. Locations with missing data points in a $bPAR_d$ file were gap-filled using a monthly mean value calculated on that pixel (i.e., $bPAR_d$ values on days with data were averaged for each corresponding month).

For each pixel, we then calculated a reference value, $bPAR_R$, which was defined as the 95th-percentile $bPAR_d$ for each calendar month observed over the decade 2003-2013. This reference value was taken to represent the $bPAR_d$ that could potentially be achieved in the best possible water quality conditions at that location and time of year. In very deep water, 'sufficient' (high) $bPAR_d$ is not achievable regardless of water quality due to attenuation of downwelling irradiance over the pathlength by seawater and constituent matter. In the context that 'high' $bPAR_d$ is subjective depending on the body of water considered (e.g., GBR vs. Chesapeake Bay), we regard 'sufficient' $bPAR_d$ as values high enough relative to our chosen threshold. In shallow water, high $bPAR_d$ should be achievable, as light availability is a function of water column depth and optical properties, however some nearshore areas may be naturally turbid and therefore highly attenuating regardless of human impacts on water quality.

To calculate the relative daily stress due to low light, S_d, (mol photons m^{-2} d^{-1}) for each day and pixel location, we used:

$$S_d = bPAR_R - bPAR_d \quad (5.1)$$

Equation (5.1) denotes that when S_d is close to zero, there is either sufficient $bPAR_d$ (hence, no stress) on that pixel on that day, i. e., no more light stress than observed in the best 5% of observed conditions for that pixel. S_d values <0 were set to zero since negative values mean there is no stress in the pixel location (i.e., there is sufficient light on that pixel compared to the PAR threshold defined as per Equation (1)). This ensures that only pixels where S_d is positive (which indicates light stress) will be used in generating the cumulative benthic light stress for that pixel for the 17+ year-period considered. The integral of S_d over a time-period of interest (seasonal or annual) thus indicates the chronic light stress due to poor water quality experienced at a given location.

Summarise relative benthic light stress over management zones

Finally, to obtain S (the cumulative stress due to benthic light levels falling below our defined bPAR threshold, with a unit of mol photons m^{-2} per year or season), we summed S_d spatially over each zone (i.e., combination of six NRM management regions and four shelf water bodies) and temporally for each 'water year' using:

$$S = \sum_{d=1}^{n} S_d \tag{5.2}$$

where n is the number of days in the time-period of interest (i.e., $n = 365$ for annual integral, or $n = 183$ for the number of days in the austral wet season (01 November to 30 April) and austral dry season (01 May to 31 October) for each 'water year', respectively).

Calculating the bPAR index over management zones

The bPAR index, I, for each zone was then obtained as:

$$I = \sum_{p=1}^{z} \left(S - S_{\max} \right)_p \tag{5.3}$$

where z is zone and $S_{max} = T*n$ where T is again the bPAR light threshold and n is the number of days in the integration period (i.e., S_{max} is the maximum theoretically possible value of S for that pixel). Note that for the Burnett-Mary NRM region, the offshore waterbody was deep throughout: there were few if any pixels that ever receive sufficient bPAR to support seagrass or coral habitats, hence excluded.

Scaling and assigning letter grades

The final scaled bPAR index, I_{bPAR}, was then obtained by linearly rescaling I to a value between 0 and 1 to allow unbiased (e.g., equally weighted) comparison of relative benthic light stress values in different zones. The scaled I_{bPAR} values range from 1.0, indicating *low benthic light stress* (very good water quality) to 0.0, indicating *the maximum observed benthic light stress in any season in the record for that zone* (very poor water quality). Finally, scaled I_{bPAR} values were mapped onto the five-point (A-E) colour-coded grading scale (Table 5.2) used in the current GBR Water Quality report cards (Robillot et al., 2018).

Table 5.1. Benthic light thresholds and responses for some key GBR coral and seagrass species and other benthic organisms.

Taxonomic group	Species	Conditions / Notes	Threshold / Response	Reference
Zooxanthellate coral	*Acropora, Isopora*	global *in-situ* coral identification and depth data	winter PAR threshold of 5.2 mol photons m^{-2} d^{-1} define colonisation depth of Acropora	(Muir et al., 2015)
Zooxanthellate coral		global limit for reef formation (net $CaCO_3$ production)	7 to 8 mol photons m^{-2} d^{-1}	(Kleypas, 1997)
Zooxanthellate coral		*in-situ* total daily PAR, Whitsunday Islands, depth limit for reef development	absolute minimum light threshold ~ 2 mol photons m^{-2} d^{-1}	(Cooper et al., 2007)
Zooxanthellate coral	*Scleractinia*	*in-situ* surface irradiance (obtained as 50% of total solar radiation above water surface), depth limit for reef development, Gulf of Siam	~ 2 mol photons m^{-2} d^{-1}	(Titlyanov and Latypov, 1991)
Zooxanthellate coral		average benthic irradiance at the maximum depth of coral colonization	1.2±1.7 mol photons m^{-2} d^{-1}	(Gattuso et al., 2006)
macroalgae	*macroalgae (general)* *Lobophora*-turfs *Halimeda*/Bryopsidales	required light levels to maintain species richness	steep decline in richness at 2 mol photons m^{-2} d^{-1} 3.6 mol photons m^{-2} d^{-1} 4.6 mol photons m^{-2} d^{-1}	(Pitcher et al., 2007; Hurrey et al., 2013)
benthic community		daily compensation irradiance of benthic communities	ranges from 0.24 to 4.4 mol photons m^{-2} d^{-1}	(Gattuso et al., 2006)
seagrass (meadow)	Predominantly *Halodule uninervis*, some *Cymodocea serrulata* and *Halophila ovalis*	*in-situ* monitoring in Northern GBR (sites: Magnetic Island, Dunk Island and Green Island), seagrass cover measure ~3-month intervals (2008 – 2011), nearshore reef habitats exposed to influence from terrigenous run-offs	increased seagrass abundance (i.e., cover) at mean daily irradiance above 5 and 8.4 mol photons m^{-2} d^{-1}, 16 to 18% of days below 3 mol photons m^{-2} d^{-1} associated with 50% seagrass cover loss	(Collier et al., 2012a)

seagrass	*Zostera muelleri sp. capricorni*	in-situ, intertidal mudbank, sheltered embayment, Gladstone Harbour, simulated dredging impacts	declined seagrass conditions (biomass, shoot density and percent cover) at ≤ 5 mol photons m^{-2} d^{-1} for periods > 4 weeks, 6 mol photons m^{-2} d^{-1} (suggested management light threshold) to mitigate dredging impacts	(Chartrand et al., 2016)
seagrass	*Cymodocea serrulata, Halodule uninervis, Halophila ovalis* and *Zostera muelleri*	aquaria-based experiments, six light treatments: 0, 5, 10, 20, 40 and 70% of surface irradiance (= 32.8 mol photons m^{-2} d^{-1}) equivalent to light levels ranging from 0 to 23 mol m^{-2} d^{-1}, warm (~23°C) and cool (~28°C) temperatures over 14 weeks	declined seagrass shoot density and leaf growth rates at lowest light levels but were maintained at highest light levels, quicker decline of shoot density and leaf growth rates at low light treatments in warm than cool temperatures	(Collier et al., 2016b)
seagrass	*Halophila sp., Zostera muelleri, Halodule uninervis, Cymodocea sp., Syringodium isoetifolium, Thalassodendron ciliatum, Thalassia hemprichii, Enhalus acoroides*	synthesis of light thresholds and guidelines for seagrass of the GBR	biological light thresholds of 2–6 mol photons m^{-2} d^{-1} for managing acute impacts; 10–13 mol photons m^{-2} d^{-1} for managing long term impacts of light limitation (except for some deep water species which require less light)	(Collier et al., 2016a)
seagrass		global synthesis of published light requirements across multiple species	minimum light requirement: range of 0.06 to 14.1 mol photons m^{-2} d^{-1}; overall median of the minimum light requirement: 5.1 mol photons m^{-2} d^{-1}	(Gattuso et al., 2006)
seagrass	*Cymodocea serrulata, Halodule uninervis, Halophila ovalis* and *Zostera muelleri*	aquaria-based experiments	suggested conservative management guideline thresholds of 7 and 13 mol photons m^{-2} d^{-1} to provide 50% and 80% protection of seagrass shoots over a 14-week period, respectively.	(Collier et al., 2016b)
coral	*Acropora tenuis*	Laboratory-simulated inshore reef field conditions, three daily light integral (DLI) treatments (no light: 0 mol photons m^{-2} d^{-1}, low: 7.92 – 9.36 mol photons m^{-2} d^{-1}, and moderate: 13.86 – 16.38 mol photons m^{-2} d^{-1}), strong water quality gradient (Burdekin region), moderate water quality conditions (Magnetic Island), ~60 km from Burdekin River mouth	decreased net photosynthesis rates, light calcification rates, and net calcification rates from low DLI (8-9.4 mol photons m^{-2} d^{-1}) to moderate light (14-16 mol photons m^{-2} d^{-1})	(Strahl et al., 2019)

Zooxanthellate coral	*Pachyseris speciosa*	laboratory experiment, variable light treatments (alternating high and low light treatments)	physiological stress in both high and low light segments, rapid declines in maximum quantum yield (i.e., photoinhibition) at 32 mol photons m^{-2} d^{-1}, recovery (photoacclimation) within 3-5 days at 6 mol photons m^{-2} d^{-1}	(DiPerna et al., 2018)
Zooxanthellate coral	*Pachyseris speciosa*	laboratory experiment, constant light treatments	low values of Q_m (or excitation pressures on PSII (an estimate of light limitation against photoinhibition); chronic light-limitation at constant low light (6 mol photons m^{-2} d^{-1}); photoinhibition at constant high light (at 32 mol photons m^{-2} d^{-1})	(DiPerna et al., 2018)
Zooxanthellate coral	*Acropora millepora*	laboratory experiment, variable light treatments (alternating high and low light treatments)	intermediate growth in variable daily light conditions, slow (>20 days) photoacclimation	(DiPerna et al., 2018)
Zooxanthellate coral	*Acropora millepora*	laboratory experiment, constant light treatments	reduced growth (i.e., buoyant weight) due to photolimitation at constant low daily light (6 mol photons m^{-2} d^{-1}) compared with constant high daily light (32 mol photons m^{-2} d^{-1})	(DiPerna et al., 2018)
Zooxanthellate coral	*Acropora tenuis* or *A. hyacinthus*	laboratory experiment, four light treatments including variable light levels (low: 2.5, medium: 7.6, and high: 12.6 mol photons m^{-2} d^{-1})	increasing growth rates from low (2.5 mol photons m^{-2} d^{-1}) to high (12.6 mol photons m^{-2} d^{-1}) light levels (growth rate linearly increased/decreased with cumulative daily light integrals received), cumulative amount of light received affects physiological response	(Robson et al., 2019)

Table 5.2. Colour-coded scoring system adapted to indicate the levels of light stress.

Grade	Light stress	Description	Numerical criteria	Colour
A	No stress	Very good	> 0.8 – 1.0	Dark green
B	Low stress	Good	> 0.6 – 0.8	Light green
C	Moderate stress	Moderate	> 0.4 – 0.6	Yellow
D	High stress	Poor	> 0.2 – 0.4	Orange
E	Very high stress	Very poor	0 – 0.2	Red

5.2.4 Relating the bPAR index to estimate of catchment-derived loads of total suspended sediments, dissolved inorganic nitrogen and river discharge

For the purpose of relating potential variability in the bPAR index to a specific water quality driver (i.e., turbidity due to increased suspended sediment concentrations, CDOM from freshwater discharge or increased availability of nutrients that can support biological processes that may also reduce light availability), we also considered estimates of total suspended sediment (TSS) loads, dissolved inorganic nutrient (DIN) loads, and river discharge data from major catchment regions that contribute most to the runoff inputs to the GBR. The methods for generating these load estimates are described below and elsewhere (Gruber et al., 2019; Gruber et al., 2020) and form an integral part in mapping the superficial dispersion of land-derived nitrogen and sediment in the GBR as part of the AIMS Inshore Water Quality Marine Monitoring Program. Briefly, the total river discharge for each basin was calculated using an approach that up-scaled available measured gauge flow data (i.e. the flow gauges rarely capture the full basin area and hence underestimate flow from the basin); available Grid-to-Grid (G2G) modelling (covers the Normanby to Mary Basins) from the Bureau of Metrology (Bureau of Meteorology, 2017; Wells et al., 2017) was used to inform the upscale factors for the flow data. An area-correction factor was applied to the four basins north of the Normanby (i.e. not modelled by G2G) and for basins which had no available flow data the flow gauge data from the nearest neighbour basin was applied (along with the relationship with the G2G model to produce the upscale factor) to calculate discharge (Gruber et al., 2020).

The TSS loads for the river basins of the GBR were derived from a systematic approach which included: 1. The measured TSS loads from the Burdekin, Pioneer and Fitzroy basins were compiled from the Great Barrier Reef Catchment Loads Monitoring Program (annual reports each year from 2010: https://www.reefplan.qld.gov.au/tracking-progress/paddock-to-reef/modelling-and-monitoring) as well as previous programs from the Burdekin (Kuhnert et al., 2012), Pioneer (Joo et al., 2012); note that for the 2002/03 to 2005/06 water years, an annual mean concentration (AMC) of 112 $mg.L^{-1}$ was applied to calculate the load for this basin) and Fitzroy (Packett et al., 2009; Joo et al., 2012) basins. As the loads measured at these sites capture >95% of the basin area they provide the most accurate measure at these locations; 2. For the remaining basins with available monitoring data, the AMC data (i.e. load

divided by flow) from available load monitoring data within the basin were compared with the Source Catchments model outputs (McCloskey et al., 2017). The most appropriate AMC (or a mean of the monitoring and modelled data) was chosen and multiplied by the annual discharge (calculated from the above method) to formulate an annual load for these basins; 3. Where no monitoring data were available in the basin, the AMC informed from the Source Catchments model (McCloskey et al., 2017) and data from neighbouring basins with similar climate and geomorphology was coupled with the annual water year river discharge to calculate the TSS load (Gruber et al., 2019). The Source Catchments model produces a load that represents a ~30-year long term mean load (McCloskey et al., 2017) but excludes annual water year loads.

Table 5.3. Relative contributions of the major rivers considered for each of the NRM regions in estimating loads of total suspended sediment (TSS), dissolved inorganic nutrient (DIN) and discharge.

Region (current study)	Region (Fabricius et al., 2016)	Relevant rivers
Cape York	Cape York	Normanby, Endeavour, Stewart
Wet Tropics: (North Wet Tropics + South Wet Tropics)	North Wet Tropics	Daintree, Barron, Russell, Mulgrave, Johnstone, Burdekin (30% of discharge)
	South Wet Tropics	Russell, Mulgrave, Johnstone, Tully, Herbert, Burdekin (50% of discharge)
Dry Tropics	Burdekin	Burdekin
Mackay-Whitsunday	Whitsundays	Proserpine, O'Connell, Pioneer
Fitzroy	Broad Sound-Pompey, Keppel Bay	Fitzroy
Burnett-Mary	Fitzroy-Swain	Burnett

Like the TSS loads, the DIN loads for the river basins of the GBR were similarly derived from a systematic approach which included: 1. The measured DIN loads from the Burdekin, Pioneer and Fitzroy basins from the same sources listed for the TSS method; 2. The method of (Lewis et al., 2014) was applied to calculate DIN loads for the basins of the Wet Tropics and the Haughton Basin. Briefly, modelled DIN loads in this method were calculated using existing load monitoring data to develop a relationship between the measured loads with flow volumes (at river monitoring sites) and the amount of fertiliser applied to calculate the percentage of applied nitrogen fertiliser lost as DIN across various discharge amounts. This relationship is then applied to upscale loads for the entire basin area; 3. For the remaining basins, similar to the TSS loads method, the AMC data from available load monitoring were compared with the Source Catchments model outputs and the most appropriate AMC (taking into account the cropping area above and below the measured site) was chosen for each basin and multiplied by the annual discharge to formulate an annual load; 4. Where no monitoring data were available, the AMC informed from the Source Catchments model (McCloskey et al., 2017) and data from neighbouring basins with similar climate and geomorphology was coupled with the annual water year

river discharge to calculate the water year loads (Gruber et al., 2019). The resulting TSS and DIN loads and river discharge were presented as stacked bar graphs.

We then compared the annual river load estimates and the proposed bPAR index using simple linear regression analysis to highlight the drivers of variability in the bPAR index from year to year. We focused the comparison using the annual I_{bPAR} based on the light threshold for corals and the estimate of the total river loads and discharge relevant for each of the zones. It is important to note that the overall flow and transport of materials from the rivers along the length of the GBR is often northward (Devlin and Brodie, 2005) along the coast (i.e., due to Coriolis effects and SE trade winds) which means that the NRM regions may also receive inputs from other rivers situated in adjacent NRM regions (zones) (Skerratt et al., 2019). The total discharge for each NRM region was hence obtained by aggregating estimates for main influential rivers for each region following Fabricius et al. (2016) (see Table 5.3). Note, however, that in the present study, estimates for the Fitzroy region are slightly different and that the Wet Tropics NRM region annual load estimate was combined and not separated to north and south sectors as in Fabricius et al. (2016).

5.3 Results

5.3.1 Defining a light threshold for calculating benthic light stress

Considering the ranges of benthic light requirements of both corals and seagrasses described in Section (5.2.3.1) and examining the inflection point of the P-E curve presented in DiPerna et al. (2018) and the results of Strahl et al. (2019), we employed a benthic PAR threshold of 16 mol photons m^{-2} d^{-1}. *Ad hoc* sensitivity analysis using other benthic light thresholds (i.e., 5, 10 and 14 mol photons m^{-2} d^{-1}) produced an index with less sensitivity to known regional and temporal variations. We note that the selected 16 mol photons m^{-2} d^{-1} threshold value represents the maximum amount of benthic light that both target benthic organisms will be able to make use of to attain optimal growth if other environmental conditions are optimal, rather than the minimum light below which net productivity will be negative regardless of other conditions. In other words, corals and seagrasses can and do exist in areas where the mean daily light is above or below 16 mol photons m^{-2} d^{-1}, but their survival and growth can be expected to be enhanced with increasing daily integrated light up to around 16 mol photons m^{-2} d^{-1}, and not substantially enhanced above this threshold.

5.3.2 Cumulative benthic light stress

The cumulative benthic light stress (S) within the GBR varied strongly both spatially and temporally. Figure 5.2 shows maps of S for selected water years highlighting this variability. Benthic light stress consistently showed greater variability in inshore locations compared to offshore areas. For example, the open coastal locations in the 2005-2006 ‘dry’ (e.g., period where below average rainfall was

recorded by the Australian Bureau of Meteorology) water year (Figure 5.2a) showed relatively low stress, but indicated considerably higher values in the 'wet' water years 2010-2011 (Figure 5.2b) and 2018-2019 (Figure 5.2c).

5.3.3 A benthic light-based index of water quality

5.3.3.1 Annual bPAR index

The time series of the annual I_{bPAR} based on the relative benthic light stress showed strong interannual variation as well as spatial variation between the zones (Figure 5.3). Regional differences followed latitudinal gradients. From north (Cape York) to south (Burnett-Mary), the annual I_{bPAR} showed an overall decreasing trend that was consistent across all the shelf water bodies except the enclosed coastal waterbody to some extent. Out of all the NRM regions, Cape York consistently showed the best water quality throughout the 2003 to 2019 water years (i.e., indicated the most water years with letter grade A – "very good" bPAR index value).

The annual I_{bPAR} also showed an across-shelf gradient decreasing from offshore to inshore coastal water bodies. Notably, there was an overall higher variability in I_{bPAR} for the two most inshore locations compared to the mid-shelf and offshore locations across all NRM regions, the latter having consistently excellent water quality conditions. The annual fluctuations in bPAR index values in the inshore water bodies appear strongest from the 2010 water year although some fluctuations in prior years can also be noted particularly in the Dry Tropics and Mackay-Whitsunday NRM regions. Overall, the temporal variations in the annual I_{bPAR} (Figure 5.3a) suggest the strong local influences of nearshore processes that drives light attenuation at depth.

Specific variability in the annual water quality during certain years can further be inferred in the I_{bPAR} timeseries. For example, in the 2010-2011 water year there was a notable decline in the I_{bPAR} across all NRMs (except for the Cape York region). This decline is again most evident in the open coastal waterbody where the bPAR index grade drops by one step in most NRMs (e.g., "good" (B) to "moderate" (C) in Wet Tropics and Fitzroy) were obtained between the 2009-2010 and 2010-2011 water years. Following this, there were several other similar but smaller declines in I_{bPAR} during the other water years, but interestingly, the variability remained confined within the coastal inshore locations across all NRM regions particularly within the open coastal waterbody.

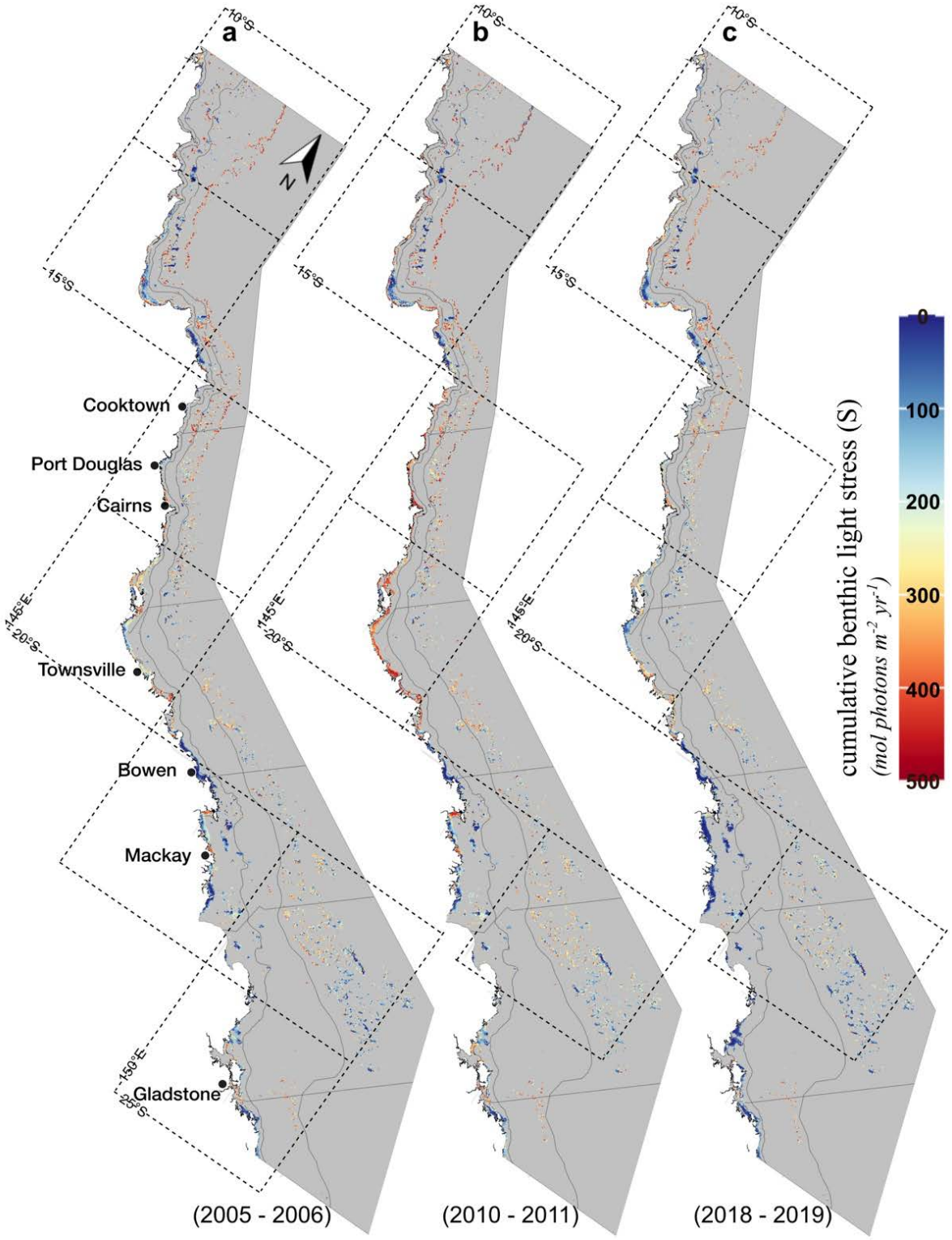

Figure 5.2. Cumulative (annual) benthic light stress (S) maps for some representative water years: (a) 2005-2006, (b) 2010-2011, and (c) 2018-2019 highlight the strong spatial and temporal variability in the amount of light stress experienced by corals and seagrasses at each zone within the GBR. Zones are indicated by solid black lines as in Figure 5.1. Note that these maps were rotated to facilitate visualisation (north compass direction indicated on the first map).

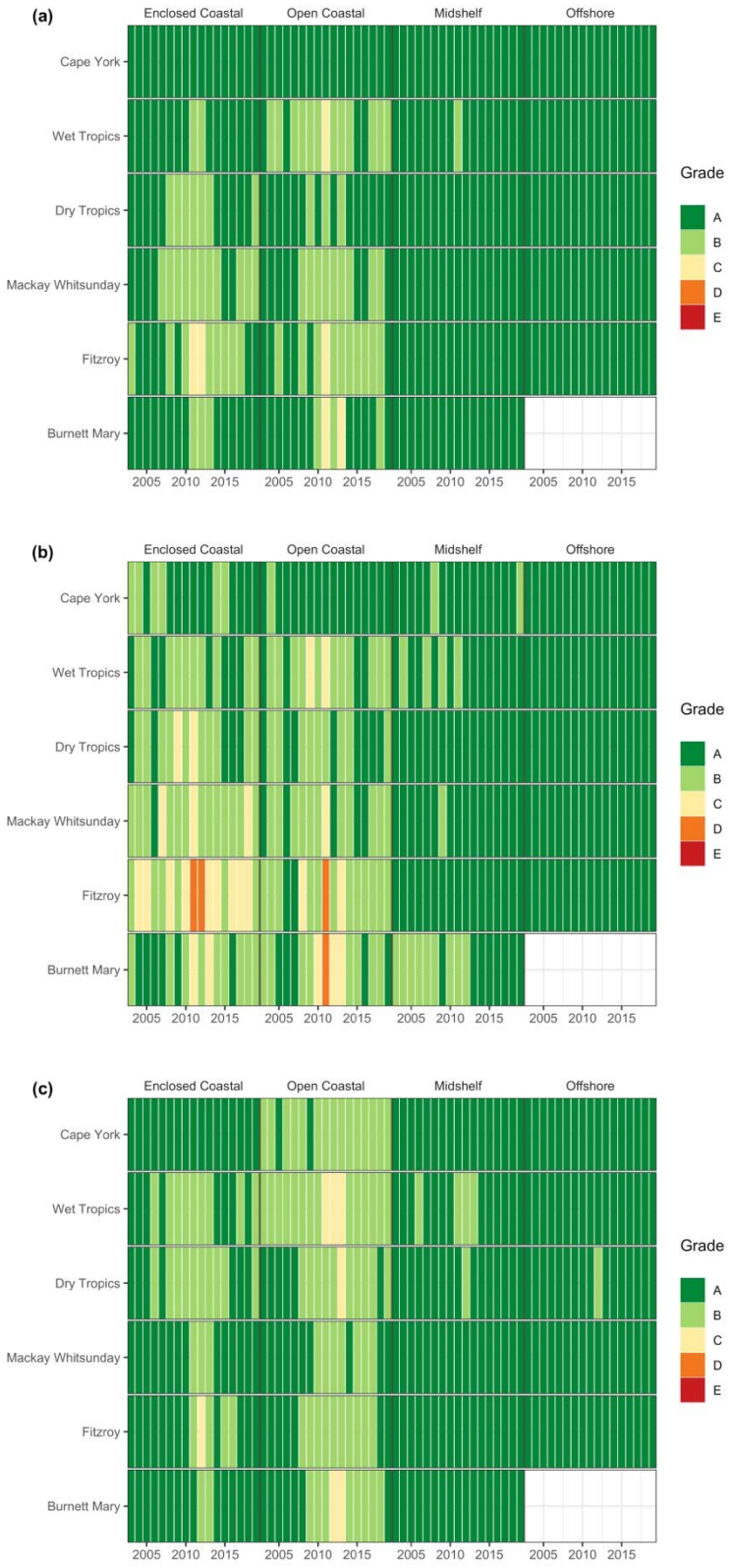

Figure 5.3. Timeseries of (a) annual, (b) austral wet season, and (c) austral dry season scaled bPAR index (I_{bPAR}) for water years (2002-2003) to (2018-2019) over locations within the 95th percentile of bPAR values ≤ 16 mol photons m^{-2} d^{-1}. Each vertical bar corresponds to a water year grouped by across-shelf waterbody. Colours correspond to letter grades that indicate the quality of the water as: very good (A, dark green), good (B, light green), moderate (C, yellow), poor (D, orange), and very poor (E, red).

5.3.3.2 Seasonal bPAR index

Inter- and intra-seasonal differences were apparent for the austral wet (Figure 5.3b) and dry (Figure 5.3c) season I_{bPAR}. The intra-seasonal patterns also displayed the same north-south latitudinal or across-shelf gradients as also observed in the annual data (Figure 5.3a) where the mid-shelf and offshore water bodies again showed more consistent and less variable I_{bPAR}, while the inshore locations (both enclosed coastal and open coastal) showed stronger variability. The time series of I_{bPAR} indicated the stronger sensitivity of the nearshore water bodies to long-term reductions in benthic light availability (i.e., lower I_{bPAR} grade for the same 'water year' and zone).

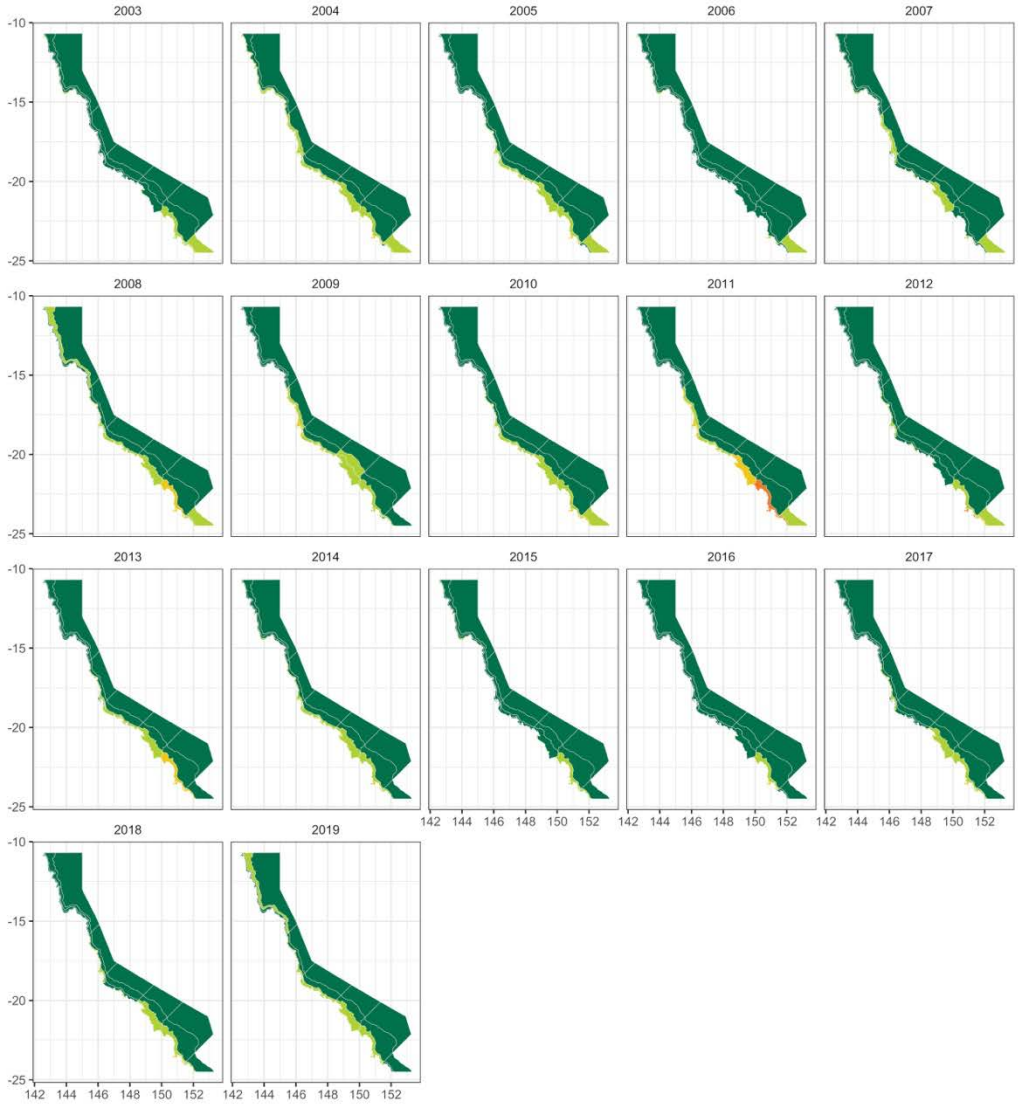

Figure 5.4. Spatial maps of austral wet season scaled bPAR index (I_{bPAR}) for water years (2002-2003) to (2018-2019) over locations within the 95th percentile of bPAR values ≤ 16 mol photons m^{-2} d^{-1} highlighting spatial distributions of scores. Colour legend as in Figure 5.3 where colours correspond to letter grades that indicate the quality of the water as: very good (A, dark green), good (B, light green), moderate (C, yellow), poor (D, orange), and very poor (E, red). White outlines indicate the boundary of the zones as in Figure 5.1.

Inter-seasonal differences between the seasonal indices indicated more pronounced variabilities during the austral wet than the austral dry season similarly with cross-shelf spatial differences being more notable in the two inshore water bodies compared to the mid-shelf and offshore locations. The spatial distribution of I_{bPAR} for the austral wet season is also highlighted in Figure 5.4 and facilitates spatial comparison of results between water years.

5.3.4 Annual river discharge, total suspended sediment (TSS) and dissolved inorganic nutrient (DIN) loads

Distinct variability in the annual river discharge (ML/year) and TSS (kt/year) and DIN (t/year) loads were observed over time for some selected major river systems (Figure 5.5). In most 'water years', the annual Burdekin River discharge was consistently larger compared to the estimates from the four other rivers (Figure 5.5a), although the Fitzroy River estimates are also worth noting as the second largest discharge. Consequently, the highest annual TSS loads were also apparent for the Burdekin River followed closely by the Fitzroy River (Figure 5.5b). The other three river systems were less significant in comparison to Burdekin and Fitzroy distinguished by relatively small discharge and TSS loads over the period covering the 2003 to 2019 water years. Nonetheless, the estimates from these three smaller river systems still showed some degree of variability over time.

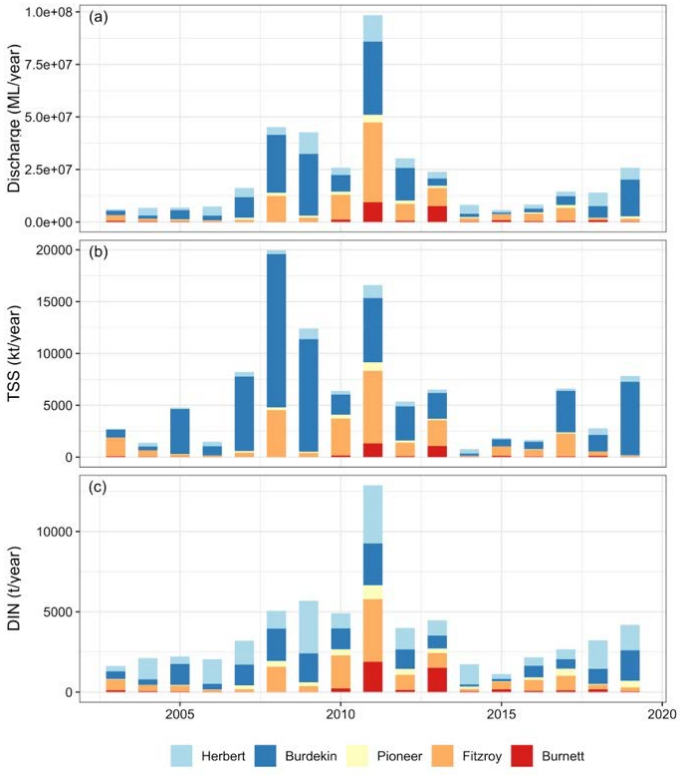

Figure 5.5. Annual estimates of (a) river freshwater discharge, (b) total suspended sediment (TSS), and (c) dissolved inorganic nutrients (DIN) loads calculated at selected five major rivers found along the length of the GBR. Colours indicate the associated river source.

For the Burdekin River, the highest TSS load was observed during the 2007-2008 water year with almost 15,000 kt/year suspended sediments recorded. Comparable TSS loads for the Burdekin River were also observed the following water year (2008-2009) and in 2018-2019 with almost 11,000 kt/year and 7000 kt/year suspended sediments recorded, respectively. The highest TSS load for Fitzroy River over the period covered occurred in the 2010-2011 water year where about 7,000 kt/year was recorded.

In terms of DIN loads, the Herbert River appear to contribute most of the catchment-derived nutrients followed very closely by the Burdekin and Fitzroy rivers (Figure 5.5c). The largest cumulative DIN load estimates throughout the period considered were recorded in the 2010-2011 water year with comparable loads obtained for Fitzroy and Herbert rivers during that water year.

Table 5.4 Summary of linear regression statistics of IbPAR versus freshwater discharge, TSS and DIN for each zone. Highlighted cells indicate the strongest correlation (i.e., highest R2 value) for each load category and zone. Correlations are statistically significant at p-value ≤ a = 0.05 and 95% confidence interval. Abbreviations: EC = enclosed coastal; OC = open coastal; Mid = mid-shelf; Off = offshore; R2 = coefficient of determination.

Region	Statistics	Discharge				TSS				DIN			
		EC	OC	Mid	Off	EC	OC	Mid	Off	EC	OC	Mid	Off
Cape York	R^2	0.06	0.46	0.57	0.48	0.06	0.46	**0.56**	**0.47**	0.06	0.46	0.57	0.48
	intercept	0.95	0.92	0.95	0.97	0.95	0.93	0.95	0.97	0.95	0.92	0.95	0.97
	slope	-0.03	-0.06	-0.06	-0.03	-0.03	-0.06	-0.06	-0.03	-0.03	-0.06	-0.06	-0.03
	p-value	0.03	0.02	0.01	0.01	0.03	0.02	0.01	0.01	0.03	0.02	0.01	0.01
Wet Tropics	R^2	0.26	0.53	**0.75**	**0.53**	0.04	0.17	0.39	0.33	0.20	0.53	**0.74**	**0.52**
	intercept	0.94	0.89	0.94	0.93	0.92	0.85	0.93	0.93	0.94	0.89	0.95	0.93
	slope	-0.07	-0.18	-0.10	-0.06	-0.02	-0.09	-0.06	-0.02	-0.06	-0.19	-0.11	-0.06
	p-value	0.03	0.04	0.02	0.02	0.03	0.05	0.02	0.02	0.03	0.05	0.02	0.02
Dry Tropics	R^2	0.62	0.27	0.69	0.52	0.33	0.10	0.29	0.17	0.55	0.22	0.56	0.37
	intercept	0.95	0.93	0.96	0.92	0.94	0.93	0.95	0.92	0.96	0.94	0.97	0.93
	slope	-0.15	-0.09	-0.11	-0.03	-0.13	-0.06	-0.08	-0.01	-0.15	-0.09	-0.10	-0.03
	p-value	0.03	0.04	0.02	0.01	0.05	0.05	0.03	0.01	0.04	0.04	0.02	0.01
Mackay Whitsunday	R^2	**0.71**	0.53	0.32	0.08	**0.66**	0.47	0.30	0.11	**0.71**	0.54	0.32	0.07
	intercept	0.84	0.87	0.94	0.94	0.84	0.86	0.93	0.94	0.84	0.87	0.94	0.94
	slope	-0.13	-0.15	-0.10	-0.02	-0.13	-0.15	-0.10	-0.02	-0.13	-0.15	-0.09	-0.02
	p-value	0.02	0.04	0.04	0.02	0.02	0.04	0.04	0.02	0.02	0.04	0.04	0.02
Fitzroy	R^2	0.44	**0.68**	0.21	0.02	0.39	**0.58**	0.25	0.00	0.40	0.63	0.26	0.01
	intercept	0.86	0.84	0.95	0.94	0.86	0.85	0.95	0.94	0.86	0.85	0.95	0.94
	slope	-0.21	-0.26	-0.05	0.01	-0.18	-0.22	-0.05	0.00	-0.19	-0.25	-0.06	0.01
	p-value	0.06	0.05	0.03	0.02	0.06	0.05	0.02	0.02	0.06	0.05	0.03	0.02
Burnett Mary	R^2	0.50	0.62	0.18	N/A	0.44	0.56	0.24	N/A	0.54	**0.65**	0.19	N/A
	intercept	0.91	0.90	0.98	N/A	0.92	0.92	0.98	N/A	0.92	0.91	0.98	N/A
	slope	-0.22	-0.39	-0.04	N/A	-0.19	-0.35	-0.05	N/A	-0.22	-0.39	-0.04	N/A
	p-value	0.06	0.08	0.02	N/A	0.06	0.08	0.02	N/A	0.05	0.08	0.02	N/A

5.3.5 Regression analysis of annual river loads and the bPAR index

Simple regression analysis showed a strong relationship between annual I_{bPAR} and annual estimates of river discharge and loads (both TSS and DIN) with a relatively steeper slope in the inshore locations (enclosed coastal and open coastal water-bodies), particularly in the southern NRM regions, compared

to the mid-shelf and offshore waters (Table 5.4 and Figure 5.7), consistent with the latitudinal and cross-shelf gradients observed in the I_{bPAR} time series. Specifically, strongest correlations (based on R^2 values summarised in Table 5.4) between I_{bPAR} and Discharge were noted in the inshore locations for Mackay Whitsunday enclosed coastal and Fitzroy open coastal zones although north of these zones, respectively, Dry Tropics enclosed coastal and Mackay Whitsunday open coastal zones also showed comparable strong correlations. On the mid-shelf and open coastal water bodies, the strongest correlations between I_{bPAR} and Discharge were noted in the Wet Tropics but the relationship obtained for Dry Tropics was also notable.

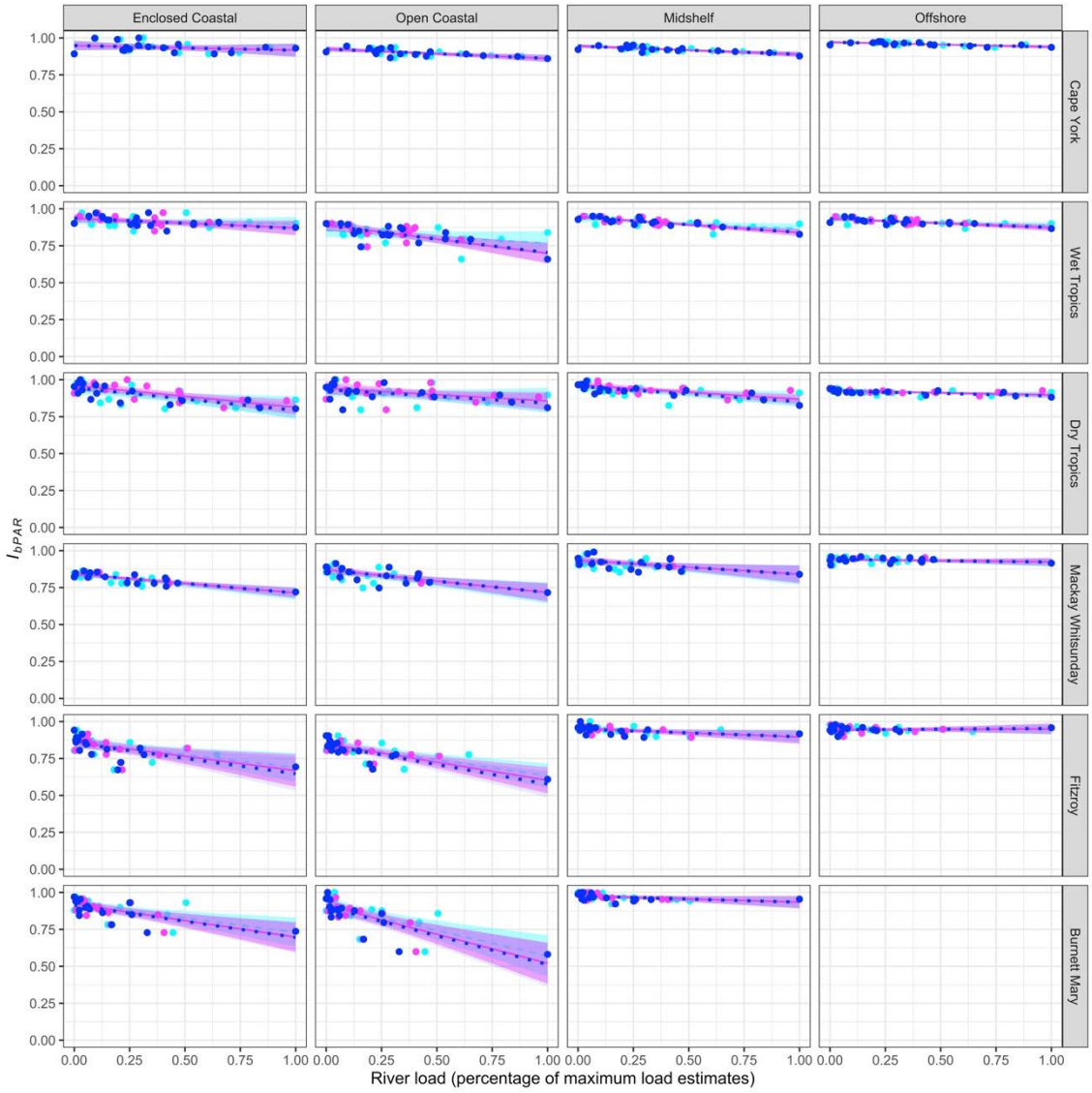

Figure 5.6 Scatterplots of scaled annual river loads of freshwater discharge (blue-filled circles), TSS (cyan-filled circles) and DIN (magenta-filled circles) for each region versus annual I_{bPAR} for each zone. For each region, river loads are scaled from 0 (the minimum observed load) to 1 (the maximum observed load for that region) to facilitate visualisation. Also shown are the 95% confidence interval indicated as shaded areas: freshwater discharge (blue), TSS (cyan), and DIN (magenta) with the mean fitted line: freshwater discharge (blue dotted line), TSS (cyan dashed line) DIN, and (magenta solid line).

The correlations between I_{bPAR} and TSS load showed a similar pattern except that the highest R^2 values for the mid-shelf and offshore water bodies were noted in the Cape York NRM instead.

The strongest correlations between I_{bPAR} and DIN load were also noted in the inshore locations in the Mackay Whitsunday-enclosed coastal and Burnett Mary-open coastal zones while Wet Tropics showed highest correlation coefficients in the water bodies away from the coast.

Overall, the relationship between I_{bPAR} and the three river-derived parameters (discharge, TSS and DIN) appear to be generally stronger in the inshore locations for the southern NRMs (Mackay Whitsundays, Fitzroy and Burnett Mary) and away from the coast for the northern NRMs (Dry and Wet Tropics and Cape York). However, the correlation coefficients obtained for the Dry Tropics-enclosed coastal for all three parameters against the I_{bPAR} are also comparably strong, diluting this correlation boundary.

5.4 Discussion

5.4.1 Drivers and patterns of variations in benthic light and the bPAR index

This study presents a novel method for calculating an index of water quality in the GBR that is responsive to changes in the quantity of light reaching corals and seagrasses. We used spatiotemporally-rich satellite-derived bPAR as a core input data along with a benthic light threshold to calculate the cumulative benthic light stress parameter, *S*, the cumulative amount of light lost (relative to a maximum benthic light threshold) where corals and seagrasses were potentially photolimited due to reduced light availability (i.e., from poor water quality). Many locations nearshore indicated as much as 500 mol photons m^{-2} yr^{-1} growth potential lost from light limitation stress (Figure 5.2). The *S* parameter served as the basis of the new bPAR index reported here as annual or seasonal values scaled for each NRM region and shelf waterbody between 0 and 1 indicating 'very poor' (very high light stress) and 'very good' (no light stress) water quality conditions, respectively. Our results showed that the benthic light stress and hence the proposed benthic light-based index (I_{bPAR}) vary both spatially and temporally within the six NRM focus regions and four coastal water bodies. Latitudinal patterns can be generalised as decreasing from north (Cape York) to south (Burnett Mary) while the cross-shelf gradients generally decrease towards the coast (e.g., higher benthic light stress calculated nearshore).

The observed patterns are closely related to the dynamics of key water quality drivers that may include river discharge (and the related factors such as suspended sediment concentrations) and potentially to the occurrence of atmospheric and physical disturbances (cyclones, wind, wave and tidal mixing) as well as the local oceanography that governs the transport and hydrodynamics of river or flood plumes within the shelf. While the inshore locations typically receive higher daily light doses due to greater potential for light penetration because of shallow bathymetry (Ackleson, 2003), the annual light stress maps (Figure 5.2) and I_{bPAR} time series (Figure 5.3) showed that these coastal locations are most vulnerable to declines in benthic light levels compared to the mid-shelf and offshore locations. River

flood plumes within the GBR can, in very wet years, simultaneously occur from the Cape York to Burnett-Mary regions but mostly impact areas within 20 km inshore, occasionally reaching beyond the mid-shelf regions (Devlin et al., 2012) and often spread in a band up to 50 km from the coast (Devlin and Brodie, 2005). The overall patterns we obtained in this study were also similar to previous simulations (Skerratt et al., 2019) of the spatial distribution of some water quality parameters directly related to or considered a proxy for light availability at depth. For example, simulated Z_{sd} from Skerratt et al. (2019) was generally greater offshore and decreased as distance from shore decreased, and from north to south, while Chl *a* concentration increased from north to south and from outer to inner coastal regions. Higher concentrations of Chl *a* are generally associated with higher light attenuation (thus, reduced light availability) and in the context of this study, high light stress (or increased stress from light attenuation) and a low I_{bPAR}. Although these two studies have similar results, using bPAR index over either Z_{sd} and/or Chl *a* still offer an advantage in that our benthic light-based WQI metric, I_{bPAR}, has a direct ecological relevance as a metric for monitoring the health of important benthic habitats.

Temporal differences in water quality and light reductions were also detected by our new index as a response to the terrestrial inputs delivered into the shelf via river discharge. Inter-seasonally, the austral wet season is generally associated with elevated river discharge in the Queensland tropical region, resulting in lower water clarity and increased light stress from light attenuation. The resulting austral wet season indices (Figure 5.4) indicated that for most of the southern NRMs, water quality conditions returned (within two years) to the "moderate to good" range within the inshore water bodies after marked decline during the 2010-2011 water year associated with high river discharges and TC Yasi. Before this, however, steady decline in water quality conditions even before 2011 can also be noted in the time series. Coincidentally, the recent inshore Marine Monitoring Program report (Gruber et al., 2019) have indicated that inshore Z_{sd} in most NRMs have declined since 2005 and have not been meeting guideline values based on *in situ* water quality data collected at several point locations within the GBR nearshore water bodies during the austral wet season. At intra-annual time scales, other processes may add variability to I_{bPAR} that may also be related to changing nutrient and suspended sediment concentrations. These temporal patterns reflect the combined effects of the transport of river-derived materials clearly indicating its role in driving light reduction (Schaffelke et al., 2012) and the influence of wind and wave driven resuspension of material from the seafloor and biological response from increased nutrient availability especially in the inshore areas.

River discharge is a major pathway for transport of land-derived sediments and pollutants into the Reef lagoon (Devlin and Brodie, 2005; Brodie et al., 2012; Petus et al., 2014). Its transport often leads to increased turbidity and decreased water clarity in regions offshore from the river mouths. The estimates of annual TSS loads for some of the major rivers (Figure 5.5) showed clear concurrence with the episodic increases in river discharge following flood and cyclone events. The 2011 water year (which encompasses the 2010-11 wet season), for example, was associated with unprecedented rain and

flooding in Queensland as early as November – December 2010 (associated with Tropical Cyclone (TC) Tasha) and the passing of severe TC Yasi in early January 2011 that further exacerbated state-wide flooding. Wet season I_{bPAR} during the same water year also reflects the immediate influence of these major events but also the subsequent effects related to resuspension and retention of flood-derived materials (Neil et al., 2002; Orpin and Ridd, 2012) and potentially flood-induced biological productivity (Devlin and Schaffelke, 2009) as reduced water quality due to light reduction across most of the zones. The role of potential drivers of variability in I_{bPAR} was explored via linear regression analysis (Figure 5.6 and Table 5.4) which confirmed the higher influence of river-derived materials in the inshore locations especially in the southern NRMs and in the water bodies away from the coast in most of the northern NRMs. These patterns were indicative of the net northward transport of anthropogenic materials in southern hemisphere coastlines (via Ekman transport and Coriolis effects). The higher correlations noted for the Mackay Whitsunday and Fitzroy inshore zones are suggestive of the chronic effects that drive light reduction from rivers located south of these NRMs, mainly the Fitzroy River and Burnett Mary River, (see Figure 5.1 for relative locations of NRMs and rivers) with materials generally retained nearshore (and resuspended) by local wind-driven and tidal circulations and potentially demarcated by oceanic intrusions from north and central regions of the lagoon. The notably stronger correlations between I_{bPAR} and TSS in the mid-shelf and offshore water bodies for most of the northern NRMs may be related to chronic light reductions at depth due to resuspension of bottom sediment materials especially during strong wind conditions.

Variability in the bPAR index was mostly confined to the inshore (and to some extent, the mid-shelf) water bodies in most NRM regions (Devlin et al., 2012). This not only underscores the overall exposure risk of the nearshore regions to light reduction as a likely response to increased turbidity and high CDOM absorption due to land-based runoffs from nearby catchments but also emphasises three key points. Firstly, it lends support to current policies and measures (i.e., Reef 2050 Water Quality Improvement Plan 2017-2022) that aim to improve the quality of the water that enters the GBR lagoon. Secondly, the movement of river plumes are indeed generally demarcated along the inner shelf (i.e., due to northward net transport of materials due to SE winds and Coriolis forcings) and while plumes may occasionally move out to the mid- or outer shelf during larger events that coincide with slack or northerly winds, pollutants that can cause light reduction beyond inshore regions are probably dispersed more quickly or deposited in the deeper zones which do not get resuspended again except potentially during strong currents generated by cyclonic conditions (Larcombe and Carter, 2004). This underscores the complex nature and interconnectedness of the many factors that determine light availability within the GBR which are important to consider if we are to better manage water quality and land practices within the GBR. Lastly and more importantly, our results clearly demonstrate the sensitivity of the proposed index to capture light variabilities that have direct impact on coral and seagrass ecosystems of the GBR, hence, also highlight the potential of the proposed new index as an

alternative water quality metric in place of/or to complement the currently used metric based on combined Chl *a* and Z_{sd} sub-indicator data that also maintains the spatial and temporal data requirements essential in studying a region as vast as the GBR.

5.5 Conclusion and future directions

We have presented a new method for developing an index of water quality based on the amount of benthic light reaching corals and seagrasses. Our method uses two core pieces of information. First, GBR-wide estimates of $bPAR_d$ obtained from a remote sensing algorithm allowed assessment of historical light conditions within the GBR on a near-daily time-step over the 17.5 years from July 2002 to December 2019. Second, we specified a combined (coral and seagrass) benthic light threshold that denotes the maximum amount of light that key coral and seagrass species can potentially use to maintain growth, above which very little increase in photosynthetic efficiency can be expected. We combined these two sets of information to derive the relative benthic light stress parameter – the stress on benthic habitats due to low light conditions. This parameter was aggregated over each water year for each 1km x 1km pixels, scaled to a value between 0 and 1 for each management region, and then mapped out to a letter grade, A to E to indicate 'very good' (no light stress) to 'very poor' (very high light stress) water quality conditions which aligned with the current format used in GBR water quality report cards.

The annual and seasonal I_{bPAR} calculated for the six NRM focus regions (Cape York to Burnett-Mary) and four water bodies (enclosed coastal to offshore) showed strong spatial and temporal variability characterised by an overall latitudinal gradient that decreases from north (Cape York) to south (Burnett Mary) and a cross-shelf gradient that improves with distance from the coast. The overall patterns of the I_{bPAR} obtained were indicative of strong response to known drivers of water quality within the GBR (e.g., variability of river discharge and associated total suspended sediment loads and dissolved organic matter, cyclone and weather-related flood events, and the transport (hydrodynamics) of flood plume in the marine environment) and emphasises the importance of robust monitoring tools able to detect exposure of relevant benthic ecosystems to these drivers to better inform water quality management policies implemented within the GBR.

The sensitivity of the proposed method to changes in water quality highlights the skill of the new index to map declines in light availability and more importantly demonstrates its potential as a more robust alternative water quality metric to what is currently used, Z_{sd}, in GBR Reef Report Cards. The new proposed index accounts for variations in bathymetry as well as the quality and quantity of light and employs a threshold that is directly relevant to photobiology. It therefore relates much more directly to ecological outcomes for corals and seagrasses than other water quality metrics such as turbidity or Z_{sd}.

Ongoing access to the underlying algorithm used to derive estimates of bPAR from satellite remote sensing observations is currently planned to be made available through existing data infrastructure within Australia (e.g., via Open Data Cube (ODC) initiative under Geoscience Australia's Digital Earth

Australia and ocean colour data processing stream at the CSIRO's Oceans and Atmosphere, Climate Science Centre) and the wider community (e.g., via NASA's SeaDAS processing software).

Benthic PAR predictions can also be obtained from the GBR eReefs biogeochemical model, which will allow the bPAR index to be calculated for counter-factual land management scenarios, to assist with decision support for GBR policy. It is anticipated that automation of the bPAR index will facilitate its uptake and use in ongoing monitoring and management of the GBR.

"If you can't yet do great things, do small things in a great way." – Napoleon Hill (1883 – 1970)

6 Thesis Conclusions and Future Directions

Benthic irradiance is essential to benthic autotrophic life in shallow aquatic ecosystems. The impact of light availability on the health of corals and seagrasses is an incentive to understand spatial and temporal variability in benthic light, including in the Great Barrier Reef (GBR). Knowledge of benthic light distribution could lead to an improved understanding of the benthic ecology and how these ecosystems may respond to environmental changes in both short-term (e.g., cyclones and anthropogenic induced pollution) and long-term (e.g., climate) time scales. Therefore, the focus of this PhD has been to develop a benthic irradiance algorithm to accurately derive benthic light intensities reaching the seafloor within the GBR from MODIS (Aqua) satellite imagery. The spatiotemporally rich dataset emanating from this project subsequently allowed the development of an ecologically relevant metric for water quality monitoring. Thus, two new methods for the GBR have been developed through this research:

(i) A remote sensing-based algorithm for the estimation of benthic irradiance (**Chapter 2**)

(ii) A benthic light index of water quality (**Chapter 5**)

In addition, the successful development of a robust yet straightforward benthic irradiance model provided the opportunity for the generation of a spatiotemporally extensive benthic PAR (bPAR) dataset for the GBR, which allowed opportunities to:

(iii) Characterise the baseline spatial and temporal patterns of benthic light in the GBR (**Chapter 3**).

(iv) Derive information about the spectral light attenuation parameter, K_d, and investigate the in-water constituent that drives light availability in the different NRM regions and cross-shelf water bodies (**Chapter 4**).

(v) Develop a benthic light index of water quality in the GBR (**Chapter 5**).

6.1.1 The benthic irradiance model

Within **Chapter 2**, a physics-based method for estimating benthic irradiance, the amount of light reaching the seafloor, was developed using MODIS Aqua satellite imagery. The model was a simple implementation of Lambert-Beer's Law of exponential decay. The surface values of the downwelling planar irradiance, $E_d(\lambda, 0^+)$ was first propagated across the air-water interface and then vertically through the water column whose depth was defined using high-resolution seafloor bathymetry data. The light penetration was calculated using an inherent optical property (IOP)-based K_d model for which the

vertically homogenous spectral IOPs, total absorption $a(\lambda)$ and total backscattering $b_b(\lambda)$ coefficients were obtained from a shallow water inversion model (SWIM). After calculating the spectral instantaneous benthic irradiance, $E_b(\lambda)$, at each of the ten MODIS wavelengths, the model integrated spectrally (between 400-700 nm) to estimate the instantaneous bPAR, $bPAR_i$. Assuming clear-sky conditions, daily integrated values, $bPAR_d$, were calculated from $bPAR_i$ as a function of location and time of the year.

The model was validated using four test sites across the GBR, where *in situ* PAR measurements were obtained by moored light sensors. As the sensors were not always moored near the seafloor, especially at the three deep sites, the modelled $E_b(\lambda)$ was calculated at the specific depth corresponding to the depth of light sensor deployment for each period of *in situ* data collection. Matchups between concurrent satellite-derived bPAR and *in situ* PAR values indicated strong agreement, slight bias, and low mean absolute error suggesting that the benthic irradiance model resolved optical properties typical in complex shallow coastal waters. The model was further tested on a full MODISA time series (July 2002 to December 2018) for a small region in the central GBR, revealing that the model could reproduce realistic patterns of temporal variability.

The results of the benthic irradiance model provided the baseline dataset to assess changes in bPAR in time and space scales relevant to the GBR (**Chapter 3**), examine its external drivers (**Chapter 4**), and form the basis of a GBR water quality metric based on benthic light availability (**Chapter 5**). This new approach is transferrable to other coastal waters for which spectral IOPs and high-resolution bathymetry data exist with the potential for operationalisation.

6.1.2 Spatiotemporal variability of benthic PAR in the GBR

The baseline spatial and temporal patterns of bPAR in the GBR were presented within **Chapter 3** using the dataset emanating from a GBR-wide implementation of the benthic irradiance model. Here, the first section was focused on the characterisation of long-term variability contained in the 16.5 years of data (July 2002 to Dec 2018), which included GBR-wide mean bPAR maps of the overall long-term, annual, seasonal, and monthly climatologies. Sub-regional aggregated values for 24 zones, i.e., National Resource Management (NRM) zones (Cape York, Wet Tropics, Dry Tropics, Mackay Whitsunday, Fitzroy, and Burnett Mary) and cross-shelf water bodies (enclosed coastal, open coastal, mid-shelf, and offshore) combination, were also produced to track changes and facilitate comparison in benthic light that is aligned to the current GBR monitoring approach.

The complete 16.5-year climatology highlighted a strong spatial variability with mostly high bPAR in the northern GBR, where the shelf is narrow. In contrast, more variable bPAR was noted for the southern GBR, where the shelf can be as wide as ~260 km. The global bPAR climatology averaged across each zone also showed long-term means varying by over 50-fold. The Fitzroy and Mackay

Whitsunday NRM regions consistently showed the lowest long-term mean bPAR across water bodies than other sub-regions.

The annual means of bPAR showed the year-to-year variation of bPAR within the GBR from 2003 to 2018, which revealed 2011 was the 'darkest' year on record with a GBR-wide annual bPAR mean of 1.6 mol photons m^{-2} d^{-1}. This value corresponds to 43% lower bPAR than the full 16.5-year long-term mean and 24% lower than the 'brightest' years in the series (highest annual bPAR of 2.1 mol photons m^{-2} d^{-1} calculated for 2005 and 2007). Since 2011 marks an extreme event in the history of the GBR, due to unprecedented rain and flooding in Queensland from November 2010 associated with Tropical Cyclone (TC) Tasha to early January 2011 during the passing of severe TC Yasi, which further exacerbated state-wide flooding and enhanced resuspension and upwelling, these results highlight that benthic light does respond to these drivers and inspecting such interaction may assist in efforts to monitor and manage benthic habitats across the GBR shelf.

The seasonal and monthly bPAR highlighted the strong seasonality and spatial variability reflecting the temporally varying incident surface radiation. As expected, due to solar angle and day length, higher bPAR values were noted during the austral summer months than the austral winter months, especially in the northern GBR. Overall, stronger spatial variability was noted in the southern GBR, both in the monthly and seasonal climatologies. Consistently low bPAR values were obtained in the two inshore coastal locations in the Fitzroy NRM region, while Mackay Whitsunday NRM regions showed the lowest bPAR in the offshore.

The second part of **Chapter 3** presented the quantitative characterisation of bPAR using three methods: Hovmöller diagrams, EOF analysis, and values of standard deviation and coefficient of variation.

- The Hovmöller diagrams depicted the temporal evolution of benthic light values across the GBR over the last 16.5 years, highlighting: (i) distinct north to south differences, (ii) distinct horizontal and vertical structures ('events'), and (iii) pronounced cyclical features.
- The EOF analysis indicated that most of the variability in bPAR within the GBR is driven by seasonal variability (Mode 1 with 56.5 %) with a temporal pattern that also reflects the patterns obtained in the seasonal and monthly climatology. EOF Mode 2, although only explaining 6.2 % of the data variance, showed a spatial feature of variability driven by the local oceanography and topographic control in the GBR shelf. These results highlighted that the benthic light patterns in the GBR are also a result of complex interactions with physical processes that operate on the shelf.
- The standard deviation (maps and global means) highlighted a gradient in bPAR variability that increases from offshore to inshore coastal locations (i.e., variability is greater inshore). Similarly, the coefficient of variation (CV) for each zone underscored the substantial variability of bPAR, especially in the enclosed coastal waterbody across all NRM regions, which was

greatest in the Fitzroy NRM and smallest in the Cape York NRM. Temporally, the greatest variability was noted during austral autumn, with a peak in April in the Mackay Whitsunday and Fitzroy NRM regions.

6.1.3 Controls of light availability in the GBR

Implementing the benthic irradiance model from July 2002 to December 2019 also produced intermediate output parameters, specifically the spectrally resolved diffuse attenuation coefficients, $K_d(\lambda)$, which describe the spectral downward attenuation of light in the GBR and can be used to calculate bPAR at any arbitrary depth. **Chapter 4** explored the drivers of the variability of K_d using a suite of optical constituents and environmental predictors and random forest model (RFM) analysis.

The results of the RFMs highlighted that:

- In the inshore coastal water bodies, CDOM and NAP (assumed derived from land and river runoff) strongly influence variations of K_d and thus justify ongoing investments focused on these regions to monitor, mitigate, and manage impacts of anthropogenic activities in nearby catchment areas.
- In the mid-shelf, variability in K_d may be due to the variability in phytoplankton (Chl *a* concentration used as a proxy) resulting from elevated phytoplankton biomass production driven by increased nutrient inputs from combined land-derived sources, resuspension, and local upwelling within the shelf. This information may provide a rationale to further assess the impacts of land-based pollutants farther from the coast, despite suggestions of the unlikely potential of the riverine materials to reach the mid-shelf. However, it is essential to note that the potential for offshore transport of land-derived materials (substantially away from the coast and reach the mid-shelf) may strongly depend on the width of the shelf. Transport of nutrient-laden waters reaching the mid-shelf is more likely in the northern GBR, where the shelf is narrow and less likely for the southern GBR except maybe during extreme flood events.
- In the offshore water bodies, variability in K_d was consistent with clear water oceanic conditions where the optical properties are driven by variations in phytoplankton biomass (Chl *a* concentrations).

The outcomes of this analysis highlighted that land-derived nutrients might also drive the high Chl *a* concentrations in the mid-shelf region of the GBR. Thus, there is a need for additional efforts to assess further the dynamics and consequences of the transport of excess nutrients to the mid-shelf region.

6.1.4 A benthic light index of water quality

Within **Chapter 5**, a new benthic light index of water quality was developed, recognising that water quality is essential to the health of marine ecosystems and that there is a need for an ecologically-relevant metric for light-dependent benthic organisms. The benthic light index has three main requirements: (i) a GBR-wide spatiotemporal bPAR dataset, (ii) a combined maximum benthic light threshold, and (iii) a method to summarise benthic light stress using the first two information. Benthic light stress in this context indicates the extent to which the observed bPAR fell short of the locally- and seasonally- specific optimum levels. The results of (iii) were then reported as a scaled value for each of the 24 zones (i.e., six NRM focus regions and four water bodies) between 0 (indicating maximum observed benthic light stress in any season in the record for a zone, thus very poor water quality) and 1 (indicating low benthic light stress, hence very good water quality) and mapped onto the five-step letter grading scale used in the current GBR Reef Report Cards.

The proposed index of water quality underscored substantial spatial and temporal variability of benthic light stress experienced within the GBR in the last 17.5 years closely related to the dynamics of key water quality drivers, the occurrence of atmospheric and physical disturbances, and local oceanography. The light stress maps (annual) and I_{bPAR} time series (annual and seasonal) showed that the inshore coastal locations are most vulnerable to declines in benthic light levels compared to the mid-shelf and offshore locations despite receiving higher daily light doses. The overall gradients in the I_{bPAR} time series are characterised by a general latitudinal decrease from the north (Cape York) to the south (Burnett Mary) and a cross-shelf gradient that improves with distance from the coast.

The benthic light index is sensitive to changes in water quality and can be used to map declines in light availability. I_{bPAR} accounts for variations in bathymetry and the quality and quantity of light and employs a threshold that is directly relevant to photobiology and therefore relates much more directly to ecological outcomes for corals and seagrasses. Thus, the new benthic light water quality index offers a robust alternative water quality metric than the Secchi disk depth (Z_{sd}) currently used in the GBR Reef Report Cards.

6.2 Implications

The benthic irradiance model developed within this PhD research has been demonstrated to estimate bPAR intensities in mid-shelf waters of the GBR with high accuracy. The maps of long-term spatial and temporal patterns and distribution of benthic light provide the first GBR-wide overview of this essential physical resource for reliant benthic organisms like corals and seagrasses. The extensive benthic PAR dataset resulting from the model implementation, using the full MODISA time-series up to December 2019, also allowed a benthic light index of water quality to be developed within this PhD research. These two new remote sensing-based methods offer a cost-efficient way to improve our

understanding of and allow monitoring of benthic light within the GBR that is not limited to discrete point locations, as is the case for *in situ* observations.

The outcomes of this research project have implications for the health of benthic organisms and the complex and interconnected GBR ecosystem. The GBR is home to extensive seagrass meadows and over 3,000 individual reefs. Before this PhD project, there was limited information on benthic light intensities. Now, it is possible to explore how historical benthic light patterns relate to the distribution and abundance of benthic habitats. The bPAR dataset may also help attain an improved understanding of the ecological impacts of benthic light intensities and possible complex interactions due to the increasing pressures from climate change. Exploring the changes and patterns in bPAR has provided an insight into the historical and spatiotemporal extent of impacts from local disturbances (i.e., cyclones and flood events) and future datasets that may be produced using the methods developed here will provide the same opportunity. Thus, bPAR can be a vital aspect of the monitoring and management of the GBR.

6.3 Future Work

6.3.1 Multi-sensor approach of benthic irradiance model implementation

There are some opportunities for future improvement and additional works to the present study. The current benthic irradiance model was only applied to the MODISA dataset extending between July 2002 and December 2019 (note: this cut-off date does not necessarily reflect the most recent data from this sensor). A longer and continuous time series of benthic PAR can be achieved using a multi-sensor approach using historical and current operational ocean colour missions. For example, with historical missions (e.g., NASA's SeaWiFS) and current observation programs (EUMETSAT's Copernicus Series and NASA/NOAA's Joint Polar Satellite Program), it is feasible to develop a bPAR time series from 1997 onwards. A multi-sensor method has been employed to validate ocean colour products (Bailey and Werdell, 2006), and similar satellite data considerations (i.e., spatial, processing, and screening) may be considered in implementing the benthic irradiance model to datasets from other missions. Ideally, the only additional requirement is implementing the SWIM model to obtain the required corresponding IOP estimates that will be used to calculate the light attenuation, in turn, used to calculate the instantaneous benthic irradiance using the Beer-Lambert's equation. The approach can be applied in other regions given adequate bathymetric maps and sufficient observational data to define the IOPs.

The benthic irradiance model developed through this PhD research project has been implemented in NASA's Ocean Color Software Suite (OCSSW), supporting multiple missions. This is also the case for the SWIM algorithm, meaning both our bPAR model and SWIM can be used in missions that NASA supports (SeaWiFS, MERIS, VIIRS, etc.). The advantage of such an exercise would be an even longer

time series that could provide insight into historical benthic light regimes, including the light conditions related to past bleaching, cyclone, and flood events. A future longer dataset would thus allow assessment of the spatiotemporal extent of the impact of disturbances to benthic light conditions experienced within the whole GBR.

The newer satellite sensors also feature higher spectral and spatial resolutions than the MODISA dataset used here, which would increase the application of the model, especially near features that are much smaller than the nominal 1 km^2 pixel size of MODISA. In addition, the other satellite missions would have a different overpass time than the MODISA sensor, which may be used to further improve the daily-integrated estimates of benthic light and potentially address some of the complications related to inherent diurnal variation of solar radiation (e.g., due to changes in cloud cover).

6.3.2 Estimates of benthic PAR over shallow reef pixels

The current estimates of bPAR over shallow reef features and bathymetry (≤ 5 m depth) over the whole GBR region are unreliable because of the bottom signal contamination and are often excluded in the analysis. Hence, it presents one of the limitations of the study. In this PhD research project, the pixel exclusion was primarily based on ancillary bathymetric data (Beaman, 2010a) superimposed with the island and reef features data (https://eatlas.org.au, date last accessed: 8 December 2021), which in the future may be improved using the output from a global high-resolution coral reef mapping initiative, including the GBR (Allen Coral Atlas, 2020). The bottom signal contamination of the water-leaving radiance also depends on water clarity and seafloor albedo aside from the bathymetry of the pixel (McKinna and Werdell, 2018). In future, identification of shallow pixels for exclusion may be improved by employing the newly developed flag called ‘OPSHAL’ (McKinna and Werdell, 2018) during the satellite data processing, which would identify optically shallow pixels considering the three abovementioned variables and may further enhance the accuracy of the bPAR estimates near these features.

Excluding optically shallow pixels is common in ocean colour remote sensing to minimise the effects of the bottom signal contamination, which can otherwise result in high estimation errors of target parameters. Since these pixels are over the coral reef and seagrass environments, this practice leads to information gaps (e.g., regarding benthic light intensities) where most critical ecological processes occur. Optical characterisation of optically shallow pixels to collect IOP data, specifically the total absorption and total backscattering coefficients, may offer the solution to address this gap. However, deriving quantitative information over the optically shallow pixels from ocean colour data is not trivial (Barnes et al., 2018; Garcia et al., 2018) because of the challenges in separating the benthic signal from that of the overlying water column where numerous absorption and scattering processes ensue (Barnes et al., 2018; Garcia et al., 2020), which are non-linear and spectrally-varying interactions (IOCCG, 2000). Still, the upcoming NASA Plankton, Aerosol, Cloud, ocean Ecosystem (PACE) mission

(https://pace.oceansciences.org/home.htm, Date accessed: 8 December 2021) has already provided opportunities for preliminary works that aim to improve the shallow water IOP retrievals over the reefs and other shallow features. The anticipated success of the development of spectral matching inversion algorithms in optically shallow waters (Barnes et al., 2018) using the future data stream from the PACE mission would benefit future versions of the benthic irradiance model if IOP data over the GBR reef features can be retrieved and used as input in the model where SWIM IOPs are not reliable to accurately estimate benthic irradiance and fill data gaps in these locations.

6.3.3 Bottom depth correction using modelled coincident tide height

Another model improvement can be achieved by using tide-corrected bathymetry to define the water column depth of light propagation. The benthic irradiance model described in **Chapter 2** used bathymetric data at mean sea level (MSL) (Beaman, 2010b). However, some locations in the GBR have strong tidal amplitude fluctuations (up to 7 m tidal amplitude), which sometimes coincide with the satellite overpass and remotely-sensed data collection. The depth-sensitivity analysis (DSA) presented in Section 2.5.5 demonstrated the impact on derived bPAR of the *in situ* (pressure) depth and the 3D-GBR MSL bathymetry at one of the model's test sites, the Yongala. The DSA results may be deemed representative of most seaward locations within the GBR but may not necessarily represent locations near shore or towards the southern GBR where tidal fluctuations can be significant (e.g., Broad Sound). The existing OSU Tidal Inversion Software (OTIS) (Egbert and Erofeeva, 2002) can be used to predict the tide height coincident during satellite overpass (e.g., considering both date and time of remote data collection). The resulting tide height prediction for each day and pixel location with valid remote sensing data can then be used to correct the water column depth for that day, ensuring that the vertical distance where the instantaneous bPAR is calculated will integrate changes in water column depth due to tide for each pixel within the GBR domain.

6.3.4 Benthic light and coral bleaching in the GBR

There has been an unprecedented frequency of warm thermal stress across the world's ocean in the last 30 years (Donner, 2011) reiterating the forbidding results of a global assessment of coral bleaching under climate change. This assessment predicted that coral bleaching could become an annual or biannual event for many of the world's coral reefs within 30 to 50 years (Donner et al., 2005). In 2015-2016, the third global-scale mass bleaching event occurred, including in the Great Barrier Reef (Hughes et al., 2017). Mass bleaching events serve to highlight the need to address human impacts, support management strategies that promote reef resilience and implement firm policy decisions to tackle global warming (Hughes et al., 2003; Hughes et al., 2018a).

In the presence of thermal stress, previous studies have noted that while irradiance is critical to maintaining the health and growth of corals, high irradiance may increase the susceptibility of corals to

bleaching (Leahy et al., 2013). Yet, at high temperatures and extreme photoinhibition, shading from high turbidity or high productivity reduces the stress on the symbiont's photosystem, which in turn lessens the risk of coral bleaching (Warner et al., 1999; Takahashi et al., 2004; Cacciapaglia and van Woesik, 2016; van Woesik and McCaffrey, 2017), suggesting the physiological benefits of reduced irradiance during thermal stress.

The outputs of this study provide an opportunity to explore the potential causal relationship between high irradiance anomalies and coral bleaching. The extensive bPAR dataset could be used to generate benthic light anomalies which span the back-to-back coral bleaching events in the GBR (2015-2016 and 2016-2017 austral summer periods) to investigate the spatial and temporal coincidence between bleaching, locations of corals that bleached, and anomalous irradiance values. This will give an overview of the potential range of acute light conditions experienced by corals in areas where thermal stress-induced bleaching conditions were noted that may have enhanced the bleaching risks in corals. However, it may be noted that the current bPAR dataset with its limitation as mentioned in Section 6.3.2 would only represent potential anomalies in nearby waters deeper than 5 m. Thus, useful estimates of anomalous irradiance directly over reefs would benefit if optical characterisation over shallow reef pixels could be realised.

6.3.5 Operationalisation of the benthic irradiance model

The methods that constitute the benthic irradiance model presented in **Chapter 2** are transferrable to any location and satellite imagery from missions other than MODISA if the other input parameters are made available. Specifically, the IOPs (spectral total absorption and spectral total backscattering coefficients) used to calculate $K_d(\lambda)$ are not tied to the inversion model used here (i.e., SWIM) and can be obtained using other methods at wavelengths that match the input satellite imagery.

In addition, the generation of the bPAR data product can be operationalised using the same MODISA imagery as presented but can be extended to use other existing (e.g., OLCI, MERIS, SeaWiFS) or upcoming remote sensing datasets (e.g., PACE). For the GBR, the discussions around the potential for operationally producing bPAR data have already started. Existing infrastructure such as the Open Data Cube (ODC), an Open-Source Geospatial data management and analysis software project by Geoscience Australia, can be leveraged to facilitate workflow for bPAR data production. The agency has already been acquiring and processing the MODIS ocean colour remote sensing data, which can be extended to include workflows for generating SWIM-derived IOPs and executing the full benthic irradiance model. As already mentioned, the underlying algorithm for generating bPAR has already been implemented on NASA's OCSSW processing suite (executed through SeaDAS) and can efficiently be run during Level 2 data processing. This exercise will benefit the GBR community and various stakeholders that require critical and reliable data on ecological parameters such as benthic light in their decision-making activities.

Operationalising the benthic irradiance model will likely increase the chance that the benthic light index of water quality (**Chapter 5**) will be adopted as an additional water quality parameter used in GBR Report Cards because of the potential ease of data access. Based on the NASA Application Readiness Level (ARL) metric, a nine-step index used to track and manage the progression and distribution of funded projects (https://www.nasa.gov/directorates/heo/scan/engineering/technology/technology_readiness_level, Date accessed: 09 December 2021), the benthic irradiance model has completed ARL 5 (Validation in Relevant Environment) where the potential of an operational system has been determined (e.g., the potential for uptake in water quality monitoring activities). Thus, at the conclusion of this PhD, the bPAR model is at ARL 6 (Demonstration in Relevant Environment) since the model's potential has already been demonstrated through the proposed benthic light index of water quality (**Chapter 5**) for water quality conditions reporting in the GBR, marking a substantial progress towards an operational bPAR data product stream.

Thesis Appendices

Appendix 1: Corrections - Magno-Canto, M., McKinna, L., Robson, B., Fabricius, K., and Garcia, R. (2020) *Model for deriving benthic irradiance in the Great Barrier Reef from MODIS satellite imagery: erratum*, Opt. Express 28, 27473-27475, https://www.osapublishing.org/oe/abstract.cfm?uri=oe-28-19-27473

Appendix 2: Monthly climatological coefficient of variation (CV, %) of bPAR for the whole GBR and different zones (defined by NRM region and waterbody combination).

Appendix 3: Long term monthly spectral diffuse light attenuation coefficients in the Great Barrier Reef.

Appendix 4: Time series plots of datasets used in the Random Forest Model analysis.

Appendix 5: Monthly images of Chlorophyll a concentration for the GBR derived from MODIS-Aqua satellite sensor.

Appendix 6: Landsat 8 True Colour image of Burdekin River floods in 2019.

.

Appendix 1: Model for deriving benthic irradiance in the Great Barrier Reef from MODIS satellite imagery: erratum

Corrections for equations in our recently published paper (Magno-Canto et al., 2019) are presented.

A post-publication review of our methods (Magno-Canto et al., 2019) has indicated that Equation (8) and Equation (12) in the original manuscript should read as:

$$bPAR_n = \int_{400}^{700} \left(t_g E_d^{0^+}(\lambda) \right) e^{-K_d(\lambda)z} d\lambda \tag{8}$$

$$bPAR_d = 2 * \int_{\phi_{rise}}^{\phi_{noon}} \int_{400}^{700} \left(t_g E_d^{0^+}(\lambda, \theta'_{solz}(\phi)) \right) e^{-K_d(\lambda)z} d\phi d\lambda \tag{12}$$

where $E_d^{0^+} = F_0 * T * \cos(\theta'_{solz}(\phi))$ following (Frouin et al., 2002). Here, $E_d^{0^+}$ is the above-water downwelling plane solar irradiance, F_0 is the extraterrestrial solar irradiance, T is a transmittance parameter that accounts for atmospheric absorption and scattering by gases, clouds, and aerosols (Frouin et al., 2002), and $\theta'_{solz(\phi)}$ is solar zenith angle at a given time between sunrise to noon at each hour angle ϕ. Note that this correction also implies that all texts pertaining to E_s or $E_s(\lambda, 0^+)$, a nomenclature that could be misinterpreted as scalar irradiance, in the original manuscript should now read as $E_d^{0^+}$ or $E_d^{0^+}(\lambda, \theta'_{solz}(\phi))$.

In addition, the term inside the parenthesis in Equation (13) is missing a negative sign (Kumar et al., 1997) and should read as:

$$\phi_{rise} = \cos^{-1}\left(-\tan(\delta)\tan(lat) \right). \tag{13}$$

We applied these corrections to our original benthic irradiance model and performed matchup and validation exercise as detailed in the original manuscript. The corrected model still shows strong agreement between the satellite-derived and *in situ* benthic PAR across all four test sites (Figure 7.1). Notably, the corrections have led to a more consistent model bias and mean absolute error (MAE) across the test sites. As previously reported, bias and MAE were smaller in clearer offshore waters (Palm Passage and Myrmidon) compared to more optically complex inshore (Yongala) and mid-shelf (Heron) waters. We note that these corrections did not affect the relevance of our results to understanding benthic light and its effects within the Great Barrier Reef World Heritage Area.

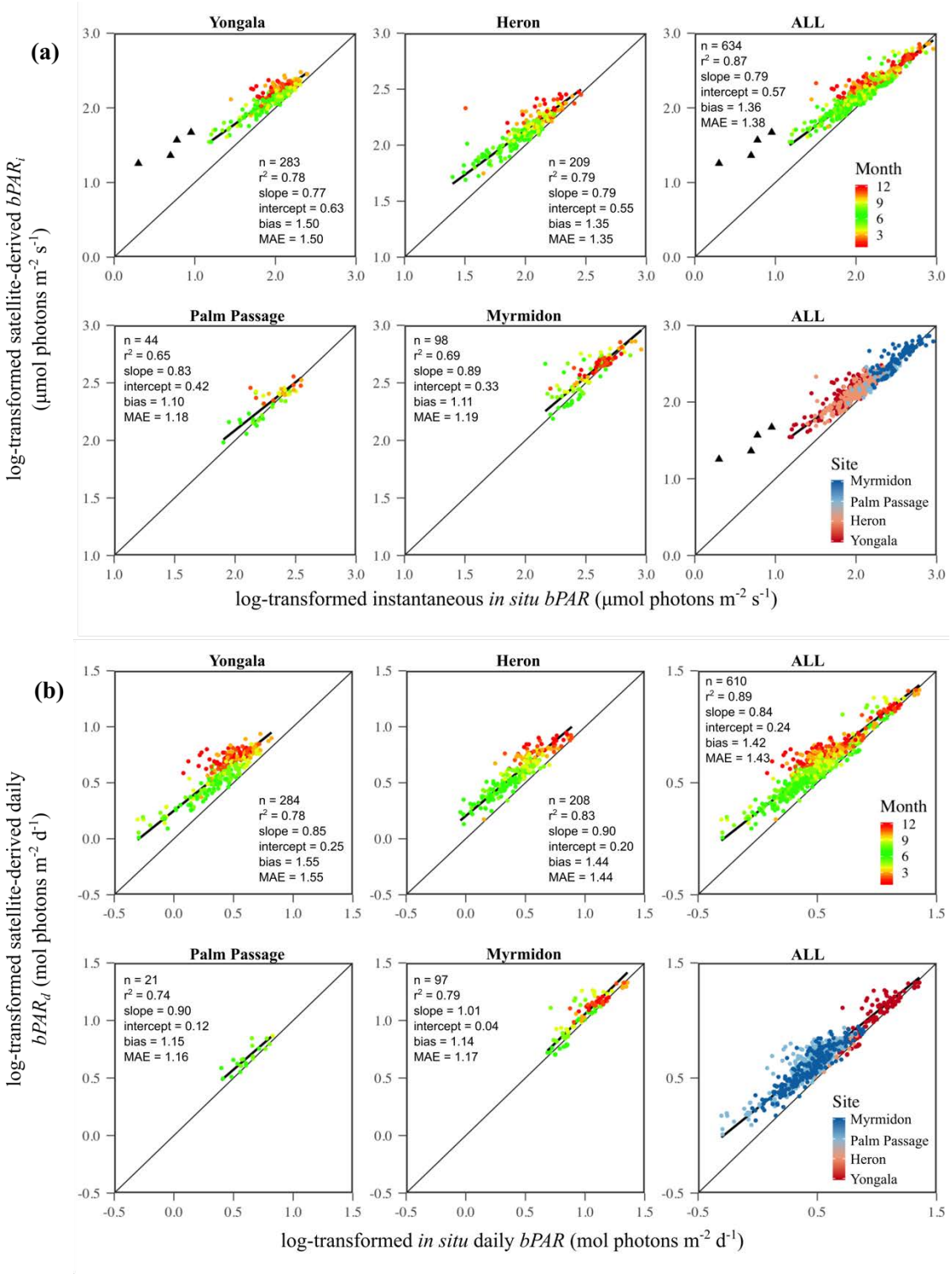

Figure A1.1: (a) Scatterplots of concurrent log-transformed satellite-derived instantaneous benthic PAR ($bPAR_i$) and in situ bPAR at four test sites (Yongala, Heron, Palm Passage, and Myrmidon). The red-yellow-green-magenta colour scale represents month of observation. The scatterplot labelled 'ALL' indicates combined observations from all test sites, plotted according to observation site (red to blue colour scale). Filled black triangles indicate values considered as outliers due to an extreme weather event experienced in the Yongala study site, which were excluded from the analysis (as previously reported). (b) The same as for (a) except log-log scaled scatterplots are of satellite-derived daily-integrated benthic PAR ($bPAR_d$) vs. in situ daily bPAR.

Appendix 2: Coefficient of variation calculated for each monthly bPAR climatology

Table A2.1: Coefficient of variation (%) of monthly bPAR climatology for the whole GBR, whole length of the GBR, and NRM regions for each cross-shelf waterbody.

Region	Waterbody	J	F	M	A	M	J	J	A	S	O	N	D
Whole GBR		42	49	55	54	50	45	42	39	39	42	39	36
Whole GBR: length North to South	EC	75	81	93	99	95	85	84	83	87	87	75	67
	OC	48	56	65	67	60	54	50	46	48	53	47	41
	MS	37	44	49	47	42	39	36	32	33	36	33	31
	OS	40	45	51	49	44	41	39	37	36	38	36	36
Cape York	EC	51	56	67	73	73	66	68	66	68	68	56	49
	OC	28	35	47	50	50	46	45	40	39	42	34	28
	MS	31	39	48	44	42	39	39	36	33	34	31	28
	OS	34	37	43	36	32	30	30	28	26	29	29	29
Wet Tropics	EC	86	95	104	115	104	93	97	107	104	103	85	74
	OC	50	56	68	77	69	63	64	55	54	58	45	36
	MS	39	48	56	59	49	45	41	34	32	37	30	27
	OS	39	46	56	59	55	47	40	34	33	37	34	33
Dry Tropics	EC	95	125	130	129	115	95	98	116	127	125	100	84
	OC	50	65	64	66	60	52	51	47	50	56	47	38
	MS	35	46	47	48	44	37	31	26	28	32	26	25
	OS	38	48	53	54	49	43	38	34	36	38	32	33
Mackay Whitsunday	EC	93	106	121	129	113	97	90	73	82	88	78	64
	OC	53	65	75	75	66	57	50	47	49	56	53	46
	MS	50	64	77	74	74	65	58	55	48	46	46	43
	OS	50	57	66	65	60	55	52	51	50	50	45	46
Fitzroy	EC	162	153	188	221	193	176	148	138	147	150	135	154
	OC	68	78	87	80	66	58	52	50	54	61	60	57
	MS	50	54	58	55	47	41	37	37	39	44	45	43
	OS	42	47	51	52	50	48	46	45	44	43	41	41
Burnett Mary	EC	89	105	127	97	70	63	52	52	68	78	67	70
	OC	54	65	73	59	46	40	34	29	36	44	39	40
	MS	28	31	33	31	30	30	25	21	25	28	28	27
	OS	52	58	65	65	71	74	72	61	57	55	55	55

Appendix 3: Long term monthly spectral diffuse light attenuation coefficients in the Great Barrier Reef

Table A3.1: Long term monthly light attenuation coefficients at 412 nm, Kd(412).

Region	Waterbody	J	F	M	A	M	J	J	A	S	O	N	D
Whole GBR		0.132	0.177	0.187	0.189	0.171	0.151	0.136	0.123	0.129	0.142	0.119	0.110
Whole GBR: length North to South	EC	1.406	1.749	2.029	2.149	2.055	1.762	1.760	1.716	1.765	1.633	1.361	1.207
	OC	0.351	0.471	0.522	0.505	0.431	0.352	0.312	0.280	0.303	0.350	0.300	0.262
	MS	0.095	0.134	0.131	0.132	0.122	0.113	0.098	0.086	0.089	0.095	0.083	0.079
	OS	0.067	0.086	0.087	0.090	0.087	0.082	0.076	0.070	0.073	0.082	0.065	0.065
Cape York	EC	0.824	0.948	1.189	1.402	1.552	1.339	1.371	1.207	1.141	1.029	0.880	0.773
	OC	0.245	0.327	0.437	0.478	0.512	0.430	0.393	0.321	0.312	0.329	0.272	0.201
	MS	0.143	0.225	0.230	0.219	0.190	0.170	0.154	0.139	0.128	0.126	0.119	0.116
	OS	0.094	0.114	0.125	0.115	0.099	0.092	0.086	0.080	0.076	0.082	0.079	0.083
Wet Tropics	EC	1.523	1.875	2.143	2.129	1.957	1.619	1.702	1.732	1.751	1.664	1.400	1.234
	OC	0.388	0.511	0.644	0.695	0.594	0.521	0.506	0.418	0.402	0.430	0.295	0.234
	MS	0.140	0.233	0.241	0.228	0.165	0.142	0.120	0.097	0.108	0.128	0.096	0.091
	OS	0.068	0.110	0.098	0.098	0.086	0.074	0.064	0.059	0.064	0.085	0.060	0.060
Dry Tropics	EC	1.626	2.161	2.407	2.599	2.331	1.824	1.894	2.133	2.343	2.159	1.605	1.364
	OC	0.415	0.648	0.601	0.608	0.507	0.394	0.361	0.360	0.428	0.474	0.335	0.266
	MS	0.091	0.166	0.124	0.125	0.106	0.096	0.077	0.066	0.080	0.096	0.069	0.067
	OS	0.051	0.068	0.068	0.072	0.067	0.063	0.058	0.053	0.063	0.072	0.049	0.051
Mackay Whitsunday	EC	1.431	1.713	2.046	2.329	2.202	1.802	1.634	1.300	1.326	1.382	1.111	0.968
	OC	0.354	0.443	0.485	0.455	0.384	0.306	0.252	0.223	0.240	0.300	0.293	0.266
	MS	0.078	0.102	0.111	0.122	0.121	0.112	0.093	0.082	0.079	0.079	0.072	0.070
	OS	0.074	0.091	0.095	0.104	0.102	0.093	0.085	0.078	0.081	0.099	0.069	0.075
Fitzroy	EC	2.436	2.907	3.208	3.236	3.120	2.961	2.883	2.818	2.863	2.700	2.463	2.345
	OC	0.357	0.472	0.528	0.471	0.354	0.289	0.253	0.245	0.280	0.338	0.315	0.305
	MS	0.085	0.100	0.103	0.110	0.112	0.104	0.091	0.080	0.080	0.085	0.079	0.072
	OS	0.062	0.078	0.077	0.084	0.088	0.085	0.080	0.074	0.077	0.080	0.067	0.064
Burnett Mary	EC	1.344	1.701	2.059	1.602	1.104	0.952	0.718	0.729	1.015	1.133	0.975	1.053
	OC	0.367	0.488	0.583	0.387	0.265	0.221	0.174	0.160	0.217	0.279	0.232	0.275
	MS	0.075	0.088	0.087	0.078	0.078	0.081	0.076	0.069	0.083	0.092	0.080	0.079
	OS	0.042	0.046	0.048	0.051	0.057	0.061	0.061	0.056	0.057	0.055	0.047	0.046

Table A3.2: Long term monthly light attenuation coefficients at 443 nm, Kd(443).

Region	Waterbody	J	F	M	A	M	J	J	A	S	O	N	D
Whole GBR		0.110	0.140	0.145	0.147	0.136	0.121	0.110	0.099	0.102	0.112	0.100	0.093
Whole GBR: length North to South	EC	1.019	1.211	1.376	1.492	1.434	1.223	1.236	1.193	1.255	1.186	1.020	0.901
	OC	0.283	0.363	0.385	0.378	0.325	0.266	0.242	0.215	0.231	0.273	0.248	0.216
	MS	0.080	0.107	0.104	0.105	0.100	0.093	0.082	0.071	0.071	0.076	0.071	0.067
	OS	0.061	0.074	0.075	0.078	0.076	0.072	0.067	0.061	0.061	0.067	0.058	0.058
Cape York	EC	0.629	0.690	0.789	0.951	1.081	0.931	0.975	0.854	0.863	0.829	0.744	0.638
	OC	0.194	0.242	0.299	0.345	0.373	0.321	0.303	0.246	0.251	0.277	0.238	0.170
	MS	0.117	0.182	0.168	0.163	0.146	0.133	0.123	0.112	0.105	0.103	0.099	0.096
	OS	0.082	0.094	0.100	0.093	0.082	0.077	0.073	0.068	0.065	0.070	0.070	0.072
Wet Tropics	EC	1.022	1.219	1.391	1.434	1.310	1.084	1.151	1.149	1.189	1.124	0.965	0.843
	OC	0.288	0.346	0.424	0.498	0.424	0.382	0.384	0.309	0.297	0.321	0.230	0.180
	MS	0.108	0.163	0.170	0.168	0.129	0.113	0.098	0.080	0.085	0.100	0.080	0.076
	OS	0.060	0.087	0.080	0.083	0.074	0.065	0.057	0.051	0.054	0.069	0.054	0.054
Dry Tropics	EC	1.178	1.505	1.656	1.854	1.651	1.274	1.334	1.484	1.657	1.535	1.171	1.001
	OC	0.317	0.478	0.430	0.456	0.383	0.296	0.279	0.274	0.317	0.354	0.267	0.211
	MS	0.075	0.129	0.098	0.100	0.088	0.079	0.065	0.056	0.064	0.075	0.060	0.058
	OS	0.048	0.061	0.060	0.063	0.060	0.056	0.052	0.047	0.052	0.059	0.045	0.047
Mackay Whitsunday	EC	1.036	1.178	1.387	1.629	1.539	1.250	1.163	0.889	0.920	0.980	0.829	0.709
	OC	0.308	0.377	0.386	0.354	0.297	0.234	0.198	0.176	0.189	0.243	0.253	0.228
	MS	0.069	0.084	0.092	0.100	0.101	0.093	0.078	0.068	0.064	0.065	0.063	0.061
	OS	0.067	0.080	0.084	0.089	0.088	0.081	0.074	0.067	0.067	0.078	0.062	0.065
Fitzroy	EC	1.760	2.039	2.205	2.238	2.177	2.065	2.015	1.967	1.995	1.901	1.762	1.702
	OC	0.282	0.359	0.390	0.351	0.273	0.222	0.198	0.190	0.208	0.254	0.250	0.247
	MS	0.073	0.082	0.087	0.091	0.095	0.088	0.077	0.067	0.064	0.067	0.067	0.062
	OS	0.057	0.068	0.070	0.074	0.078	0.076	0.072	0.064	0.064	0.065	0.059	0.057
Burnett Mary	EC	0.986	1.229	1.472	1.179	0.822	0.689	0.533	0.528	0.683	0.786	0.711	0.767
	OC	0.272	0.353	0.428	0.292	0.209	0.172	0.140	0.125	0.155	0.198	0.180	0.207
	MS	0.066	0.074	0.075	0.068	0.069	0.071	0.066	0.059	0.065	0.071	0.068	0.068
	OS	0.040	0.042	0.044	0.046	0.053	0.057	0.057	0.050	0.048	0.046	0.043	0.042

Table A3.3: Long term monthly light attenuation coefficients at 469 nm, Kd(469).

Region	Waterbody	J	F	M	A	M	J	J	A	S	O	N	D
Whole GBR		0.092	0.113	0.116	0.117	0.110	0.098	0.091	0.082	0.083	0.092	0.085	0.079
Whole GBR: length North to South	EC	0.782	0.901	1.015	1.101	1.064	0.907	0.921	0.892	0.947	0.910	0.798	0.705
	OC	0.231	0.287	0.299	0.291	0.253	0.209	0.191	0.171	0.183	0.220	0.205	0.179
	MS	0.067	0.087	0.084	0.086	0.083	0.078	0.069	0.061	0.060	0.063	0.061	0.058
	OS	0.053	0.062	0.064	0.066	0.065	0.062	0.058	0.053	0.052	0.056	0.051	0.051
Cape York	EC	0.499	0.530	0.575	0.699	0.806	0.695	0.732	0.648	0.677	0.680	0.627	0.532
	OC	0.156	0.189	0.223	0.261	0.287	0.250	0.238	0.195	0.203	0.230	0.203	0.143
	MS	0.096	0.149	0.129	0.127	0.117	0.108	0.102	0.093	0.088	0.086	0.084	0.081
	OS	0.070	0.077	0.081	0.076	0.069	0.065	0.063	0.059	0.057	0.060	0.061	0.062
Wet Tropics	EC	0.745	0.872	0.999	1.035	0.950	0.786	0.840	0.839	0.868	0.823	0.712	0.623
	OC	0.223	0.256	0.314	0.372	0.323	0.293	0.296	0.239	0.228	0.249	0.181	0.142
	MS	0.087	0.123	0.128	0.128	0.103	0.092	0.082	0.067	0.071	0.082	0.068	0.064
	OS	0.052	0.071	0.066	0.069	0.063	0.056	0.050	0.045	0.047	0.058	0.048	0.048
Dry Tropics	EC	0.902	1.118	1.239	1.381	1.228	0.946	0.993	1.106	1.239	1.154	0.897	0.774
	OC	0.249	0.360	0.327	0.349	0.296	0.231	0.218	0.215	0.245	0.275	0.214	0.171
	MS	0.063	0.100	0.079	0.081	0.073	0.067	0.056	0.049	0.054	0.062	0.052	0.051
	OS	0.043	0.053	0.052	0.054	0.053	0.050	0.046	0.042	0.046	0.050	0.041	0.042
Mackay Whitsunday	EC	0.797	0.879	1.026	1.206	1.144	0.929	0.865	0.662	0.686	0.741	0.643	0.549
	OC	0.265	0.315	0.315	0.281	0.234	0.186	0.160	0.143	0.154	0.202	0.216	0.194
	MS	0.060	0.071	0.078	0.083	0.084	0.078	0.066	0.059	0.055	0.057	0.055	0.053
	OS	0.058	0.068	0.071	0.074	0.074	0.069	0.063	0.057	0.056	0.064	0.054	0.056
Fitzroy	EC	1.347	1.513	1.636	1.657	1.616	1.537	1.500	1.471	1.493	1.427	1.338	1.305
	OC	0.228	0.278	0.300	0.269	0.213	0.175	0.157	0.151	0.164	0.201	0.202	0.202
	MS	0.062	0.068	0.073	0.076	0.079	0.074	0.066	0.057	0.054	0.057	0.058	0.054
	OS	0.050	0.059	0.060	0.064	0.067	0.066	0.062	0.056	0.054	0.055	0.051	0.050
Burnett Mary	EC	0.755	0.919	1.102	0.881	0.616	0.518	0.404	0.397	0.506	0.582	0.537	0.584
	OC	0.208	0.263	0.321	0.222	0.163	0.136	0.111	0.100	0.118	0.149	0.140	0.160
	MS	0.057	0.062	0.063	0.058	0.059	0.061	0.057	0.051	0.054	0.059	0.058	0.058
	OS	0.037	0.039	0.040	0.042	0.047	0.051	0.050	0.045	0.042	0.041	0.039	0.039

Table A3.4: Long term monthly light attenuation coefficients at 488 nm, Kd(488).

Region	Waterbody	J	F	M	A	M	J	J	A	S	O	N	D
Whole GBR		0.084	0.100	0.102	0.103	0.098	0.089	0.083	0.075	0.076	0.083	0.078	0.073
Whole GBR: length North to South	EC	0.657	0.741	0.829	0.900	0.872	0.745	0.758	0.736	0.787	0.766	0.680	0.602
	OC	0.205	0.247	0.255	0.247	0.216	0.180	0.166	0.150	0.160	0.193	0.183	0.160
	MS	0.063	0.078	0.076	0.077	0.076	0.072	0.065	0.058	0.057	0.059	0.057	0.055
	OS	0.051	0.058	0.059	0.061	0.061	0.059	0.055	0.051	0.050	0.053	0.049	0.049
Cape York	EC	0.429	0.446	0.465	0.570	0.664	0.573	0.607	0.541	0.578	0.599	0.561	0.473
	OC	0.137	0.162	0.185	0.219	0.244	0.214	0.205	0.170	0.179	0.206	0.185	0.129
	MS	0.087	0.133	0.111	0.110	0.104	0.098	0.093	0.085	0.081	0.079	0.078	0.074
	OS	0.065	0.070	0.073	0.070	0.064	0.062	0.059	0.056	0.055	0.057	0.058	0.059
Wet Tropics	EC	0.604	0.697	0.801	0.832	0.767	0.634	0.682	0.682	0.705	0.670	0.582	0.511
	OC	0.191	0.211	0.258	0.308	0.271	0.248	0.251	0.203	0.194	0.212	0.158	0.124
	MS	0.078	0.104	0.109	0.110	0.092	0.084	0.075	0.063	0.065	0.074	0.063	0.060
	OS	0.050	0.064	0.061	0.064	0.060	0.054	0.049	0.045	0.046	0.054	0.047	0.047
Dry Tropics	EC	0.757	0.918	1.021	1.135	1.008	0.776	0.815	0.910	1.022	0.957	0.753	0.653
	OC	0.214	0.299	0.275	0.294	0.252	0.198	0.188	0.185	0.209	0.234	0.187	0.150
	MS	0.059	0.087	0.071	0.073	0.068	0.062	0.054	0.048	0.051	0.058	0.051	0.049
	OS	0.043	0.051	0.050	0.052	0.051	0.049	0.046	0.042	0.044	0.048	0.041	0.042
Mackay Whitsunday	EC	0.672	0.725	0.840	0.989	0.940	0.763	0.712	0.545	0.567	0.618	0.546	0.465
	OC	0.242	0.281	0.278	0.244	0.203	0.163	0.141	0.128	0.138	0.182	0.197	0.177
	MS	0.058	0.065	0.072	0.076	0.077	0.072	0.062	0.056	0.053	0.054	0.054	0.052
	OS	0.055	0.063	0.066	0.068	0.068	0.064	0.059	0.055	0.053	0.059	0.052	0.053
Fitzroy	EC	1.128	1.240	1.341	1.356	1.325	1.262	1.233	1.214	1.233	1.181	1.115	1.095
	OC	0.200	0.237	0.254	0.227	0.184	0.152	0.138	0.133	0.143	0.175	0.178	0.180
	MS	0.058	0.063	0.067	0.069	0.073	0.069	0.062	0.055	0.051	0.054	0.055	0.052
	OS	0.049	0.055	0.057	0.060	0.062	0.062	0.058	0.053	0.051	0.052	0.050	0.049
Burnett Mary	EC	0.633	0.756	0.907	0.724	0.508	0.429	0.336	0.330	0.415	0.477	0.446	0.487
	OC	0.175	0.217	0.266	0.186	0.140	0.118	0.098	0.088	0.102	0.126	0.121	0.137
	MS	0.054	0.057	0.058	0.055	0.056	0.058	0.054	0.049	0.051	0.054	0.054	0.054
	OS	0.037	0.039	0.040	0.042	0.046	0.050	0.049	0.044	0.041	0.040	0.040	0.039

Table A3.5: Long term monthly light attenuation coefficients at 531 nm, Kd(531).

Region	Waterbody	J	F	M	A	M	J	J	A	S	O	N	D
Whole GBR		0.091	0.100	0.102	0.104	0.102	0.097	0.093	0.089	0.089	0.093	0.090	0.085
Whole GBR: length North to South	EC	0.461	0.499	0.553	0.602	0.587	0.505	0.518	0.510	0.550	0.544	0.490	0.435
	OC	0.174	0.197	0.203	0.197	0.179	0.157	0.149	0.139	0.145	0.169	0.162	0.145
	MS	0.077	0.086	0.085	0.088	0.089	0.087	0.083	0.079	0.077	0.078	0.076	0.073
	OS	0.069	0.072	0.074	0.076	0.077	0.076	0.074	0.072	0.071	0.072	0.069	0.069
Cape York	EC	0.319	0.319	0.313	0.390	0.460	0.403	0.429	0.391	0.428	0.457	0.436	0.367
	OC	0.124	0.137	0.146	0.174	0.195	0.177	0.173	0.152	0.159	0.181	0.167	0.124
	MS	0.094	0.126	0.104	0.108	0.108	0.105	0.103	0.098	0.095	0.092	0.090	0.087
	OS	0.076	0.079	0.081	0.082	0.080	0.079	0.078	0.076	0.074	0.075	0.075	0.074
Wet Tropics	EC	0.412	0.457	0.529	0.551	0.511	0.426	0.462	0.467	0.484	0.464	0.407	0.359
	OC	0.156	0.160	0.192	0.228	0.208	0.195	0.199	0.169	0.162	0.174	0.138	0.114
	MS	0.085	0.097	0.102	0.106	0.098	0.094	0.090	0.081	0.082	0.087	0.079	0.076
	OS	0.068	0.075	0.075	0.078	0.077	0.075	0.072	0.069	0.069	0.073	0.068	0.067
Dry Tropics	EC	0.525	0.612	0.685	0.759	0.669	0.518	0.545	0.614	0.693	0.657	0.528	0.461
	OC	0.172	0.219	0.209	0.223	0.198	0.165	0.160	0.158	0.172	0.189	0.159	0.134
	MS	0.074	0.090	0.082	0.085	0.084	0.081	0.076	0.072	0.073	0.076	0.071	0.069
	OS	0.064	0.069	0.069	0.071	0.072	0.071	0.069	0.067	0.067	0.069	0.065	0.064
Mackay Whitsunday	EC	0.479	0.497	0.568	0.668	0.635	0.519	0.489	0.386	0.404	0.445	0.399	0.342
	OC	0.209	0.234	0.231	0.205	0.177	0.151	0.137	0.128	0.135	0.168	0.178	0.162
	MS	0.076	0.080	0.085	0.089	0.091	0.088	0.083	0.079	0.076	0.077	0.076	0.073
	OS	0.071	0.075	0.077	0.079	0.080	0.078	0.076	0.074	0.073	0.075	0.071	0.070
Fitzroy	EC	0.773	0.810	0.886	0.894	0.874	0.834	0.822	0.820	0.839	0.798	0.759	0.751
	OC	0.168	0.188	0.200	0.182	0.157	0.138	0.130	0.127	0.133	0.155	0.157	0.158
	MS	0.074	0.076	0.080	0.082	0.086	0.084	0.081	0.076	0.073	0.073	0.073	0.071
	OS	0.067	0.071	0.072	0.075	0.077	0.077	0.076	0.073	0.071	0.071	0.069	0.068
Burnett Mary	EC	0.432	0.496	0.597	0.475	0.342	0.294	0.240	0.237	0.290	0.331	0.311	0.338
	OC	0.139	0.162	0.196	0.148	0.122	0.110	0.099	0.092	0.098	0.112	0.109	0.117
	MS	0.070	0.071	0.073	0.073	0.075	0.076	0.074	0.071	0.071	0.072	0.071	0.070
	OS	0.062	0.062	0.064	0.066	0.069	0.071	0.071	0.068	0.066	0.064	0.064	0.063

Table A3.6: Long term monthly light attenuation coefficients at 547 nm, Kd(547).

Region	Waterbody	J	F	M	A	M	J	J	A	S	O	N	D
Whole GBR		0.097	0.105	0.106	0.109	0.108	0.104	0.101	0.096	0.096	0.100	0.097	0.092
Whole GBR: length North to South	EC	0.423	0.451	0.497	0.541	0.529	0.458	0.470	0.465	0.502	0.499	0.453	0.403
	OC	0.173	0.192	0.196	0.192	0.177	0.157	0.151	0.141	0.147	0.168	0.163	0.147
	MS	0.085	0.092	0.091	0.095	0.096	0.095	0.092	0.088	0.085	0.086	0.084	0.081
	OS	0.077	0.080	0.081	0.084	0.085	0.085	0.084	0.081	0.080	0.080	0.078	0.077
Cape York	EC	0.300	0.297	0.285	0.355	0.420	0.370	0.395	0.363	0.399	0.430	0.413	0.348
	OC	0.127	0.137	0.142	0.169	0.190	0.175	0.172	0.153	0.160	0.180	0.168	0.128
	MS	0.100	0.129	0.108	0.112	0.114	0.112	0.110	0.105	0.102	0.099	0.098	0.094
	OS	0.084	0.086	0.087	0.089	0.089	0.088	0.087	0.085	0.083	0.083	0.083	0.083
Wet Tropics	EC	0.372	0.407	0.471	0.492	0.458	0.385	0.418	0.422	0.438	0.421	0.371	0.328
	OC	0.154	0.154	0.183	0.216	0.200	0.189	0.193	0.166	0.160	0.170	0.139	0.117
	MS	0.091	0.100	0.105	0.110	0.105	0.102	0.098	0.090	0.090	0.094	0.087	0.083
	OS	0.076	0.082	0.082	0.086	0.086	0.084	0.081	0.078	0.078	0.081	0.077	0.076
Dry Tropics	EC	0.480	0.550	0.617	0.681	0.601	0.468	0.492	0.554	0.625	0.594	0.483	0.424
	OC	0.168	0.207	0.200	0.213	0.193	0.164	0.159	0.157	0.169	0.185	0.159	0.136
	MS	0.082	0.095	0.089	0.093	0.092	0.090	0.085	0.081	0.081	0.084	0.080	0.078
	OS	0.073	0.077	0.077	0.080	0.081	0.080	0.079	0.076	0.076	0.077	0.074	0.073
Mackay Whitsunday	EC	0.440	0.451	0.512	0.601	0.573	0.470	0.445	0.355	0.372	0.409	0.371	0.320
	OC	0.208	0.229	0.226	0.202	0.177	0.153	0.141	0.133	0.139	0.169	0.179	0.163
	MS	0.084	0.087	0.093	0.097	0.099	0.097	0.092	0.088	0.086	0.086	0.085	0.082
	OS	0.079	0.082	0.085	0.087	0.088	0.087	0.085	0.083	0.081	0.083	0.079	0.079
Fitzroy	EC	0.699	0.723	0.791	0.798	0.782	0.747	0.738	0.739	0.756	0.718	0.686	0.681
	OC	0.167	0.182	0.194	0.178	0.157	0.140	0.133	0.131	0.136	0.155	0.157	0.158
	MS	0.082	0.083	0.087	0.090	0.094	0.093	0.090	0.085	0.082	0.082	0.082	0.079
	OS	0.076	0.079	0.080	0.083	0.086	0.086	0.084	0.082	0.080	0.079	0.078	0.076
Burnett Mary	EC	0.395	0.447	0.537	0.429	0.314	0.273	0.226	0.223	0.268	0.304	0.288	0.312
	OC	0.137	0.156	0.186	0.146	0.124	0.114	0.104	0.098	0.103	0.114	0.112	0.118
	MS	0.078	0.079	0.081	0.082	0.084	0.085	0.083	0.080	0.080	0.080	0.079	0.078
	OS	0.071	0.071	0.073	0.076	0.079	0.081	0.080	0.077	0.075	0.074	0.073	0.072

Table A3.7: Long term monthly light attenuation coefficients at 555 nm, Kd(555).

Region	Waterbody	J	F	M	A	M	J	J	A	S	O	N	D
Whole GBR		0.103	0.105	0.111	0.114	0.113	0.109	0.107	0.102	0.102	0.105	0.102	0.098
Whole GBR: length North to South	EC	0.410	0.413	0.476	0.518	0.508	0.441	0.453	0.448	0.484	0.482	0.440	0.392
	OC	0.175	0.183	0.197	0.193	0.179	0.161	0.154	0.146	0.151	0.171	0.166	0.151
	MS	0.090	0.094	0.097	0.101	0.103	0.102	0.098	0.094	0.092	0.092	0.090	0.088
	OS	0.083	0.083	0.087	0.090	0.092	0.092	0.090	0.088	0.086	0.086	0.085	0.083
Cape York	EC	0.294	0.266	0.276	0.343	0.405	0.359	0.383	0.353	0.389	0.421	0.406	0.343
	OC	0.130	0.130	0.144	0.170	0.191	0.177	0.174	0.156	0.163	0.183	0.171	0.132
	MS	0.105	0.127	0.112	0.117	0.120	0.118	0.116	0.111	0.108	0.105	0.104	0.100
	OS	0.089	0.086	0.093	0.095	0.095	0.094	0.093	0.091	0.089	0.090	0.090	0.089
Wet Tropics	EC	0.358	0.389	0.449	0.470	0.439	0.370	0.402	0.407	0.421	0.405	0.358	0.318
	OC	0.155	0.154	0.181	0.213	0.200	0.190	0.194	0.168	0.162	0.172	0.142	0.121
	MS	0.097	0.104	0.110	0.115	0.110	0.108	0.104	0.096	0.096	0.100	0.093	0.090
	OS	0.082	0.088	0.088	0.092	0.092	0.091	0.088	0.085	0.084	0.087	0.084	0.082
Dry Tropics	EC	0.462	0.526	0.590	0.651	0.575	0.449	0.472	0.531	0.599	0.570	0.467	0.411
	OC	0.170	0.205	0.199	0.212	0.194	0.167	0.162	0.160	0.171	0.185	0.161	0.139
	MS	0.088	0.100	0.095	0.099	0.098	0.096	0.092	0.088	0.088	0.090	0.086	0.084
	OS	0.079	0.083	0.083	0.086	0.088	0.087	0.086	0.083	0.083	0.084	0.081	0.080
Mackay Whitsunday	EC	0.426	0.414	0.491	0.576	0.550	0.453	0.429	0.345	0.361	0.397	0.362	0.313
	OC	0.209	0.217	0.226	0.203	0.180	0.158	0.146	0.139	0.144	0.173	0.182	0.167
	MS	0.090	0.089	0.099	0.103	0.105	0.104	0.098	0.095	0.092	0.092	0.091	0.088
	OS	0.085	0.086	0.090	0.093	0.094	0.093	0.091	0.089	0.088	0.089	0.086	0.085
Fitzroy	EC	0.670	0.624	0.754	0.760	0.745	0.713	0.705	0.707	0.723	0.687	0.657	0.653
	OC	0.169	0.172	0.194	0.179	0.160	0.144	0.138	0.136	0.140	0.158	0.160	0.161
	MS	0.088	0.084	0.093	0.096	0.100	0.100	0.096	0.092	0.089	0.088	0.088	0.085
	OS	0.082	0.080	0.086	0.089	0.092	0.092	0.091	0.088	0.086	0.085	0.084	0.083
Burnett Mary	EC	0.382	0.403	0.513	0.412	0.305	0.266	0.223	0.220	0.262	0.295	0.280	0.303
	OC	0.139	0.148	0.185	0.148	0.128	0.119	0.110	0.104	0.107	0.118	0.116	0.121
	MS	0.084	0.080	0.088	0.088	0.090	0.092	0.090	0.087	0.086	0.086	0.085	0.084
	OS	0.077	0.073	0.080	0.083	0.086	0.088	0.087	0.084	0.082	0.080	0.080	0.079

Table A3.8: Long term monthly light attenuation coefficients at 645 nm, Kd(645).

Region	Waterbody	J	F	M	A	M	J	J	A	S	O	N	D
Whole GBR		0.399	0.403	0.413	0.427	0.437	0.438	0.433	0.422	0.413	0.412	0.408	0.400
Whole GBR: length North to South	EC	0.625	0.622	0.651	0.691	0.698	0.658	0.666	0.658	0.683	0.691	0.669	0.628
	OC	0.463	0.471	0.482	0.489	0.490	0.481	0.473	0.459	0.455	0.470	0.466	0.448
	MS	0.389	0.394	0.403	0.418	0.430	0.434	0.428	0.416	0.406	0.401	0.398	0.391
	OS	0.382	0.384	0.394	0.408	0.419	0.423	0.418	0.408	0.399	0.395	0.392	0.387
Cape York	EC	0.554	0.536	0.509	0.569	0.629	0.601	0.619	0.597	0.635	0.680	0.678	0.617
	OC	0.423	0.424	0.427	0.462	0.490	0.485	0.481	0.462	0.464	0.482	0.474	0.435
	MS	0.403	0.424	0.407	0.423	0.437	0.440	0.436	0.426	0.417	0.412	0.411	0.405
	OS	0.389	0.386	0.393	0.405	0.414	0.417	0.414	0.405	0.399	0.397	0.397	0.394
Wet Tropics	EC	0.559	0.564	0.613	0.641	0.636	0.597	0.619	0.615	0.616	0.606	0.576	0.546
	OC	0.436	0.426	0.454	0.491	0.496	0.495	0.496	0.469	0.456	0.462	0.439	0.417
	MS	0.392	0.392	0.405	0.423	0.432	0.435	0.429	0.414	0.406	0.407	0.400	0.393
	OS	0.381	0.383	0.392	0.407	0.417	0.420	0.414	0.403	0.396	0.395	0.391	0.386
Dry Tropics	EC	0.662	0.683	0.740	0.789	0.746	0.664	0.679	0.713	0.754	0.737	0.674	0.634
	OC	0.451	0.469	0.476	0.499	0.499	0.483	0.477	0.467	0.466	0.474	0.457	0.435
	MS	0.386	0.392	0.399	0.415	0.425	0.427	0.420	0.409	0.400	0.398	0.394	0.389
	OS	0.379	0.382	0.390	0.404	0.415	0.418	0.414	0.404	0.395	0.392	0.389	0.384
Mackay Whitsunday	EC	0.641	0.626	0.666	0.736	0.732	0.670	0.652	0.588	0.593	0.622	0.605	0.563
	OC	0.502	0.516	0.519	0.508	0.497	0.484	0.472	0.459	0.455	0.478	0.485	0.466
	MS	0.390	0.392	0.407	0.422	0.434	0.436	0.429	0.418	0.407	0.403	0.400	0.392
	OS	0.383	0.387	0.398	0.411	0.422	0.425	0.420	0.411	0.401	0.397	0.393	0.388
Fitzroy	EC	0.812	0.791	0.846	0.859	0.863	0.849	0.841	0.840	0.843	0.816	0.803	0.805
	OC	0.456	0.462	0.480	0.479	0.478	0.471	0.463	0.454	0.447	0.458	0.458	0.456
	MS	0.387	0.389	0.402	0.417	0.431	0.435	0.429	0.417	0.404	0.399	0.396	0.389
	OS	0.381	0.384	0.395	0.410	0.422	0.426	0.422	0.411	0.400	0.395	0.392	0.386
Burnett Mary	EC	0.603	0.621	0.690	0.632	0.570	0.549	0.518	0.505	0.520	0.539	0.531	0.545
	OC	0.422	0.431	0.465	0.452	0.450	0.449	0.439	0.425	0.416	0.418	0.415	0.413
	MS	0.383	0.386	0.398	0.411	0.423	0.429	0.424	0.414	0.402	0.396	0.393	0.387
	OS	0.377	0.380	0.390	0.405	0.418	0.424	0.420	0.409	0.398	0.392	0.389	0.383

Table A3.9: Long term monthly light attenuation coefficients at 667 nm, Kd(667).

Region	Waterbody	J	F	M	A	M	J	J	A	S	O	N	D
Whole GBR		0.524	0.528	0.541	0.560	0.574	0.576	0.569	0.554	0.542	0.540	0.536	0.526
Whole GBR: length North to South	EC	0.757	0.751	0.782	0.826	0.838	0.799	0.805	0.793	0.814	0.823	0.804	0.763
	OC	0.591	0.599	0.612	0.623	0.629	0.620	0.611	0.593	0.586	0.600	0.597	0.577
	MS	0.513	0.518	0.531	0.550	0.567	0.572	0.564	0.549	0.534	0.529	0.525	0.517
	OS	0.506	0.509	0.522	0.540	0.555	0.561	0.555	0.541	0.528	0.523	0.519	0.513
Cape York	EC	0.685	0.665	0.636	0.699	0.764	0.737	0.753	0.728	0.767	0.815	0.815	0.753
	OC	0.549	0.550	0.554	0.593	0.625	0.622	0.617	0.594	0.594	0.613	0.604	0.564
	MS	0.528	0.548	0.532	0.552	0.569	0.574	0.569	0.555	0.545	0.539	0.538	0.531
	OS	0.514	0.511	0.519	0.534	0.547	0.551	0.546	0.535	0.526	0.524	0.525	0.521
Wet Tropics	EC	0.679	0.682	0.732	0.766	0.768	0.731	0.751	0.742	0.738	0.726	0.699	0.669
	OC	0.562	0.551	0.582	0.624	0.635	0.635	0.635	0.602	0.586	0.591	0.568	0.545
	MS	0.515	0.515	0.531	0.553	0.567	0.572	0.564	0.545	0.534	0.534	0.526	0.518
	OS	0.505	0.506	0.518	0.538	0.552	0.556	0.549	0.534	0.524	0.522	0.518	0.512
Dry Tropics	EC	0.795	0.814	0.876	0.929	0.892	0.811	0.824	0.852	0.889	0.869	0.808	0.769
	OC	0.580	0.597	0.607	0.636	0.639	0.624	0.616	0.603	0.597	0.605	0.588	0.564
	MS	0.510	0.516	0.526	0.546	0.561	0.564	0.555	0.541	0.528	0.525	0.521	0.514
	OS	0.502	0.506	0.517	0.535	0.550	0.555	0.549	0.535	0.523	0.519	0.515	0.509
Mackay Whitsunday	EC	0.769	0.752	0.794	0.870	0.873	0.813	0.792	0.721	0.721	0.749	0.737	0.693
	OC	0.630	0.644	0.650	0.641	0.635	0.623	0.609	0.593	0.585	0.608	0.615	0.595
	MS	0.514	0.516	0.534	0.555	0.571	0.574	0.564	0.550	0.535	0.530	0.526	0.517
	OS	0.508	0.512	0.527	0.545	0.560	0.564	0.557	0.544	0.530	0.525	0.521	0.514
Fitzroy	EC	0.950	0.929	0.984	1.001	1.012	1.001	0.988	0.981	0.977	0.954	0.943	0.946
	OC	0.584	0.590	0.611	0.615	0.618	0.612	0.602	0.589	0.577	0.588	0.588	0.585
	MS	0.511	0.513	0.531	0.551	0.569	0.574	0.566	0.550	0.533	0.527	0.523	0.514
	OS	0.505	0.509	0.525	0.544	0.560	0.567	0.560	0.545	0.530	0.523	0.519	0.512
Burnett Mary	EC	0.741	0.761	0.836	0.782	0.721	0.701	0.665	0.647	0.656	0.671	0.668	0.682
	OC	0.551	0.560	0.598	0.591	0.593	0.592	0.580	0.562	0.548	0.548	0.546	0.543
	MS	0.508	0.511	0.527	0.546	0.562	0.569	0.563	0.548	0.533	0.525	0.521	0.513
	OS	0.500	0.503	0.518	0.538	0.555	0.563	0.558	0.543	0.527	0.520	0.515	0.507

Table A3.10: Long term monthly light attenuation coefficients at 678 nm, Kd(678).

Region	Waterbody	J	F	M	A	M	J	J	A	S	O	N	D
Whole GBR		0.556	0.560	0.574	0.593	0.609	0.612	0.604	0.588	0.575	0.572	0.568	0.559
Whole GBR: length North to South	EC	0.790	0.784	0.814	0.860	0.874	0.835	0.840	0.826	0.847	0.856	0.838	0.797
	OC	0.623	0.631	0.645	0.657	0.664	0.656	0.646	0.627	0.619	0.633	0.630	0.610
	MS	0.545	0.550	0.563	0.584	0.602	0.607	0.599	0.582	0.567	0.561	0.557	0.549
	OS	0.538	0.541	0.555	0.574	0.590	0.596	0.589	0.574	0.561	0.555	0.552	0.545
Cape York	EC	0.719	0.698	0.669	0.732	0.797	0.771	0.786	0.760	0.800	0.849	0.850	0.788
	OC	0.582	0.582	0.587	0.626	0.660	0.657	0.651	0.627	0.627	0.646	0.638	0.597
	MS	0.559	0.579	0.564	0.585	0.603	0.608	0.602	0.588	0.577	0.571	0.571	0.564
	OS	0.547	0.543	0.551	0.567	0.581	0.585	0.580	0.568	0.559	0.557	0.557	0.553
Wet Tropics	EC	0.708	0.711	0.761	0.796	0.800	0.764	0.784	0.773	0.768	0.755	0.729	0.700
	OC	0.595	0.583	0.615	0.658	0.670	0.671	0.670	0.636	0.619	0.624	0.601	0.578
	MS	0.547	0.547	0.564	0.587	0.601	0.606	0.598	0.578	0.567	0.566	0.559	0.550
	OS	0.536	0.538	0.551	0.572	0.586	0.590	0.583	0.567	0.556	0.555	0.550	0.544
Dry Tropics	EC	0.829	0.847	0.910	0.964	0.929	0.849	0.861	0.888	0.922	0.902	0.842	0.804
	OC	0.613	0.630	0.641	0.671	0.675	0.660	0.651	0.637	0.631	0.638	0.621	0.597
	MS	0.541	0.547	0.559	0.580	0.595	0.599	0.590	0.574	0.561	0.557	0.553	0.546
	OS	0.534	0.537	0.549	0.569	0.585	0.590	0.584	0.569	0.556	0.551	0.547	0.541
Mackay Whitsunday	EC	0.802	0.783	0.826	0.902	0.908	0.849	0.827	0.754	0.752	0.780	0.770	0.726
	OC	0.663	0.677	0.683	0.675	0.669	0.658	0.644	0.627	0.618	0.641	0.648	0.627
	MS	0.545	0.547	0.567	0.588	0.605	0.609	0.599	0.584	0.568	0.562	0.558	0.549
	OS	0.540	0.544	0.560	0.579	0.595	0.600	0.593	0.578	0.563	0.557	0.553	0.546
Fitzroy	EC	0.985	0.964	1.018	1.037	1.049	1.039	1.025	1.016	1.010	0.988	0.978	0.982
	OC	0.617	0.623	0.644	0.649	0.654	0.648	0.638	0.623	0.611	0.621	0.621	0.617
	MS	0.543	0.545	0.564	0.585	0.605	0.610	0.601	0.584	0.566	0.559	0.555	0.546
	OS	0.537	0.541	0.558	0.578	0.596	0.602	0.596	0.580	0.563	0.556	0.552	0.544
Burnett Mary	EC	0.778	0.798	0.874	0.822	0.761	0.741	0.704	0.684	0.690	0.704	0.703	0.717
	OC	0.584	0.594	0.633	0.626	0.630	0.629	0.616	0.597	0.582	0.581	0.580	0.576
	MS	0.540	0.543	0.561	0.580	0.598	0.605	0.598	0.582	0.566	0.558	0.554	0.545
	OS	0.531	0.535	0.551	0.572	0.590	0.599	0.594	0.577	0.560	0.552	0.547	0.539

Appendix 4: Time series plots of datasets used in the Random Forest Model analysis

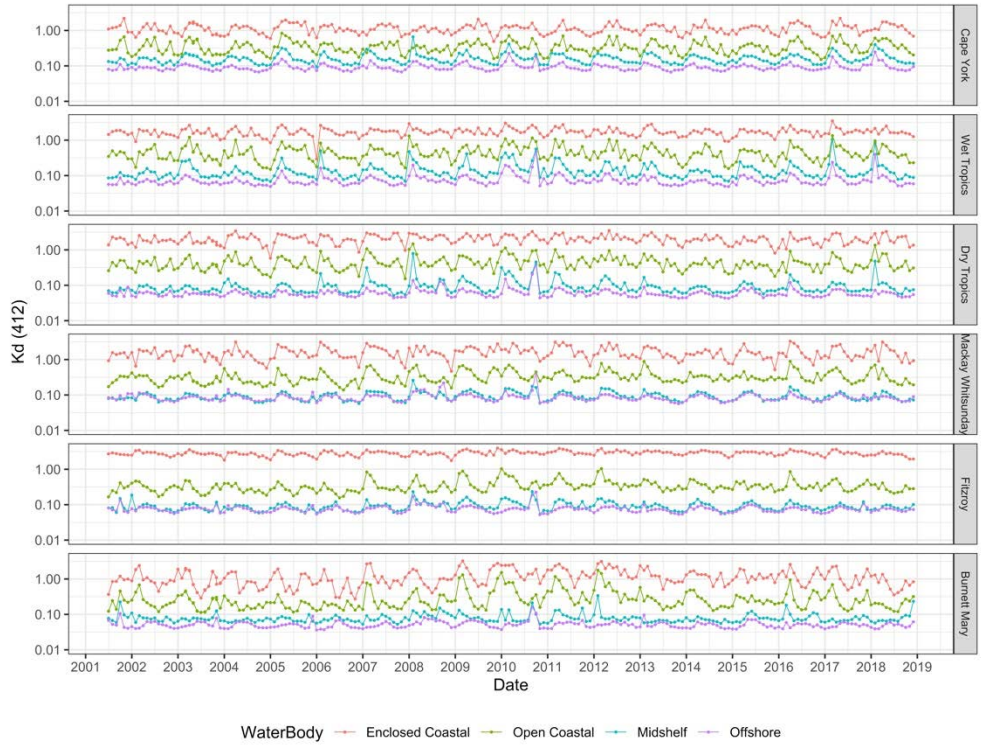

Figure A4.1: Time series plots of monthly light attenuation coefficients at 412 nm, $K_d(412)$, for each NRM region (rows) and cross-shelf waterbody (colour) from July 2002 to December 2019. Note that the y-axis is in logarithmic scale (limits: 0.01 to 4.0).

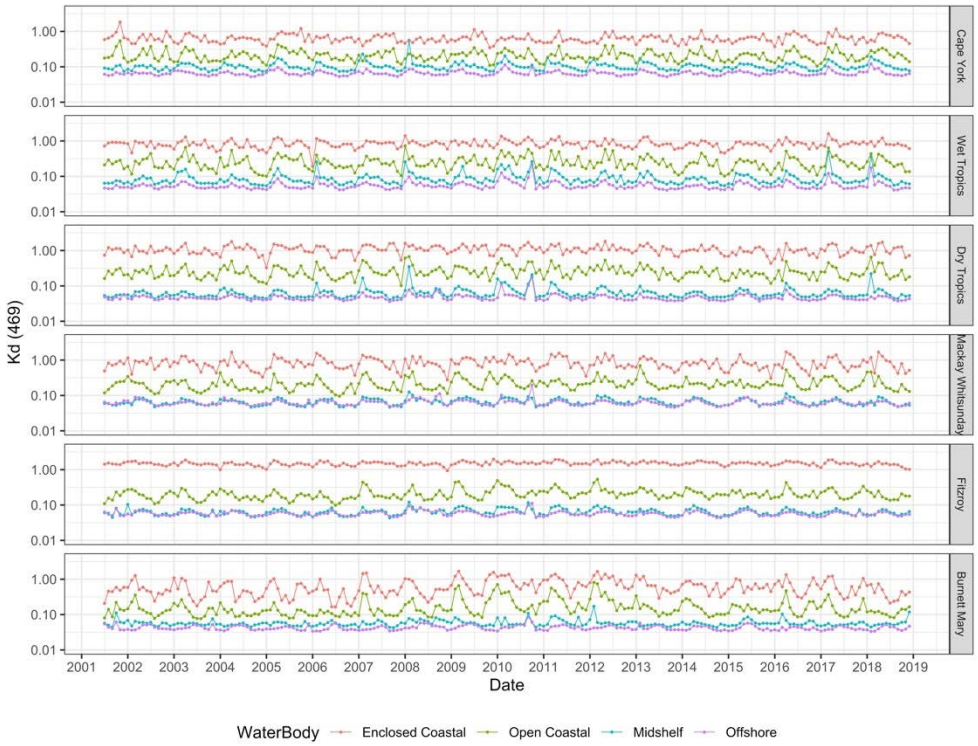

Figure A4.2: Same as Figure A4.1 but for light attenuation coefficients at 469 nm, $K_d(469)$.

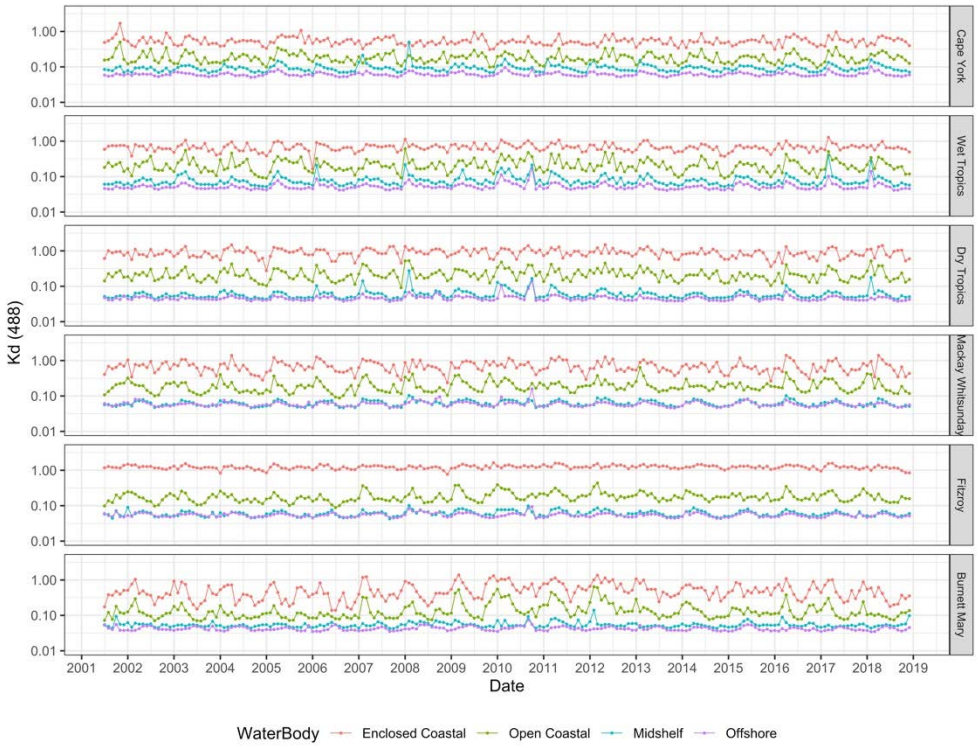

Figure A4.3: Same as Figure A4.1 but for light attenuation coefficients at 488 nm, $K_d(488)$.

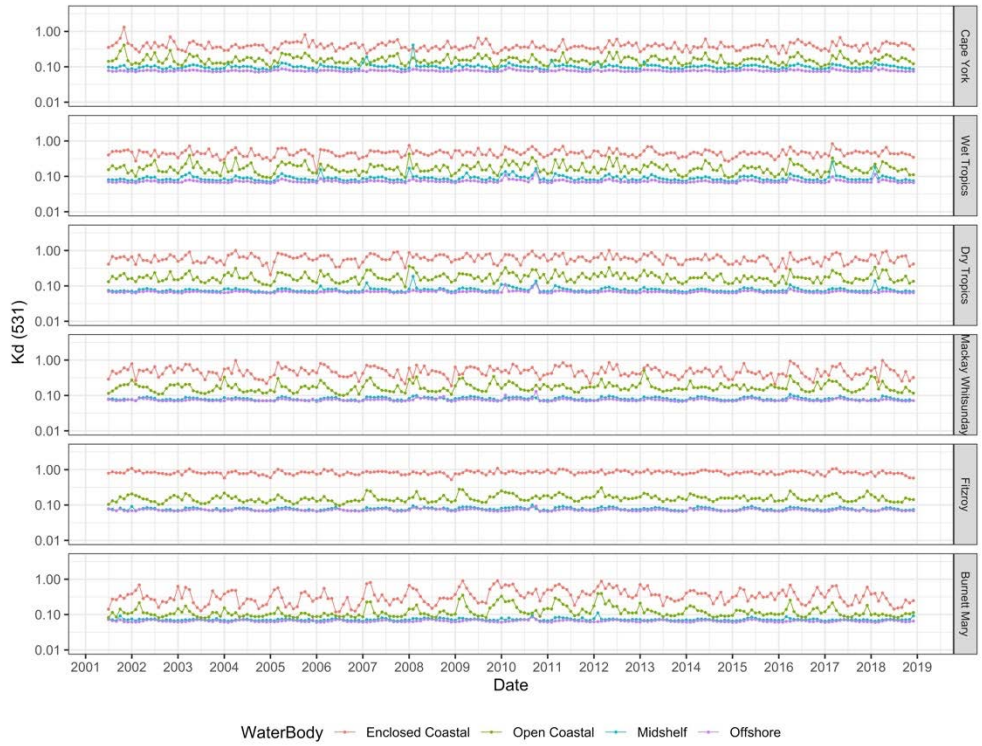

Figure A4.4: Same as Figure A4.1 but for light attenuation coefficients at 531 nm, $K_d(531)$.

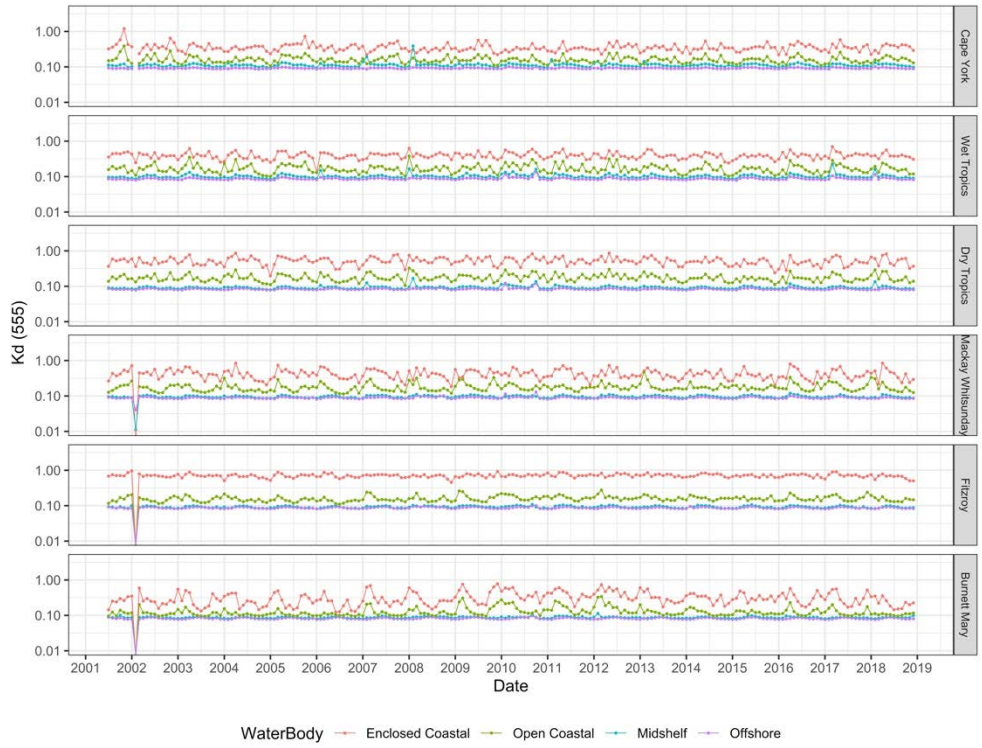

Figure A4.5: Same as Figure A4.1 but for light attenuation coefficients at 555 nm, $K_d(555)$.

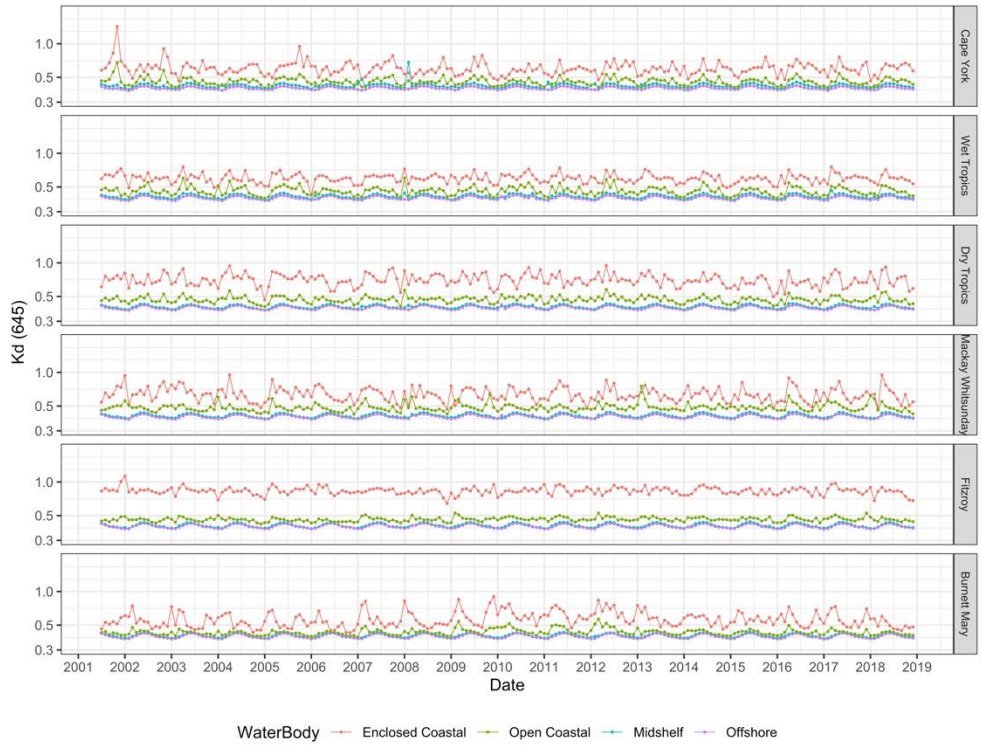

Figure A4.6. Time series plots of monthly light attenuation coefficients at 645 nm, $K_d(645)$, for each NRM region (rows) and cross-shelf waterbody (colour) from July 2002 to December 2019. Note that the y-axis is in logarithmic scale (limits: 0.3 to 2.0).

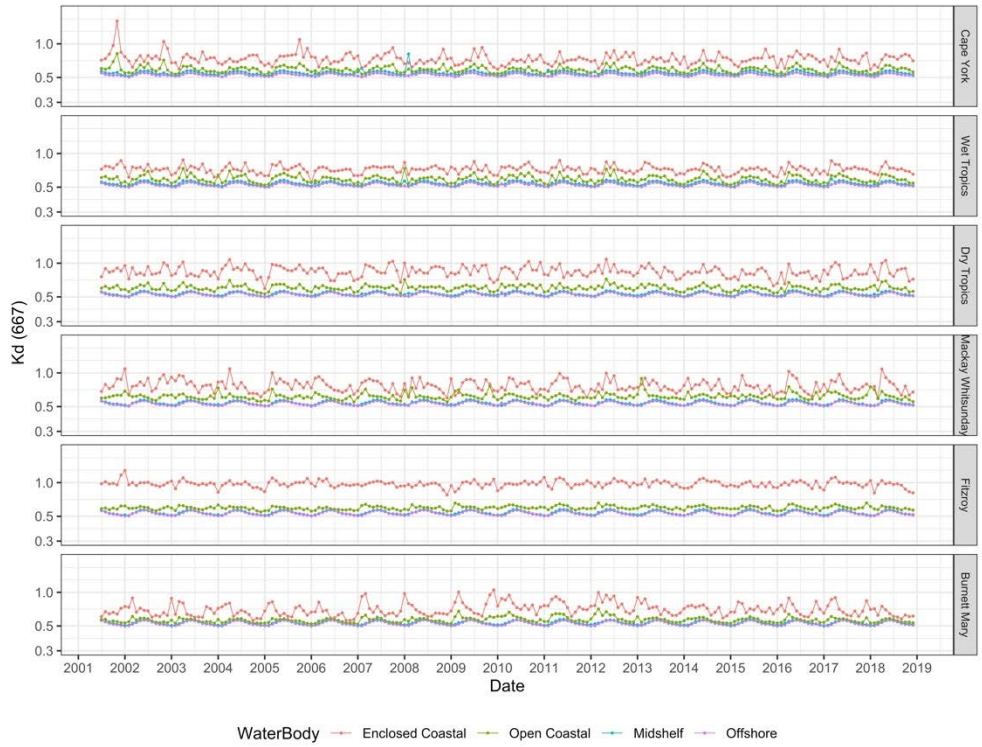

Figure A4.7. Same as Figure A4.6 but for light attenuation coefficients at 667 nm, $K_d(667)$.

Appendix 5: Monthly images of Chlorophyll *a* concentration for the GBR derived from MODIS-Aqua satellite sensor

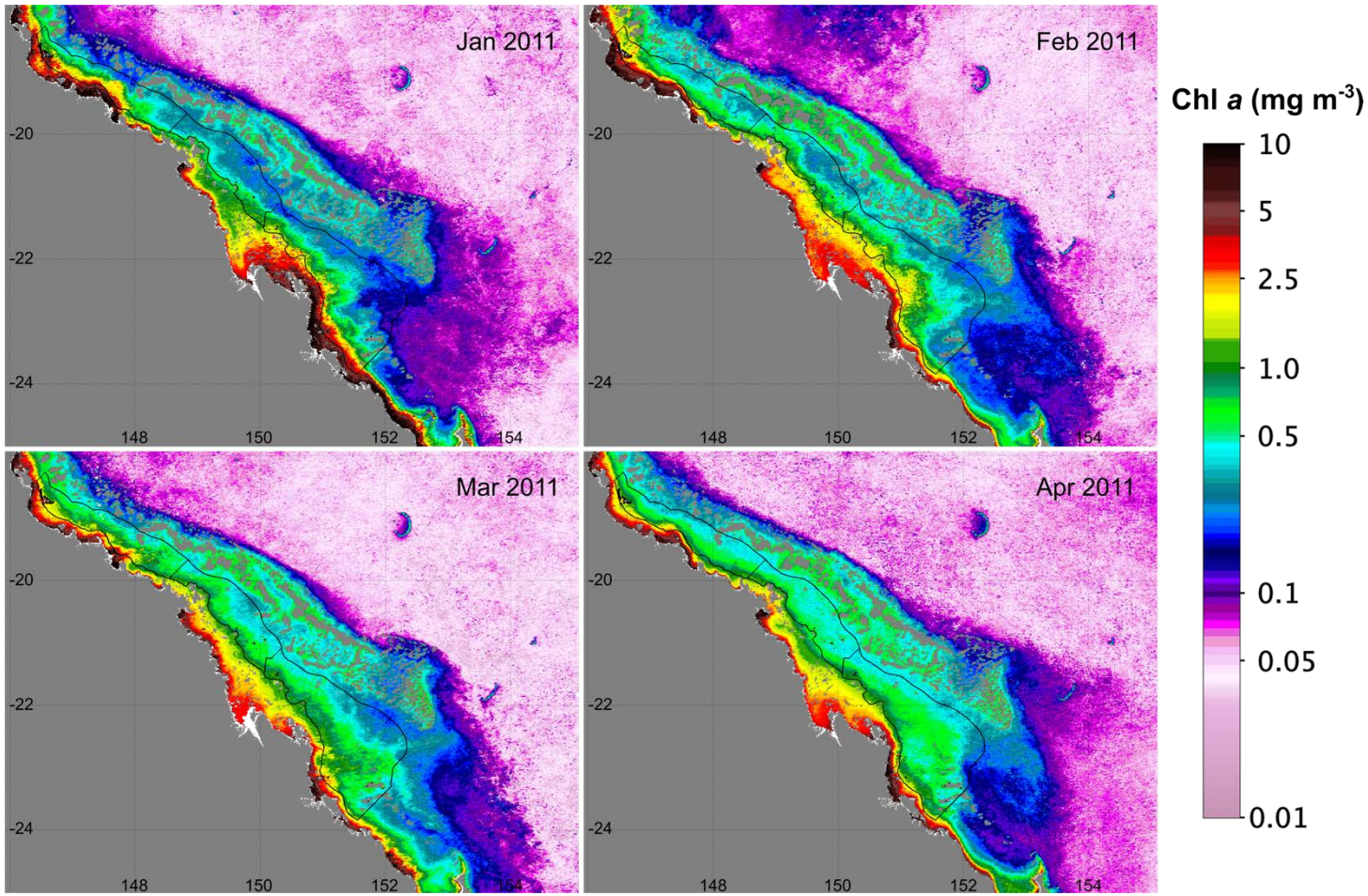

Figure A5.1. A series of monthly mean Chl a concentration from MODISA from January to April 2011 showing the patterns of Chl a after Tropical Cyclone event in January 2011. The images show the (i) intrusions of oceanic waters early in the year (top left of the Jan 2011 image), (ii) spread of high Chl a onto the mid-shelf, and (iii) overall high Chl a concentration especially near the coast. The black outline indicates the boundary of the mid-shelf within three southern NRM regions (N to S: Dry Tropics, Mackay Whitsunday, and Fitzroy.

Appendix 6: Landsat 8 True Colour image of Burdekin River floods in 2019

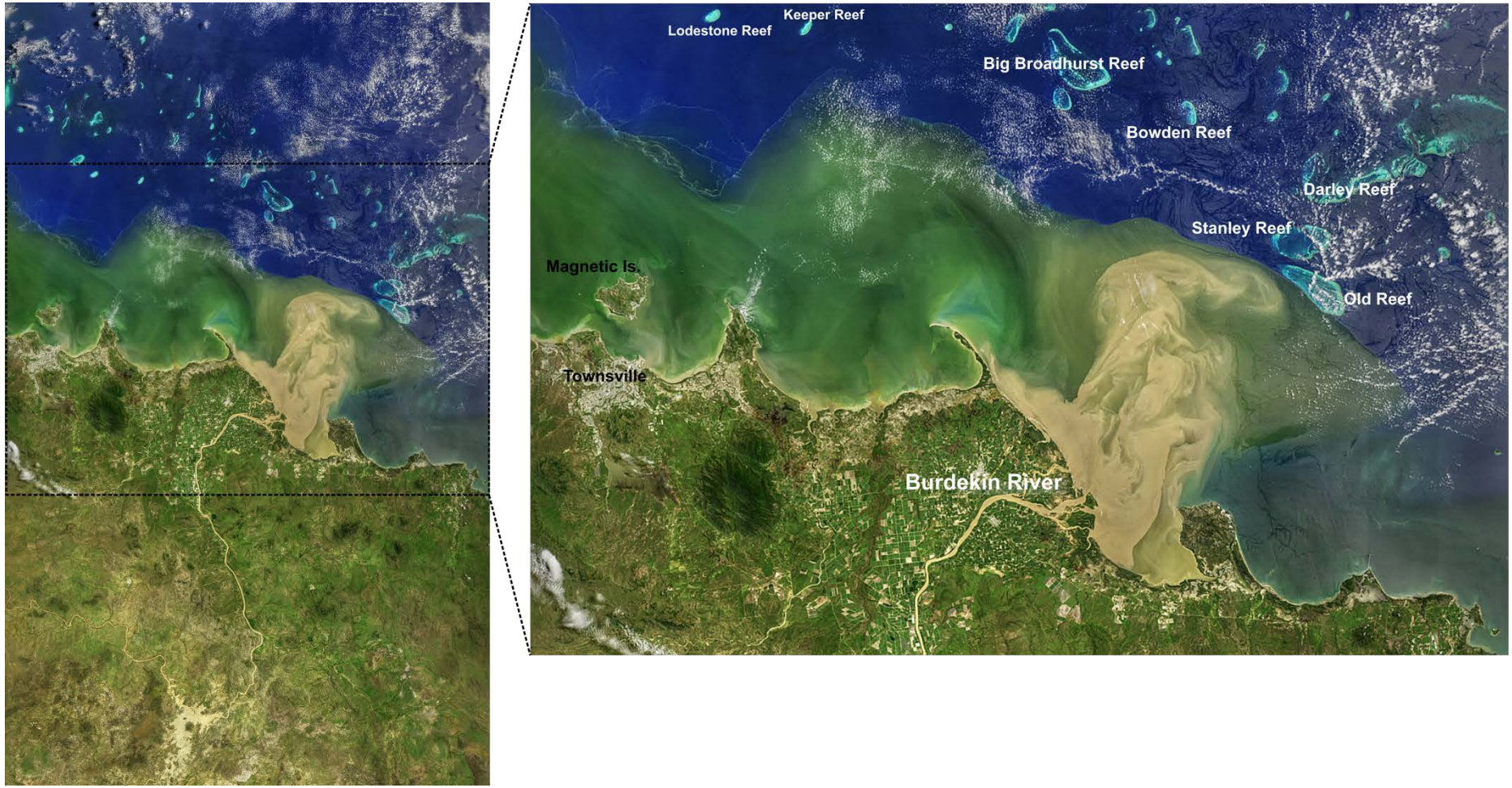

Figure A6.1. Landsat 8 satellite image of the Burdekin River floods taken on the 9th of February 2019 courtesy of the Ocean Biology Processing Group (OBPG), NASA Goddard Space Flight Centre (https://oceancolor.gsfc.nasa.gov/gallery/). The image on the right-hand side shows a zoomed-in region indicated by a dashed rectangle on the left image.

References

1. Ackleson, S.G., 2003. Light in shallow waters: A brief research review. Limnology and Oceanography 48, 323-328.

2. Adams, M.P., Hovey, R.K., Hipsey, M.R., Bruce, L.C., Ghisalberti, M., Lowe, R.J., Gruber, R.K., Ruiz-Montoya, L., Maxwell, P.S., Callaghan, D.P., Kendrick, G.A., O'Brien, K.R., 2016. Feedback between sediment and light for seagrass: Where is it important? Limnology and Oceanography 61, 1937-1955.

3. Ahmad, Z., Franz, B.A., McClain, C.R., Kwiatkowska, E.J., Werdell, J., Shettle, E.P., Holben, B.N., 2011. New aerosol models for the retrieval of aerosol optical thickness and normalized water-leaving radiances from the SeaWiFS and MODIS sensors over coastal regions and open oceans: publisher's note. Appl. Opt. 50, 626-626.

4. Allen Coral Atlas, 2020. Imagery, maps and monitoring of the world's tropical coral reefs.

5. Alongi, D.M., McKinnon, A.D., 2005. The cycling and fate of terrestrially-derived sediments and nutrients in the coastal zone of the Great Barrier Reef shelf. Marine Pollution Bulletin 51, 239-252.

6. Alvarez-Romero, J.G., Devlin, M., da Silva, E.T., Petus, C., Ban, N.C., Pressey, R.L., Kool, J., Roberts, J.J., Cerdeira-Estrada, S., Wenger, A.S., Brodie, J., 2013. A novel approach to model exposure of coastal-marine ecosystems to riverine flood plumes based on remote sensing techniques. Journal of Environmental Management 119, 194-207.

7. Andrews, J.C., Furnas, M.J., 1986. Subsurface intrusions of Coral Sea water into the central Great Barrier Reef—I. Structures and shelf-scale dynamics. Continental Shelf Research 6, 491-514.

8. Anthony, K., Ridd, P.V., Orpin, A.R., Larcombe, P., Lough, J., 2004. Temporal variation of light availability in coastal benthic habitats: Effects of clouds, turbidity, and tides. Limnology and Oceanography 49, 2201-2211.

9. Austin, R.W., Petzold, T.J., 1981. The Determination of the Diffuse Attenuation Coefficient of Sea Water Using the Coastal Zone Color Scanner, in: Gower, J.F.R. (Ed.), Oceanography from Space. Springer US, Boston, MA, pp. 239-256.

10. Bailey, S.W., Franz, B.A., Werdell, P.J., 2010. Estimation of near-infrared water-leaving reflectance for satellite ocean color data processing. Opt. Express 18, 7521-7527.

11. Bailey, S.W., Werdell, P.J., 2006. A multi-sensor approach for the on-orbit validation of ocean color satellite data products. Remote Sensing of Environment 102, 12-23.

12. Baird, M.E., Cherukuru, N., Jones, E., Margvelashvili, N., Mongin, M., Oubelkheir, K., Ralph, P.J., Rizwi, F., Robson, B.J., Schroeder, T., Skerratt, J., Steven, A.D.L., Wild-Allen, K.A., 2016. Remote-sensing reflectance and true colour produced by a coupled hydrodynamic, optical, sediment, biogeochemical model of the Great Barrier Reef, Australia: Comparison with satellite data. Environmental Modelling & Software 78, 79-96.

13. Baird, M.E., Wild-Allen, K.A., Parslow, J., Mongin, M., Robson, B., Skerratt, J., Rizwi, F., Soja-Woźniak, M., Jones, E., Herzfeld, M., Margvelashvili, N., Andrewartha, J., Langlais, C., Adams, M.P., Cherukuru, N., Gustafsson, M., Hadley, S., Ralph, P.J., Rosebrock, U., Schroeder, T., Laiolo, L., Harrison, D., Steven, A.D.L., 2020. CSIRO Environmental Modelling Suite (EMS): scientific description of the optical and biogeochemical models (vB3p0). Geosci. Model Dev. 13, 4503-4553.

14. Baith, K., Lindsay, R., Fu, G., McClain, C.R., 2001. Data analysis system developed for ocean color satellite sensors. Eos, Transactions American Geophysical Union 82, 202-202.

15. Baker, K., Smith, R.C., 1990. Irradiance transmittance through the air/water interface, Ocean Optics X, pp. 556-565.

16. Bakun, A., 2012. Patterns in the Ocean: Ocean Processes and Population Dynamics. CALIFORNIA SEA GRANT/CIB.

17. Barnes, B.B., Garcia, R., Hu, C., Lee, Z., 2018. Multi-band spectral matching inversion algorithm to derive water column properties in optically shallow waters: An optimization of parameterization. Remote Sensing of Environment 204, 424-438.

18. Barnes, B.B., Hu, C., Cannizzaro, J.P., Craig, S.E., Hallock, P., Jones, D.L., Lehrter, J.C., Melo, N., Schaeffer, B.A., Zepp, R., 2014. Estimation of diffuse attenuation of ultraviolet light in optically shallow Florida Keys waters from MODIS measurements. Remote Sensing of Environment 140, 519-532.

19. Barnes, B.B., Hu, C., Schaeffer, B.A., Lee, Z., Palandro, D.A., Lehrter, J.C., 2013. MODIS-derived spatiotemporal water clarity patterns in optically shallow Florida Keys waters: A new approach to remove bottom contamination. Remote Sensing of Environment 134, 377-391.

20. Beaman, R., 2010a. 3DGBR: A high-resolution depth model for the Great Barrier Reef and Coral Sea. Marine and Tropical Sciences Facility (MTSRF) Project 2.

21. Beaman, R., 2010b. Project 3DGBR: A high-resolution depth model for the Great Barrier Reef and Coral Sea. Marine and Tropical Sciences Research Facility (MTSRF) Project 2.5i.1a, final report, 100.

22. Benthuysen, J.A., Tonin, H., Brinkman, R., Herzfeld, M., Steinberg, C., 2016. Intrusive upwelling in the Central Great Barrier Reef. Journal of Geophysical Research: Oceans 121, 8395-8416.

23. Bertelli, C.M., Unsworth, R.K.F., 2018. Light Stress Responses by the Eelgrass, Zostera marina (L). Front. Environ. Sci. 6, 13.

24. Bessell-Browne, P., Negri, A.P., Fisher, R., Clode, P.L., Duckworth, A., Jones, R., 2017a. Impacts of turbidity on corals: The relative importance of light limitation and suspended sediments. Marine Pollution Bulletin 117, 161-170.

25. Bessell-Browne, P., Negri, A.P., Fisher, R., Clode, P.L., Jones, R., 2017b. Impacts of light limitation on corals and crustose coralline algae. Scientific Reports 7, 11553.

26. Blondeau-Patissier, D., Brando, V.E., Oubelkheir, K., Dekker, A.G., Clementson, L.A., Daniel, P., 2009. Bio-optical variability of the absorption and scattering properties of the Queensland inshore and reef waters, Australia. Journal of Geophysical Research: Oceans 114.

27. Blondeau-Patissier, D., Schroeder, T., Brando, V.E., Maier, S.W., Dekker, A.G., Phinn, S., 2014. ESA-MERIS 10-Year Mission Reveals Contrasting Phytoplankton Bloom Dynamics in Two Tropical Regions of Northern Australia. Remote Sensing 6, 2963-2988.

28. Brando, V.E., Dekker, A.G., Park, Y.J., Schroeder, T., 2012. Adaptive semianalytical inversion of ocean color radiometry in optically complex waters. Appl. Opt. 51, 2808-2833.

29. Breiman, L., 2001. Random Forests. Machine Learning 45, 5-32.

30. Briggs, A.A., Carpenter, R.C., 2019. Contrasting responses of photosynthesis and photochemical efficiency to ocean acidification under different light environments in a calcifying alga. Scientific reports 9, 3986-3986.

31. Brinkman, R., Wolanski, E., Deleersnijder, E., McAllister, F., Skirving, W., 2002. Oceanic inflow from the Coral Sea into the Great Barrier Reef. Estuarine, Coastal and Shelf Science 54, 655-668.

32. Bristow, L.A., Mohr, W., Ahmerkamp, S., Kuypers, M.M.M., 2017. Nutrients that limit growth in the ocean. Current Biology 27, R474-R478.

33. Brodie, J., De'Ath, G., Devlin, M., Furnas, M., Wright, M., 2007. Spatial and temporal patterns of near-surface chlorophyll a in the Great Barrier Reef lagoon. Marine and freshwater research 58, 342-353.

34. Brodie, J., Schroeder, T., Rohde, K., Faithful, J., Masters, B., Dekker, A., Brando, V., Maughan, M., 2010. Dispersal of suspended sediments and nutrients in the Great Barrier Reef

lagoon during river-discharge events: conclusions from satellite remote sensing and concurrent flood-plume sampling. Marine and Freshwater Research 61, 651-664.

35. Brodie, J., Waterhouse, J., 2012. A critical review of environmental management of the 'not so Great' Barrier Reef. Estuarine, Coastal and Shelf Science 104–105, 1-22.

36. Brodie, J.E., Devlin, M., Haynes, D., Waterhouse, J., 2011. Assessment of the eutrophication status of the Great Barrier Reef lagoon (Australia). Biogeochemistry 106, 281-302.

37. Brodie, J.E., Kroon, F.J., Schaffelke, B., Wolanski, E.C., Lewis, S.E., Devlin, M.J., Bohnet, I.C., Bainbridge, Z.T., Waterhouse, J., Davis, A.M., 2012. Terrestrial pollutant runoff to the Great Barrier Reef: An update of issues, priorities and management responses. Marine Pollution Bulletin 65, 81-100.

38. Brodie, J.E., McKergow, L.A., Prosser, I.P., Furnas, M., Hughes, A.O., Hunter, H., 2003. Sources of sediment and nutrient exports to the Great Barrier Reef World Heritage Area. Australian Centre for Tropical Freshwater Research,Townsville, Australia.

39. Browne, N.K., Smithers, S.G., Perry, C.T., Ridd, P.V., 2012. A Field-Based Technique for Measuring Sediment Flux on Coral Reefs: Application to Turbid Reefs on the Great Barrier Reef. Journal of Coastal Research 28, 1247-1262.

40. Bureau of Meteorology, 2017. eReefs Catchments: simulations, nowcasts, and forecasts of water quantity and quality flowing to the Great Barrier Reef, Final Report, eReefs Project Phase 3, Great Barrier Reef Foundation, Brisbane, QLD Australia.

41. Bureau of Meteorology, 2018. Tropical Cyclone Debbie Technical Report, A comprehensive summary of meteorological and hydrological data associated with Severe Tropical Cyclone Debbie that affected Queensland and New South Wales during March and April 2017. Department of Natural Resources and Mines, The State of Queensland, Melbourne, Victoria.

42. Cacciapaglia, C., van Woesik, R., 2016. Climate-change refugia: shading reef corals by turbidity. Global Change Biology 22, 1145-1154.

43. Chartrand, K.M., Bryant, C.V., Carter, A.B., Ralph, P.J., Rasheed, M.A., 2016. Light Thresholds to Prevent Dredging Impacts on the Great Barrier Reef Seagrass, Zostera muelleri ssp. capricorni. Frontiers in Marine Science 3.

44. Cherukuru, N., Brando, V.E., Blondeau-Patissier, D., Ford, P.W., Clementson, L.A., Robson, B.J., 2017. Impact of wet season river flood discharge on phytoplankton absorption properties in the southern Great Barrier Reef region coastal waters. Estuarine, Coastal and Shelf Science 196, 379-386.

45. Choukroun, S., Ridd, P.V., Brinkman, R., McKinna, L.I.W., 2010. On the surface circulation in the western Coral Sea and residence times in the Great Barrier Reef. Journal of Geophysical Research: Oceans 115, n/a-n/a.

46. Collier, C., Chartrand, K., Honchin, C., Fletcher, A., Rasheed, M., 2016a. Light thresholds for seagrasses of the GBR: a synthesis and guiding document. Including knowledge gaps and future priorities, Report to the National Environmental Science Programme. Reef and Rainforest Research Centre Limited, p. 41.

47. Collier, C., Waycott, M., 2009. Drivers of change to seagrass distributions and communities on the Great Barrier Reef: literature review and gaps analysis. Reef and Rainforest Research Centre.

48. Collier, C.J., Adams, M.P., Langlois, L., Waycott, M., O'Brien, K.R., Maxwell, P.S., McKenzie, L., 2016b. Thresholds for morphological response to light reduction for four tropical seagrass species. Ecological Indicators 67, 358-366.

49. Collier, C.J., Waycott, M., McKenzie, L., 2012a. Light thresholds derived from seagrass loss in the coastal zone of the northern Great Barrier Reef, Australia. Ecological Indicators 23, 211-219.

50. Collier, C.J., Waycott, M., Ospina, A.G., 2012b. Responses of four Indo-West Pacific seagrass species to shading. Marine Pollution Bulletin 65, 342-354.

51. Commonwealth of Australia, 2015. Reef 2050 long-term sustainability plan.

52. Cooper, T.F., Uthicke, S., Humphrey, C., Fabricius, K.E., 2007. Gradients in water column nutrients, sediment parameters, irradiance and coral reef development in the Whitsunday Region, central Great Barrier Reef. Estuarine, Coastal and Shelf Science 74, 458-470.

53. D'Errico, J., 2021. inpaint_nans (https://www.mathworks.com/matlabcentral/fileexchange/4551-inpaint_nans), 1.1.0.0 ed. MATLAB Central File Exchange. Retrieved February 11, 2021.

54. Davies, P.J., 2011. Great Barrier Reef: Origin, Evolution, and Modern Development, in: Hopley, D. (Ed.), Encyclopedia of Modern Coral Reefs: Structure, Form and Process. Springer Netherlands, Dordrecht, pp. 504-534.

55. De'ath, G., Fabricius, K., 2008. Water quality of the Great Barrier Reef: distributions, effects on reef biota and trigger values for the protection of ecosystem health. Final Report to the Great Barrier Reef Marine Park Authority, Australian Institute of Marine Science, Townsville, p. 104.

56. De'ath, G., Fabricius, K., 2010. Water quality as a regional driver of coral biodiversity and macroalgae on the Great Barrier Reef. Ecological Applications 20, 840-850.

57. De'ath, G., Venables, B., 2013. GDs AcrossAlong. R package version 1.0.

58. De'ath, G., Fabricius, K.E., Sweatman, H., Puotinen, M., 2012. The 27–year decline of coral cover on the Great Barrier Reef and its causes. Proceedings of the National Academy of Sciences 109, 17995-17999.

59. Deloitte Access Economics, 2013. Economic contribution of the Great Barrier Reef, Great Barrier Reef Marine Park Authority Townsville.

60. Deloitte Access Economics, 2017. At what price? The economic, social and icon value of the Great Barrier Reef.

61. Dennison, W.C., 1987. Effects of light on seagrass photosynthesis, growth and depth distribution. Aquatic Botany 27, 15-26.

62. Deser, C., Alexander, M.A., Xie, S.-P., Phillips, A.S., 2010. Sea Surface Temperature Variability: Patterns and Mechanisms. Annual Review of Marine Science 2, 115-143.

63. Devlin, M., McKinna, L., Alvarez-Romero, J., Petus, C., Abott, B., Harkness, P., Brodie, J., 2012. Mapping the pollutants in surface riverine flood plume waters in the Great Barrier Reef, Australia. Marine pollution bulletin 65, 224-235.

64. Devlin, M., Petus, C., da Silva, E., Tracey, D., Wolff, N., Waterhouse, J., Brodie, J., 2015. Water quality and river plume monitoring in the Great Barrier Reef: an overview of methods based on ocean colour satellite data. Remote Sensing 7, 12909.

65. Devlin, M., Schaffelke, B., 2009. Spatial extent of riverine flood plumes and exposure of marine ecosystems in the Tully coastal region, Great Barrier Reef. Marine and Freshwater Research 60, 1109-1122.

66. Devlin, M., Waterhouse, J., Taylor, J., Brodie, J., 2001. Flood plumes in the Great Barrier Reef: spatial and temporal patterns in composition and distribution. GBRMPA research publication 68.

67. Devlin, M.J., Brodie, J., 2005. Terrestrial discharge into the Great Barrier Reef Lagoon: nutrient behavior in coastal waters. Marine Pollution Bulletin 51, 9-22.

68. Dickey, T.D., Simpson, J.J., 1983. The influence of optical water type on the diurnal response of the upper ocean. Tellus B 35B, 142-154.

69. Dierssen, H.M., Zimmerman, R.C., Drake, L.A., Burdige, D., 2010. Benthic ecology from space

70. optics and net primary production in seagrass and benthic algae across the Great Bahama Bank. Marine Ecology Progress Series 411, 1-15.

71. DiPerna, S., Hoogenboom, M., Noonan, S., Fabricius, K., 2018. Effects of variability in daily light integrals on the photophysiology of the corals Pachyseris speciosa and Acropora millepora. PLOS ONE 13, e0203882.

72. Donner, S.D., 2011. An evaluation of the effect of recent temperature variability on the prediction of coral bleaching events. Ecological Applications 21, 1718-1730.

73. Donner, S.D., Skirving, W.J., Little, C.M., Oppenheimer, M., Hoegh-Guldberg, O., 2005. Global assessment of coral bleaching and required rates of adaptation under climate change. Global Change Biology 11, 2251-2265.

74. Drew, E.A., 2000. Ocean nutrients to sediment banks via tidal jets and Halimeda meadows, in: Wolanski, E. (Ed.), Oceanographic processes of coral reefs: physical and biological links in the Great Barrier Reef, pp. 255-267.

75. Dubinsky, Z., Falkowski, P., 2011. Light as a source of information and energy in zooxanthellate corals. Springer.

76. Dubinsky, Z., Iluz, D., 2016. Corals and Light: From Energy Source to Deadly Threat, in: Goffredo, S., Dubinsky, Z. (Eds.), The Cnidaria, Past, Present and Future: The world of Medusa and her sisters. Springer International Publishing, Switzerland, pp. 469-487.

77. Egbert, G.D., Erofeeva, S.Y., 2002. Efficient Inverse Modeling of Barotropic Ocean Tides. Journal of Atmospheric and Oceanic Technology 19, 183-204.

78. Emery, W.J., Thomson, R.E., 2001. Chapter 4 - The Spatial Analyses of Data Fields, in: Emery, W.J., Thomson, R.E. (Eds.), Data Analysis Methods in Physical Oceanography. Elsevier Science, Amsterdam, pp. 305-370.

79. Exelis Visual Information Solutions, Boulder, Colorado.

80. Fabricius, K.E., 2005. Effects of terrestrial runoff on the ecology of corals and coral reefs: review and synthesis. Marine Pollution Bulletin 50, 125-146.

81. Fabricius, K.E., 2011. Factors Determining the Resilience of Coral Reefs to Eutrophication: A Review and Conceptual Model, in: Dubinsky, Z., Stambler, N. (Eds.), Coral Reefs: An Ecosystem in Transition. Springer Netherlands, Dordrecht, pp. 493-505.

82. Fabricius, K.E., De'ath, G., Humphrey, C., Zagorskis, I., Schaffelke, B., 2013. Intra-annual variation in turbidity in response to terrestrial runoff on near-shore coral reefs of the Great Barrier Reef. Estuarine, Coastal and Shelf Science 116, 57-65.

83. Fabricius, K.E., Logan, M., Weeks, S., Brodie, J., 2014. The effects of river run-off on water clarity across the central Great Barrier Reef. Marine Pollution Bulletin 84, 191-200.

84. Fabricius, K.E., Logan, M., Weeks, S.J., Lewis, S.E., Brodie, J., 2016. Changes in water clarity in response to river discharges on the Great Barrier Reef continental shelf: 2002–2013. Estuarine, Coastal and Shelf Science 173, A1-A15.

85. Fabricius, K.E., Okaji, K., De'ath, G., 2010. Three lines of evidence to link outbreaks of the crown-of-thorns seastar Acanthaster planci to the release of larval food limitation. Coral Reefs 29, 593-605.

86. Fisher, R., Bessell-Browne, P., Jones, R., 2019. Synergistic and antagonistic impacts of suspended sediments and thermal stress on corals. Nature Communications 10, 2346.

87. Foster, S.D., Griffin, D.A., Dunstan, P.K., 2014. Twenty Years of High-Resolution Sea Surface Temperature Imagery around Australia: Inter-Annual and Annual Variability. PLOS ONE 9, e100762.

88. Franz, B.A., Werdell, P.J., 2010. A Generalized Framework for Modeling of Inherent Optical Properties in Remote Sensing Applications, Proceedings Ocean Optics 2010, Anchorage, Alaska, USA, 27 September – 1 October 2010.

89. Frouin, R., Franz, B.A., Werdell, J.P., 2002. The SeaWIFS PAR product, in: Hooker, S.B., Firestone, E.R. (Eds.), Algorithm Updates for the Fourth SeaWIFS Data Reprocessing, NASA Technical Memorandum 2003-206892, NASA Goddard Space Flight Center, Greenbelt, Maryland, pp. 46 - 50.

90. Frouin, R., McPherson, J., 2012. Estimating photosynthetically available radiation at the ocean surface from GOCI data. Ocean Science Journal 47, 313-321.

91. Frouin, R., McPherson, J., Ueyoshi, K., Franz, B.A., 2012. A time series of photosynthetically available radiation at the ocean surface from SeaWiFS and MODIS data, pp. 852519-852519-852512.

92. Furnas, M., 2003a. Catchments and corals: terrestrial runoff to the Great Barrier Reef. Australian Institute of Marine Science:CRC Reef Research Centre, Townsville, Qld.

93. Furnas, M., Mitchell, A., 2001. Runoff of Terrestrial Sediment and Nutrients into the Great Barrier Reef World Heritage Area, in: Wolanski, E. (Ed.), Oceanographic Processes of Coral Reefs: Physical and Biological Links in the Great Barrier Reef, pp. 37-52.

94. Furnas, M.J., 2003b. Catchments and corals : terrestrial runoff to the Great Barrier Reef. Australian Institute of Marine Science:CRC Reef Research Centre, Townsville, Qld.

95. Furnas, M.J., Mitchell, A.W., 1996. Nutrient inputs into the central Great Barrier Reef (Australia) from subsurface intrusions of Coral Sea waters: a two-dimensional displacement model. Continental Shelf Research 16, 1127-1148.

96. Garcia, R.A., Lee, Z., Barnes, B.B., Hu, C., Dierssen, H.M., Hochberg, E.J., 2020. Benthic classification and IOP retrievals in shallow water environments using MERIS imagery. Remote Sensing of Environment 249, 112015.

97. Garcia, R.A., Lee, Z., Hochberg, E.J., 2018. Hyperspectral Shallow-Water Remote Sensing with an Enhanced Benthic Classifier. Remote Sensing 10, 147.

98. Garrison, T., Ellis, R., 2016. Oceanography: An Invitation to Marine Science, 9e [9th edition] ed. National Geographic Learning, Boston, MA.

99. Gattuso, J.-P., Gentili, B., Duarte, C.M., Kleypas, J.A., Middelburg, J.J., Antoine, D., 2006. Light availability in the coastal ocean: impact on the distribution of benthic photosynthetic organisms and contribution to primary production. Biogeosciences Discussions 3, 895-959.

100. Gattuso, J.P., Gentili, B., Antoine, D., Doxaran, D., 2020. Global distribution of photosynthetically available radiation on the seafloor. Earth Syst. Sci. Data 12, 1697-1709.

101. Great Barrier Marine Park Authority, 2010a. Water quality guidelines for the Great Barrier Reef Marine Park. Great Barrier Marine Park Authority, Townsville.

102. Great Barrier Marine Park Authority, 2010b. Water quality guidelines for the Great Barrier Reef Marine Park (Revised Edition), Revised Edition ed. Great Barrier Reef Marine Park Authority, Townsville, Queensland.

103. Great Barrier Marine Park Authority, 2014. Great Barrier Reef Outlook Report 2014, GBRMPA, Townsville.

104. Grigg, R.W., 2006. Depth limit for reef building corals in the Au'au Channel, S.E. Hawaii. Coral Reefs 25, 77-84.

105. Gruber, R., Waterhouse, J., Logan, M., Petus, C., Howley, C., Lewis, S., Tracey, D., Langlois, L., Tonin, H., Skuza, M., Costello, P., Davidson, J., Gunn, K., Lefevre, C., Moran, D., Robson, B., Shanahan, M., Zagorskis, I., Shellberg, J., Neilen, A., 2020. Marine Monitoring Program: Annual Report for Inshore Water Quality Monitoring 2018-19, Report for the Great Barrier Reef Marine Park Authority, Great Barrier Reef Marine Park Authority, Townsville.

106. Gruber, R., Waterhouse, J., Logan, M., Petus, C., Howley, C., Lewis, S., Tracey, D., Langlois, L., Tonin, H., Skuza, M., Costello, P., Davidson, J., Gunn, K., Lefevre, C., Shanahan, M., Wright, M., Zagorskis, I., Kroon, F., Neilen, A., 2019. Marine Monitoring Program: Annual report for inshore water quality monitoring 2017-18, Report for the Great Barrier Reef Marine Park Authority.

107. Haltrin, V.I., Johnson, D.R., Urdenko, V.A., 2002. Connection between light-field parameters and optical properties of seawater, pp. 123-132.

108. Haltrin, V.I., McBride, W.E., Weidemann, A.D., 2000. Fresnel reflection by wavy sea surface, IGARSS 2000. IEEE 2000 International Geoscience and Remote Sensing Symposium. Taking the Pulse of the Planet: The Role of Remote Sensing in Managing the Environment. Proceedings (Cat. No.00CH37120), pp. 1863-1865 vol.1865.

109. Hatcher, B.G., 1997. Coral reef ecosystems: how much greater is the whole than the sum of the parts? Coral Reefs 16, S77-S91.

110. Haynes, D., Michalek-Wagner, K., 2000. Water Quality in the Great Barrier Reef World Heritage Area: Past Perspectives, Current Issues and New Research Directions. Marine Pollution Bulletin 41, 428-434.

111. Heron, S.F., Eakin, C.M., Douvere, F., Anderson, K., Day, J., Geiger, E., Hoegh-Guldberg, O., Hooidonk, R.v., Hughes, T., Marshall, P., Obura, D., 2017. Impacts of Climate Change on World Heritage Coral Reefs: A First Global Scientific Assessment. UNESCO, Paris, France: UNESCO World Heritage Centre.

112. Herzfeld, M., 2006. An alternative coordinate system for solving finite difference ocean models. Ocean Modelling 14, 174-196.

113. Hooker, S.B., Esaias, W.E., 1993. An overview of the SeaWiFS Project. EOS, Transactions American Geophysical Union 74, 241-246.

114. Hoyer, S., Hamman, J., 2017. xarray: N-D labeled Arrays and Datasets in Python. Journal of Open Research Software 5(1), 10.

115. Hu, C., Lee, Z., Franz, B., 2012. Chlorophyll aalgorithms for oligotrophic oceans: A novel approach based on three-band reflectance difference. Journal of Geophysical Research: Oceans 117.

116. Hughes, T.P., Baird, A.H., Bellwood, D.R., Card, M., Connolly, S.R., Folke, C., Grosberg, R., Hoegh-Guldberg, O., Jackson, J.B.C., Kleypas, J., Lough, J.M., Marshall, P., Nyström, M., Palumbi, S.R., Pandolfi, J.M., Rosen, B., Roughgarden, J., 2003. Climate Change, Human Impacts, and the Resilience of Coral Reefs. Science 301, 929-933.

117. Hughes, T.P., Kerry, J.T., Álvarez-Noriega, M., Álvarez-Romero, J.G., Anderson, K.D., Baird, A.H., Babcock, R.C., Beger, M., Bellwood, D.R., Berkelmans, R., Bridge, T.C., Butler, I.R., Byrne, M., Cantin, N.E., Comeau, S., Connolly, S.R., Cumming, G.S., Dalton, S.J., Diaz-Pulido, G., Eakin, C.M., Figueira, W.F., Gilmour, J.P., Harrison, H.B., Heron, S.F., Hoey, A.S., Hobbs, J.-P.A., Hoogenboom, M.O., Kennedy, E.V., Kuo, C.-y., Lough, J.M., Lowe, R.J., Liu, G., McCulloch, M.T., Malcolm, H.A., McWilliam, M.J., Pandolfi, J.M., Pears, R.J., Pratchett, M.S., Schoepf, V., Simpson, T., Skirving, W.J., Sommer, B., Torda, G., Wachenfeld, D.R.,

Willis, B.L., Wilson, S.K., 2017. Global warming and recurrent mass bleaching of corals. Nature 543, 373.

118. Hughes, T.P., Kerry, J.T., Baird, A.H., Connolly, S.R., Dietzel, A., Eakin, C.M., Heron, S.F., Hoey, A.S., Hoogenboom, M.O., Liu, G., McWilliam, M.J., Pears, R.J., Pratchett, M.S., Skirving, W.J., Stella, J.S., Torda, G., 2018a. Global warming transforms coral reef assemblages. Nature 556, 492-496.

119. Hughes, T.P., Kerry, J.T., Simpson, T., 2018b. Large-scale bleaching of corals on the Great Barrier Reef. Ecology 99, 501-501.

120. Hurrey, L.P., Pitcher, C.R., Lovelock, C.E., Schmidt, S., 2013. Macroalgal species richness and assemblage composition of the Great Barrier Reef seabed. Marine Ecology Progress Series 492, 69-83.

121. Hutchings, P., Kingsford, M., Hoegh-Guldberg, O., 2008. The Great Barrier Reef: Biology, Environment and Management. CSIRO Publishing, Victoria, AUSTRALIA.

122. Hutchings, P.A., Kingsford, M.J., Hoegh-Guldberg, O., 2019. Introduction to the Great Barrier Reef, in: Hutchings, P.A., Kingsford, M.J., Hoegh-Guldberg, O. (Eds.), The Great Barrier Reef: Biology, Environment and Management, Second ed. CSIRO, p. 489.

123. IOCCG, 2000. Remote Sensing of Ocean Colour in Coastal, and Other Optically-Complex, Waters, in: Sathyendranath, S. (Ed.), Reports of the International Ocean-Colour Coordinating Group, IOCCG, Dartmouth, Canada.

124. James, G., Witten, D., Hastie, T., Tibshirani, R., 2013. An introduction to statistical learning: with applications in R. New York: Springer.

125. Jerlov, N.G., 1976. Marine Optics. Elsevier, Amsterdam.

126. Jones, E.M., Baird, M.E., Mongin, M., Parslow, J., Skerratt, J., Lovell, J., Margvelashvili, N., Matear, R.J., Wild-Allen, K., Robson, B., Rizwi, F., Oke, P., King, E., Schroeder, T., Steven, A., Taylor, J., 2016a. Use of remote-sensing reflectance to constrain a data assimilating marine biogeochemical model of the Great Barrier Reef. Biogeosciences 13, 6441-6469.

127. Jones, R., Bessell-Browne, P., Fisher, R., Klonowski, W., Slivkoff, M., 2016b. Assessing the impacts of sediments from dredging on corals. Marine Pollution Bulletin 102, 9-29.

128. Jones, R., Giofre, N., Luter, H.M., Neoh, T.L., Fisher, R., Duckworth, A., 2020. Responses of corals to chronic turbidity. Scientific Reports 10, 4762.

129. Joo, M., Raymond, M.A.A., McNeil, V.H., Huggins, R., Turner, R.D.R., Choy, S., 2012. Estimates of sediment and nutrient loads in 10 major catchments draining to the Great Barrier Reef during 2006–2009. Marine Pollution Bulletin 65, 150-166.

130. Kirk, J., 1981. Monte Carlo study of the nature of the underwater light field in, and the relationships between optical properties of turbid yellow waters. Marine and Freshwater Research 32, 517-532.

131. Kirk, J.T., 1997. Absorption coefficients of the ocean: their measurement and implications for remote sensing, pp. 192-197.

132. Kirk, J.T.O., 1977. Attenuation of light in natural waters. Marine & Freshwater Research 28, 497-508.

133. Kirk, J.T.O., 1980. Spectral absorption properties of natural waters: contribution of the soluble and particulate fractions to light absorption in some inland waters of south-eastern Australia. Marine & Freshwater Research 31, 287-296.

134. Kirk, J.T.O., 1992. The Nature and Measurement of the Light Environment in the Ocean, in: Falkowski, P.G., Woodhead, A.D., Vivirito, K. (Eds.), Primary Productivity and Biogeochemical Cycles in the Sea. Springer US, Boston, MA, pp. 9-29.

135. Kirk, J.T.O., 2011. Light and Photosynthesis in Aquatic Ecosystems, 3rd Ed. Cambridge University Press.

136. Kleypas, J.A., 1997. Modeled estimates of global reef habitat and carbonate production since the Last Glacial Maximum. Paleoceanography 12, 533-545.

137. Kleypas, J.A., McManus, J.W., Meñez, L.A., 1999. Environmental limits to coral reef development: where do we draw the line? American Zoologist 39, 146-159.

138. Kluibenschedl, A., Lamare, M.D., Nelson, W.A., Barr, N.G., Hepburn, C.D., 2021. Low irradiance amplifies negative effects of ocean acidification on recruitment of coralline algae communities. Marine Ecology Progress Series 674, 103-113.

139. Kroon, F.J., 2012. Towards ecologically relevant targets for river pollutant loads to the Great Barrier Reef. Marine Pollution Bulletin 65, 261-266.

140. Kuhnert, P.M., Henderson, B.L., Lewis, S.E., Bainbridge, Z.T., Wilkinson, S.N., Brodie, J.E., 2012. Quantifying total suspended sediment export from the Burdekin River catchment using the loads regression estimator tool. Water Resour. Res. 48, 18.

141. Kumar, L., Skidmore, A.K., Knowles, E., 1997. Modelling topographic variation in solar radiation in a GIS environment. International Journal of Geographical Information Science 11, 475-497.

142. Lalli, C., Parsons, T.R., 1997. Biological oceanography: an introduction. Butterworth-Heinemann.

143. Larcombe, P., Carter, R.M., 2004. Cyclone pumping, sediment partitioning and the development of the Great Barrier Reef shelf system: a review. Quaternary Science Reviews 23, 107-135.

144. Leahy, S.M., Kingsford, M.J., Steinberg, C.R., 2013. Do Clouds Save the Great Barrier Reef? Satellite Imagery Elucidates the Cloud-SST Relationship at the Local Scale. PLOS ONE 8, e70400.

145. Lee, Z., 2009. KPAR: An optical property associated with ambiguous values. J. Lake Sci 21, 159-164.

146. Lee, Z., Carder, K.L., Arnone, R.A., 2002. Deriving inherent optical properties from water color: a multiband quasi-analytical algorithm for optically deep waters. Appl. Opt. 41, 5755-5772.

147. Lee, Z., Carder, K.L., Mobley, C.D., Steward, R.G., Patch, J.S., 1998. Hyperspectral remote sensing for shallow waters. I. A semianalytical model. Appl. Opt. 37, 6329-6338.

148. Lee, Z., Shang, S., Du, K., Wei, J., Arnone, R., 2014. Usable solar radiation and its attenuation in the upper water column. Journal of Geophysical Research: Oceans 119, 1488-1497.

149. Lee, Z.-P., Darecki, M., Carder, K.L., Davis, C.O., Stramski, D., Rhea, W.J., 2005a. Diffuse attenuation coefficient of downwelling irradiance: An evaluation of remote sensing methods. Journal of Geophysical Research: Oceans 110, n/a-n/a.

150. Lee, Z.-P., Du, K.-P., Arnone, R., 2005b. A model for the diffuse attenuation coefficient of downwelling irradiance. Journal of Geophysical Research: Oceans 110.

151. Legendre, P., 2018. lmodel2: Model II Regression, R package version 1.7-3.

152. Lesser, M.P., 2011. Coral Bleaching: Causes and Mechanisms, in: Dubinsky, Z., Stambler, N. (Eds.), Coral Reefs: An Ecosystem in Transition. Springer Netherlands, Dordrecht, pp. 405-419.

153. Lesser, M.P., Farrell, J.H., 2004. Exposure to solar radiation increases damage to both host tissues and algal symbionts of corals during thermal stress. Coral Reefs 23, 367-377.

154. Lewis, S., Brodie, J., Endo, G.G.K., Lough, J., Bainbridge, Z., 2014. Synthesizing Historical Land Use Change, Fertiliser and Pesticide Usage and Pollutant Load Data in the Regulated Catchments to Quantify Baseline and Changing Pollutant Loads Exported to the Great Barrier Reef, Centre for Tropical Water & Aquatic Ecosystem Research (TropWATER) Technical Report 14/20, James Cook University, Townsville, p. 105.

155. Lewis, S.E., Brodie, J.E., Bainbridge, Z.T., Rohde, K.W., Davis, A.M., Masters, B.L., Maughan, M., Devlin, M.J., Mueller, J.F., Schaffelke, B., 2009. Herbicides: A new threat to the Great Barrier Reef. Environmental Pollution 157, 2470-2484.

156. Liaw, A., Wiener, M., 2002. Classification and Regression by randomForest. R News 2, 18-22.

157. Logan, M., Fabricius, K., Weeks, S., Canto, M., Noonan, S., Wolanski, E., Brodie, J., 2013. The relationship between Burdekin River discharges and photic depth in the central Great Barrier Reef, Report to the National Environmental Research Program. Reef and Rainforest Research Centre Limited, Cairns p. 29 pp.

158. Loisel, H., Stramski, D., Mitchell, B.G., Fell, F., Fournier-Sicre, V., Lemasle, B., Babin, M., 2001. Comparison of the ocean inherent optical properties obtained from measurements and inverse modeling. Appl. Opt. 40, 2384-2397.

159. Lønborg, C., McKinna, L.I.W., Slivkoff, M.M., Carreira, C., 2021. Coloured dissolved organic matter dynamics in the Great Barrier Reef. Continental Shelf Research 219, 104395.

160. Long, M., Rheuban, J., Berg, P., Zieman, J., 2012. A comparison and correction of light intensity loggers to photosynthetically active radiation sensors. Limnology and Oceanography: Methods 10, 416-424.

161. Lucas, P., Webb, T., Valentine, P., Marsh, H., 1997. The outstanding universal value of the Great Barrier Reef World Heritage Area. Great Barrier Reef Marine Park Authority, Townsville, Australia.

162. MacNeil, M.A., Mellin, C., Matthews, S., Wolff, N.H., McClanahan, T.R., Devlin, M., Drovandi, C., Mengersen, K., Graham, N.A.J., 2019. Water quality mediates resilience on the Great Barrier Reef. Nat. Ecol. Evol. 3, 620-627.

163. Magno-Canto, M.M., McKinna, L.I.W., Robson, B.J., Fabricius, K.E., 2019. Model for deriving benthic irradiance in the Great Barrier Reef from MODIS satellite imagery. Opt. Express 27, A1350-A1371.

164. Magno-Canto, M.M., McKinna, L.I.W., Robson, B.J., Fabricius, K.E., Garcia, R., 2020. Model for deriving benthic irradiance in the Great Barrier Reef from MODIS satellite imagery: erratum. Opt. Express 28, 27473-27475.

165. Manov, D.V., Chang, G.C., Dickey, T.D., 2004. Methods for Reducing Biofouling of Moored Optical Sensors. Journal of Atmospheric and Oceanic Technology 21, 958-968.

166. Maritorena, S., Siegel, D.A., Peterson, A.R., 2002. Optimization of a semianalytical ocean color model for global-scale applications. Appl. Opt. 41, 2705-2714.

167. Mascarenhas, V., Keck, T., 2018. Marine Optics and Ocean Color Remote Sensing, in: Jungblut Simon, Liebich Viola, Maya, B. (Eds.), YOUMARES 8 – Oceans Across Boundaries: Learning from each other., Springer, Cham, pp. 41-54.

168. Mathews, E.J., Heap, A.D., Woods, M., 2007. Inter-reefal seabed sediments and geomorphology of the Great Barrier Reef, a spatial analysis. Geoscience Australia, p. 140.

169. McCave, I.N., 2009. Nepheloid Layers, in: Steele, J.H. (Ed.), Encyclopedia of Ocean Sciences (Second Edition). Academic Press, Oxford, pp. 8-18.

170. McClain, C.R., Feldman, G.C., Hooker, S.B., 2004. An overview of the SeaWiFS project and strategies for producing a climate research quality global ocean bio-optical time seris. Deep-Sea Res. Part II 51, 5-42.

171. McCloskey, G., Waters, D., Baheerathan, R., Darr, S., Dougall, C., Ellis, R., Fentie, B., Hateley, L., 2017. Modelling pollutant load changes due to improved management practices in the Great Barrier Reef catchments: updated methodology and results, Technical Report for Reef Report Card 2014, Queensland Department of Natural Resources and Mines, Brisbane, Queensland, Australia, p. 185.

172. McKenzie, L., Collier, C., Waycott, M., Unsworth, R., Yoshida, R., Smith, N., 2012. Monitoring inshore seagrasses of the GBR and responses to water quality, 12th International Coral Reef Symposium, 9-13 July 2012, Cairns, Queensland, Australia.

173. McKenzie, L.J., Unsworth, R.K.F., Waycott, M., 2010. Reef Rescue Marine Monitoring Program: Intertidal Seagrass, Annual Report for the sampling period 1st September 2009 – 31st May 2010, Fisheries Queensland, Cairns, Australia, p. 136.

174. McKergow, L.A., Prosser, I.P., Hughes, A.O., Brodie, J., 2005. Sources of sediment to the Great Barrier Reef World Heritage Area. Marine Pollution Bulletin 51, 200-211.

175. McKinna, L.I.W., Fearns, P.R.C., Weeks, S.J., Werdell, J.P., Reichstetter, M., Franz, B.A., Shea, D.M., Feldman, G.C., 2015. A semianalytical ocean color inversion algorithm with explicit water column depth and substrate reflectance parameterization. Journal of Geophysical Research: Oceans 120, 1741-1770.

176. McKinna, L.I.W., Werdell, P.J., 2018. Approach for identifying optically shallow pixels when processing ocean-color imagery. Opt. Express 26, A915-A928.

177. Mitchell, B.G., Bricaud, A., Carder, K., Cleveland, J., Ferrari, G., Gould, R., Kahru, M., Kishino, M., Maske, H., Moisan, T., Moore, L., Nelson, N., Phinney, D., Reynolds, R., Sosik, H., Stramski, D., Tassan, S., Trees, C., Weidemann, A., Wieland, J., Vodacek, A., 2000. Determination of spectral absorption coefficients of particles, dissolved material and

phytoplankton for discrete water samples, in: Fargion, F., Mueller, J.L. (Eds.), Ocean optics protocols for satellite ocean color sensor validation, revision 2. NASA Goddard Space Flight Center, Greenbelt, Maryland, pp. 125 - 153.

178. Mobley, C., 2001. Radiative transfer in the ocean, in: Steele, J.H., Thorpe, S.A., Turekian, K.K. (Eds.), Encyclopedia of Ocean Sciences. Academic Press, pp. 2321-2330.

179. Mobley, C., Stramski, D., Bissett, W., Boss, E., 2004. Optical Modeling of Ocean Waters: Is the Case 1 - Case 2 Classification Still Useful? Oceanography (Washington D.C.) 17.

180. Mobley, C.D., 1994. Light and water: radiative transfer in natural waters. Academic Press.

181. Mobley, C.D., Sundman, L.K., 2008. Hydrolight 5 Ecolight 5 Users' Guide. Sequoia Scientific.

182. Mobley, C.D., Werdell, J., Franz, B., Ahmad, Z., Bailey, S., 2016. Atmospheric correction for satellite ocean color radiometry, NASA Technical Memorandum 2016–217551, GSFC-E-DAA-TN35509, NASA Goddard Space Flight Center.

183. Moore, T.S., Dowell, M.D., Bradt, S., Verdu, A.R., 2014. An optical water type framework for selecting and blending retrievals from bio-optical algorithms in lakes and coastal waters. Remote sensing of environment 143, 97-111.

184. Morel, A., 1988. Optical modeling of the upper ocean in relation to its biogenous matter content (case I waters). Journal of Geophysical Research: Oceans 93, 10749-10768.

185. Morel, A., 1997. Optical properties of oceanic case 1 waters revisited, Ocean Optics XIII. SPIE.

186. Morel, A., Gentili, B., 2009. A simple band ratio technique to quantify the colored dissolved and detrital organic material from ocean color remotely sensed data. Remote Sensing of Environment 113, 998-1011.

187. Morel, A., Huot, Y., Gentili, B., Werdell, P.J., Hooker, S.B., Franz, B.A., 2007. Examining the consistency of products derived from various ocean color sensors in open ocean (Case 1) waters in the perspective of a multi-sensor approach. Remote Sensing of Environment 111, 69-88.

188. Morel, A., Prieur, L., 1977. Analysis of variations in ocean color. Limnology and Oceanography 22, 709-722.

189. Morgan, K.M., Perry, C.T., Johnson, J.A., Smithers, S.G., 2017. Nearshore Turbid-Zone Corals Exhibit High Bleaching Tolerance on the Great Barrier Reef Following the 2016 Ocean Warming Event. Frontiers in Marine Science 4.

190. Mueller, J.L., 2000. Chapter 3: SeaWIFS algorithm for the diffuse attenuation coefficient, K(490), using water-leaving radiances at 490 and 555 nm, SeaWiFS Postlaunch Techinal Report Series, SeaWIFS Postlaunch Calibration and Validation Analyses, in: Hooker, S.B.,

Firestone, E.R. (Eds.), SeaWIFS Postlaunch Calibration and Validation Analyses NASA Goddard Space Flight Center, pp. 24-27.

191. Muir, P.R., Wallace, C.C., Done, T., Aguirre, J.D., 2015. Limited scope for latitudinal extension of reef corals. Science 348, 1135-1138.

192. Mumby, P.J., Chisholm, J.R., Edwards, A.J., Andrefouet, S., Jaubert, J., 2001. Cloudy weather may have saved Society Island reef corals during the 1998 ENSO event. Marine Ecology Progress Series 222, 209-216.

193. NASA Goddard Space Flight Center, Ocean Ecology Laboratory, Ocean Biology Processing Group, Moderate-resolution Imaging Spectroradiometer (MODIS) Aqua Ocean Color Data; 2018 Reprocessing, NASA OB.DAAC, Greenbelt, MD, USA. data/10.5067/AQUA/MODIS/L2/OC/2018. Accessed on 07/06/2020.

194. National Climate Centre - BOM, 2012. Special Climate Statement 38: Australia's wettest two-year period on record; 2010–2011, in: Meteorology, B.o. (Ed.), Special Climate Statement 38. Bureau of Meteorology, Bureau of Meteorology, Melbourne VIC 3001 Australia.

195. Neil, D.T., Orpin, A.R., Ridd, P.V., Yu, B., 2002. Sediment yield and impacts from river catchments to the Great Barrier Reef lagoon: a review. Marine and Freshwater Research 53, 733-752.

196. O'Reilly, J.E., Maritorena, S., Mitchell, B.G., Siegel, D.A., Carder, K.L., Garver, S.A., Kahru, M., McClain, C., 1998. Ocean color chlorophyll algorithms for SeaWiFS. Journal of Geophysical Research: Oceans 103, 24937-24953.

197. O'Reilly, J.E., et al., 2000. SeaWiFS postlaunch calibration and validation analyses, Part 3, NASA Tech. Memo., NASA, TM-2000-206892, vol. 11, p. 49.

198. Orpin, A.R., Ridd, P.V., 2012. Exposure of inshore corals to suspended sediments due to wave-resuspension and river plumes in the central Great Barrier Reef: A reappraisal. Continental Shelf Research 47, 55-67.

199. Oubelkheir, K., Clementson, L.A., Webster, I.T., Ford, P.W., Dekker, A.G., Radke, L., Daniel, P.J., 2006. Using inherent optical properties to investigate biogeochemical dynamics in a tropical macrotidal coastal system. Journal of Geophysical Research 111.

200. Packett, R., Dougall, C., Rohde, K., Noble, R., 2009. Agricultural lands are hot-spots for annual runoff polluting the southern Great Barrier Reef lagoon. Marine pollution bulletin 58, 976-986.

201. Petus, C., da Silva, E.T., Devlin, M., Wenger, A.S., Álvarez-Romero, J.G., 2014. Using MODIS data for mapping of water types within river plumes in the Great Barrier Reef,

Australia: Towards the production of river plume risk maps for reef and seagrass ecosystems. Journal of Environmental Management 137, 163-177.

202. Petus, C., Devlin, M., Teixera da Silva, E., Lewis, S., Waterhouse, J., Wenger, A., Bainbridge, Z., Tracey, D., 2018. Defining wet season water quality target concentrations for ecosystem conservation using empirical light attenuation models: A case study in the Great Barrier Reef (Australia). Journal of environmental management 213, 451-466.

203. Pitcher, R., Doherty, P., Arnold, P., Hooper, J., Gribble, N., Bartlett, C., Browne, M., Campbell, N., Cannard, T., Cappo, M., Carini, G., Chalmers, S., Cheers, S., Chetwynd, D., Colefax, A., Coles, R., Cook, S., Davie, P., De'ath, G., Devereux, D., Done, B., Donovan, T., Ehrke, B., Ellis, N., Ericson, G., Fellegara, I., Forcey, K., Furey, M., Gledhill, D., Good, N., Gordon, S., Haywood, M., Jacobsen, I., Johnson, J., Jones, M., Kinninmoth, S., Kistle, S., Last, P., Leite, A., Marks, S., McLeod, I., Oczkowicz, S., Rose, C., Seabright, D., Sheils, J., Sherlock, M., Skelton, P., Smith, D., Smith, G., Speare, P., Stowar, M., Strickland, C., Sutcliffe, P., Van der Geest, C., Venables, W., Walsh, C., Wassenberg, T., Welna, A., Yearsley, G., 2007. Seabed biodiversity on the continental shelf of the Great Barrier Reef World Heritage Area, AIMS/CSIRO/QM/QDPI CRC Reef Research Task Final Report., p. 315.

204. Platt, T., Sathyendranath, S., White, G.N., III, Ravindran, P., 1994. Attenuation of visible light by phytoplankton in a vertically structured ocean: solutions and applications. Journal of Plankton Research 16, 1461-1487.

205. Preisendorfer, R.W., 1986. Secchi disk science: Visual optics of natural waters1. Limnology and Oceanography 31, 909-926.

206. Preisendorfer, R.W., Mobley, C.D., 1988. Principal Component Analysis in Meteorology and Oceanography. Elsevier.

207. R Core Team, 2017. R: A Language and Environment for Statistical Computing. R Foundation for Statistical Computing, Vienna, Austria.

208. R Core Team, 2019. R: A language and environment for statistical computing. R Foundation for Statistical Computing, Vienna, Austria.

209. R Core Team, 2021. R: A Language and Environment for Statistical Computing. R Foundation for Statistical Computing, Vienna, Austria.

210. Ralph, P.J., Durako, M.J., Enríquez, S., Collier, C.J., Doblin, M.A., 2007. Impact of light limitation on seagrasses. Journal of Experimental Marine Biology and Ecology 350, 176-193.

211. Reichstetter, M., 2016. Parameterization of bottom spectral reflectance for shallow water ocean color inversion models, School of Geography, Planning and Environmental Management. The University of Queensland.

212. Reichstetter, M., Fearns, P., Weeks, S., McKinna, L., Roelfsema, C., Furnas, M., 2015. Bottom Reflectance in Ocean Color Satellite Remote Sensing for Coral Reef Environments. Remote Sensing 7, 15852.

213. Richmond, R.H., Wolanski, E., 2011. Coral Research: Past Efforts and Future Horizons, in: Dubinsky, Z., Stambler, N. (Eds.), Coral Reefs: An Ecosystem in Transition. Springer Netherlands, Dordrecht, pp. 3-10.

214. Ridgway, K.R., 2007. Long-term trend and decadal variability of the southward penetration of the East Australian Current. Geophysical Research Letters 34.

215. Rigby, P., Steinberg, C.R., Williams, D.K., Brinkman, G., Brinkman, R., Tonin, H., Hughes, D., 2014. Real-Time marine observing systems: Challenges, benefits and opportunities in Australian coastal waters. Australian Journal of Civil Engineering 12, 83-99.

216. Robillot, C., Logan, M., Baird, M., Waterhouse J., Martin, K., Schaffelke, B., 2018. Testing and implementation of an improved water quality index for the 2016 and 2017 Great Barrier Reef Report Cards: Summary Report, Report to the National Environmental Science Program., Reef and Rainforest Research Centre Limited, Cairns, p. 65.

217. Robinson, I.S., 1985. Satellite Oceanography: An introduction for oceanographers and remote sensing scientists. Ellis Horwood Series in Marine Science.

218. Robinson, I.S., 2004. Measuring the Oceans from Space: The principles and methods of satellite oceanography, 1 ed. Springer-Verlag Berlin Heidelberg.

219. Robinson, W.D., Franz, B.A., Patt, F.S., Bailey, S.W., Werdell, P.J., 2003. Masks and flags update, in: Hooker, S.B., Firestone, E.R. (Eds.), NASA Technical Memorandum 2003–206892, SeaWIFS Postlaunch Technical Report Series, Algorithm updates for the fourth SeaWiFS data reprocessing, NASA Goddard Space Flight Center, pp. 34-40.

220. Robson, B., Canto, M., Collier, C., DiPerna, S., Logan, M., Menendez, P., McKinna, L., Noonan, S., Fabricius, K., 2019. Benthic light as ecologically-validated GBR-wide indicator for water quality, Report to the National Environmental Science Programme. Reef and Rainforest Research Centre Limited, Cairns, Queensland, Australia, p. 40.

221. Sakshaug, E., Bricaud, A., Dandonneau, Y., Falkowski, P.G., Kiefer, D.A., Legendre, L., Morel, A., Parslow, J., Takahashi, M., 1997. Parameters of photosynthesis: definitions, theory and interpretation of results. Journal of Plankton Research 19, 1637-1670.

222. Schaeffer, B., Hagy, J., Stumpf, R., 2013. Approach to developing numeric water quality criteria for coastal waters: transition from SeaWiFS to MODIS and MERIS satellites. APPRES 7, 073544.

223. Schaffelke, B., Carleton, J., Skuza, M., Zagorskis, I., Furnas, M.J., 2012. Water quality in the inshore Great Barrier Reef lagoon: Implications for long-term monitoring and management. Marine Pollution Bulletin 65, 249-260.

224. Schaffelke, B., Collier, C., Kroon, F., Lough, J., McKenzie, L., Ronan, M., Uthicke, S., Brodie, J., 2017. Scientific Consensus Statement 2017: A synthesis of the science of land-based water quality impacts on the Great Barrier Reef. Chapter 1: The condition of coastal and marine ecosystems of the Great Barrier Reef and their responses to water quality and disturbances, State of Queensland, 2017.

225. Schroeder, T., Devlin, M.J., Brando, V.E., Dekker, A.G., Brodie, J.E., Clementson, L.A., McKinna, L., 2012. Inter-annual variability of wet season freshwater plume extent into the Great Barrier Reef lagoon based on satellite coastal ocean colour observations. Marine Pollution Bulletin 65, 210-223.

226. Schulzweida, U., 2020. CDO User Guide (Version 1.9.9), in: Zenodo (Ed.). Zenodo.

227. Seegers, B.N., Stumpf, R.P., Schaeffer, B.A., Loftin, K.A., Werdell, P.J., 2018. Performance metrics for the assessment of satellite data products: an ocean color case study. Opt. Express 26, 7404-7422.

228. Shaw, M., Furnas, M.J., Fabricius, K., Haynes, D., Carter, S., Eaglesham, G., Mueller, J.F., 2010. Monitoring pesticides in the Great Barrier Reef. Marine Pollution Bulletin 60, 113-122.

229. Siegel, D.A., Wang, M., Maritorena, S., Robinson, W., 2000. Atmospheric correction of satellite ocean color imagery: the black pixel assumption. Appl. Opt. 39, 3582-3591.

230. Skerratt, J.H., Mongin, M., Baird, M.E., Wild-Allen, K.A., Robson, B.J., Schaffelke, B., Davies, C.H., Richardson, A.J., Margvelashvili, N., Soja-Wozniak, M., Steven, A.D.L., 2019. Simulated nutrient and plankton dynamics in the Great Barrier Reef (2011-2016). Journal of Marine Systems 192, 51-74.

231. Slivkoff, M.M., 2014. Ocean colour remote sensing of the Great Barrier Reef waters, School of Science, Department of Imaging & Applied Physics. Curtin University.

232. Smith, R.C., Baker, K.S., 1986. Analysis of ocean optical data II, Ocean Optics VIII. International Society for Optics and Photonics, pp. 95-108.

233. Smith, R.C., Tyler, J.E., 1976. Transmission of Solar Radiation into Natural Waters, in: Smith, K.C. (Ed.), Photochemical and Photobiological Reviews: Volume 1. Springer US, Boston, MA, pp. 117-155.

234. State of Queensland, 2013. Reef Water Quality Protection Plan 2013 Securing the health and resilience of the Great Barrier Reef World Heritage Area and adjacent catchments.

235. State of Queensland, 2018. Reef 2050 Water Quality Improvement Plan 2017-2022

236. Strahl, J., Rocker, M.M., Fabricius, K.E., 2019. Contrasting responses of the coral Acropora tenuis to moderate and strong light limitation in coastal waters. Marine Environmental Research 147, 80-89.

237. Stramski, D., Babin, M., Wozniak, S.B., 2007. Variations in the optical properties of terrigenous mineral-rich particulate matter suspended in seawater. Limnology and Oceanography 52, 2418-2433.

238. Stramski, D., Kiefer, D.A., 1991. Light scattering by microorganisms in the open ocean. Progress in Oceanography 28, 343-383.

239. Suggett, D.J., Dong, L.F., Lawson, T., Lawrenz, E., Torres, L., Smith, D.J., 2013. Light availability determines susceptibility of reef building corals to ocean acidification. Coral Reefs 32, 327-337.

240. Sully, S., van Woesik, R., 2020. Turbid reefs moderate coral bleaching under climate-related temperature stress. Global Change Biology 26, 1367-1373.

241. Takahashi, S., Nakamura, T., Sakamizu, M., Woesik, R.v., Yamasaki, H., 2004. Repair machinery of symbiotic photosynthesis as the primary target of heat stress for reef-building corals. Plant and Cell Physiology 45, 251-255.

242. The State of Queensland and Commonwealth of Australia, 2003. Reef Water Quality Protection Plan; for catchments adjacent to the Great Barrier Reef World Heritage Area, Queensland, Department of Premier and Cabinet, Brisbane.

243. Titlyanov, E.A., Latypov, Y.Y., 1991. Light-dependence in scleractinian distribution in the sublittoral zone of South China Sea Islands. Coral Reefs 10, 133-138.

244. Unidata, 2021. Network Common Data Form (netCDF) version 4.4.1.1 [software], Boulder, CO: UCAR/Unidata.

245. van Woesik, R., McCaffrey, K.R., 2017. Repeated Thermal Stress, Shading, and Directional Selection in the Florida Reef Tract. Frontiers in Marine Science 4.

246. Vogel, N., Meyer, F.W., Wild, C., Uthicke, S., 2015. Decreased light availability can amplify negative impacts of ocean acidification on calcifying coral reef organisms. Marine Ecology Progress Series 521, 49-61.

247. Warner, M.E., Fitt, W.K., Schmidt, G.W., 1999. Damage to photosystem II in symbiotic dinoflagellates: a determinant of coral bleaching. Proceedings of the National Academy of Sciences 96, 8007-8012.

248. Waterhouse, J., Brodie, J., Lewis, S., Mitchell, A., 2012. Quantifying the sources of pollutants in the Great Barrier Reef catchments and the relative risk to reef ecosystems. Marine Pollution Bulletin 65, 394-406.

249. Waterhouse, J., Lønborg, C., Logan M., Petus, C., Tracey, D., Lewis, S., Tonin, H., Skuza, M., da Silva, E., Carreira, C., Costello, P., Davidson, J., Gunn, K., Wright, M., Zagorskis, I., Brinkman R., Schaffelke, B., 2017. Marine Monitoring Program: Annual Report for inshore water quality monitoring 2015-2016. Report for the Great Barrier Reef Marine Park Authority, Townsville, Australia, p. 227.

250. Weeks, S., Werdell, P., Schaffelke, B., Canto, M., Lee, Z., Wilding, J., Feldman, G., 2012. Satellite-Derived Photic Depth on the Great Barrier Reef: Spatio-Temporal Patterns of Water Clarity. Remote Sensing 4, 3781-3795.

251. Weeks, S.J., Bakun, A., Steinberg, C.R., Brinkman, R., Hoegh-Guldberg, O., 2010. The Capricorn Eddy: a prominent driver of the ecology and future of the southern Great Barrier Reef. Coral Reefs 29, 975-985.

252. Wells, S.C., Cole, S.J., Moore, R.J., Black, K.B., Khan, U., Hapuarachchi, P., Gamage, N., Hasan, M., MacDonald, A., Bari, M., Tuteja, N., 2017. Forecasting the water flows draining to the Great Barrier Reef using the G2G distributed hydrological model [Draft]. Natural Environment Research Council, Centre for Ecology & Hydrology, Wallingford, UK, p. 60.

253. Werdell, P.J., Franz, B.A., Bailey, S.W., Feldman, G.C., Boss, E., Brando, V.E., Dowell, M., Hirata, T., Lavender, S.J., Lee, Z., Loisel, H., Maritorena, S., Mélin, F., Moore, T.S., Smyth, T.J., Antoine, D., Devred, E., d'Andon, O.H.F., Mangin, A., 2013. Generalized ocean color inversion model for retrieving marine inherent optical properties. Appl. Opt. 52, 2019-2037.

254. Werdell, P.J., McKinna, L.I.W., Boss, E., Ackleson, S.G., Craig, S.E., Gregg, W.W., Lee, Z., Maritorena, S., Roesler, C.S., Rousseaux, C.S., Stramski, D., Sullivan, J.M., Twardowski, M.S., Tzortziou, M., Zhang, X., 2018. An overview of approaches and challenges for retrieving marine inherent optical properties from ocean color remote sensing. Progress in Oceanography 160, 186-212.

255. Whinney, J., Jones, R., Duckworth, A., Ridd, P., 2017. Continuous in situ monitoring of sediment deposition in shallow benthic environments. Coral Reefs 36, 521-533.

256. Wolanski, E., Drew, E., Abel, K.M., O'Brien, J., 1988. Tidal jets, nutrient upwelling and their influence on the productivity of the alga Halimeda in the Ribbon Reefs, Great Barrier Reef. Estuarine, Coastal and Shelf Science 26, 169-201.

257. Wolanski, E., Lambrechts, J., 2020. The net water circulation in the far Northern Great Barrier Reef. Estuarine, Coastal and Shelf Science 235, 106569.

258. Wolanski, E., Marshall, K., Spagnol, S., 2003. Nepheloid Layer Dynamics in Coastal Waters of the Great Barrier Reef, Australia. Journal of coastal research 19, 748-752.

259. Wolanski, E., Spagnol, S., 2000. Pollution by Mud of Great Barrier Reef Coastal Waters. Journal of coastal research 16, 1151-1156.

260. Wolff, N.H., Mumby, P.J., Devlin, M., Anthony, K.R.N., 2018. Vulnerability of the Great Barrier Reef to climate change and local pressures. Global Change Biology 24, 1978-1991.

261. Yaakub, S.M., Chen, E., Bouma, T.J., Erftemeijer, P.L.A., Todd, P.A., 2014. Chronic light reduction reduces overall resilience to additional shading stress in the seagrass Halophila ovalis. Marine Pollution Bulletin 83, 467-474.

262. Yentsch, C.S., Yentsch, C.M., Cullen, J.J., Lapointe, B., Phinney, D.A., Yentsch, S.W., 2002. Sunlight and water transparency: cornerstones in coral research. Journal of Experimental Marine Biology and Ecology 268, 171-183.

263. Zaneveld, J.R.V., 2013. Fifty years of inherent optical properties. Methods in Oceanography 7, 3-20.